LINEAR LIBRARY
C01 0068 2510

Department of Physics, UCT

Simulation of Muon-Catalysed Fusion Experiments

C. G. L. Henderson

A thesis submitted to the
University of Cape Town
for the degree of
Master of Science

April 2, 1991

The copyright of this thesis vests in the author. No quotation from it or information derived from it is to be published without full acknowledgement of the source. The thesis is to be used for private study or non-commercial research purposes only.

Published by the University of Cape Town (UCT) in terms of the non-exclusive license granted to UCT by the author.

University of Cape Town

Abstract

A Monte Carlo code MUGLU has been written for the simulation of experiments to measure alpha–muon sticking in muon catalysed deuterium–tritium fusion. The experiments simulated are those which measure the ratio of $\alpha\mu$ to α from fusion in a low density gas target by detecting collinear alpha–neutron coincidences and relying on the differing stopping powers of the α and $\alpha\mu$ ions. The Monte Carlo simulations provide estimates of geometrical and detection efficiency factors required for the calculation of the sticking coefficient from the experimental measurements. Simulations have been made of alternative experimental geometries in order to investigate the α–neutron coincidence signature and other characteristics of existing and proposed systems. The characteristics of a neutron detector used in one of the current sticking experiments (Rutherford Appleton Laboratory) have been studied experimentally, as well as simulated, using the T(d,n)α reaction to emulate the fusion source. The results obtained show that the that the dependence of the neutron detection efficiency on the position and angle of neutron incidence on the detector is significant and should be taken into account when determining sticking coefficients from alpha-neutron coincidence measurements.

I should like to thank Prof F.D. Brooks in particular, for many discussions, much encouragement, and constant availability, which made this project interesting, stimulating and enjoyable. Amongst the postgraduate students and technical staff of the physics department of UCT I should also like to thank messrs Steyn and Murray for much unasked for help with the computing and LaTeX side of things, the Allion and the Bufflon and mlle Mu for much encouragement, many suggestions and numerous games of pool. In general I should like to thank the Nuclear physics group at UCT, Dr W.A. Cilliers, the staff at NAC, the kog and the guv, my parents, siblings, flatmates and dogs.

This research was funded in part by a grant from the Foundation for Research and Development.

Contents

List of Tables

List of Figures

Preface

A brief history of Muon Catalysed Fusion

Muon catalysed fusion (MCF) was first suggested by F.C. Frank [1] of Bristol University in 1947, at about the same time that the work of Powell and collaborators [2], at the same university established the distinction between the π and the μ. In the nuclear emulsions where the pion was first observed, 600 micron tracks were seen starting from the point where the pions from cosmic rays came to rest (figure .1). These corresponded to a charged particle of mass 110 MeV and energy 4.1 MeV. These were interpreted as a π meson decaying into a μ meson[1] and an uncharged particle, possibly a photon or a neutrino.

$$\pi \longrightarrow \mu + \overline{\nu}_{\mu} \qquad (.1)$$

As the idea of having two mesons instead of one was revolutionary, a large number of ways that the meson could be injected with the required amount of energy *after* being brought to rest were investigated by Frank, and shown to be very unlikely. Among them was the fusion of a proton with a deuteron catalysed by a negative meson, giving the meson the 5.4 MeV released from the reaction.

MCF was first experimentally observed in 1957 when Alvarez et al. [5] detected tracks corresponding to muons of energy 5.4 MeV in photographs from a bubble-chamber experiment with kaons. The beam was contaminated

[1]At that time, and for some years after, the term *meson* referred simply to a particle of mass intermediate between proton and electron, not necessarily feeling the strong interaction.

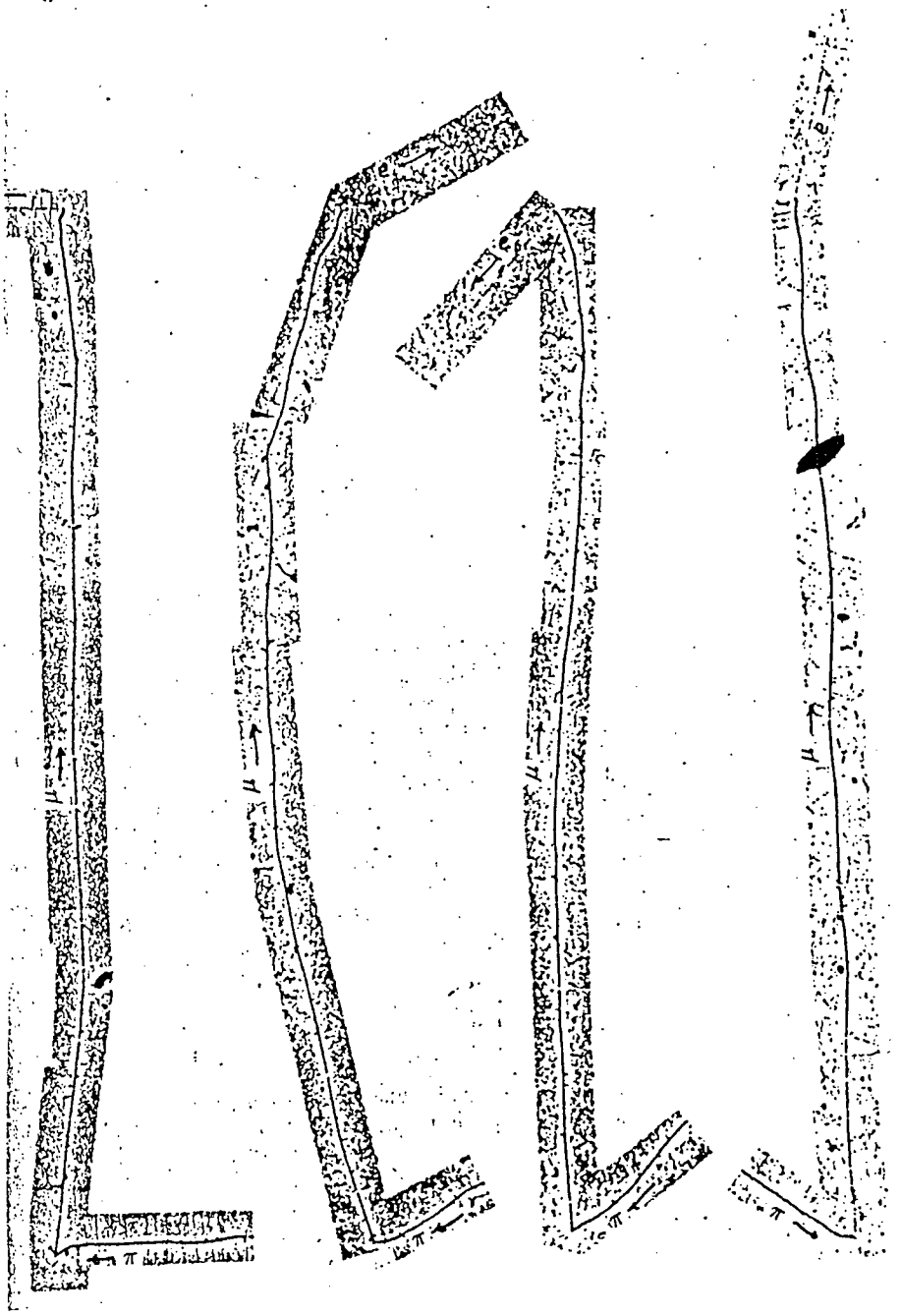

Figure .1: Four separate examples of the successive decay of a pion into a muon and then into an electron, as recorded in Kodak NT 4 emulsion. (From The Study of Elementary Particles by the Photographic Method by C.F. Powell et al. via [3]

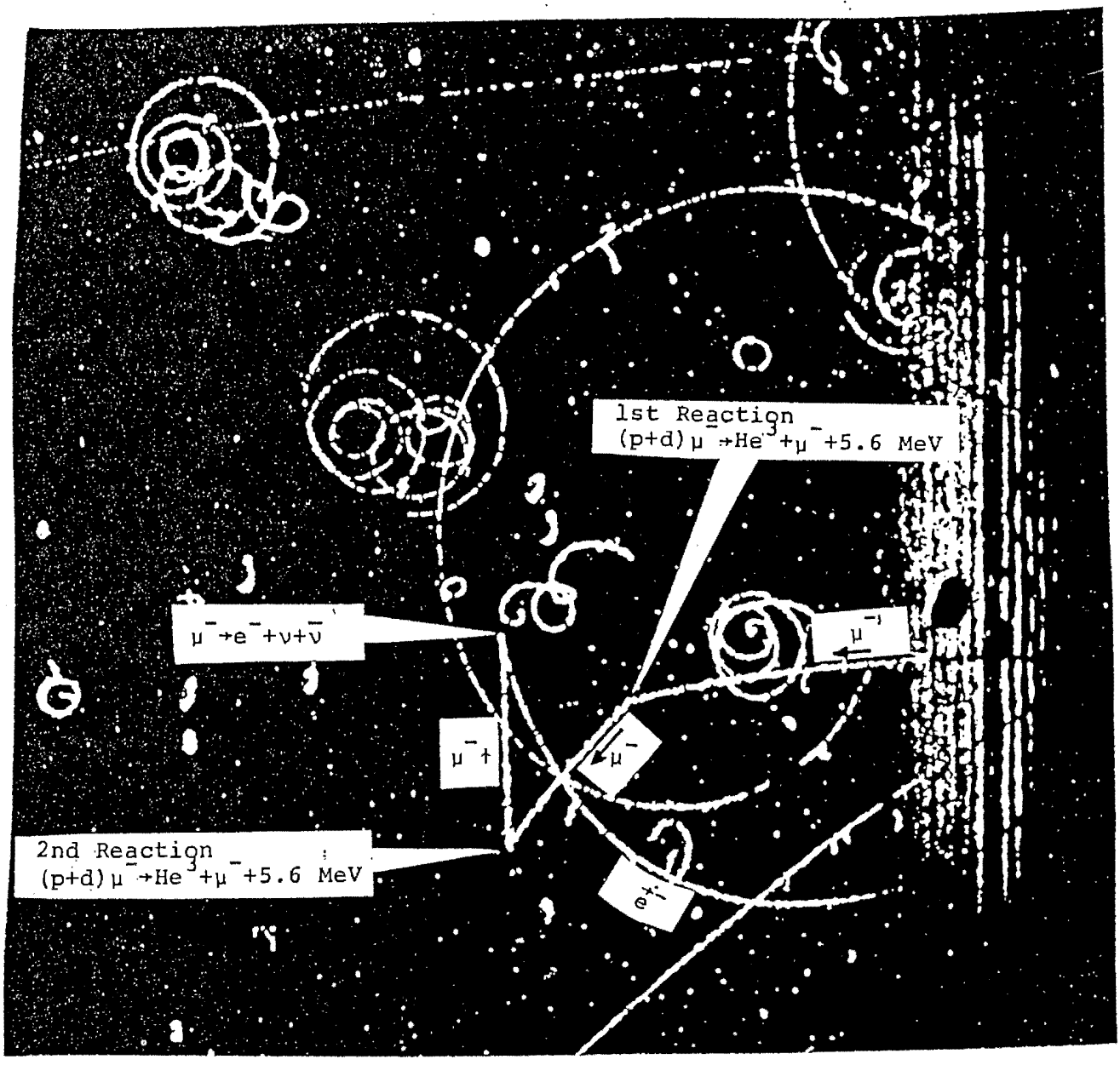

Figure .2: One of the bubble-chamber pictures showing pdμ fusion. Figure reproduced from Alvarez et al. *Adventures in Experimental Physics* α (1972),72-9 [4]

with negative pions and hence negative muons. The muon tracks were seen to stop, and then, after a gap of a millimetre or so, another muon track corresponding with an energy of about 5 MeV started. (fig 1.1)

This was consistent with a muon coming to rest in the hydrogen, being captured by a proton and transferring to a deuteron; fusion then occurring quickly on contact between the resulting $d\mu$ atom and a proton in a hydrogen molecule, resulting in the muon being released with 5.4 MeV.

Release of the muon after fusion was later discovered to be a relatively rare process, most fusions resulting in the emission of a gamma [6] and the muon remaining bound to the ^{3}He product. This ruled out any application of $pd\mu$ fusion to energy production. More attention was transferred to the study of a close relative, muon catalysed fusion in pure deuterium gas.

After observations that the speed of the muon-catalysed deuterium ($dd\mu$) fusion cycle was strongly temperature dependent [7] while hydrogen deuterium fusion ($pd\mu$) was not, Vesman suggested in 1967 [8] that mesomolecules could be formed by a resonant formation process (the transfer of energy to the excited vibrational states of molecules), as well as by the emission of an electron (Auger process). In the same vein, it was predicted by Gershtein and Ponomarev in 1977 [9] that the $td\mu$ mesomolecule formation rate should be much larger. This might allow some few thousand fusions per muon in absence of the muon sticking to the fusion product. Catalysis loss by sticking reduces this calculation to the order of a few hundreds of fusions per muon. Bystritsky measured this rate in 1980 [10], setting a lower limit on the fusion rate per muon (catalysis cycling rate) of about 100 which confirmed these predictions, generating much interest in schemes for using muon-catalysed deuterium-tritium ($dt\mu$) fusion for energy generation.

For energy production to be feasible, obviously the energy one muon releases by inducing fusions must be greater than the energy required to produce one, after taking efficiencies of accelerators, generators and muon capture into account. It is necessary to measure the number of fusions one muon can catalyse before decaying (the free muon lifetime τ_μ is 2.2μs) or becoming irretrievably bound to a charged product from fusion, namely an alpha particle. The average time for one catalysis cycle (from free muon to fusion) is much shorter than τ_μ, so the limiting factor in $dt\mu$ fusion is the fraction of muons which stick to the alpha particles and hence are removed from the catalysis cycle.

Petrov [11] estimates that the cost in energy to produce a π^- is around 4.5 GeV, so if all the pion decays are utilised, many fusions (about 200, if the residual charged particles in the accelerator beam are used for energy

production) are required per muon to give a net energy gain. Power generation, once efficiencies have been taken into account, appears to require around 500 fusions per muon. Petrov has also suggested ways to utilise the 14 MeV fusion neutrons more effectively, and reduce the effective pion production energy by using the residual charged particles in the beam for isotope production. Nevertheless, the feasibility of power generation, whether pure MCF or hybrid, relies strongly on the number of fusions per muon, the one important factor in the process which is not known to any great degree of accuracy. Once this is known, large technical problems will have to be solved, among them the need for very efficient, high-current accelerators. Ways of snaring all the muons from pion decay are also attracting attention.

The first estimates of dtμ fusion rates and catalyst losses were obtained from measuring the yield of muonic helium X-rays [12,13], and from studies of the time evolution of the fusion neutron flux [14,15,16,17,11] after a known quantity of muons was injected into a DT mixture. By fitting decay exponentials to the flux measurements, the catalysis cycling rate, λ_c, could be estimated. As the fusion neutron flux depends on the number of free muons in the mixture, its decrease with time is a direct indication of how quickly muons are removed from the catalysis cycle, either by decay, sticking to the alpha fusion product, or scavenging by other nuclei present in the gas not undergoing fusion. From this, the sticking coefficient ω_s of muons to alphas, that is, the ratio of the number of muons that remain bound to the alpha after fusion to the number which are liberated, could be calculated. Jones et al. in 1986 [15] saw unexpected density effects, with the sticking coefficient continuing to drop at higher pressures. Other experiments [18,14] measured the cycling rate, though not as dependent on temperature as originally expected, still to be increasing at temperatures of 800K, long after the expected peak [19] at 550K. The feasibility of MCF for power generation seemed good. At worst, physicists were having fun studying a richly diverse field.

However, these indirect measurements of sticking coefficients in muon catalysed fusion require knowledge of absolute efficiencies of the neutron detectors (to calculate the initial number of fusion neutrons) and muon monitors, which measure the number of muons stopping in the DT mixture. Hence the measurements of ω_s and λ_c are prone to the large systematic errors inherent in these efficiencies. Direct measurements of the sticking coefficient, where both products of the fusion process are observed, [20,21,22] are now being performed.

Chapter 1

Introduction

1.1 Physics of muon catalysed fusion

Muon Catalysed Fusion (MCF) is a process involving several branches of physics — atomic, molecular and nuclear. It is a valuable tool in the study of the physics of exotic atoms, as the formation rates are dependent on the energy levels and spins of the atoms and molecules and these can be studied by looking at fusion rates at various temperatures, pressures and mixtures of gas. There are several reviews of muon catalysed fusion, references [18,27,28,29,30] being a selection. Table 1.1 gives information about the various types of MCF in hydrogen.

Table 1.1: Types of muon catalysed fusion and their Q values, catalysis cycling rates λ_c, and their sticking coefficients ω.

Fusion type	Q value (MeV)	$\lambda_c(s^{-1})$	ω (%)	reference
$pd\mu \longrightarrow {}^3He+\gamma$	5.4	$\sim 3 \times 10^5$	84	[23]
$pt\mu \longrightarrow {}^4He+\gamma$	19.8	$\sim 7 \times 10^4$	~ 90	[24]
$dd\mu \longrightarrow {}^3He+n$	3.3	$\sim 1 \times 10^5$	12	[18]
$dd\mu \longrightarrow {}^3H+p$	4		-	
$dt\mu \longrightarrow {}^4He+n$	17.6	$\sim 1 \times 10^9$	0.6	[25,18]
$tt\mu \longrightarrow {}^4He+2n$	11.3		~ 10	[26]

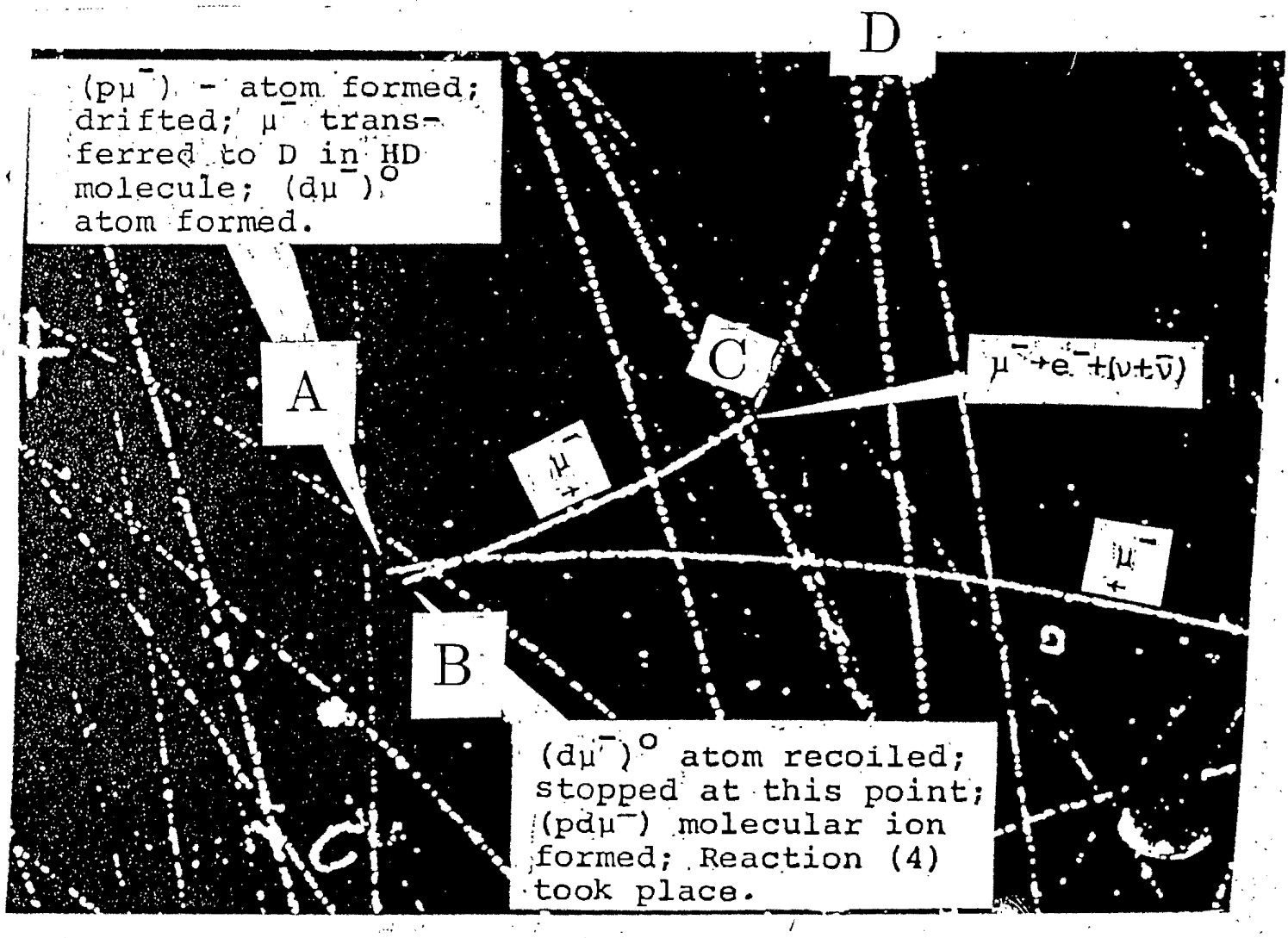

Figure 1.1: One of the bubble-chamber pictures showing pdμ fusion. Figure reproduced from Alvarez et al. *Adventures in Experimental Physics* α (1972),72-9 [4]
A: muon brought to rest; captured by a Hydrogen nucleus; transferred to a Deuteron. B: pdμ mesomolecule formed. C: Muon decays into an electron and neutrino-antineutrino pair.

1.1.1 pdμ Fusion — The Auger process

Firstly, let us consider the simplest and first observed case, that of pdμ fusion, observed by Alvarez et al. in 1957. [5] One of their bubble chamber photographs is shown in fig 1.1

A negative muon (from here on *muon* and μ will refer always to a negative muon) is brought to rest via ionising collisions (A) in a hydrogen bubble chamber, and captured by a proton by the Auger process:

$$H + \mu \longrightarrow p\mu + e^- \tag{1.1}$$

Since the muon orbits the proton 200 times more closely than the electron on account of its greater mass, the charge on the proton is screened and the pμ is essentially a neutral particle. It diffuses in the bubble chamber until it collides with a H-D molecule. Muon transfer from p to d is favoured due to isotopic mass shift and happens quickly and irrevocably:

$$p\mu + D \longrightarrow d\mu + p + e^- + 135eV \tag{1.2}$$

The difference in binding energy goes into the recoil of the deuteron. This explains the gap between A and B seen in most bubble chamber photographs of MCF.

The dμ then comes into contact with a hydrogen molecule and a pdμ *mesomolecule*[1] is formed (B) by ejecting one of the electrons.

$$d\mu + H_2 \longrightarrow pd\mu + H + e^- \tag{1.3}$$

The internuclear distance and vibrational energy of the mesomolecule are such that it has similar properties to a plasma with temperature and pressure equivalent to that at the centre of a white dwarf star [27]. Needless to say, fusion follows extremely rapidly: (figure 1.2a)

$$pd\mu \longrightarrow {}^3He\mu + \gamma \quad (Q = 5.4\ MeV). \tag{1.4}$$

Occasionally the ^{3}Heμ undergoes the analogue to internal conversion. The muon absorbs a virtual photon (figure 1.2b), and the conversion muon is released from the ^{3}He fusion product with 5.4 MeV:

$$pd\mu \longrightarrow {}^3He + \mu(5.4\ MeV) \tag{1.5}$$

[1] A more correct term would be 'muonic molecular' or 'mesomolecular' ion. 'Muomolecule' is also used. For the sake of familiarity, and because 'mesomolecule' rolls more easily off the tongue, I will stick to the old usage.

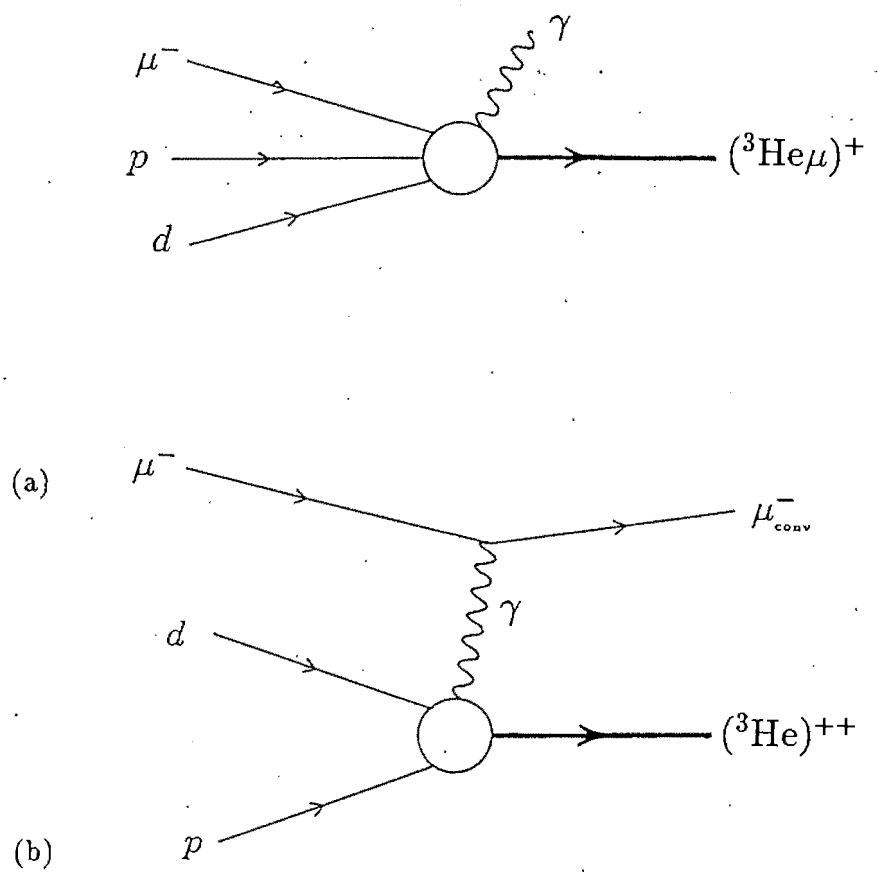

Figure 1.2: Feynman diagrams of pdμ fusion (a) with and (b) without muon sticking

(fig 1.1) producing a track (B–C). The muon may or may not catalyse subsequent fusions before decaying into a 15–50 MeV electron and two (unobserved) neutrinos as in this photograph

$$\mu \longrightarrow e^- + \overline{\nu}_e + \nu_\mu \tag{1.6}$$

(track C–D). If the muon does not absorb a virtual photon (as happens more than 80% of the time) it sticks to the helium nucleus. The latter process is not observable in bubble chamber experiments.

1.1.2 ddμ and dtμ fusion — a resonant process

While some interest still remains in the study of pdμ fusion, especially in the study of the Wolfenstein-Gershtein effect [23], most of the effort is being channelled into the research of the fusion of the heavier hydrogen isotopes, ddμ and dtμ fusion, which have the advantage of a lower proportion of muon sticking, and (in the case of dtμ fusion), much higher rates and a higher Q value.

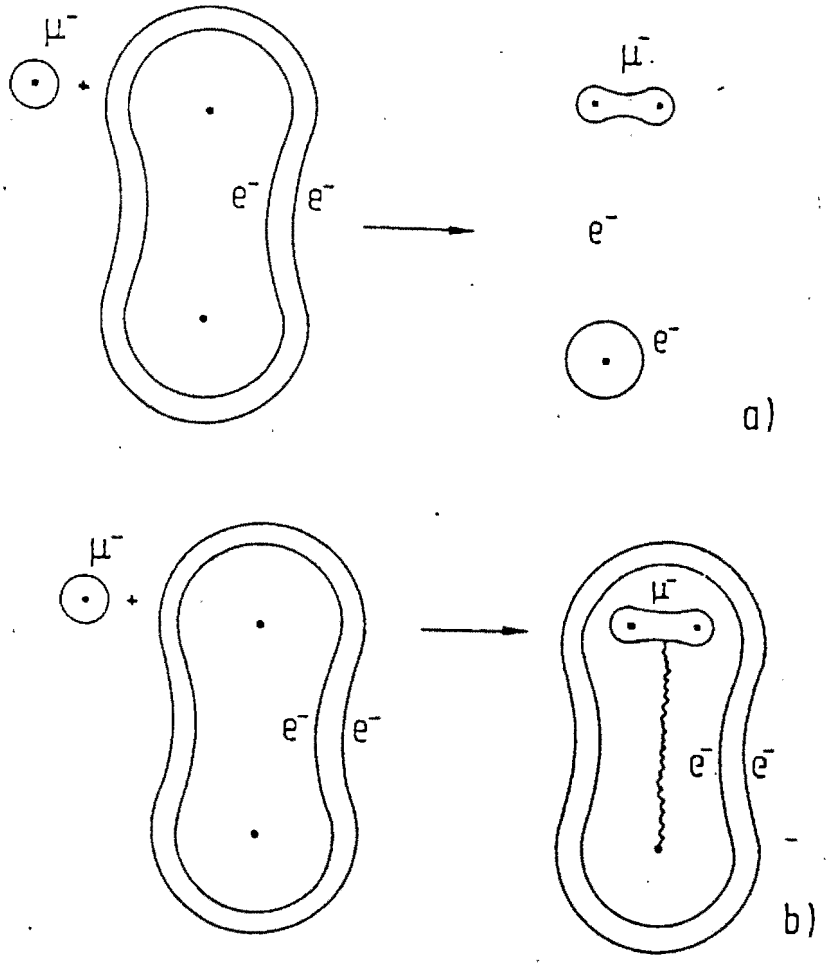

Figure 1.3: The two types of mesomolecule formation leading to muon catalysed fusion. (a) Auger, where the e.g. $[pd\mu]^+$ mesomolecule shares kinetic energy with an electron and an atom;
(b) Resonant, where the mesomolecule is formed as one of the nuclei in a molecule in an excited vibrational state. Diagram from ref. [28]

The pdμ mesomolecule is formed via the Auger process (fig 1.3a):

$$d\mu + H_2 \longrightarrow [pd\mu]^+ + H + e^- \tag{1.7}$$

where the binding energy of the mesomolecule is transferred to the Auger electron. This is a relatively slow process compared to the free muon lifetime, most muons decaying before fusion can occur.

The ddμ and dtμ mesomolecule formation, on the other hand, occur by the transferring of energy to a low-lying vibrational state of the 'host' molecule[2] in which it takes place. [31,19] (fig 1.3b). This vibrational state must be a weakly bound state, able to absorb both the kinetic energy of the incoming muonic atom and the binding energy of the mesomolecule. Thus the molecule formed will not dissociate:

$$t\mu + D_2 \longrightarrow ([dt\mu]d2e)^* \tag{1.8}$$

Mesomolecule formation within the molecule is most rapid when the sum of kinetic and binding energies is equal (within the finite width) to that of the vibrational state. Both ddμ and dtμ mesomolecules have the required bound state energy levels (figure 1.4) for resonant formation.

This scenario was recognised [7] in the temperature dependence of the ddμ formation rate, since the average kinetic energy (or peak of the Maxwellian distribution) of the participating nuclei is dependent on temperature. At low temperatures the Auger process dominates, while at temperatures above 200K the resonance process is much stronger, peaking at 500K.

In the case of ddμ fusion, (fig 1.5) the lowest vibrational level excited is the $v = 7$ level. (see figure 1.4) This is important as the formation rate depends on the matrix element W of the electric dipole operator[3] between the initial and final states of the system, which is strongly dependent on the vibrational number.

In the case of dtμ fusion, (fig 1.6) the muon is captured either by the d or the t but transfer almost always occurs from d to t owing to the isotopic mass shift[4]:

$$d\mu + T_2 \longrightarrow t\mu + d + e^- + T + 19eV \tag{1.9}$$

[2]It is important to avoid confusion here between the mesomolecule e.g. dtμ and the molecule e.g. D_2, one of the nuclei of which joins with the tμ to make up the mesomolecule. If the molecule is able to absorb the energy released in such a conversion of one of its nuclei, resonant mesomolecular formation takes place. If not, it falls apart and the Auger process takes place.

[3]The mesomolecule is formed in the $l = 0$ state

[4]The reason for the moderate temperature dependence of tdμ formation is partially explained by the fact that about half the tμ muonic atoms are formed by reaction 1.9. This

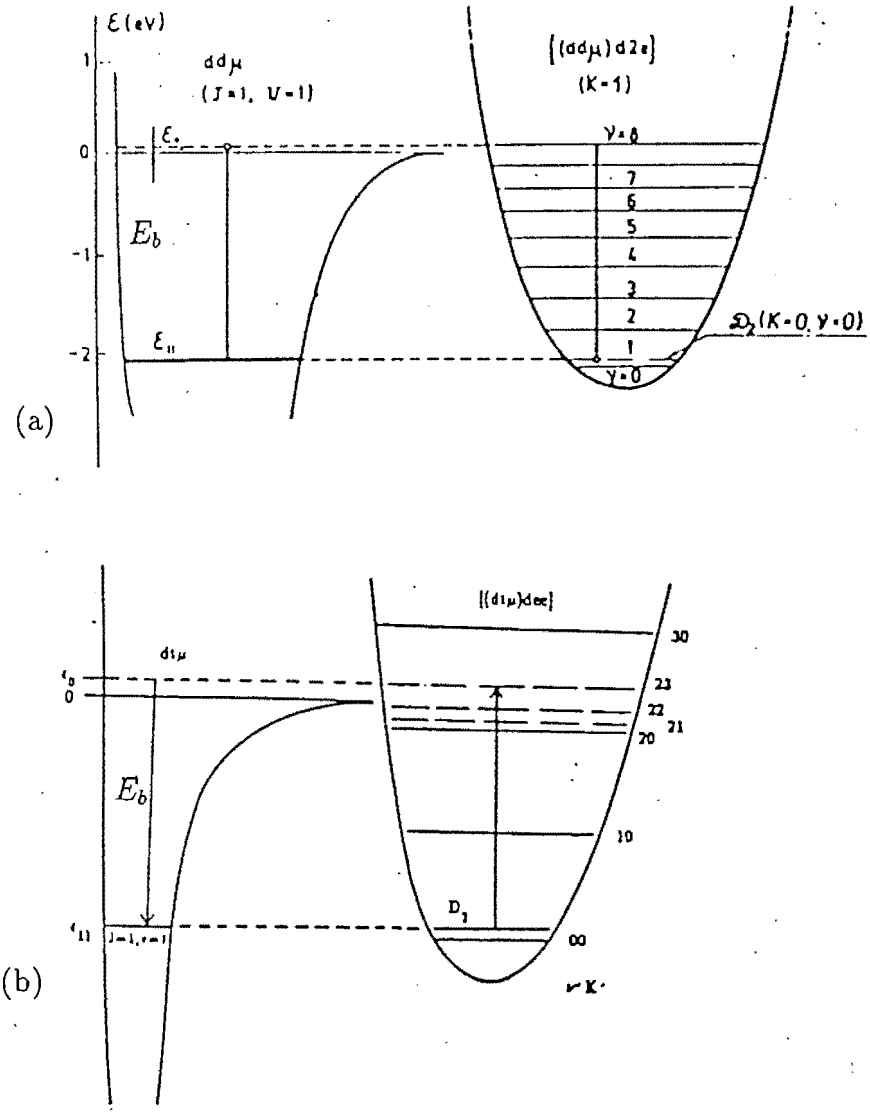

Figure 1.4: Energy levels of (a) the ([ddμ]d2e) and (b) the ([dtμ]d2e) molecules and the ddμ and dtμ binding energies. Figures reproduced from refs. [27] and [7]
On the left of each diagram is the binding energy E_b of the mesomolecule. The potential wells for the molecules are on the right with the vibrational energy levels incorporated. The ([ddμ]d2e) molecule is excited to $v = 7$ while the ([dtμ]d2e) molecule is excited to the $v = 3$ level.

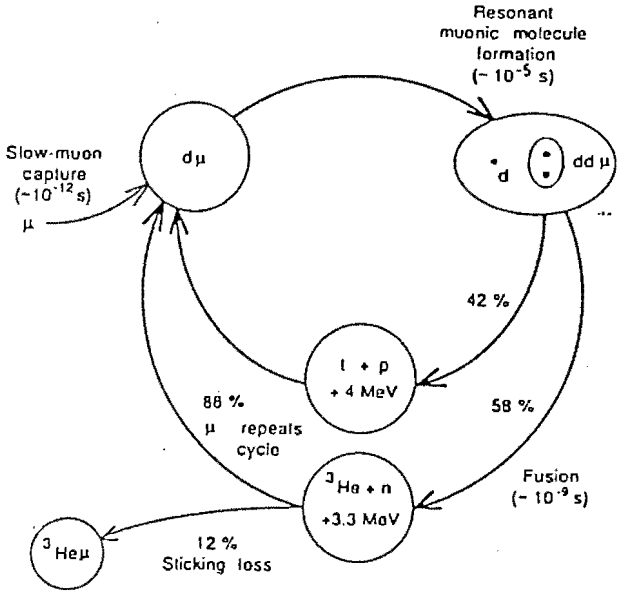

Figure 1.5: The ddμ catalysis cycle

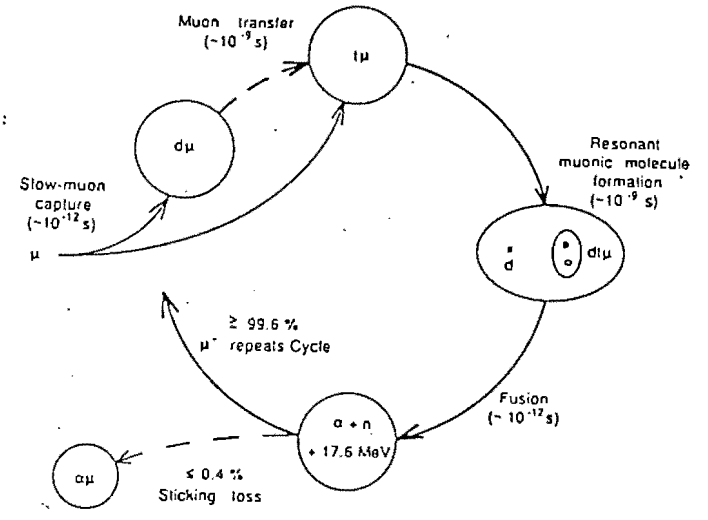

Figure 1.6: The tdμ catalysis cycle (this and figure above from ref.[18])

The binding energy of the tdμ mesomolecule is lower than that of the ddμ, hence a lower vibrational state $v = 3$ [9] (figure 1.4) of the host molecule can be excited. This enhances W by three orders of magnitude. Hence the mesomolecule formation rate is greatly increased for dtμ fusion.

The rest of the catalysis cycle (muon capture and transfer, and fusion) occurs very quickly, in the order of nanoseconds, three orders of magnitude smaller than the muon lifetime. Hence if there were no sticking, an average of some 1000 fusions per muon could be attained.

The catalysis cycle rate increases with temperature and density of the hydrogen, and the optimal deuterium to tritium ratio appears to be about 1:1. An excess of deuterium leads to more muons being captured by deuterons, adding a step to the catalysis process. Transfer from d to t (reaction 1.9) produces 'hot' tμ muonic atoms, which then have to be thermalised before resonant mesomolecule formation can take place. More d-d fusions take place with the increase in ddμ mesomolecule formation. An excess of tritium results in more ttμ mesomolecules being formed. Both processes are much slower than their dt counterparts.

The pressure (or density) affects the rate by broadening the vibrational levels of the mesomolecule, due to the proximity of a third body which can carry away momentum during mesomolecule formation. This is similar to Stark broadening. Higher pressure also decreases the distances the various constituents of the catalysis cycle have to travel, and decreases the thermalising time of tμ and μ.

Finally, the cycling rate in a mixture of D_2T_2 gas is time dependent, as the D_2 and T_2 molecules are broken up and DT molecules formed, until equilibrium between the three types of molecules is reached. DT molecules can also host mesomolecule formation, but the process is again slower than for formation in D_2 molecules. HD molecules have also been found to host the process.

1.1.3 Muon Sticking

The dtμ fusion reaction has two final states:

$$dt\mu \longrightarrow \begin{cases} {}^4\mathrm{He} + n + \mu & (1 - \omega_s^0) \\ {}^4\mathrm{He}\mu + n & \omega_s^0 \end{cases} \qquad (1.10)$$

results in non-thermal tμ muonic atoms, which are not thermalised before mesomolecule formation takes place.[27]

where ω_s^0 is the probability that a muon will stick initially to the alpha fusion product.

The μ may be stripped from the $\alpha\mu$ with probability R *after* fusion by collision with atoms in the surrounding medium. R is known as the *reactivation coefficient.* The effective sticking coefficient ω_s is thus a product of ω_s^0 and R:

$$\omega_s = \omega_s^0(1 - R) \tag{1.11}$$

Both ω_s^0 and R are, in addition to the properties of the DT environment, dependent on the initial energy of the alpha (simplistically, the larger the energy given to the alpha on fusion, the larger the chances of its leaving the muon behind, and the longer its slowing down path in the medium). For ddμ fusion, producing a 0.82 MeV ^{3}He, ω_s^0 is much larger and R smaller than for dtμ fusion, with its 3.6 MeV α. By the above argument, reactions such as

$$d + {}^3\mathrm{He} \longrightarrow p(14.6\mathrm{MeV}) + {}^4\mathrm{He}(3.7\mathrm{MeV}) \tag{1.12}$$

$$t + {}^3\mathrm{He} \longrightarrow d(9.5\mathrm{MeV}) + {}^4\mathrm{He}(4.8\mathrm{MeV}) \tag{1.13}$$

should have even smaller ω^0 and larger R.

The initial sticking may also depend on the fact that the muon becomes bound to the alpha while they are still interacting with each other in an intermediate state and not with the surrounding DT gas — leading to one of the final states in reaction 1.10. Rafelski [32] argues that the properties of the DT gas can affect this intermediate state between fusion and interaction with the surrounding DT environment, thus giving the initial sticking coefficient ω_s^0 the possibility of temperature and pressure dependence, the so - called *convoy effects.* He also argues [33] that the resonant strong d-t nuclear interaction affects the wavefunction of the intermediate state. This could reduce ω_s^0 to 0.1%, given the right conditions.

Figure 1.7 shows the theoretical calculations and some indirect measurements of ω_s for dtμ fusion. Note that the pre-1981 theory predicted that R (hence ω_s) would be independent of pressure, probably considering only number density effects on the stripping and stopping.

The initial sticking was calculated by the sudden approximation method in 1981 [29,34] to be 1.2%. Later, more sophisticated calculations using the Born - Oppenheimer approximation [35] and Monte Carlo techniques [36] have estimated ω_s^0 to be around 0.9%.

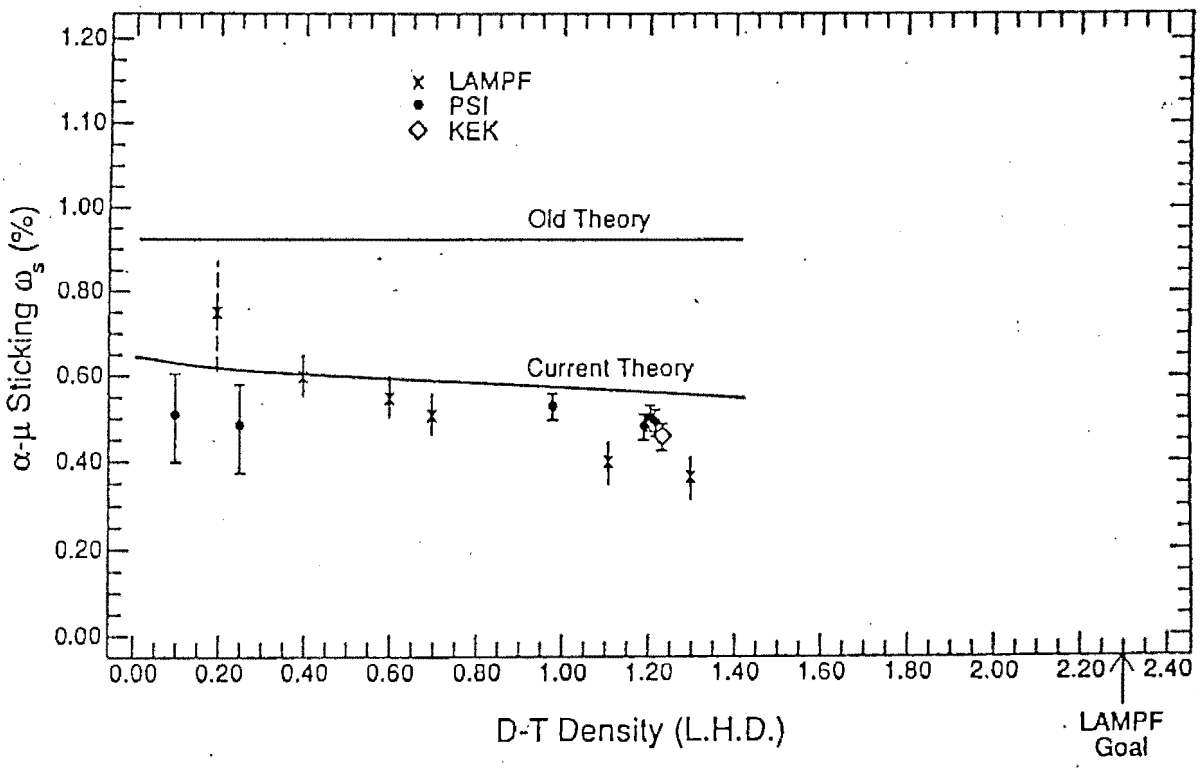

Figure 1.7: Calculated alpha-muon sticking ω_s showing density-dependence in a current model [38] along with the observed sticking in d-t- mixtures from LAMPF [15], PSI [11] and KEK. From S. E. Jones *μCF89*, Oxford, RAL rep. no. 90-022 p 21

R has been calculated at 27% [37] for densities corresponding to liquid hydrogen density (LHD), increasing to about 30% at 2 x LHD.

These calculations set ω_s at 0.6%, restricting the average number of fusions per muon to about 170.

Measurements at LAMPF [15] suggest that ω_s is in fact strongly pressure dependent. This dependence is not at present understood and hitherto the measurements at LAMPF have not been verified by an independent experiment. Much work is needed in the measurement of ω_s at various pressures, temperatures and deuterium-tritium ratios. Indirect measurements can only estimate ω_s, from a large number of other muon loss factors. Direct measurements of ω_s^0 and ω_s for dt fusion are now required.

1.2 Direct Measurements of Muon Sticking

Direct measurements of muon sticking in $dt\mu$ fusion are now being performed. These experiments detect a signal from the α from fusion, which

allows them to differentiate between α and $\alpha\mu$. In some experiments, the alpha signals are often detected in conjunction with the associated fusion neutron. These experiments rely on fewer theoretical assumptions than indirect measurements.

The methods for direct measurements of sticking include the following:

1. The detection of muonic X-rays [12,13] from decay of the captured muon to the 1s orbital in the alpha-muon system. These measurements are less indirect than the measurements of the time structure of the fusion neutron flux in that the number of alphas with muons stuck to them is measured, but the total number of fusions, as well as the theoretical calculations of the X-ray spectra are still subject to much uncertainty.

2. At PSI [39,25], the gas fusion vessel, filled with a mixture of H_2, D_2 and T_2 is used as a proportional counter. Singly and doubly charged alphas will give different signals[5], as will the energetic muons themselves. Certain signatures, that is different pulses in various patterns, from the proportional chamber, often in conjunction with a neutron detector recording fusion neutrons, allow identification of fusions and stuck muons, providing a good measurement of final[6] sticking ω_s of 0.59 $\pm$ 0.07 % [25].

3. The detection of collinear neutrons and alphas in coincidence. These experiments are being performed at Los Alamos Meson Production Facility (LAMPF) [21,40] and at the Rutherford Appleton Laboratory (RAL). The measurements rely on the different ranges of α and $\alpha\mu$ in matter to differentiate between them. These experiments provide a measurement of the initial[7] sticking ω_s^0 in contrast to the PSI measurements of ω_s.

   The experiment at RAL uses a similar philosophy to the LAMPF experiment and the two shall be referred to as the LRG (LAMPF/RAL geometry) experiments for convenience. This dissertation concerns the modelling of these experiments and some similar experiments which may be considered in future.

[5]This is due to the *recombination effect*,which depends on the charge density of the track of an ion in the chamber. Alphas have shorter tracks than $\alpha\mu$ and hence greater charge density. Consequently, larger signals will be produced by $\alpha\mu$.

[6]The $\alpha\mu$ are stopped in the gas

[7]The $\alpha\mu$ are not stopped in the gas

1.3 LAMPF/RAL Sticking Experiments

Figure 1.9 is a diagram of the type of apparatus used in the LRG sticking experiments.

1.3.1 Range Selection

To measure ω_s^0, the doubly charged alphas (α^{++}) need to be separated from singly charged alphas with attendant muons ($\alpha\mu^+$). This is done using the dependence of the range of a particle on its charge $\mathcal{Z}$.

Since from the Bethe Bloch[41] formula for the energy loss of ions in matter,

$$-\frac{dE}{dx} \propto \mathcal{Z}^2 \tag{1.14}$$

and

$$r = \int \left(\frac{dE}{dx}\right)^{-1} dE \tag{1.15}$$

it follows that

$$r \propto \left(\mathcal{Z}^2\right)^{-1} \tag{1.16}$$

where r is the range of the charged particle. The $\alpha\mu$ has four times — to a first approximation — the range in DT gas of the alpha.

We define two gas pressures:

1. p_μ, which ensures that even the α formed closest to the alpha detector are stopped in the gas, while all the $\alpha\mu$ are counted. See (fig 1.8).

2. p_α, which allows all alphas to be counted. In practice, it is difficult to range the α out entirely, but they are easily separated from the $\alpha\mu$ in analysis.

By ranging out the α and counting only coincidences between $\alpha\mu$ and neutrons, and comparing this with the number expected if all α reached the detector, ω_s^0 can be calculated.

1.3.2 Determining ω_s^0

The sticking coefficient can be measured by taking the ratio of $\alpha\mu$ to α arising from a large number of fusions:

$$\omega_s^0 = \frac{N_{\alpha\mu}}{N_\alpha + N_{\alpha\mu}} \tag{1.17}$$

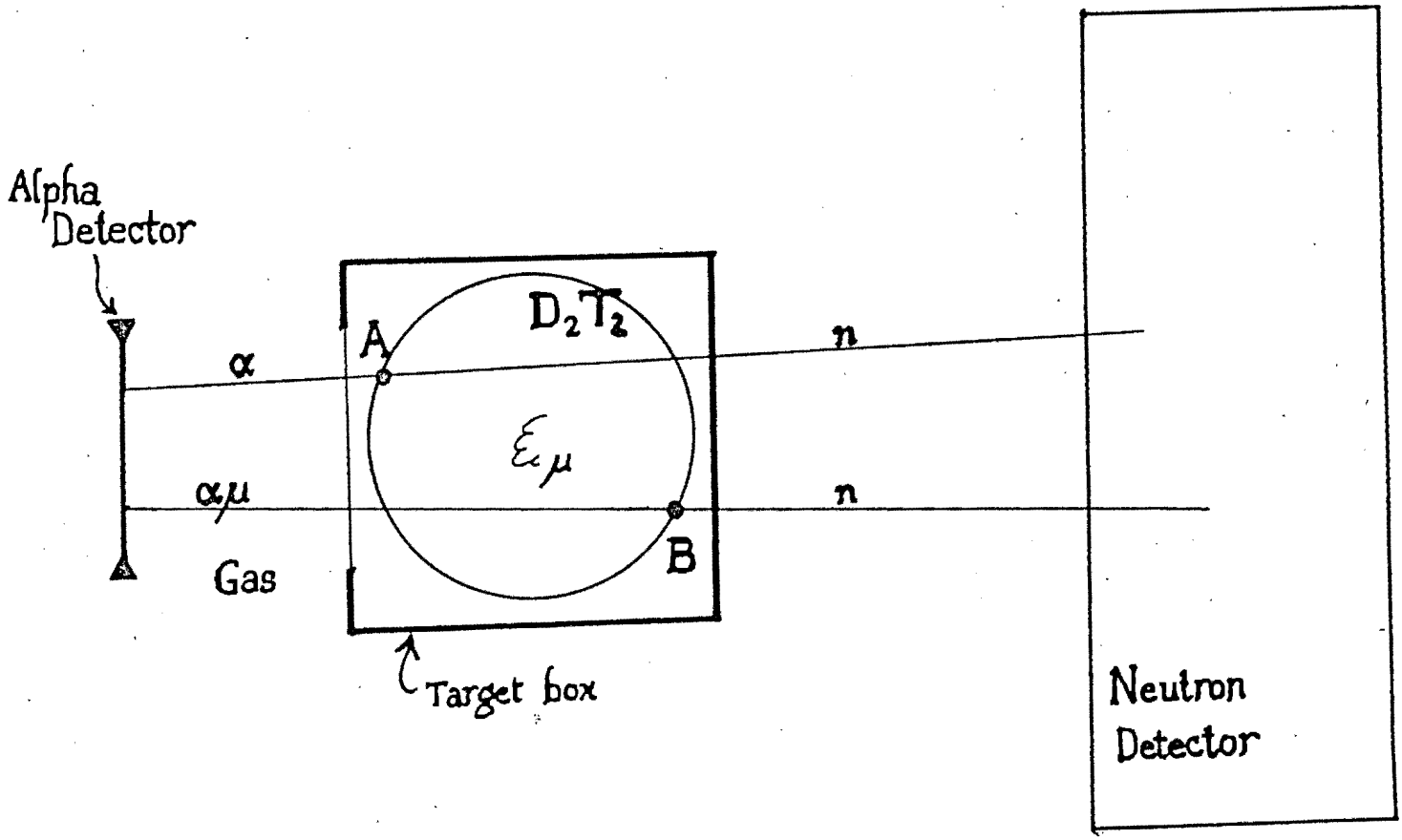

Figure 1.8: A diagram showing the principle behind the LRG experiment. Alphas from point A will be ranged out at high pressure while $\alpha\mu$ from point B will reach the alpha detector at the same pressure. At low pressure, α from B will also penetrate to the alpha detector.

This ratio can be obtained by taking two measurements of the alpha neutron coincidences N_c normalised for the same number of fusions, one at p_μ and the other at p_α:

$$\omega_s^0 = \frac{N_c(p = p_\mu)}{N_c(p \leq p_\alpha)} \tag{1.18}$$

assuming that no corrections have to be made for the ranging out of $\alpha\mu$ due to stripping. The LAMPF experiment was performed in such a way [21]. A problem arises with the normalisation of the two measurements to the same number of fusions. There is the expected uncertainty in the number of incident muons, and the fusion distribution and number of fusions per muon changes with pressure. The calculation of the scaling with pressure is plagued with considerable systematic error, estimated at about 15 % [21].

Another method was evolved for the RAL measurements where due to a different muon beam time structure, backgrounds could be cut out more effectively and measurements of singles fusion neutrons could be taken. Measurements at a single pressure p, near p_μ, were performed. The number N_0 of dt fusions in the target cell is related to the neutron singles N_n, since:

$$N_n = \epsilon N_0 \tag{1.19}$$

and $N_0 = N_\alpha + N_{\alpha\mu}$, and where ϵ is a product of the solid angle the neutron detector subtends, averaged over the fusion distribution, and its absolute efficiency for the detection of fusion neutrons.

We need to calculate how many of the fusions producing $\alpha\mu$ would give rise to a n-$\alpha\mu$ coincidence. We define a factor B thus:

B = [The probability that the extrapolated geometric path of a collinear $\alpha\mu$ associated with a detected fusion neutron intersects the alpha detector]. (1.20)

$N_{\alpha\mu}$ is related to the number of coincidences N_c, assuming that all the α have been rejected by ranging out or by analysis, since:

$$N_c = B\Phi\epsilon N_{\alpha\mu}. \tag{1.21}$$

where Φ is a correction for the $\alpha\mu$ which are stripped and ranged out or reach the detector with energy such that they are rejected in analysis. Hence:

$$N_{\alpha\mu} = \frac{N_c}{B\Phi\epsilon} \tag{1.22}$$

and, from eq. 1.19

$$N_\alpha + N_{\alpha\mu} = \frac{N_n}{\epsilon} \tag{1.23}$$

Combining equations 1.17, 1.23, 1.22, The ϵ cancel and we get:

$$\omega_s^0 = \frac{N_c}{B\Phi N_n} \tag{1.24}$$

In this way, ω_s^0 can be calculated by simultaneously measuring N_c and N_n at $p = p_\mu$ and using appropriate values of B and Φ, which are calculated by Monte Carlo method.

Comparing equations 1.24 and 1.18, the B factor can also be seen as the ratio of α-n coincidences to neutron singles for measurements at gas pressure p_α.

$$B = \frac{N_c}{N_n} \tag{1.25}$$

Were the B factors constant with pressure, the B factor would effectively be determined by taking measurements of coincidences at p_α and p_μ. The Monte Carlo calculations determine B by taking one spatial fusion distribution at all pressures and measuring the ratio in equation 1.25 at p_α.

For an alternative derivation of equation 1.24, see appendix A, page 1536.

1.3.3 Outline of the RAL Experimental Procedure

For the RAL experiment [20], the muons were obtained from the ISIS pulsed muon beam facility [42]. 800 MeV protons impinged on a graphite target, producing positively and negatively charged pions amid other charged and uncharged particles. The pions decay into muons and muon neutrinos. The negatively charged muons were selected using an analysing magnet. The beam has a very low duty cycle [42], with a set of two short ($\sim$ 100 ns broad, 330 ns apart) muon pulses every 20 ms. This ensured that all the muons arrive at the target within about 300 ns of each other. This feature, not present in the LAMPF experiment, allows the considerable background produced by muons interacting in the walls of the target cell to be substantially reduced by time cuts. This facilitated the counting of singles fusion neutrons.

The muons passed through a series of degraders, which were chosen such that the number of muons stopping in the gas was maximised, before

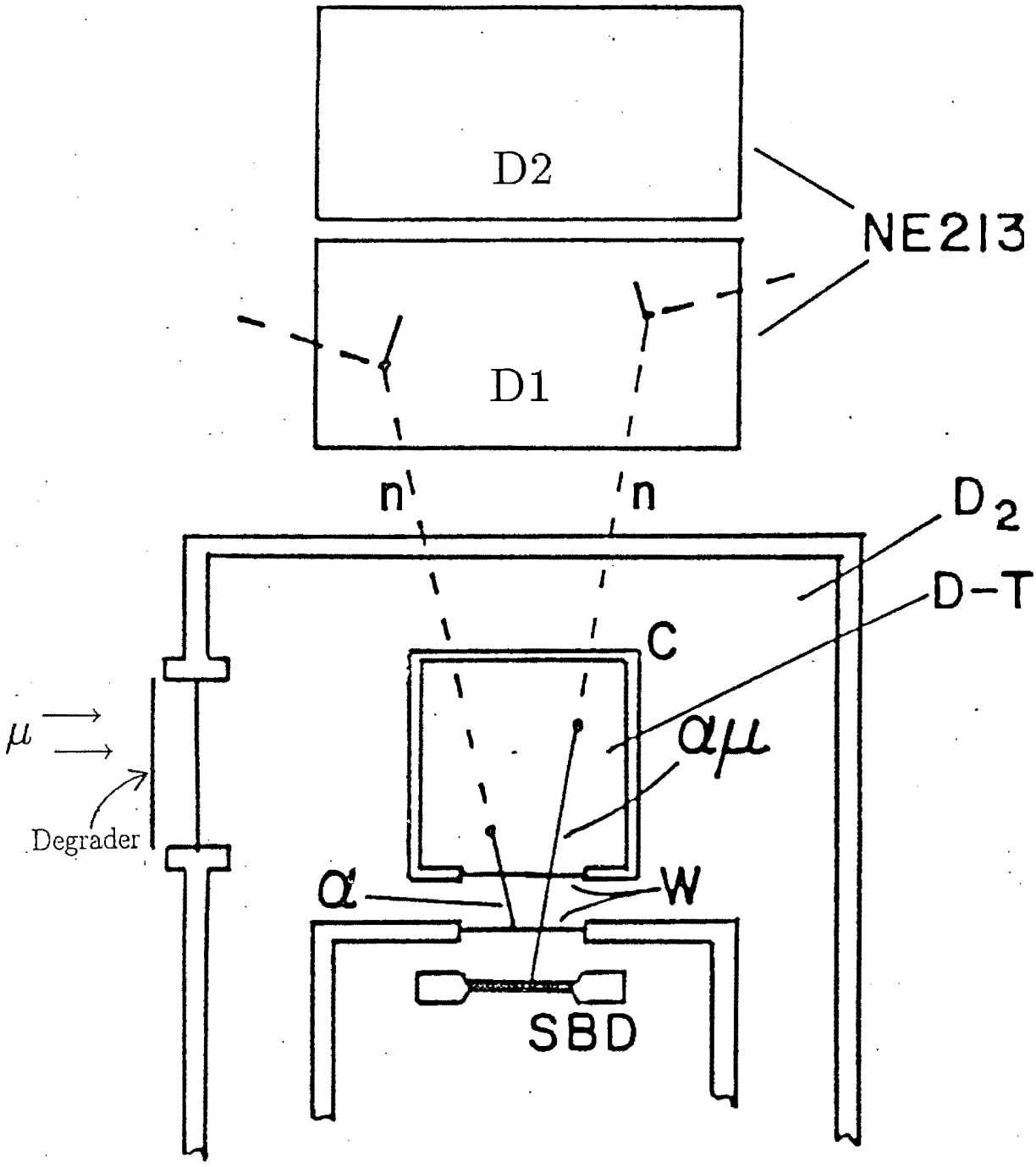

Figure 1.9: A schematic diagram of the target-detector geometry used in LRG experiments. Detector A is a Si SBD. D1 and D2 are identical NE213 neutron detectors. The third neutron detector D3 is out of the plane of the diagram.

falling on the silver target vessel. Weak interactions with heavier Z materials reduces the lifetime of the muons from 2.2 μs to less than 100ns. The electronics were inhibited for about 500 ns after each pulse so that the flux of charged particles caused by muons interacting weakly with the silver in the walls had time to subside and thus did not swamp the detectors. The experiment at LAMPF used a target cell lined with Beryllium which reduces the background produced by muons interacting with the target walls.

Three NE213 neutron detectors were used in the RAL experiment (figure 1.9), two collinear with the SBD (D1 and D2) to measure α-n coincidences, and the third (D3) orthogonal to measure accidental coincidences. The alphas had to travel through two aluminised mylar windows (W), and through 2.5–9.5 cm gas before striking the SBD, a 4cm diameter Si detector.

Both coincidences and neutron singles were recorded. For coincidences the time between neutron detector signals and alpha detector signals was recorded.

Measurements were taken for three pressures of the DT gas: 490 torr (p_α), allowing all alphas to penetrate through to the detector, 710 torr, being an intermediate pressure, where some of the alphas were ranged out; and 1510 torr (near p_μ). The time dependence of all events (single and coincidence) relative to the muon beam pulse was also recorded.

The sticking coefficient was calculated from measurements at 1510 torr where the fusion rate is reasonably high and the α and $\alpha\mu$ are clearly separated in energy by the time they reach the alpha detector. B and Φ were calculated by Monte Carlo simulation of the experiment. The paper describing the experiment is reproduced in appendix A.

1.3.4 Modelling the LAMPF/RAL Experiments

The LRG experiments require intense μ beams, and substantial tritium targets, which require specialised handling and technology owing to the high levels of radioactivity ($\sim$ 1kCi) involved. Modelling of these experiments, especially by MCS, is therefore particularly valuable, as it provides a relatively inexpensive method of checking and optimising the experimental method and for exploring alternative methods. The MC calculations are also essential for calculating the B and Φ factors discussed in section 1.3.2. The work discussed here is primarily about the development of and use of a Monte Carlo code MUGLU to model the LRG experiments. In addition to this it includes emulation (or experimental simulation) of some aspects of the sticking experiment using the ^{3}H(d,n)^{4}He reaction. The emulations are

also used to check some areas of MUGLU.

The main objects of the modelling are as follows:

1. Determination of B and Φ for the geometries used in the LRG experiments and some geometries under consideration for further experiments.

2. To investigate the fusion 'signatures' (from which ω_s^0 is extracted)

3. To study also the other characteristics for different geometries, especially those of the neutron detectors used.

The simulations may also provide some unexpected information regarding other measurements which can be made using similar apparatus. A flexible computer code for the simulations with easily adjustable parameters is essential for the task.

The following chapters describe the development of MUGLU (chapter 2) and the results (chapters 3 and 4), which are compared with data from the t(d,n)α reaction and the LAMPF and RAL experiments.

The neutron detector simulations by MUGLU were extended for use at a neutron energy of 63 MeV to aid analysis of an n-p capture experiment [43] at that energy using NE213 as an active target. This is described in appendix D.

Chapter 2

MUGLU

2.1 Modelling sticking experiments

The LRG sticking experiments to determine ω_s^0 have been outlined in the last chapter. This chapter presents the physical detail involved in modelling these experiments as incorporated in the Monte Carlo simulation program MUGLU. The effects included are almost entirely macroscopic effects of particle interactions with matter.

Sticking experiments of the LRG kind involve a distribution of fusion points in a target vessel, and alphas and neutrons emerging from this vessel at various angles and positions. For a given experiment at a certain DT gas pressure the position of fusion in the target uniquely determines the energy and time of flight of the alpha particle of given charge when it is detected. This correlation between the energy and time is used to separate $\alpha\mu$ from α. The neutron detector produces a pulse height spectrum from which the singles 14.1 MeV fusion neutrons must be extracted.

It is the aim of the MUGLU simulation of the LRG experiment to model the above. Apart from modelling by Monte Carlo methods, the experiment can be modelled (although the scope is more limited) by using the t(d,n)α reaction. This is described in chapter 3.

The MUGLU simulations can be broadly divided into four parts (the numbers refer to figure 2.1):

1. Selection of fusion sites from a fusion spatial distribution constrained by the characteristics of the incident muon beam and the geometry of the target vessel.

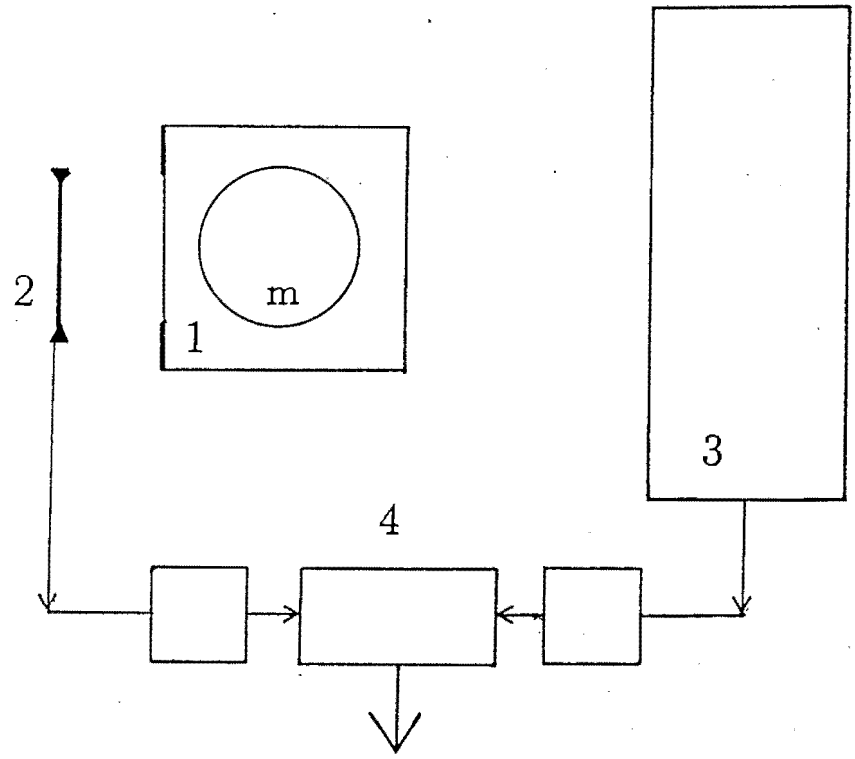

Figure 2.1: Schematic diagram of a coincidence-type sticking experiment. m—muon beam; 1—target box; 2—alpha detector; 3—neutron detector; 4—electronics

2. The alpha fusion product: Slowing alphas in the gas and other material; stripping of μ from $\alpha\mu$; detection by the alpha detector; calculation of time of flight and energy of (or pulse height produced by) the alpha.

3. Detection of the fusion neutron.

4. Output: Recording of energies, pulse heights and other information for both singles events and for n-α or n-$\alpha\mu$ coincidences.

The method used to simulate these processes are outlined in this chapter. A listing of the code MUGLU is available on request.

2.2 Geometry

The geometry of the target box is naturally of paramount importance in the LRG experiments. It affects factors such as fusion rates, fusion detection probability, B factors, and the distribution in time and energy of the

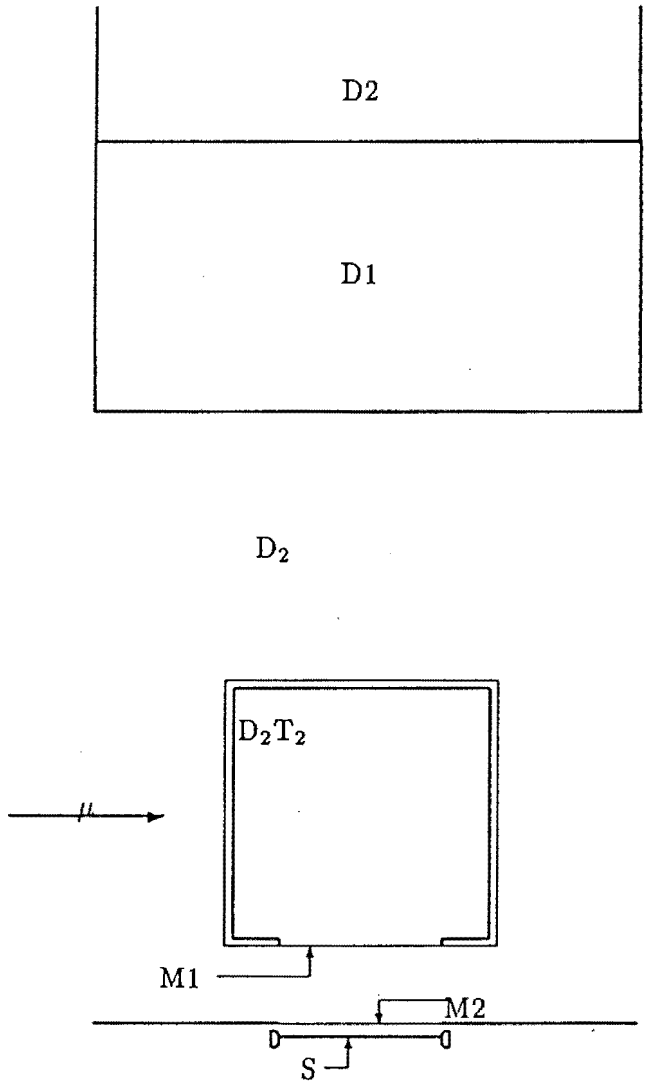

Figure 2.2: Geometry A: The geometry of the 1988 RAL MCF experiment. S: Silicon SBD; M1 & M2: Aluminised mylar windows; D1 & D2: NE213 neutron detectors.

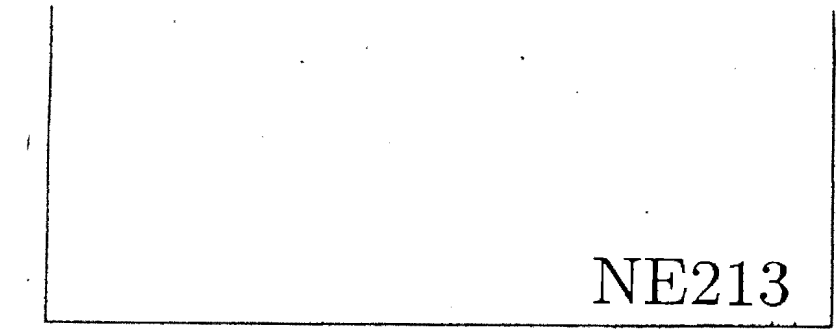

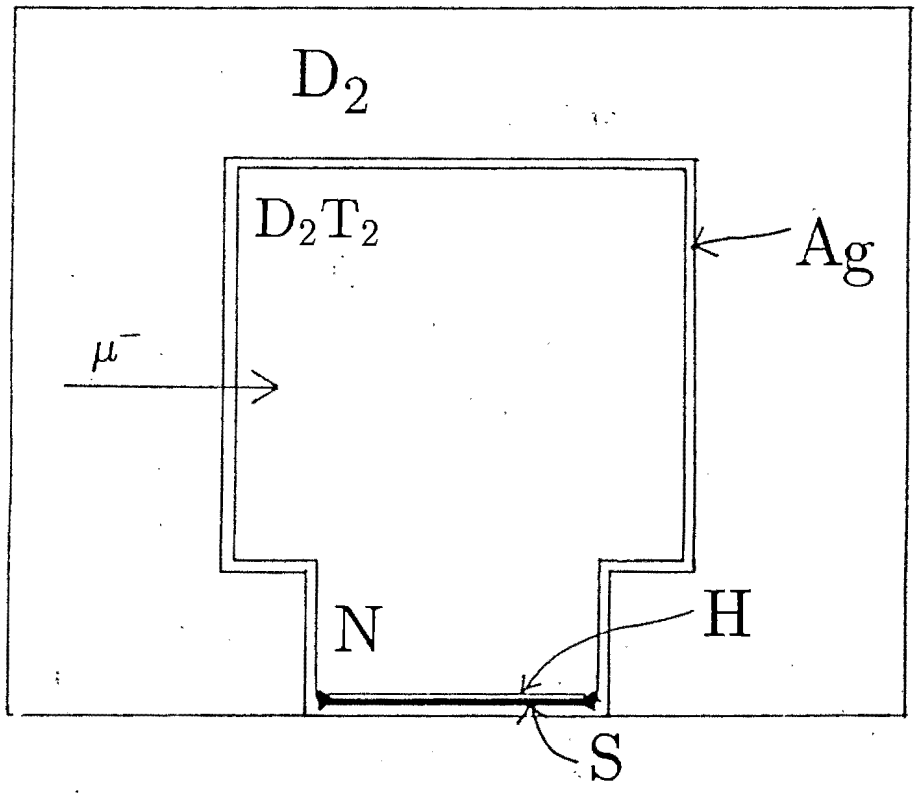

Figure 2.3: Geometry B: The geometry of a proposed MCF experiment, similar to geometry A above but without the mylar windows sealing the fusion vessel from the neck region (N). The SBD (S) has a barrier (H) to protect it against tritium.

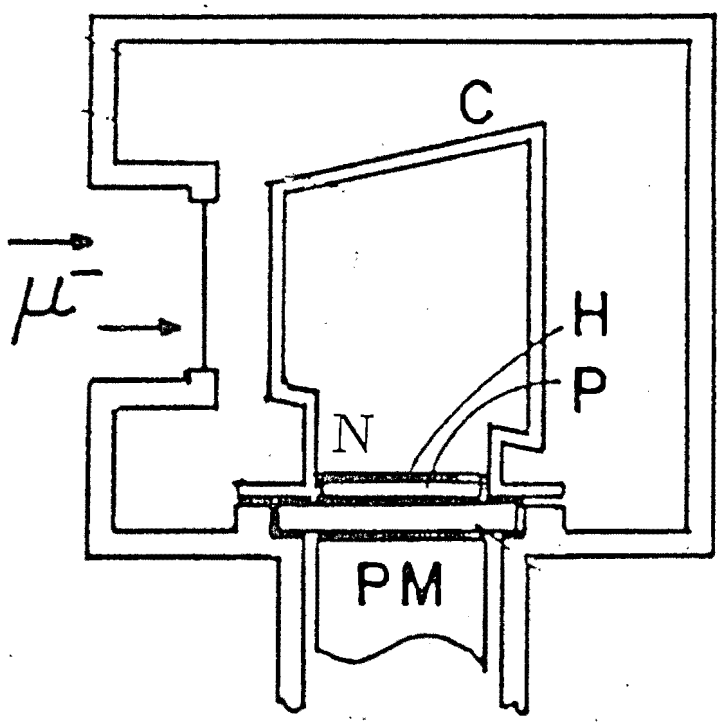

Figure 2.4: Geometry C: The geometry modified to maximise the percentage effective fusion volume. The target vessel C is conical increasing in diameter with the increase in beam width. The SBD alpha detector has been replaced by a thin film plastic scintillator P covered by a barrier H.

detected alphas. The geometries need to be optimised for maximum separation of the α and $\alpha\mu$, and may vary considerably. The MUGLU code has to be flexible to explore various geometrical possibilities. For illustration of MUGLU however attention is restricted to three geometries: A – the geometry used for the 1988 RAL ω_s^0 measurement; B – a simplified variant of A, proposed for use in the next ω_s^0 experiment at RAL; and C – a smaller fusion vessel using an alternative α detector.

Geometry A (figure 2.2) is a 7 by 7 by 7 cm silver-walled cube filled with a mixture of deuterium and tritium gas in which fusions can take place. There are two 1.5 μm aluminised mylar windows between the gas and the alpha detector, which is a further 2.5 cm from one face of the cube. Between the windows is ideally only deuterium gas, so that no dt fusions occur in this region. This serves to protect the alpha detector from tritium beta decay, as well as providing the fusion alphas with the required amount of gas to range them out. The alpha detector is a 4 cm diameter semiconductor detector (SBD), while neutrons are detected by two 13 by 13 by 7 cm volumes of NE213, the first 14 cm from the centre of the cube, and the other 21 cm from the centre of the cube.

Geometry B (figure 2.3) is a box similar to A but without the mylar windows between the SBD and the DT gas. Instead, the detector is coated with a 1.6 μm thick layer of aluminium oxide or metal such as Havar, also for protection from tritium.

Geometry C (figure 2.4) [44] is a truncated cone, also silver-walled, with a circular neck (N in figure 2.4 and 2.8) 5 cm in diameter extending to the alpha detector. The rate at which the cone increases in diameter is designed to be equal to the rate at which the muon beam is increasing in FWHM. This is an attempt to maximise the effective volume of the fusion vessel. The neutrons are detected in a similar manner to geometry A, while the alpha detector is an NE102 thin film plastic scintillator with a 1.6 μm thick layer of Havar on the front surface of the detector to protect it against tritium beta decay and diffusion of gas into the scintillator. The Havar will probably be replaced by a layer of e.g. Al_2O_3 in practice.

Geometry A was modelled for comparison with the only existing experimental results and as a standard with which to compare the performance of alternative systems. Geometries B and C were chosen because they are being considered for future experiments.

2.3 Spatial distribution of fusion

The spatial distribution of the fusion sites can, to a first approximation, be taken as the muon stopping distribution. A more exact treatment would allow for diffusion of muonic atoms and molecules prior to fusion. For the work reported here a homogenous parallel beam, diameter 30mm was assumed to be incident on the energy degrader just in front of the outer target window (figure 1.9). The muons enter parallel to the Z-axis (see figure 2.5), and spread out over the target volume. Scattering and energy loss in the degraders and windows was estimated using the MC code DEGRAD [45] provided by the Birmingham University. The results can be approximated by cylindrically symmetric gaussian distributions, the amplitudes and widths of which are functions of z, the distance along the muon beam. DEGRAD predicts that about 2% of the muons will stop in the gas. Figure 2.6 shows the distribution calculated in this way. The walls or windows of the target vessels set limits on the extent of the distribution, since the muons are stopped in the silver walls. as can be seen in figure 2.7. The z and y scales are identical for figures 2.6, 2.7 and 2.9.

Modelling the fusion distribution for geometry A involves constraining the fusions to the 7 by 7 by 7 cube (figure 2.7). This is because the tritium is confined to the target cell in the absence of diffusion through the mylar windows. The* muons can escape from the target chamber through the windows before being thermalised.

Figure 2.9 shows a isometric plot of the muon distribution in the YZ plane for geometry C.

The muon stopping distribution for geometries B involves constraining the fusions to the cube, but provision has to be made for muons scattering into the 'neck' region (marked 'N' in figure 2.8). The stopping distribution in the neck N for geometry B is estimated by calculating a line of shadow (marked 'S' in figure 2.8) of the same slope as that of the increasing width of the beam. Then another gaussian (marked 'G') starting at zero width and increasing in width at the same rate is added to the shadow line.

Similarly for geometry C, the fusions are contained in the truncated cone, with fusions occurring in the neck with intensity increasing downstream along the beam. Thus for fusions opposite the neck region, the distribution (x,y,z) is calculated as follows:

The detectors lie on the Y axis (fig. 2.5) so the region N is a cylinder described by the equation

$$x^2 + z^2 < r^2; \quad b(a) < y < d_a \tag{2.1}$$

* incident

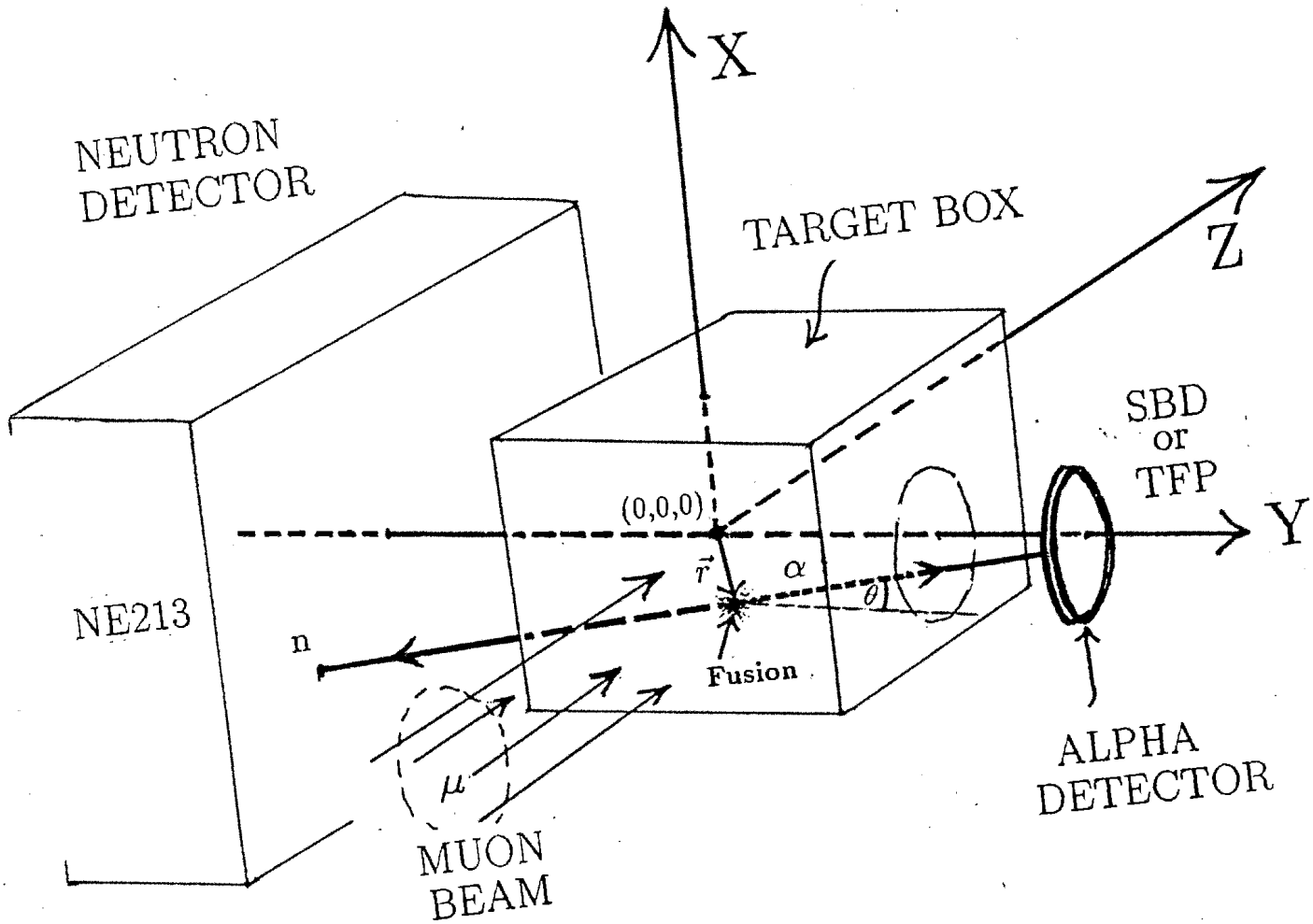

Figure 2.5: The coordinates describing the position of a fusion $\vec{r}$ and the angles the products travel. The origin is at the centre of the target cell. The neutron and alpha detectors lie on the y-axis. θ is measured from this axis.

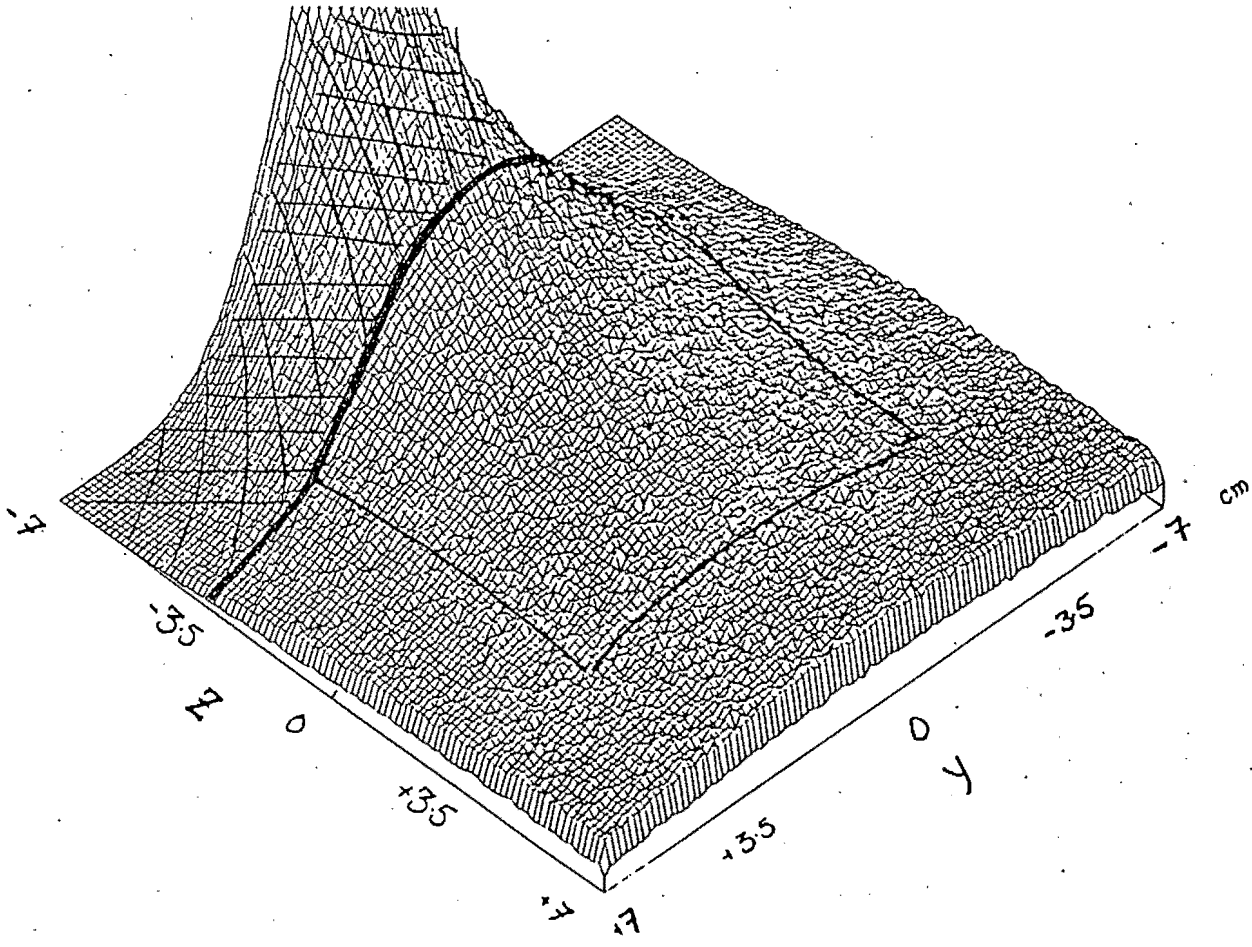

Figure 2.6: Muon stopping distribution as estimated from calculations by DEGRAD. The vertical axis is intensity, while the horizontal axes are Z and Y axes in the target box geometry The distribution is integrated over all x. The hatched region is behind the entrance window into the cell and can be ignored.

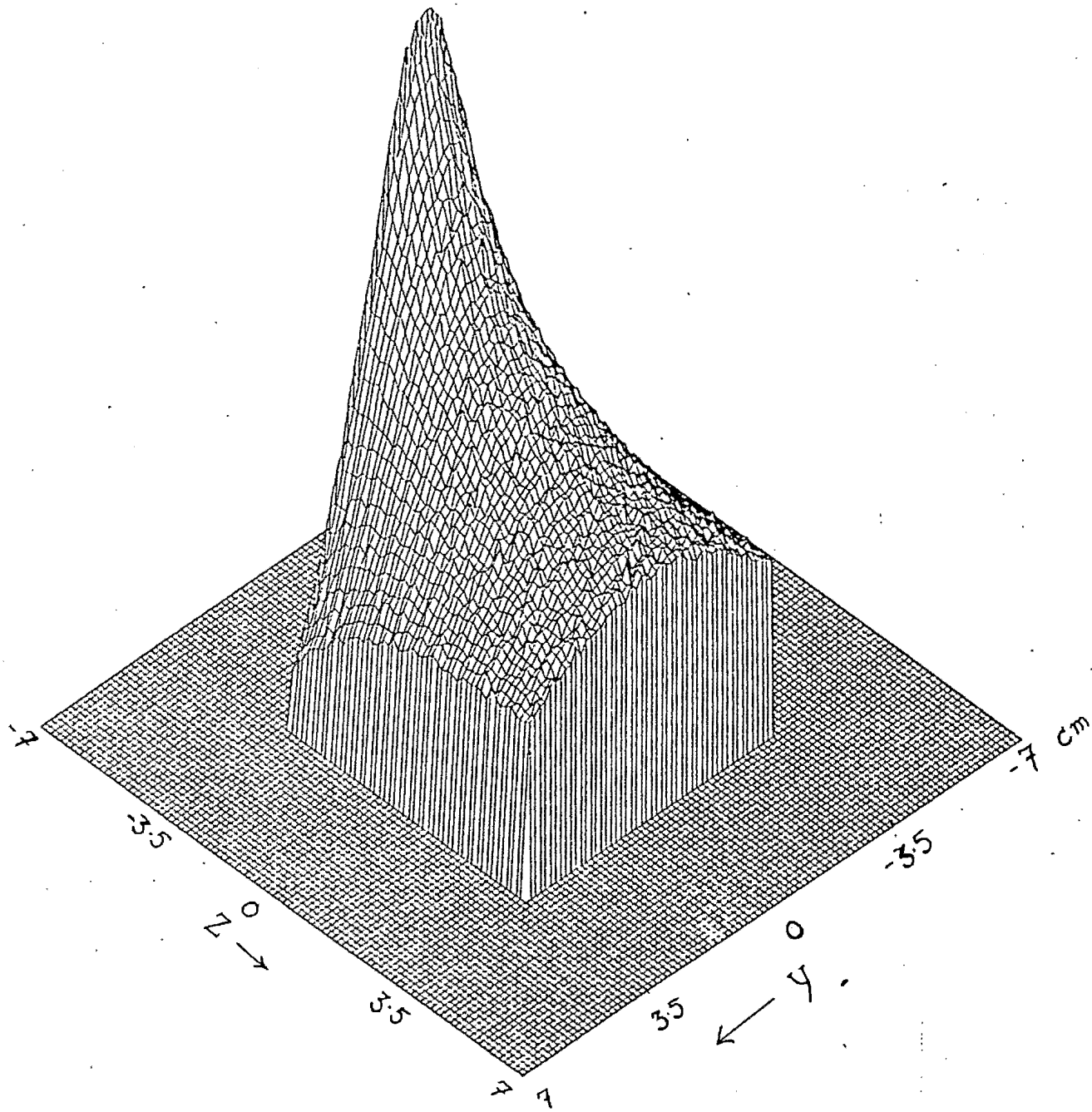

Figure 2.7: Muon stopping distribution for geometry A. Axes the same as for the above figure. Integrated over all values for x within the target box.

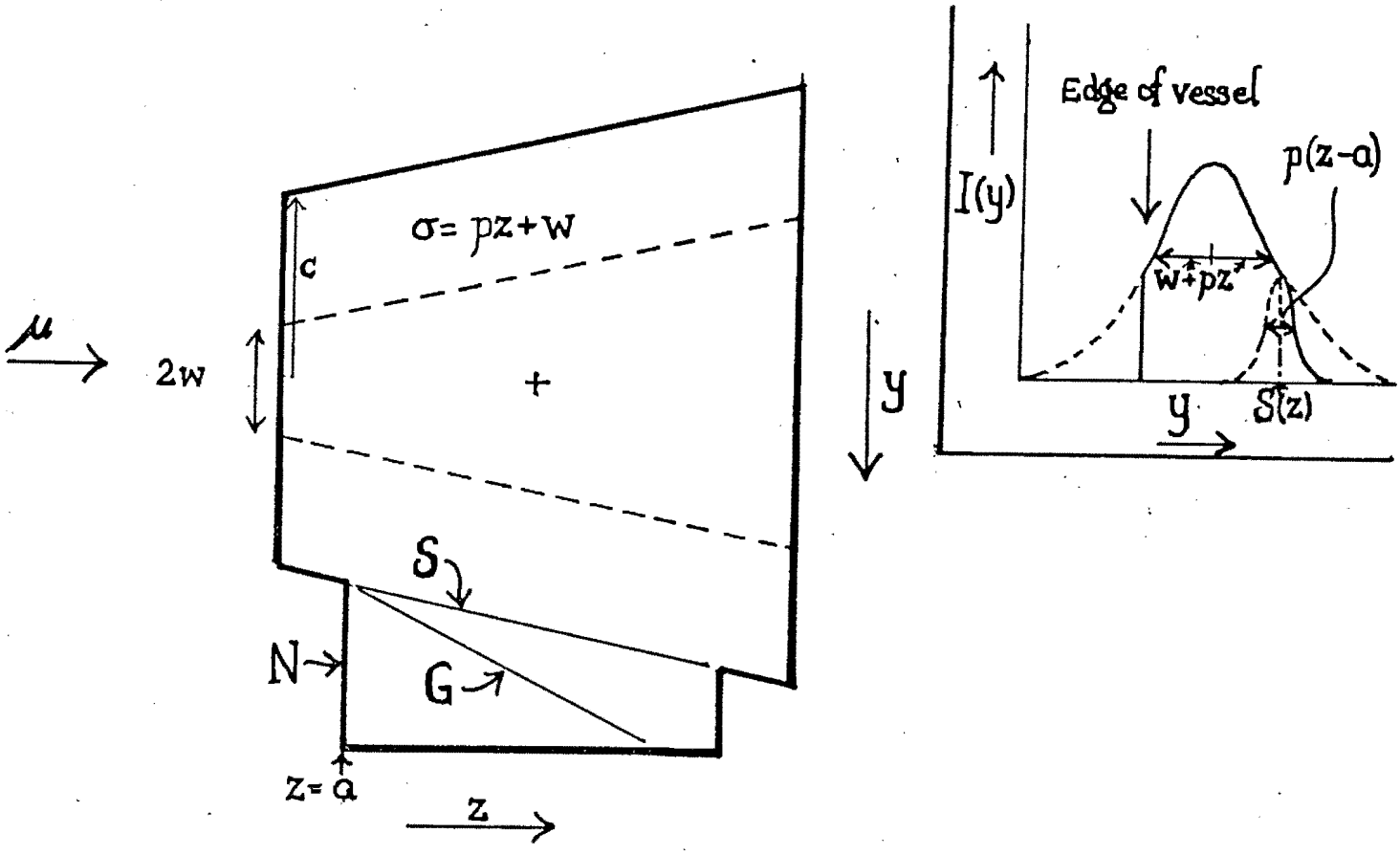

Figure 2.8: Estimation of the fusion distribution in the neck region for geometry C.

where $b(a)$ is the container breadth at the point a ($z = a$), and d_α is the distance of the alpha detector from the centre of the beam. For geometry B (figure 2.3) , $b(a)$ is constant for all a. For geometry C (figure 2.4) $b(a) \approx fa + c$ where c is the initial container radius and f is the rate at which the container radius is increasing. Note that geometry C is designed so that $f \approx p$, though have been made independent of one another to allow experimentation with different stopping distributions. It is a reasonable approximation to make $b(a)$ independent of x, as the radius of the neck is smaller than the radius of the container. The equation for the shadow line is thus:

$$S(z) = p(z - a) + b(a) \tag{2.2}$$

where p is the slope that the radius of the beam is increasing. If the beam has initial radius w on entering the target chamber, the distribution is given by:

$$[y] = \begin{cases} \exp\left(\frac{-y^2}{2(w+pz)^2}\right) & y < S(z) \\ \exp\left(\frac{-[S(z)]^2}{2(w+pz)^2}\right) \exp\left(\frac{-(y-S(z))^2}{2(p(z-a))^2}\right) & y > S(z) \end{cases} \tag{2.3}$$

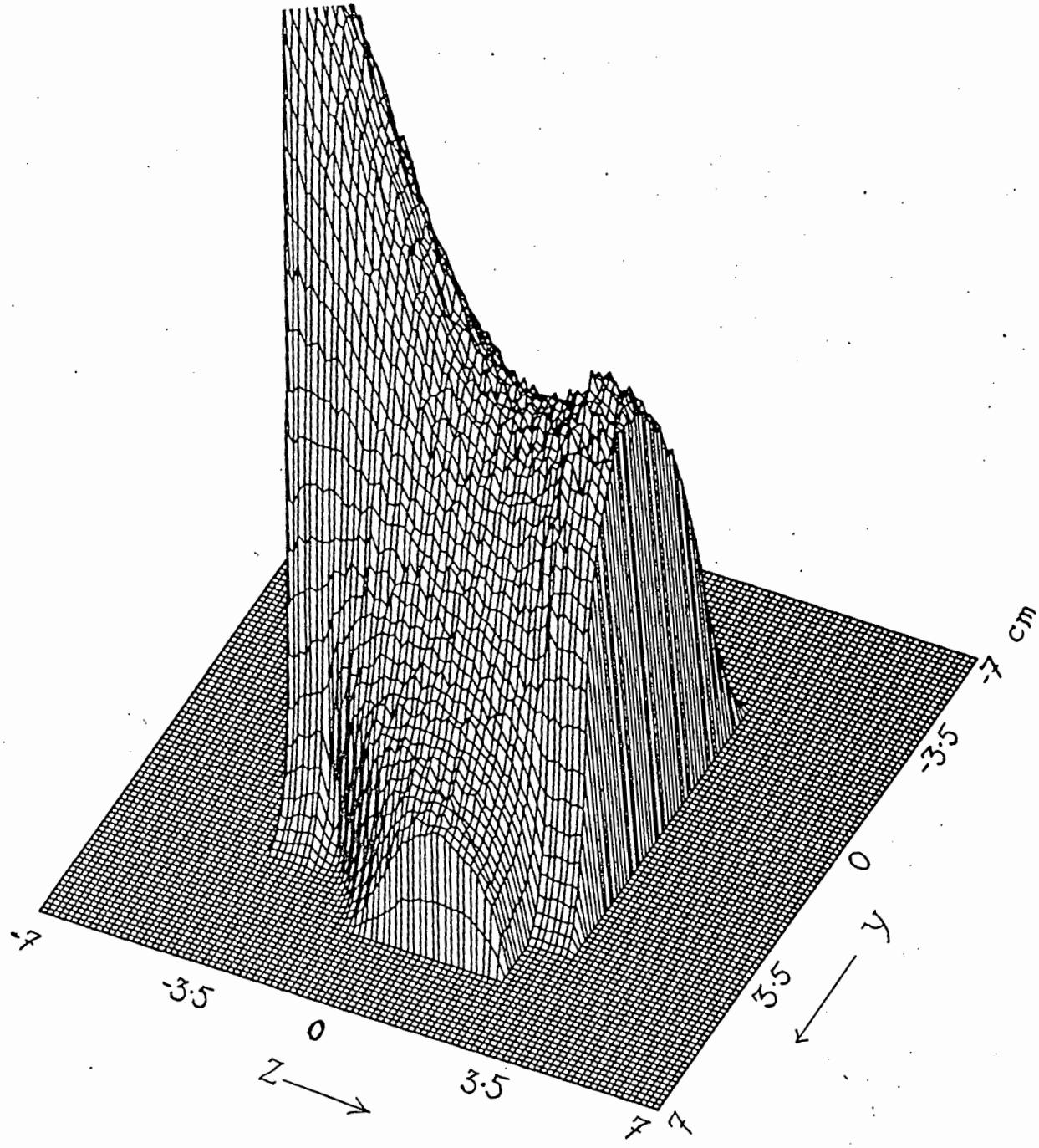

Figure 2.9: The distribution of stopped muons for geometry C projected for all permissible values of x onto the YZ plane.

In this way, z is chosen to be constant along the beam, x is chosen with a gaussian distribution increasing in width with z, and y is chosen with the above constraints, dictated by x,z and the container geometry.

Ultimately, it will be necessary to improve the approximations to obtain more meaningful results from MUGLU. The incident beam is neither axially symmetric nor homogeneous in energy. It should be fairly easy to link up DEGRAD and MUGLU and follow muons into the target individually. A suitable approximation then could be made of the diffusion of muonic atoms and molecules prior to fusion. MUGLU would then complete the detection process.

2.4 Flowchart and outline of the code

The coordinates used to describe the positions and angles in the simulation are shown in figure 2.5. The sequence of events in the simulation of one fusion is summarised in figure 2.10, which shows an abbreviated flowchart of the program written to model the sticking experiments. Each fusion history is tracked from the position of fusion to the various detectors:

1. Fusion occurs at a point $\vec{r}$ in the chamber.
2. The collinear products of the fusion, the alpha and the neutron, are ejected at angle $(\theta, \phi)_\alpha$ and $(\theta, \phi)_n$ and with energies 3.5 and 14.1 MeV respectively.
3. If the alpha falls in the solid angle Ω_α subtended by the alpha detector from $\vec{r}$, the slowing in the gas and other media, and time of flight of the alpha are calculated.
4. The muon sticks to the alpha with a certain probability, usually chosen arbitrarily as 50% to give similar statistics for α and $\alpha\mu$. Where applicable, the position at which the muon is stripped is calculated.
5. If the neutron falls in the solid angle Ω_N subtended by the neutron detector, the probability of interaction with a nucleus in the detector is calculated.
6. If a charged particle is released in this interaction, the scintillation pulse height which it produces is calculated.

   Obviously, if the neutron or alpha do not fall into the solid angles of their respective detectors, and if the alpha is ranged out or the

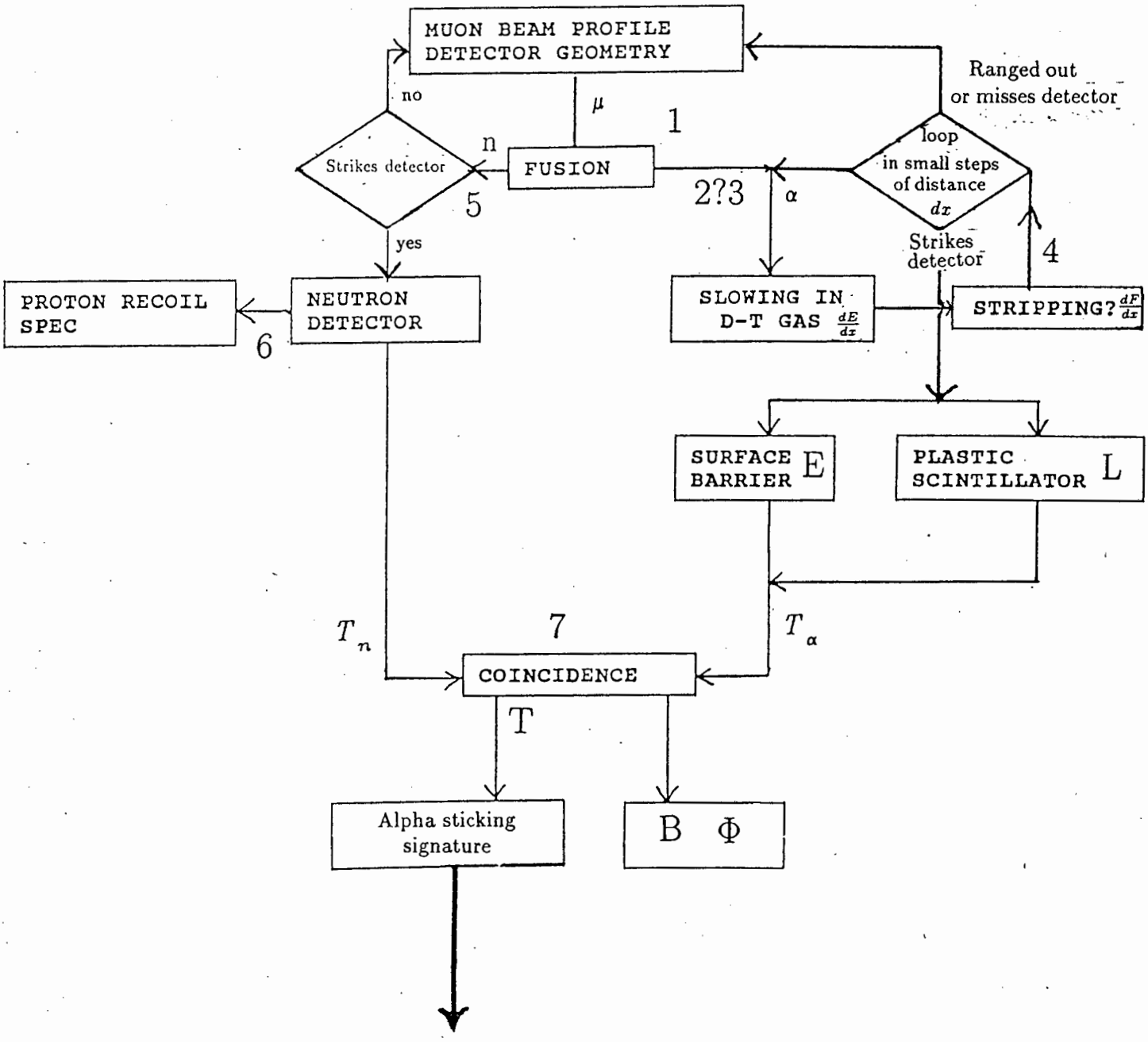

Figure 2.10: An abbreviated flowchart of the program

neutron does not interact or produce sufficient scintillations in the neutron detector, the respective particles are not 'detected'.

7. The coordinates of all coincidence events are written to magnetic tape. For every coincidence the following record is output:

$$[E_\alpha; T; \vec{r}; L_n; n_{\alpha n}]$$

where E_α is the energy of the α, as recorded at the detector, T is the time difference between the arrival of the α particle and the neutron at their respective detectors; $\vec{r}$ is the position in space of the fusion; L_n is the pulse height produced in the neutron detector and $n_{\alpha n}$ is a pattern register, the two least significant bits showing which neutron detector counted the neutron, and the next three bits showing whether an α initially had a muon stuck to it or not, and if so, whether or where the muon had been stripped off.

8. The two neutron (one for each detector) and the two alpha (one for α, the other for $\alpha\mu$) singles registers are incremented accordingly. If there has been a coincidence, i.e. if both a neutron and alpha are detected from the same fusion, the coincidence register is incremented. This produces the data for the calculation of ω_s^0 and neutron detection efficiencies.

9. Control returns to step 1.

Whether an event occurs or not, or where it occurs, e.g. muon stripping, is determined using von Neumann rejection. This is the basis of Monte Carlo technique. Distributions are also sampled in this way. A description of the technique appears in appendix D.

2.5 Alpha Detection

The simulations were run for two types of alpha detectors:

1. A silicon surface barrier detector (SBD). This type of detector gives a linear response to energy (geometries A and B). This type of detector can be segmented, replacing a single large detector with several smaller detectors, each with its own preamplifier. The large detector in the

LRG experiments is made very thin to make it less sensitive to high-energy charged particles, especially from the weak interactions of the muons in the material surrounding the target gas. This leads to a high detector capacitance and relatively poor time resolution, typically 3 ns FWHM or greater. The segmenting of the detector reduces the capacitance per segment and improves the time resolution to better than 1 ns.

2. A NE102 thin film plastic detector (TFP). The energy of the alpha has to be converted to pulse height since the detector is a scintillator (geometry C). Time resolution is typically 1 ns and pulse height resolution 30% at 3 MeV.

2.5.1 Passage of alphas through matter

D_2 T_2 Gas

The non-relativistic Bethe-Bloch formula for energy loss of ions of kinetic energy T and charge $\mathcal{Z}e$ in matter is as follows:

$$-\frac{dE}{dx} = \frac{2\pi e^4 \mathcal{Z}^2}{T} N_v Z \ln\left(\frac{4T}{I}\right) \tag{2.4}$$

where N_v is the number density and Z the charge of the medium through which the α is travelling.

For α above 1.7 MeV and $\alpha\mu$ above 0.6 MeV $\mathcal{Z}^2$ may be taken as 4 and 1 respectively. Below these energies, charge exchange occurs and the effective charge drops considerably, reducing energy loss. Curves (fig 2.11) from the energy loss calculating program ELOSS [46] show this quite clearly. Apart from the charge on the α and the energy of the ion, the energy loss in the gas is proportional to N_v. N_v can be obtained from the expression

$$pV = N_v kT \tag{2.5}$$

An empirical fit to the dE/dx curves for protons [47] (an $\alpha\mu$ behaves like a hydrogen isotope of mass 4) and α in hydrogen gas at 1 atmosphere (p fixed at 760 Torr) of

$$-\frac{dE}{dx} = \frac{pa\mathcal{Z}^2}{T} \ln\left(\frac{T}{I}\right) \tag{2.6}$$

fixed constants a and I. The variation of charge $\mathcal{Z}$ with energy for α was obtained from reference [47], shown in figure 2.12.

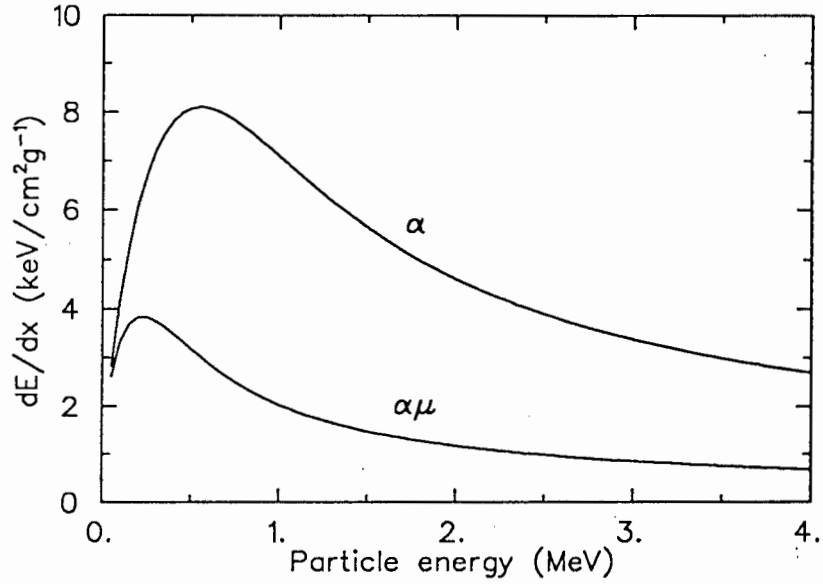

Figure 2.11: Specific energy loss for α particles in hydrogen gas at 1 atm

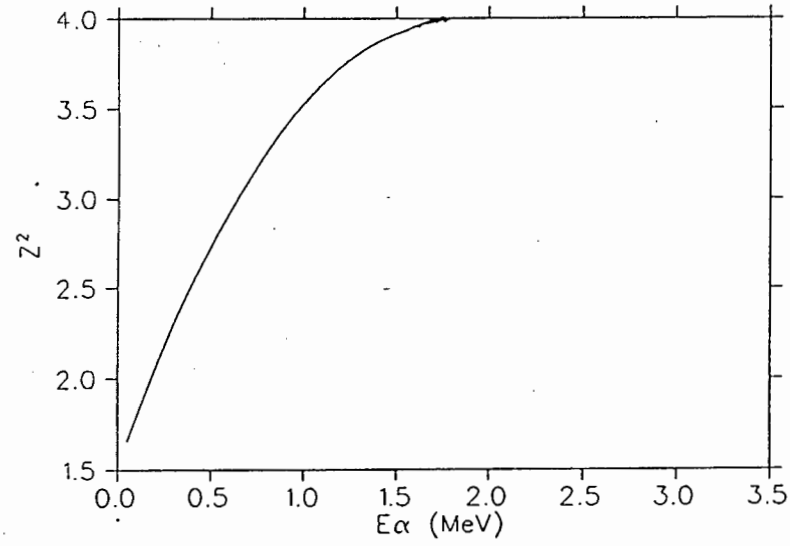

Figure 2.12: The variation of the square of the charge on α travelling through media with energy.

These fits were improved upon by using subroutines from ELOSS. ELOSS uses formulae from Anderson and Ziegler [48] for the stopping power of ions in matter, and claims 1% accuracy for ions in elements, and 5% for ions in compounds.

The formulae for $\alpha\mu$ and hence protons from Ziegler and Anderson were considered unnecessarily complicated and expensive in computing time for the accuracy required, as they included relativistic terms and log terms up to the power of 4, so the output from ELOSS was parameterised using two curves:

$$\frac{dE}{dx} = \begin{cases} -535.5E^{0.643}\ln\left(\frac{E}{1.12}\right) & E < 0.5MeV \\ 1.78E^{-0.756} & E > 0.5MeV \end{cases} \tag{2.7}$$

which were appropriately scaled for pressure.

The energy loss curves for alphas in gas were used directly from ELOSS, being:

$$\frac{dE}{dx} = \frac{pas_l s_h}{s_l + s_h} \tag{2.8}$$

where

$$s_l = b_{1,z}E^{b_{2,z}}$$

and

$$s_h = \frac{b_{3,z}}{E}\ln\left(\frac{b_{1,z}}{E} + b_{5,z}E\right) \tag{2.9}$$

The $b_{n,z}$ are parameters depending on the charge of the medium through which the α is travelling. Note the similarity of equation 2.8 to equation 2.6. The extra terms s_l and $b_{5,z}E$ correct for the charge exchange of the α.

Foils and Films

The energy loss of α in solids is calculated in a similar way, except that the number density is obtained differently, from

$$N_v = \frac{\rho N_A}{m} \tag{2.10}$$

where ρ is the density of the material, N_A Avogadro's number and m the molecular mass of the medium.

Specific energy loss curves for α in (a) NE102 and (b) Havar are in figure 2.13.

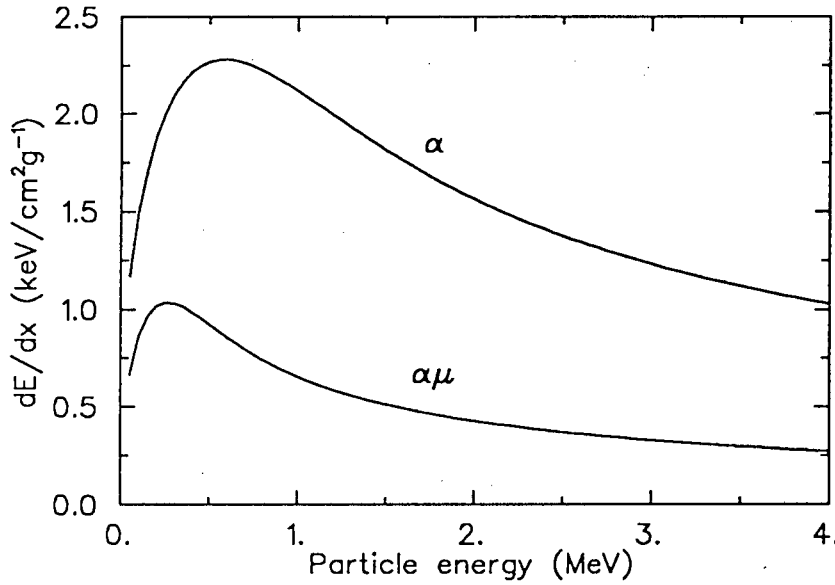

(a)

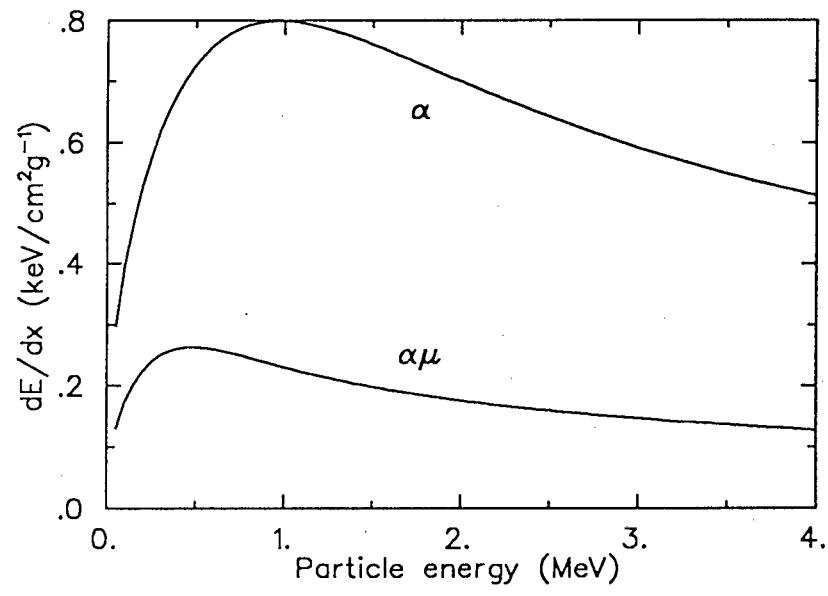

(b)

Figure 2.13: Specific Energy Loss curves for alphas in (a) NE102 and (b) Havar

2.5.2 Muon stripping

Theory [38] suggests that there is about a 27% chance that an $\alpha\mu$ will be stripped if it is brought to rest in the gas for pressures of the order of one or two atmospheres. Of course, the pressures and distances involved in LRG type experiments up to now ensure that $\alpha\mu$ only lose at the most 1.5 MeV (about half) and so the stripping in the gas is considerably less (about a third of 27%). The stripping in the windows and/or barrier contributes a similar amount to the stripping.

An expression for the muon stripping cross-section, σ_{str} was obtained from J. S. Cohen's paper [49] on muon stripping in various foils:

$$\frac{\sigma_{str}}{Z} = \frac{c}{X}\exp\left[-\frac{a}{MZ^{0.6}X}\right](1-e^{-bX}) \tag{2.11}$$

where Z is the atomic number of the medium through which the $\alpha\mu$ is travelling at speed v, X is the reduced variable v^2/Z, and M the reduced interatomic mass of the medium in atomic mass units. The factors a, b and c are constants, equal to 0.44, 0.4 and 5.4 respectively[1]. Plots of $\frac{\sigma_{str}}{Z}$ versus X for hydrogen (1), NE102 (2) and Havar (3) calculated using equation 2.11 can be seen in figure 2.14.

The effective muon stripping cross section from the $\alpha\mu$ as it traverses a distance dx of the material is:

$$\sigma_{str}^{eff} = N_v\sigma_{str}dx \tag{2.12}$$

where N_v is again the number density and can be obtained from the pressure (equation 2.5).

Hence we can set up a differential equation describing the change in the flux of unstripped $\alpha\mu$:

$$\frac{dF_{\alpha\mu}}{dx} = -F_{\alpha\mu}N_v\sigma_{str} \tag{2.13}$$

separating the parts:

$$\int\frac{dF_{\alpha\mu}}{F_{\alpha\mu}} = N_v\int_0^d\sigma_{str}dx \tag{2.14}$$

integrating and taking antilog:

$$F(d) = F_0\exp\left(-N_v\int_0^d\sigma_{str}dx\right) \tag{2.15}$$

[1] Cohen uses muonic atomic units ($\hbar = e = m_\mu = 1$). Hence the velocity is in μa.u. (1μa.u.$= 2.19\times10^{-8}$ms^{-1}) and σ_{str} is in a_μ^2 ($1a_\mu^2 = 655$b).

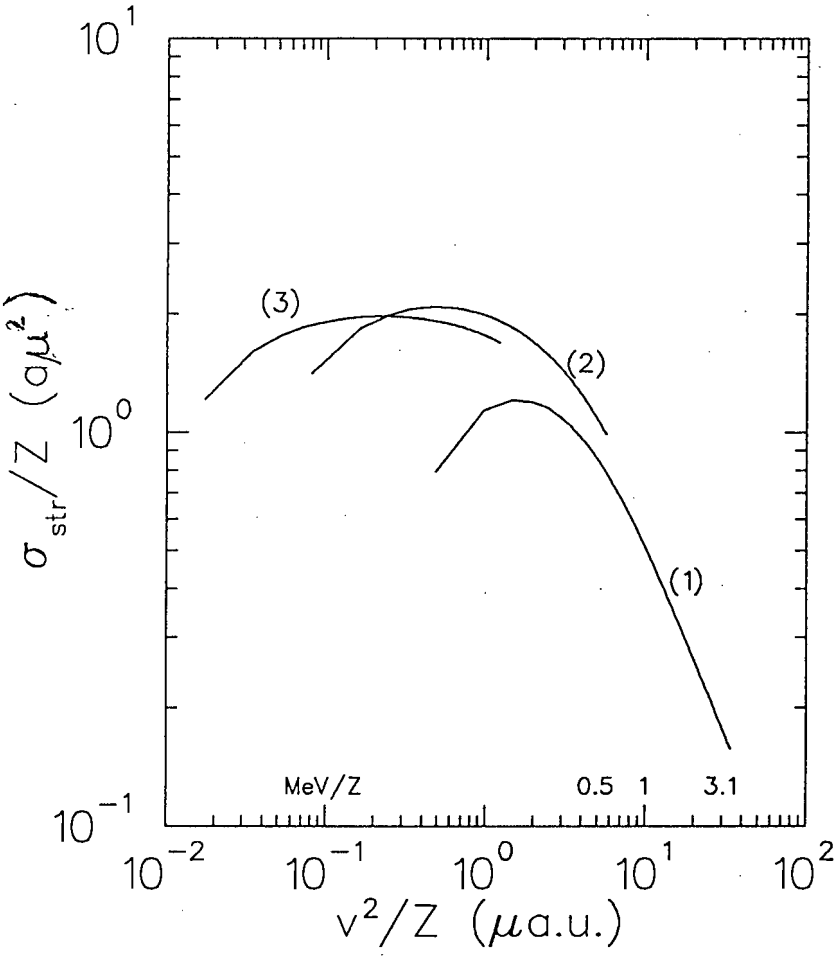

Figure 2.14: Plots of σ_{str}/Z versus X for (1) hydrogen, (2) NE102 and (3) Havar calculated using equation 2.11.

where F_0 is the flux entering the medium and d the distance travelled by the $\alpha\mu$ in the medium. The integration has to be performed numerically because σ_{str} is a function of energy and hence depth, as the energy of the $\alpha\mu$ is decreasing as a function of depth.

The Monte Carlo does this integration by stepping through the medium in small steps of distance. Essentially the integral in equation 2.15 is replaced with a sum. If the distance d is divided into n steps Δx long, the $\alpha\mu$ energy will, after step i, be E_i. So:

$$\exp\left[-N_v \int_0^d \sigma_{str}(E)dx\right] \approx \exp\left[-N_v \sum_{i=1}^{n} \sigma_{str}(E_i)\Delta x\right] \tag{2.16}$$

The sum can be replaced by a product, so

$$F(d) = F_0 \prod_i^n \exp\left[-N_v \sigma_{str}(E_i)\Delta x\right] \tag{2.17}$$

The Monte Carlo calculates this product by determining at each position $n\Delta x$ whether the $\alpha\mu$ is stripped while traversing distance Δx. The probability of stripping is simply

$$p_s = 1 - \exp\left[-N_v \sigma_{str}(E_i)\Delta x\right] \tag{2.18}$$

If a random number chosen between 0 and 1 is less than p_s — see appendix D — then the $\alpha\mu$ is considered stripped of its muon and a marker set to show where it was stripped.

Stripping was calculated for the DT gas, mylar windows, NE102 plastic scintillator, Havar foil, and Aluminium Oxide. Cohen states that equation 2.11 overestimates the stripping cross-section for hydrogen for $v^2 < 1\ \mu a.u.$, but as the $\alpha\mu$ never lose that much energy in the gas, it was considered a reasonable approximation. The results and a comparison with calculations by Cohen are given in section 4.3.

2.5.3 Alpha-neutron time difference T

The time difference recorded with the alpha energy/pulse height is:

$$T = T_\alpha - T_n \tag{2.19}$$

where T_α and T_n are the times of flight between fusion and detection of the alpha and neutron respectively. For the former,

$$T_\alpha = \int_0^{d_\alpha} \frac{dx}{v(x)} \tag{2.20}$$

where d_α is the distance the α travels between fusion and detection, and $v(x)$ its velocity, obtained from

$$v(x) = \sqrt{\frac{2E(x)}{m}} \tag{2.21}$$

Also:

$$T_n = d_n / \sqrt{\frac{2E_n}{m}} \tag{2.22}$$

where d_n is the distance the neutron travels between fusion and detection. No integration is necessary as the velocity of the neutron is constant.

2.5.4 Detection by plastic scintillator

The response of the TFP to alphas is, unlike the SBD, non-linear with energy. The pulse height of the scintillations caused in the detector by alphas is calculated using the Birks relation [50,51]:

$$\frac{dL}{dx} = \frac{A\frac{dE}{dx}}{1 + B\frac{dE}{dx}} \tag{2.23}$$

where A is a scaling factor and B is the Birks quenching constant for the particular scintillator, in this case NE102A. A fit to measured response of a TFP to alphas set B at 0.238 cm keV^{-1}.

Equation 2.23 is designed to give smaller pulse heights for particles with larger specific energy loss. For doubly charged alphas, there is more quenching of the pulse than for $\alpha\mu$ owing to the higher dE/dx at the same energy. Hence the pulse height for an $\alpha\mu$ will be larger than that for an α of similar energy. This has useful implications, which are discussed in section 4.1.5.

The computer code calculated the integral of dL/dx by integrating the $dE(E)/dx$ numerically over the distance travelled in the scintillator.

The timing resolution of a TFP has been measured in the lab as 1.2 ns FWHM or better. Batsch and Moszynski [52] obtain values as low as 300 ps FWHM for 5 MeV alphas incident on NE102.

2.6 Neutron detection

The neutron detectors ('K') used in the RAL experiments were 13 by 13 by 7 cm rectangular cells of NE213 liquid scintillator viewed by four photomultiplier tubes. Simulations were also made for the standard Nuclear Enterprises cylindrical detector, the 5cm diameter by 5cm long BA1 cell.

2.6.1 Outline of the detection process

A flowchart of the processes involved in the neutron detector can be seen in fig 2.15

NE213 consists mainly of carbon and hydrogen nuclei. Several processes, singly or collectively, may be involved in detection of a neutron:

1. The neutron undergoes an interaction with a carbon or hydrogen nucleus, producing one or more energetic charged particles.

2. The charged particle deposits energy in the scintillator, exciting the atomic or molecular states. If the interaction is close to the surface of the scintillator, there is a chance that the particle will escape before depositing all its energy in the scintillator.

3. A flash of light is detected by the photomultiplier.

The neutron interactions can be grouped roughly into two categories, which I have called *moderating* and *charged particle producing*. The moderating interactions serve to reduce the energy of the neutrons and only play a role if the neutron subsequently produces a light charged particle, a proton or alpha. This is because heavier particles (recoil carbon nuclei in this case) do not produce enough light at these energies to be detected, and gammas resulting from inelastic collisions are discriminated against if they produce pulses via energetic electrons.

Table 2.1 shows the various neutron interactions considered in the scintillator and their cross-sections while figure 2.17 shows the neutron energy spectrum after moderation by n-Carbon interactions. Fig 2.16 shows the dependence of the cross sections on energy. Of the charged particle producing reactions, only the H(n,n)H cross-section increases with decreasing energy at energies 0-14 MeV. This is an important factor, since moderation of neutrons increases their chance of subsequently producing detectable protons via elastic scattering, thus increasing the number of events at low pulse heights.

2.6.2 H(n,n)H Scattering and Proton Energy

The largest contribution to the detection process ($\sim$ 60% at zero threshold, increasing with increasing threshold) is neutron-proton elastic scattering. The energy of the recoil proton depends on the angle at which the neutron

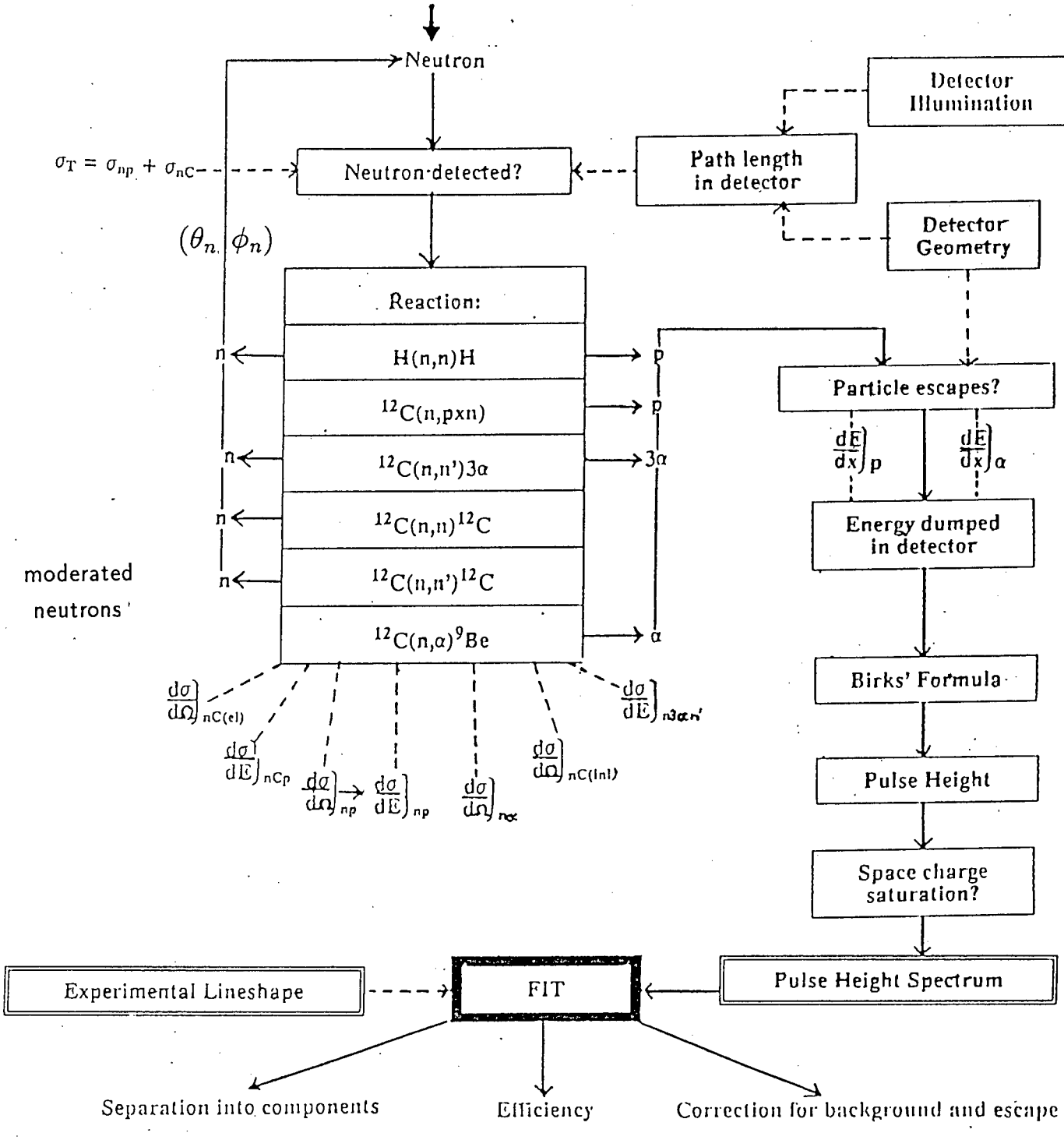

Figure 2.15: A flowchart of the steps involved in neutron detection as modelled by Monte Carlo simulations.

(a)

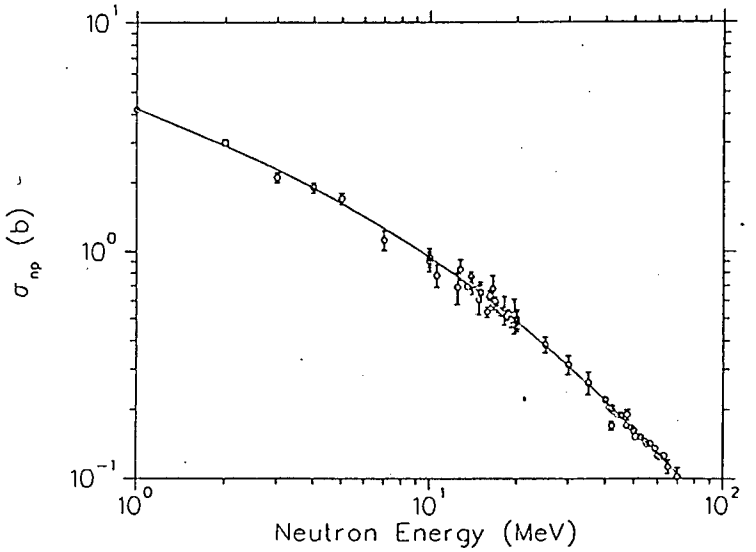

(b)

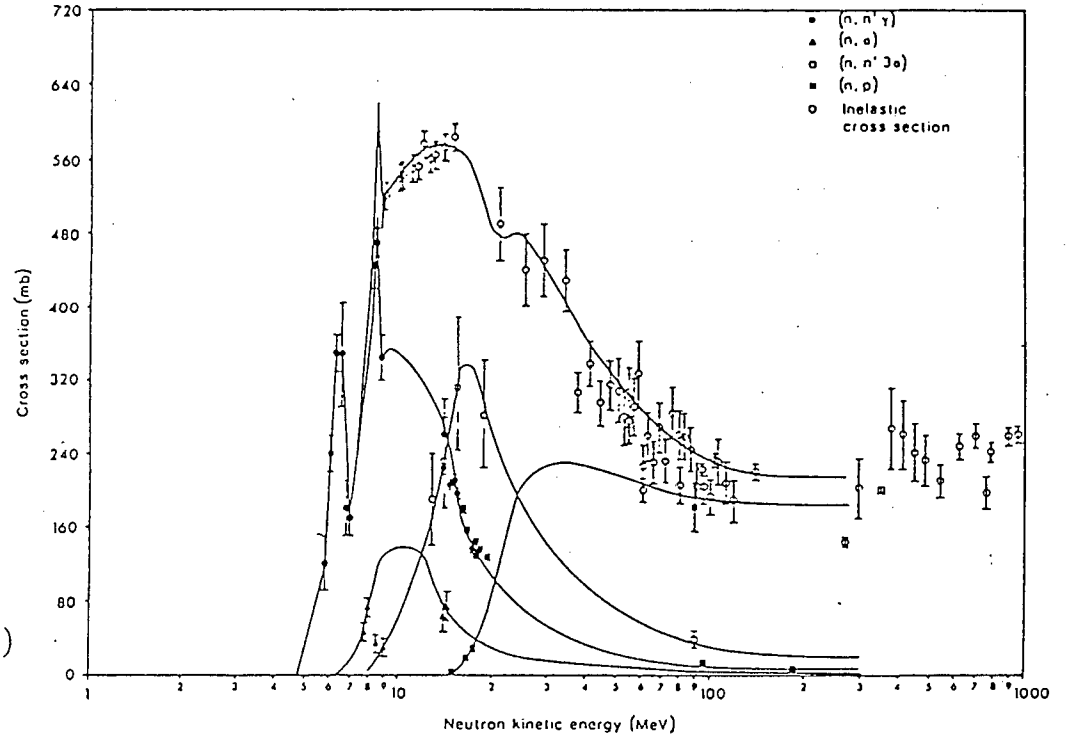

Figure 2.16: Neutron cross sections for (a) hydrogen: data from ref. [53], curve from equation 2.28. (b) carbon: reproduced from ref. [53]

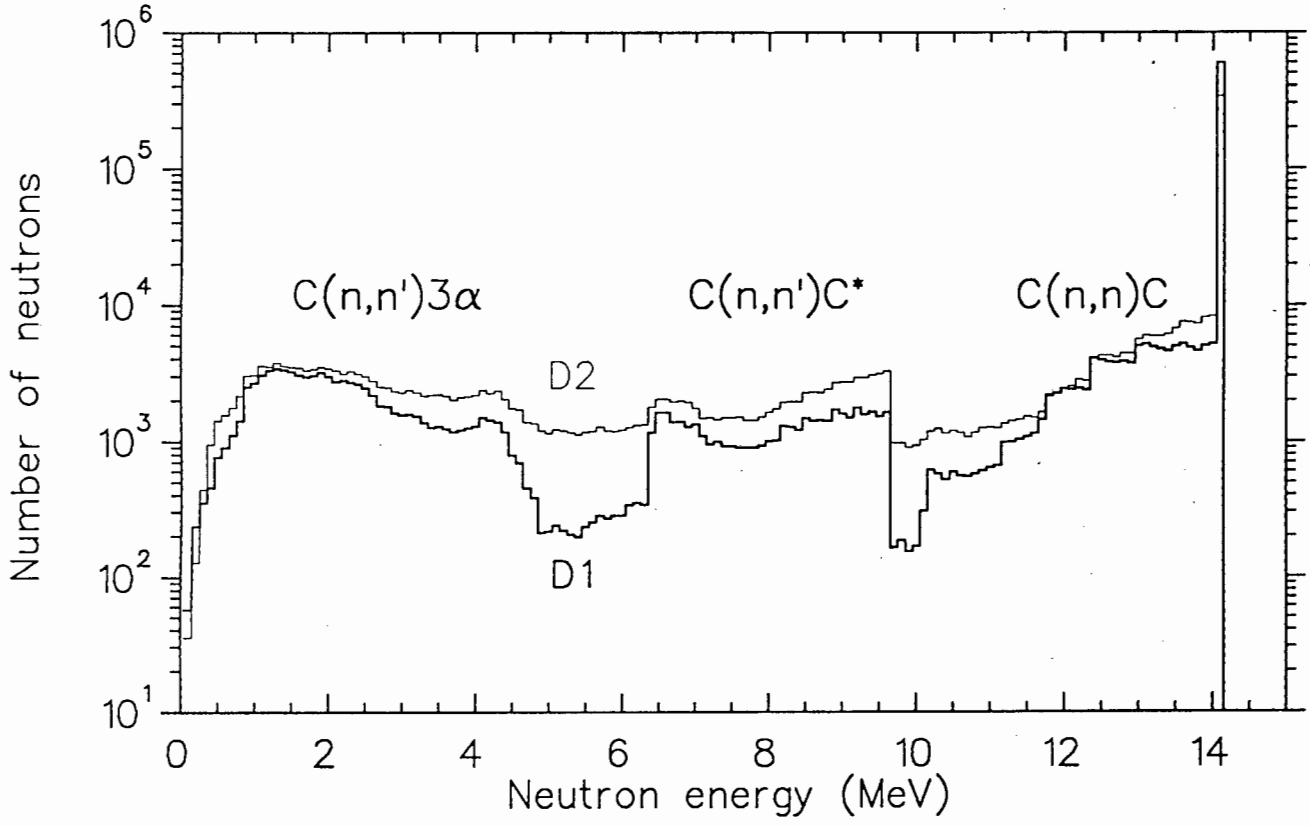

Figure 2.17: Energy spectrum of neutrons interacting for the first time with hydrogen. Most are 14 MeV, while the rest have been moderated by interactions with carbon nuclei.

	Cross section (mb)		
	14 MeV	63 MeV	
H(n,n)H	700	118	Charged Particle producers
$^{12}C(n,\alpha)^{9}Be$	80	4	
$^{12}C(n,pxn)$	1	150	
$^{12}C(n,n')3\alpha$	250	45	Moderators
$^{12}C(n,n)^{12}C$	790	200	
$^{12}C(n,n')^{12}C$	180	15	

Table 2.1: Types of neutron interactions in NE213 and their cross sections.

is scattered. As the scattering is almost entirely s-wave at 14.1 MeV the neutron angular distribution in n-p elastic scattering is very nearly isotropic, yielding a flat distribution in proton energy (fig 2.18). The angular differential cross section for n-p elastic scattering was approximated by the following expression from Gammel [54]:

$$\frac{d\sigma}{d\Omega} = \frac{\sigma}{4\pi}\left[\frac{1 + b\cos^2\theta_{\mathrm{COM}}}{1 + b/3}\right] \tag{2.24}$$

where $b = (E_n/90)^2$ and θ_{COM} is the centre of mass angle of the recoil proton. This expression yields a very nearly flat curve for E_n=14 MeV.

$$E_{p,\mathrm{COM}} = E_{n,\mathrm{COM}}\frac{1 - \cos\theta_{\mathrm{COM}}}{2} \tag{2.25}$$

The energies and angles must be converted into the lab frame, so:

$$E_{p,\mathrm{Lab}} = E_{n,\mathrm{Lab}}\cos^2\theta_{\mathrm{Lab}} \tag{2.26}$$

The scattered neutron now has the remaining energy:

$$E_{n',\mathrm{Lab}} = E_{n,\mathrm{Lab}}\sin^2\theta_{\mathrm{Lab}} \tag{2.27}$$

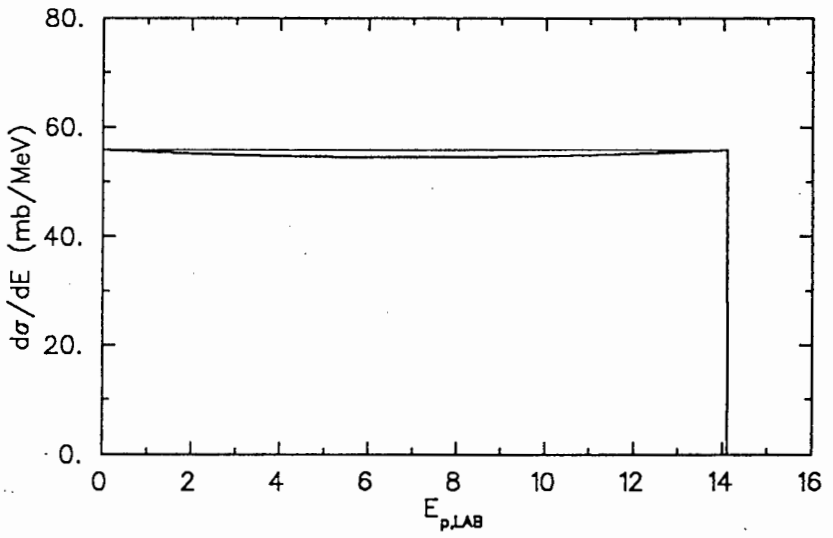

Figure 2.18: The energy distribution for recoil protons from H(n,n)p scattering at 14.1 MeV (bold curve) The feint line shows a flat distribution.

This moderated neutron may scatter on another proton or on a carbon, producing further charged particles. The H(n,n)H cross section was calculated using the following empirical expression [55]:

$$\begin{aligned}\sigma_{np} &= 3\pi[1.206E_n + (-1.86 + 0.09415E_n + 0.0001307E_n^2)^2]^{-1} \\ &\quad + \pi[1.206E_n + (0.4223 + 0.13E_n)^2]^{-1} \end{aligned} \tag{2.28}$$

2.6.3 ^{12}C(n,α)^{9}Be reaction

Neutron induced breakup of carbon nuclei in the scintillator becomes significant at 14 MeV. The neutron can knock out an α from a carbon nucleus, leaving the residual nucleus, ^{9}Be in the ground state. The Q value for the reaction is -5.7 MeV and as the ^{9}Be nucleus is only 9/4 times as heavy as the α, it can carry off up to 5.6 of the 8.4 MeV available in the centre of mass, if the alpha is released in the backward direction. If the alpha is released at zero degrees, it carries off 8 MeV while the Be nucleus carries off 0.4 MeV. The differential cross-section of the reaction is shown in fig 2.19 together with the α energy spectrum resulting from the kinematics. The spectrum is forward–backward peaked. These, together with the cross section, were

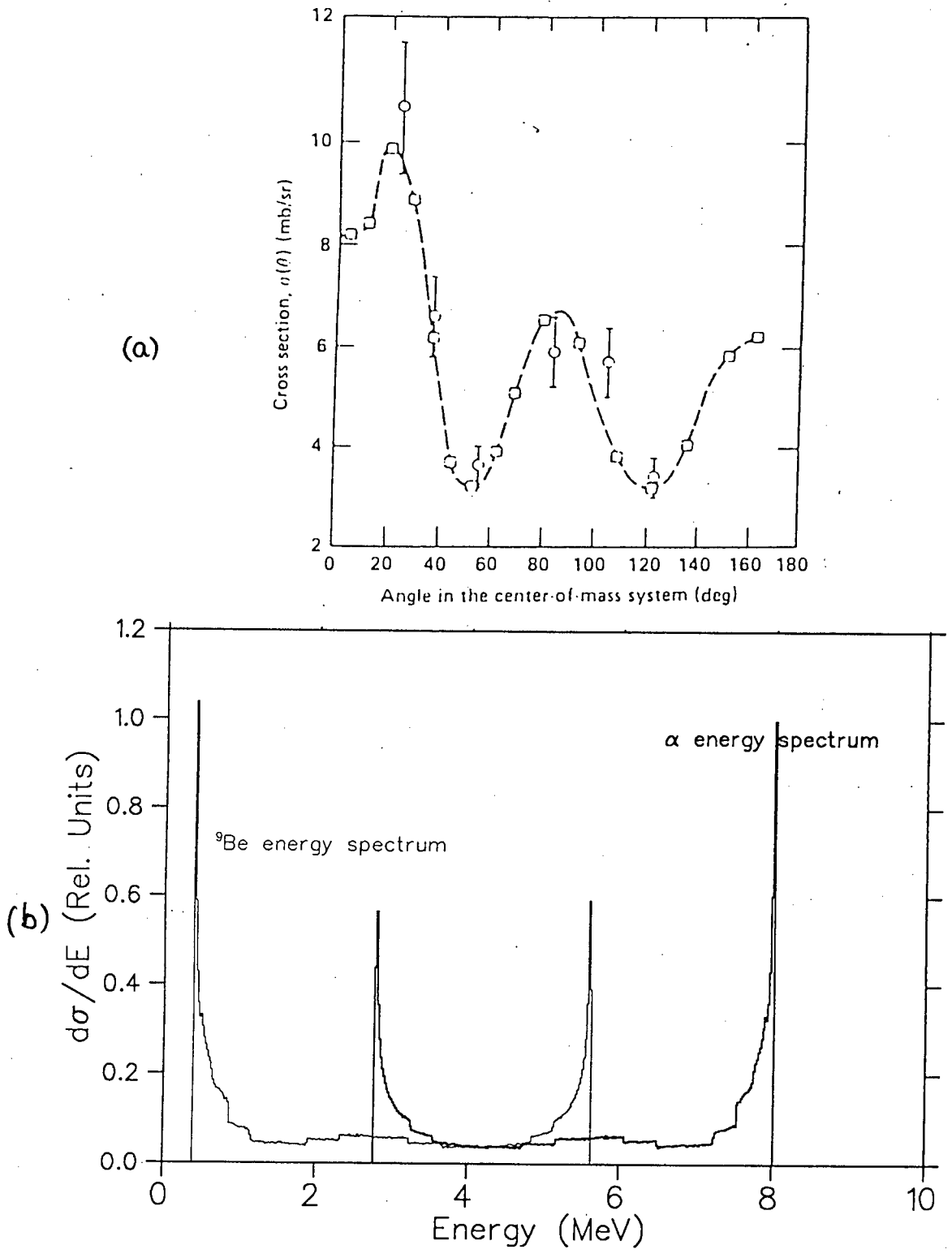

Figure 2.19: (a) The differential cross section of the $^{12}C(n,\alpha)\ ^{9}Be$ reaction reproduced from ref. [56] and (b) the resulting α energy spectrum

obtained from Haight et al. [56] Although the maximum α energy is some 8 MeV, the pulse height from α is very much less than that from protons of similar energy, because the heavier the ion, the greater the specific energy loss and hence the less efficient the scintillation (see equation 2.23). The beryllium nuclei will in turn produce even less light. The light output from Be nuclei does, however, make an appreciable contribution to the pulses from the α, Be reaction and was approximated from the α pulse height spectrum using the following form:

$$L_{Be}(E) = \frac{\mathcal{Z}_{\alpha}^2 m_{Be}}{\mathcal{Z}_{Be}^2 m_{\alpha}} L_{\alpha}\left(\frac{m_{\alpha}}{m_{Be}}E\right) \tag{2.29}$$

which is obtained from comparing the Bethe-Bloch formulae for α and Be ions. As the specific energy loss of ions in matter depends on velocity rather than kinetic energy, so does the pulse height. Stevens [57] suggests that $\mathcal{Z}_{Be}$ be set to 2.

Excitation of the ^{9}Be to higher energies results in its breaking up into two α and a neutron, the reaction outlined in the next section.

2.6.4 ^{12}C(n,n')3α reaction.

The excited states of ^{12}C above the 4.44 MeV level are very unstable against alpha emission [58]. Since ^{8}Be is unbound against decay into two alpha particles, the other states, when populated by inelastic scattering break up into three α particles [56]. One may assume that any n–^{12}C interaction producing an excited beryllium nucleus or leaving the carbon nucleus in an excited state higher than 4.436 MeV will almost certainly cause the carbon to fall apart into three α particles — i.e. the gamma decay of states above 4.4 MeV in carbon appears to be negligible relative to breakup.

The 3α and scattered neutron spectra from this reaction were obtained from Antolkovic et al. [58,59] As the physics behind the reaction is very complicated, the reaction being a four body breakup, no attempt was made to estimate the neutron angular distribution and it was considered isotropic. The scattered neutron spectrum was taken directly from their measurements, which show structure displaying the energy levels of the carbon nucleus excited (fig 2.20). If the code is to be generalised for a range of energies, an attempt to model this structure will have to be made. The model in the code SCINFUL written by J.K. Dickens [60,61] should be a good starting point.

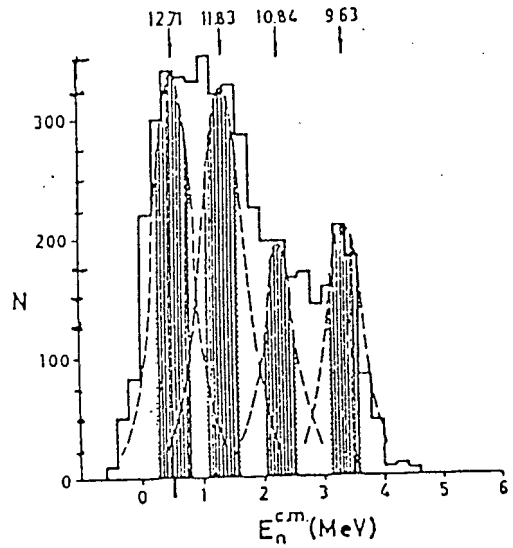

Figure 2.20: The scattered neutron energy spectrum from the ^{12}C(n,n')3α reaction. Reproduced from reference [58]

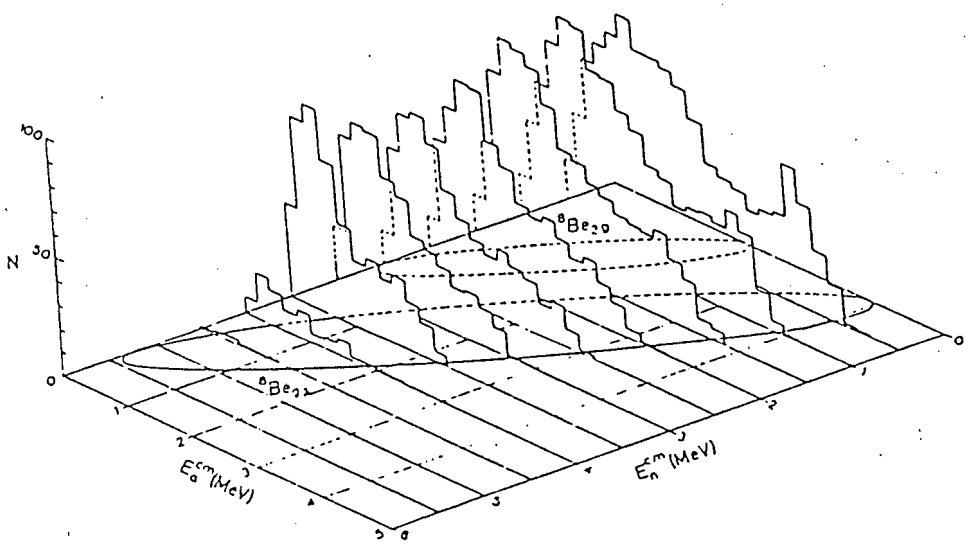

Figure 2.21: Alpha energy spectra from the ^{12}C(n,n')3α reaction for various scattered neutron energies. Reproduced from reference [58]

The α spectrum was measured for several neutron energies and displays the typical four-body distribution with a peak around a third of the maximum α energy. The MC picked a neutron energy from the distribution and then picked three α from the corresponding α distribution. This is shown in figure 2.21.

The moderated neutron, between 0 and 4 MeV, could then interact further in the detector.

2.6.5 ^{12}C(n,n)^{12}C Elastic and Inelastic scattering

The other two interactions considered in the scintillator were the elastic and inelastic ($Q = -4.436$) scattering of neutrons by carbon. Neither of these produces detectable charged particles, so their only role is to alter the energy of the neutrons. These contributions enhance the lower pulse height regions of the neutron detector lineshape via multiple scattering.

The energy change to neutrons via elastic scattering on carbon is purely due to the kinematics, the scattered neutron leaving with energy between 10 and 14 MeV. Since the elastic scattering cross-section on carbon is comparable with that for n-p elastic scattering at 14 MeV, as many neutrons scatter on the carbon elastically as on the hydrogen, so this contribution should cause an appreciable change in the shape of the n-p edge at 14 MeV, decreasing the number of recoil protons between 12 and 14 MeV per incident neutron slightly, and enhancing the lineshape between 10 and 12 MeV.

The ^{12}C(n,n')^{12}C* scattering has a lower cross section but moderates the neutrons into an energy region where the n-p elastic cross-section is much higher. Thus it enhances the intermediate and low pulse-height region of the proton recoil spectrum. Both cross-sections are regarded in the code as constant above threshold. The gamma emitted on decay of the excited carbon nucleus is unlikely to be detected via compton scattering or pair production. If it were detected, the event might be rejected as a gamma event in the detector by pulse shape discrimination (see next section). The calculated lineshape fits the data well at the region discussed, so the effect appears to be small.

The differential cross sections for elastic and inelastic scattering of neutrons by carbon, as well as their absolute cross sections, were obtained from Haouat et al. [62] and Mezzetti et al. [63]

Figure 2.22 shows the contribution from the various processes in in the detector to the lineshape. Note that the largest contribution to the higher pulse height part of the spectrum is from single np elastic scattering, while

for the low pulse height region the alpha breakup of carbon dominates.

2.6.6 Pulse Shape Discrimination

NE213 liquid scintillator is often used for neutron detection work, mainly for its good light output and excellent pulse-shape discrimination (PSD) properties.

The scintillation pulse produced by a charged particle consists of two components, a fast decay component F and a slow decay component S. The higher a particle's specific energy loss on average, the more highly ionising it will be, and the larger the slow component it will produce. Pulses from particles such as protons will thus have larger slow components than electrons. PSD involves separation of particles depositing energy in a scintillator by comparing the ratio of slow components to total pulse produced.

The gamma background, which gives rise to energetic electrons in the scintillator, is easily removed from the neutron signal by rejecting the particles labelled as electrons by PSD.

The PSD was done in the RAL experiment by integrating the pulse from the detector over two different times, one to include the whole pulse and the other to include only the beginning [64]. These are called the L and F components respectively. The slow decay component (S) is then isolated by subtracting the fast (F) component from the total (L) pulse.

Cuts to reject certain energetic particles such as electrons are positioned by plotting L versus S and identifying the loci on the LS plot formed by the various particles causing scintillations. Figure 2.24 shows one of these plots.

Figure 2.23 shows a plot of dE/dx versus distance penetrated into the scintillator for 14 MeV protons incident in NE213. Superimposed on this curve is the decreasing energy of the proton. The specific energy loss of the proton climbs steadily with distance as it loses energy. Very near the end of the proton's path, the effective charge on the proton drops as a result of charge exchange and the specific energy loss decreases. A large fraction of the proton's energy is deposited over a short distance towards the end of its path in the scintillator, marked 'B' in diagram 2.23. Since the proton at B is most highly ionising, it is at this region of high dE/dx that the slow component S of the pulse is most enhanced, and the total scintillation L least efficient. Hence if the proton escapes from the scintillator, most probably the part of the curve marked B will be missing, which will cause a greater loss in the slow component S than the total pulse L. Thus the event might not fall on the locus in the L–S plane defined by the protons which do not

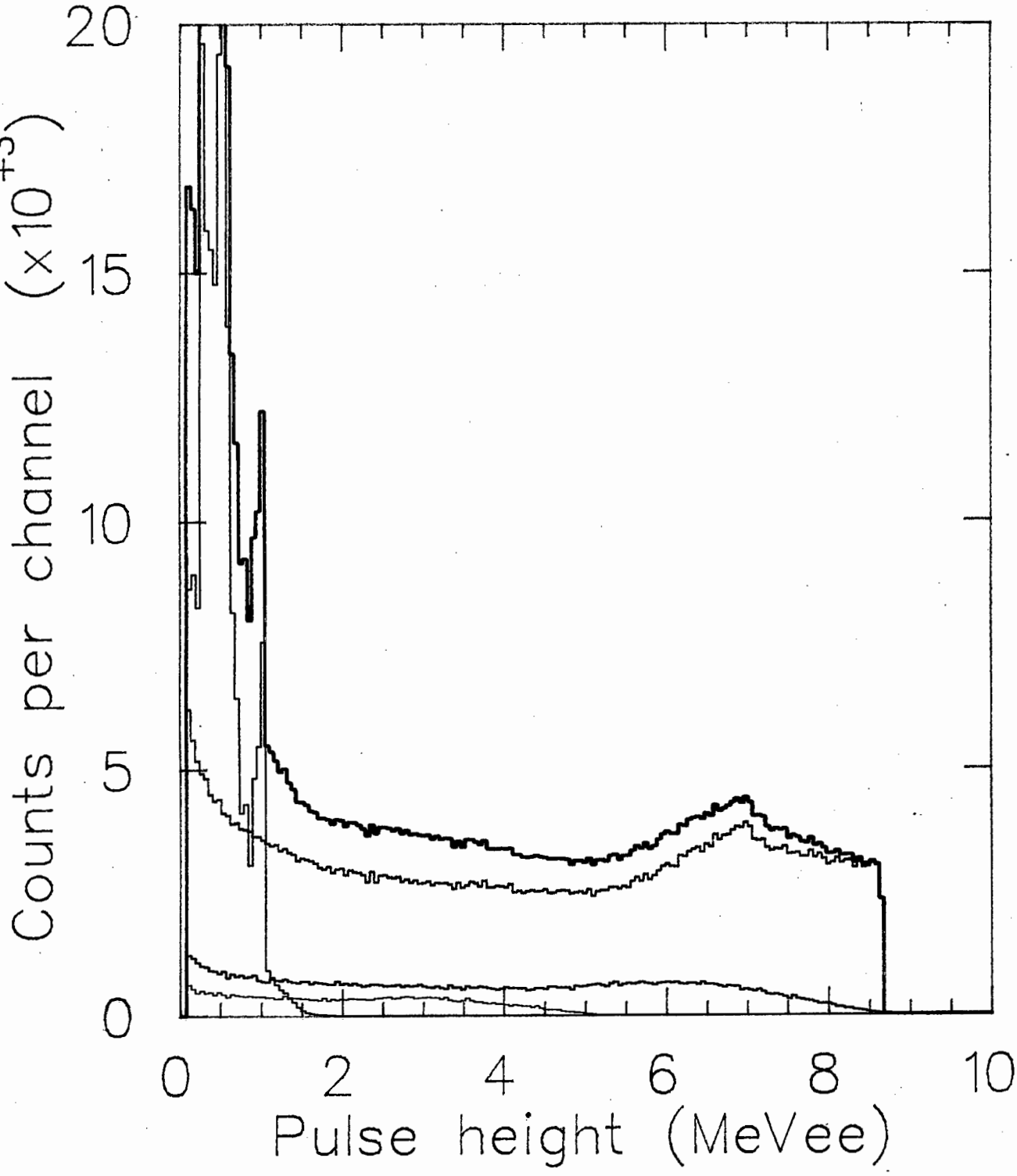

Figure 2.22: The unbroadened theoretical lineshape for the K detector with the contributions from the various processes included.
Bold black: total. Feint black: np scattering alone. Red: C(n,n)C elastic scattering followed by np elastic scattering. Green: C(n,n')C inelastic scattering followed by np elastic scattering, and purple: the C(n,xαyn') contribution.

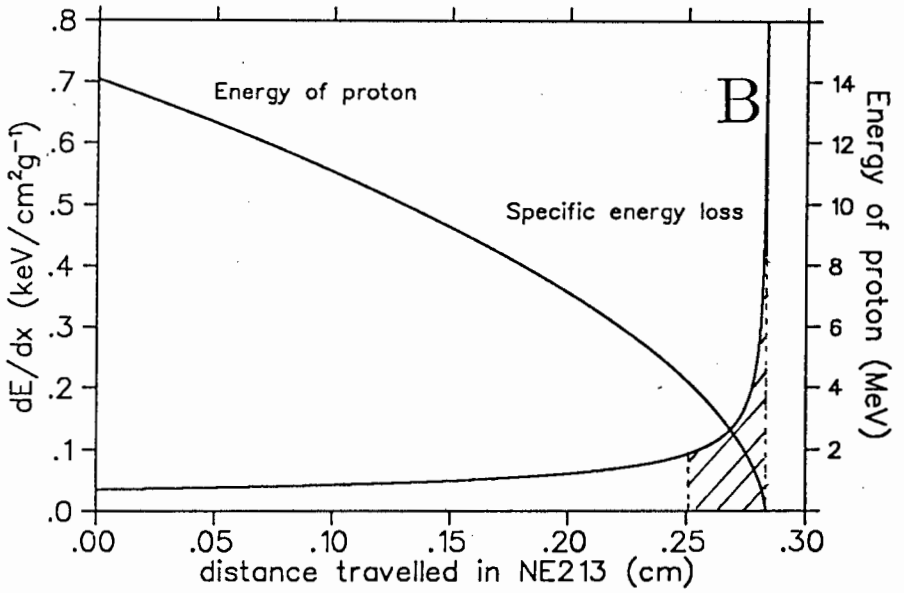

Figure 2.23: The calculated specific energy loss of 14 MeV protons incident on NE213 (increasing), and energy of proton (decreasing), as a function of distance penetrated into the scintillator.

escape, but between the proton locus and the electron locus.

The other effect this energy loss with distance has is that the lower the energy of the particle, the greater the ratio of energy lost at B to the total energy lost. This means that the lower the energy of a particle, the higher the ratio of slow component to total pulse. Hence two protons of, say, 6 and 8 MeV will not only give a total L less than that of a single 14 MeV proton, but they will give a higher S.

2.6.7 Pulse height spectrum for 14 MeV neutrons

As mentioned in section 2.5.4, the response of an organic scintillation detector to protons and heavier charged particles is non-linear with energy. This has several implications: The recoil proton spectrum is altered (fig 2.28) so that the lower energy region is enhanced.

If the detector were linear with energy, the hump from multiple scattering

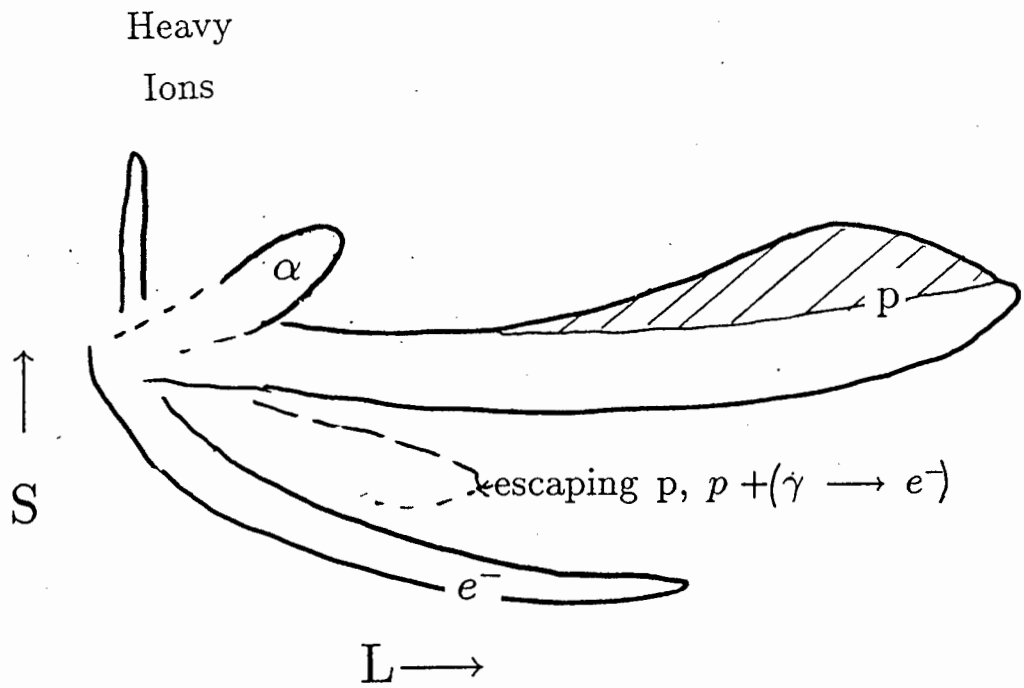

Figure 2.24: A diagram of the LS plane

would ride on the edge, whereas the hump lies at a lower pulse height region (fig 2.30) as two protons, one of, say, 8 MeV and the other of 6 MeV, will give a lower combined pulse height than a single proton of 14 MeV. The other effect is that with two protons instead of one, there will be two regions of very high dE/dx ('B' on figure 2.23) instead of one, where the protons are more highly ionising. This will lead to an enhancement in the LS plane, shown as a bulge towards higher S at a pulse height equivalent to about 12 MeV protons. This is shown by the shaded region in figure 2.24

Multiple consecutive np scatters occurs for about 10 % of incident neutrons for a detector of about 1 ℓ volume, decreasing with detector size. This process removes counts from low pulse-hight regions and places them at higher pulse heights. As the scattered neutron energy decreases, the n-p elastic scattering cross section increases, so triple and quadruple scattering occur in non negligible numbers, enhancing pulses at around 10-12 MeV.

The range of a 14 MeV proton in NE213 is about 2.5 mm and in a detector of the size used in the RAL experiment, the effect of protons escaping from the scintillator before depositing all their energy is small. Nevertheless, it is quite a visible effect and should not be neglected. The amount of energy a proton of energy E_0 travelling a distance x deposits in the detector was calculated as follows: A curve was fitted to data for specific energy loss

of protons in NE213 [47]:

$$\frac{dE}{dx} = -311E^{-0.793}\ keVcm^2mg^{-1} \tag{2.30}$$

$$\int_0^x dx' = \int_{E_0}^{E} \frac{dE'}{311E^{-0.793}} \tag{2.31}$$

$$\Rightarrow x = 1.793 \times 10^{-3}(E_0^{1.793} - E^{1.793})$$

$$E_0 - E = E_0 - \left[558(E_0^{1.793} - x)\right]^{(1/1.793)}\ \text{MeV}$$

where E is the energy of the proton on leaving the scintillator. By dividing equation 2.23 through by dE/dx we have:

$$\frac{dL}{dE} = \frac{A}{1 + B\frac{dE}{dx}} \tag{2.32}$$

For $BdE/dx \ll 1$, which is true for moderately ionising particles such as protons, we have

$$\int_0^L dL' = A\int_{E_0}^{E}\left(1 - B\frac{dE}{dx}\,dE'\right) \tag{2.33}$$

$$\Rightarrow L = A\left(E_0 - E + B\int_{E_0}^{E} 311E^{-0.793}dE'\right)$$

$$\Rightarrow L = A\left[E_0 - E + 1500B(E^{0.207} - E_0^{0.207})\right] \tag{2.34}$$

This relation, while adequate for escaping protons, was not a good enough fit to the energy – pulse height data for protons. The lineshape from the proton recoil spectrum is very sensitive to the proton energy – pulse height relation: The position of the 'hump' due to multiple scattering depends on the concavity of the function used to describe the E – L relation, as is the increase in distribution at lower pulse heights. A fit by Madey et al. [65] of the form:

$$L = aE - b(1 - e^{-cE^d})\text{MeVee} \tag{2.35}$$

was modified to agree with data from Smith et al. [66], Verbinsky et al. [67] and Uwamino et al. [68]. The same formula, but with different coefficients,

Table 2.2: Coefficients for equation 2.35 for protons and alphas used in this work

	a	b	c	d
protons	0.77	2.62	0.25	0.90
alphas	0.54	5.89	0.09	1.08

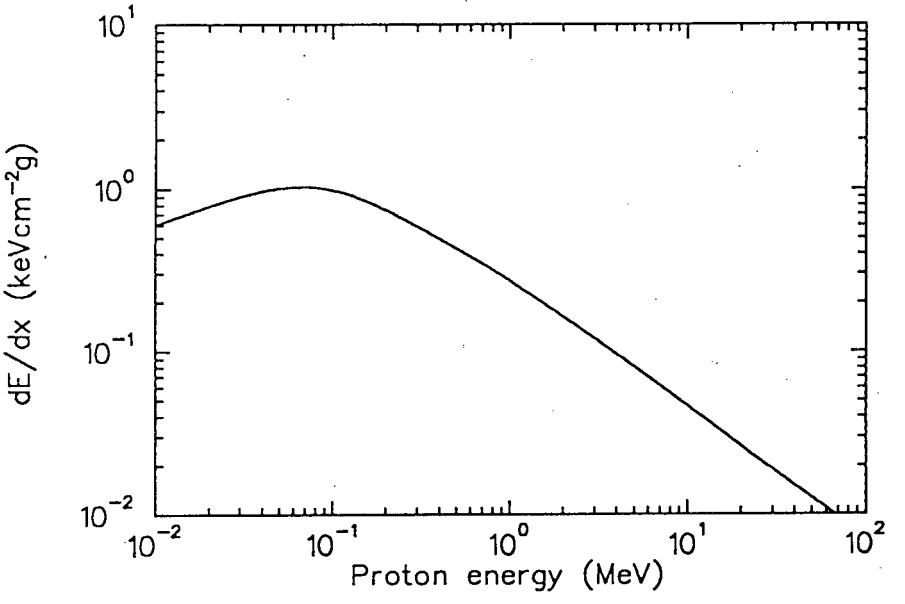

Figure 2.25: The specific energy loss curve for protons in NE213

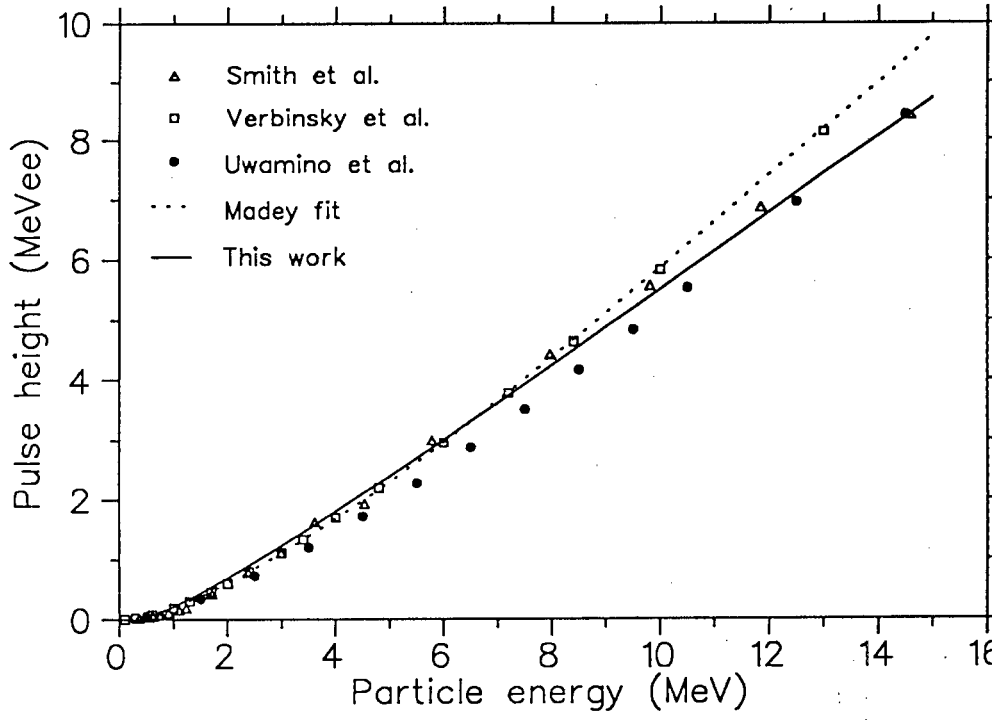

Figure 2.26: The energy-pulse height relation for protons in NE213. The curves are from equation 2.35.

(table 2.2) was used for alphas and Beryllium. These calculations are shown in figures 2.26 and 2.27.

Figure 2.25 shows the specific energy loss versus energy for protons in NE213 (calculations from Ziegler and Anderson [48]). The dE/dx rises sharply as the energy of the proton decreases, and then falls off as charge exchange occurs. As this occurs only at very low energies, it was considered a negligible effect.

The effect of proton leakage on the pulse-height spectrum can be seen in fig 2.29

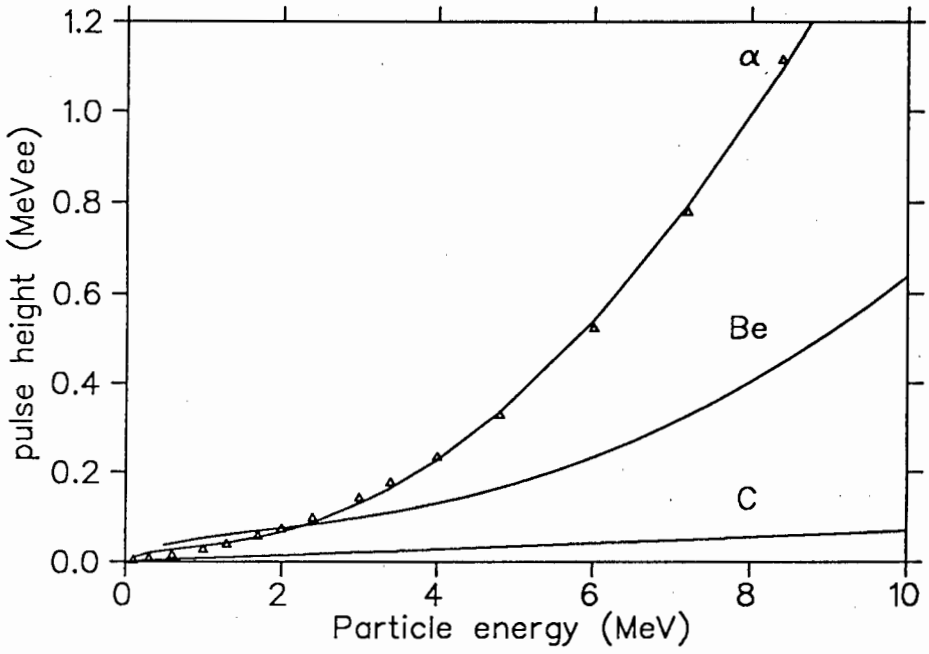

Figure 2.27: Energy–pulse height relation for carbon, beryllium and alphas in NE213

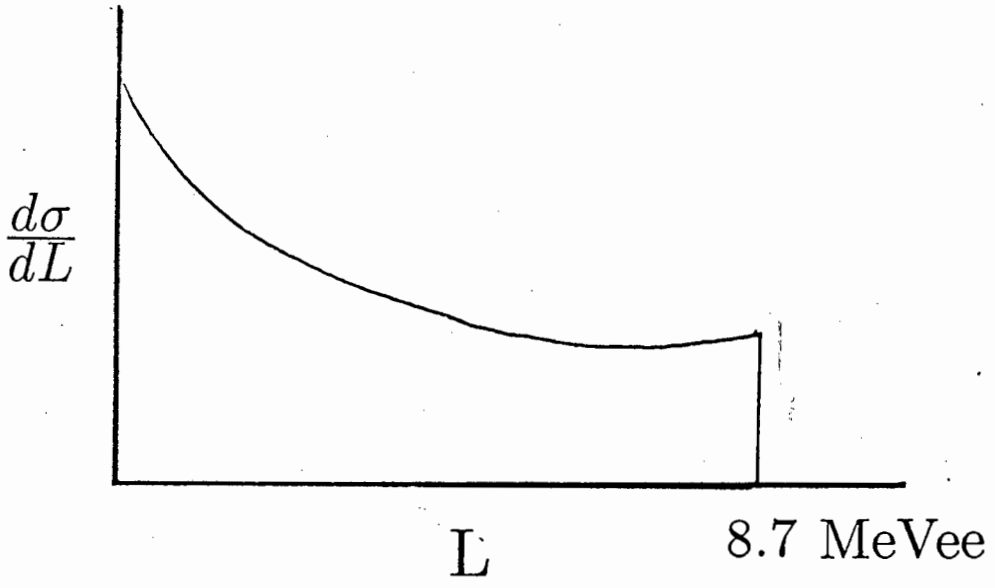

Figure 2.28: A schematic diagram of the pulse height spectrum from single proton recoil

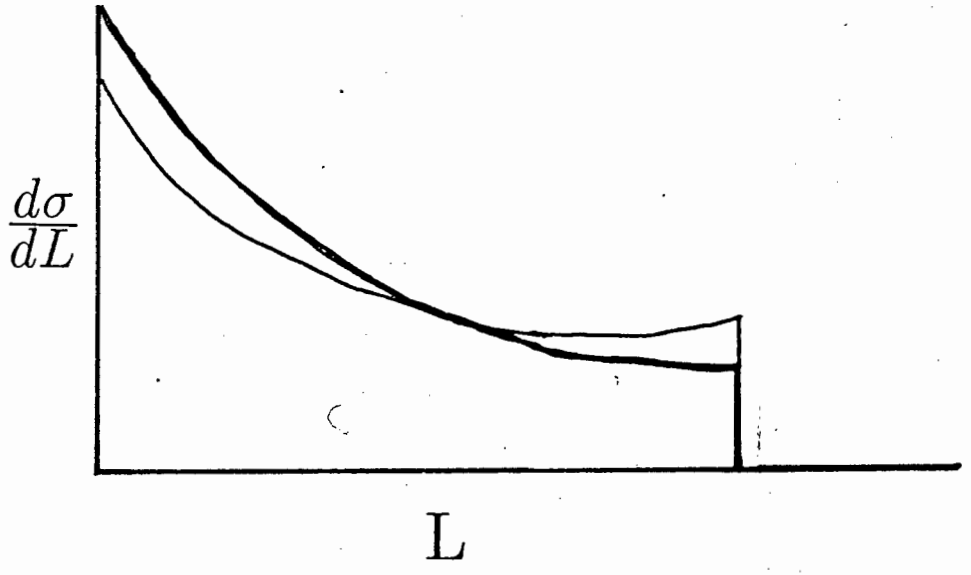

Figure 2.29: A schematic diagram of the effect of proton escape on the pulse-height spectrum (bold curve).

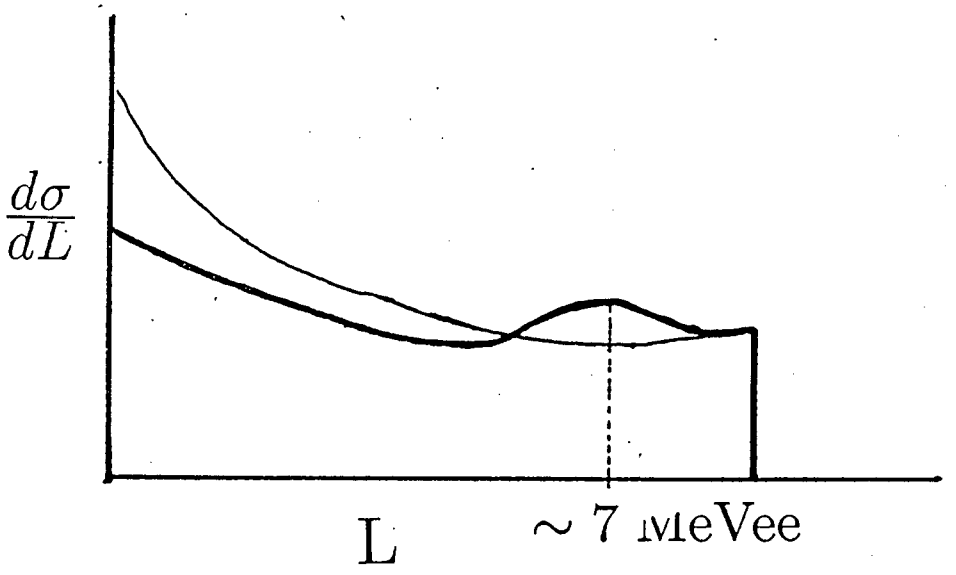

Figure 2.30: The contribution of multiple scattering to the proton pulse height spectrum

2.6.8 Light attenuation effects

Large detectors are sensitive to the position of interaction of the neutron in the scintillator volume, as the light is attenuated by the medium, and scattering off the walls of the scintillator cell is not uniformly efficient.

For a cell of length smaller than diameter, the attenuation is calculated using the following relation from Clark [69], refined by de Leo [70] for the fraction F of scintillation photons reaching the photocathode:

$$F = \frac{st}{1 - rt(1 - s)} \tag{2.36}$$

where s is the fraction of total solid angle subtended by the phototube window, calculated by the approximation suggested by Gardner and Verghese [71]; r is the reflection coefficient of the scintillation container walls; and t is the average survival probability for a photon travelling through the scintillator material, given by:

$$t = exp(-a < p >) \tag{2.37}$$

where a is the linear light absorption coefficient for the material (calculated to be $\frac{1}{150}$ cm^{-1} by Kuijper et al. [72]) and $< p >$ is the average path length between successive reflections on the cell walls. $< p >$ is approximated by [73] :

$$< p >= 4V/S \tag{2.38}$$

where V and S are the volume and surface area of the cylindrical cell respectively. The value for r was taken to be 0.96, from data from Nuclear Enterprises.

The effect of attenuation for the BA1 detector, where the length is comparable to the diameter, was estimated using a formula from Nakayama et al.:

$$F = st_0 + (1 - s)rt_1 \tag{2.39}$$

where

$$\begin{aligned} t_0 &= exp(-al_0) \\ t_1 &= exp(-al_1) \\ l_0 &= h \\ l_1 &= 2L - h \end{aligned}$$

where h is the distance of point of interaction from the photomultiplier face and L is the length of the detector.

The use of light attenuation to estimate the position of neutron interaction in the K neutron detectors is being investigated, with plans for use in the next RAL MCF experiment. The neutron detector code may be adapted to simulate this.

2.6.9 Neutron detector lineshapes

The calculated detector lineshape were fitted to measured ones using the non-linear least-squares fitting program MINUIT[74]. The calculated pulse height spectra were scaled vertically and horizontally, and convoluted with a gaussian varying in width with $\sqrt{L}$ to fit the measured lineshape (figure 2.31).

2.7 Summary

The MUGLU has as input:

1. parameters describing the shape and size of the target box,
2. the positions and sizes of the alpha and neutron detectors and thicknesses of foil through which the alpha travels,
3. the muon stopping distribution.

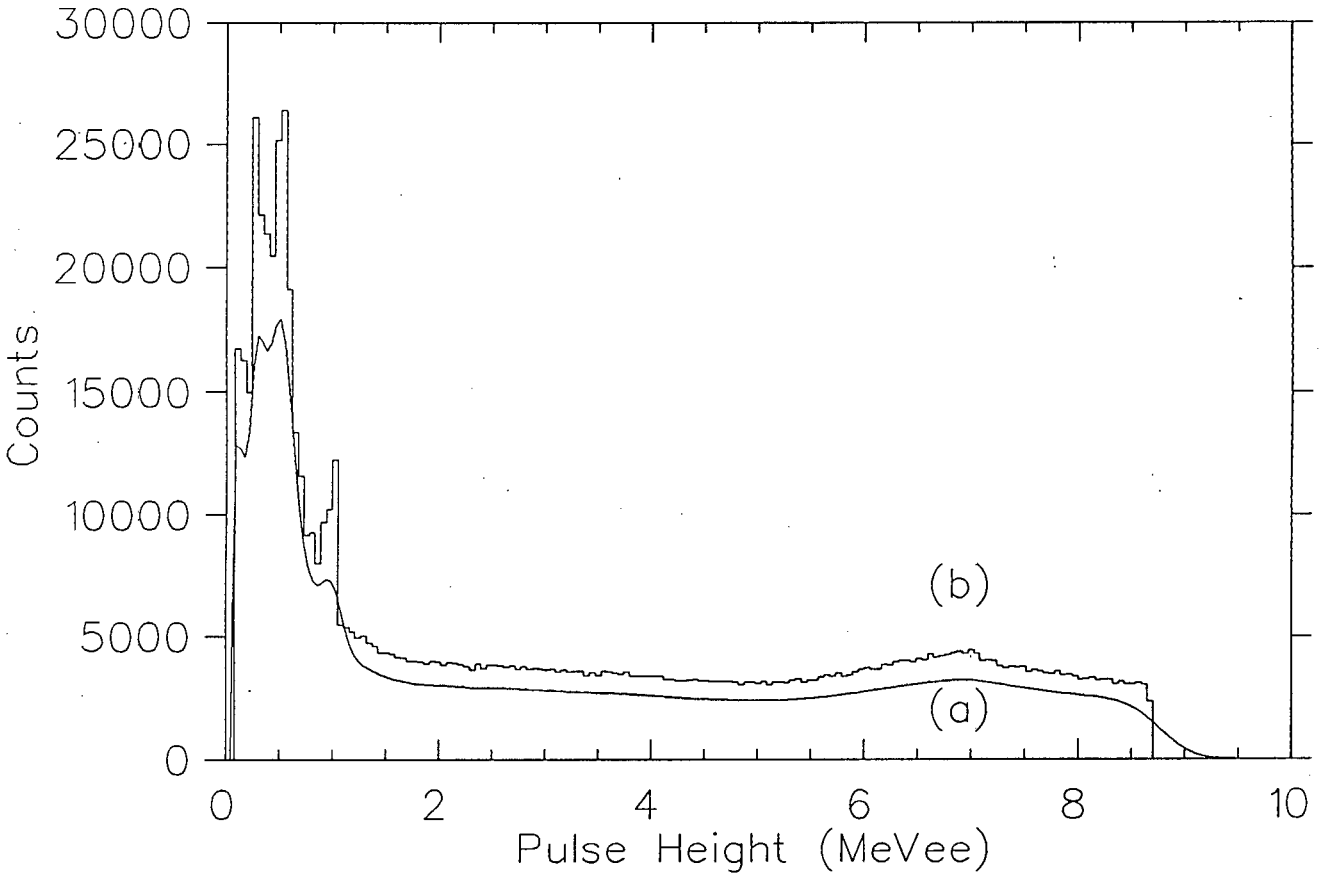

Figure 2.31: The Monte Carlo lineshape for 14 MeV neutrons (a) convoluted with a gaussian of width $\propto \sqrt{L}$ and (b) unbroadened.

Output includes:

1. the neutron detector lineshapes,
2. the alpha energy spectra,
3. the time–energy distribution of the coincidence alphas,
4. the B and Φ factors.

Since the experiment at RAL is based on singles and coincidence measurements for the calculation of ω_s^0, discussion of the output from the MC in the following chapters is divided in a similar way.

Neutron singles lineshapes from the NE213 detectors as calculated by the MC are compared with measurements made at the NAC/SUNI Van de Graaff using neutrons from the $T(d,n)\alpha$ reaction. This is presented in detail in chapter 3.

Coincidence output includes the B factors, the alpha energy/pulse height spectra, and the alpha energy–time scatter plots. These are presented and compared with existing measurements from RAL and LAMPF in chapter 4.

Chapter 3

The T(d,n)α reaction — measuring the neutron detector lineshape

Collinear α–n coincidences from fusion are readily simulated by the T(d,n)α reaction

$$d + T \longrightarrow n(14.1MeV) + \alpha(3.5MeV) \tag{3.1}$$

initiated by deuterons near threshold (20 keV). The reaction induced in a cell of tritium gas [75] provides a copious source of α–n coincidences in a geometry which very nearly emulates MCF. This is very useful for modelling several aspects of MCF experiments in the laboratory as opposed to simulations using computer codes. Furthermore, reaction 3.1 can be used to check various aspects of the monte-carlo simulations. The aspects modelled in this work centre mainly on the response of the neutron detectors used in LRG experiments to 14.1 MeV fusion neutrons, as the d-t fusion reaction has been widely used in associated particle measurements [76,77,78] of neutron detector response and efficiencies.

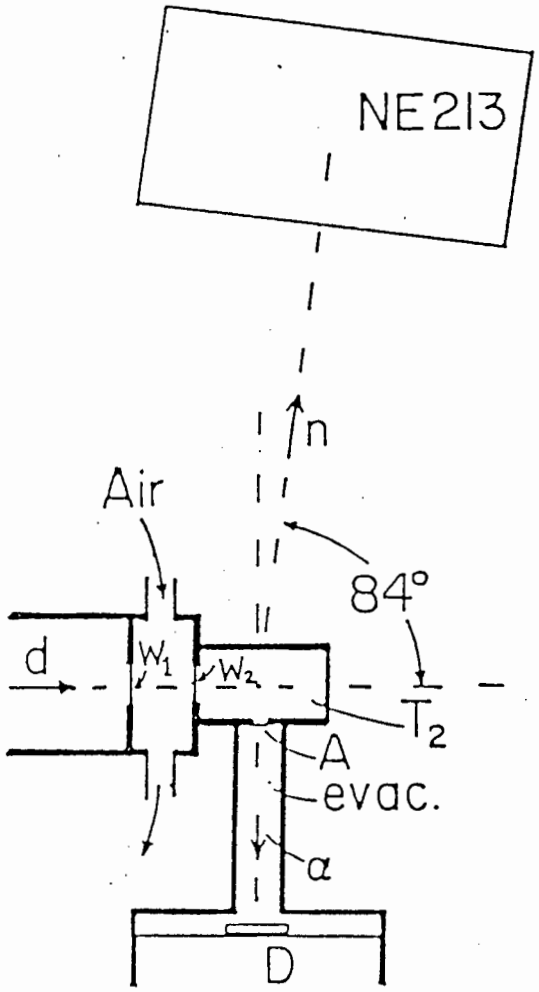

Figure 3.1: The apparatus for the T(d,n)α emulations.

3.1 Experimental Procedure

The measurements were carried out using a tritium gas cell and an alpha detector with a small acceptance angle. In this way, the associated neutron beam was tightly collimated and very nearly monoenergetic.
Figure 3.1 shows the apparatus for the measurements. The target consisted of a 4 cm by 2 cm diameter tritium cell with a 1.6 μm havar window (A) to allow the α to leave the cell and impinge on the alpha detector. An evacuated tube to select the α emitted at 90±4° to the beam connected the alpha detector to the window. The neutron detector could be moved to different distances d_n from the cell and angles $180° - \theta_n$ to the incident deuteron beam.
The deuterons from the NAC 5 MV Van de Graaff accelerator passed through two air cooled havar windows (W_1 and W_2 in figure 3.1) before entering the cell. The deuteron beam current was about 50 nA.

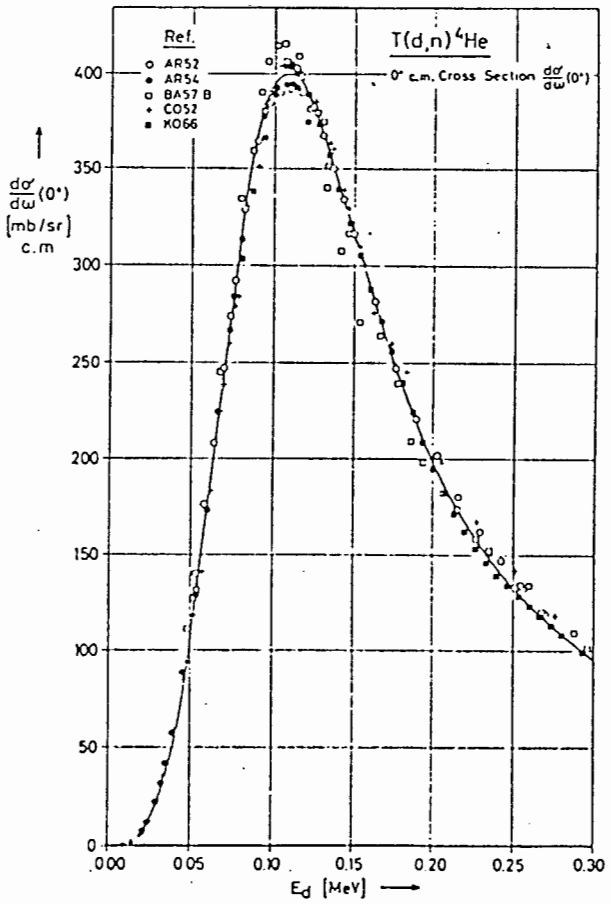

Figure 3.2: The 0° cross section of the reaction T(d,n)α as a function of incident deuteron energy. Reproduced from reference [79]

The reaction has a sharp resonance just above threshold [79], the cross section reaching a maximum for a deuteron with 108 keV striking a triton (figure 3.2). By varying the deuteron energy incident on W1, and monitoring the coincidence count rate, an energy could be found where the deuteron energy at a point opposite window A was in the resonance.

Figure 3.3 shows the count rate as a function of incident deuteron energy. As the incident deuteron increases in energy from 1.54 MeV to 1.64 MeV the point in the cell where it has been degraded in energy to 108 keV moves 1.5 cm downstream. This point is directly opposite window A when the incident deuteron energy is 1.585 MeV.

Once the resonance had been found, the deuteron energy was fixed and a 1 cm diameter organic scintillator crystal was used to scan the associated neutron beam. Figure 3.4 shows this sweep. The points are measurements while the trapezoidal solid line is a fit to find the width of the beam. Its triangular shape is due to the finite size of the crystal. As the crystal moves out of the beam, it is progressively less and less illuminated. If the beam is sharp ($\Delta\theta$ small compared with the angle subtended by the detector) and the detector is symmetrically placed, the centre of the detector should be at the edge of the beam when the intensity has dropped by half. The

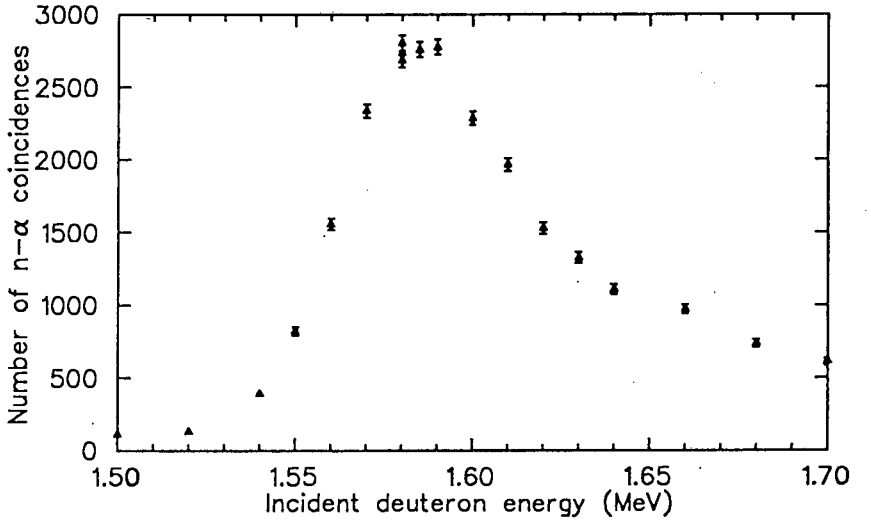

Figure 3.3: The α-n coincidence rate from the t(d,n)α reaction as a function of deuteron energy incident on W1 (fig. 3.1).

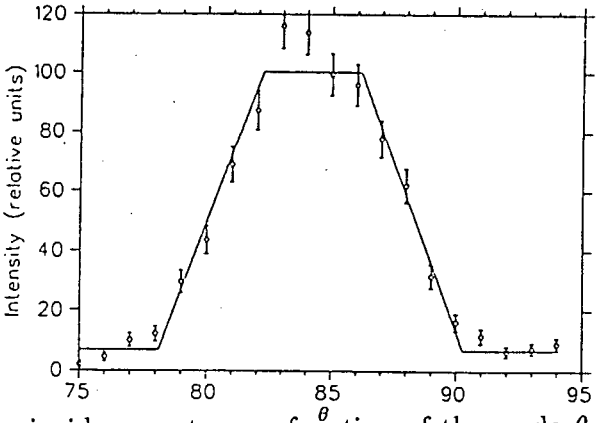

Figure 3.4: α-n coincidence rate as a function of the angle θ_n (see fig 3.1) measured using a neutron detector subtending an angle of 2°. Solid line (see text) shows calculated distribution.

linear drop-off at the edges of the measured distribution suggest this behaviour, therefore we fit the data using a truncated triangle with sides of slope corresponding to the size of the crystal. This gives us a beam cross sectional angle of 8°, which corresponds with the solid angle subtended by the alpha detector and shows that there must be little in the way of alpha scattering at the window or off the walls of the tube connecting the alpha detector to the target cell. The horizontal lines above 90° and below 79° are estimates of the non-correlated neutron-alpha coincidence background events. The signal-to-background ratio was about 15 to 1 and was further reduced by decreasing the width of the window on the time between neutron and alpha detection from the full TAC range (500ns) to 10 ns, and reducing the current of the incident beam of deuterons.

3.2 Electronics

Figure 3.5 is a diagram of the electronics used for the α–n coincidence experiments. Signals from the NE213 scintillator detector were processed by a Link Systems model 5010 pulse shape discriminator unit (LINK) which provided the following outputs: a fast timing signal T_N; logic signals n or γ to indicate the pulse shape identification of the type of event; an integrated output L proportional to the sum of fast and slow components in the scintillator; and a 'fast' output F proportional to the integral of the fast component only.
Alphas were detected using either a surface barrier detector or, as shown in fig. 3.5, using a thin film plastic scintillator (NE102, 50 μm thick). The TAC, operated by the fast timing signals from the two detectors provided the output T corresponding the time difference between n and α detection. The integrated output A from the alpha detector was obtained from the slow signal from the alpha detector via a pre-amp and linear amplifier. The T, L, F and A outputs were gated by a signal from the Coincidence unit (UCO) which required the n output from the LINK, the SCA output from the TAC, and a signal from the alpha detector. For gamma calibrations, the UCO required the γ signal from the LINK only. The T, F, L and A outputs were recorded event by event by a four parameter data acquisition system based on a PDP11 minicomputer. The singles alpha spectrum was simultaneously accumulated by the same data acquisition system and thus subject to the same dead time as the 4-parameter (T, L, F and A). The ratio of coincidences to alpha singles measured in this way

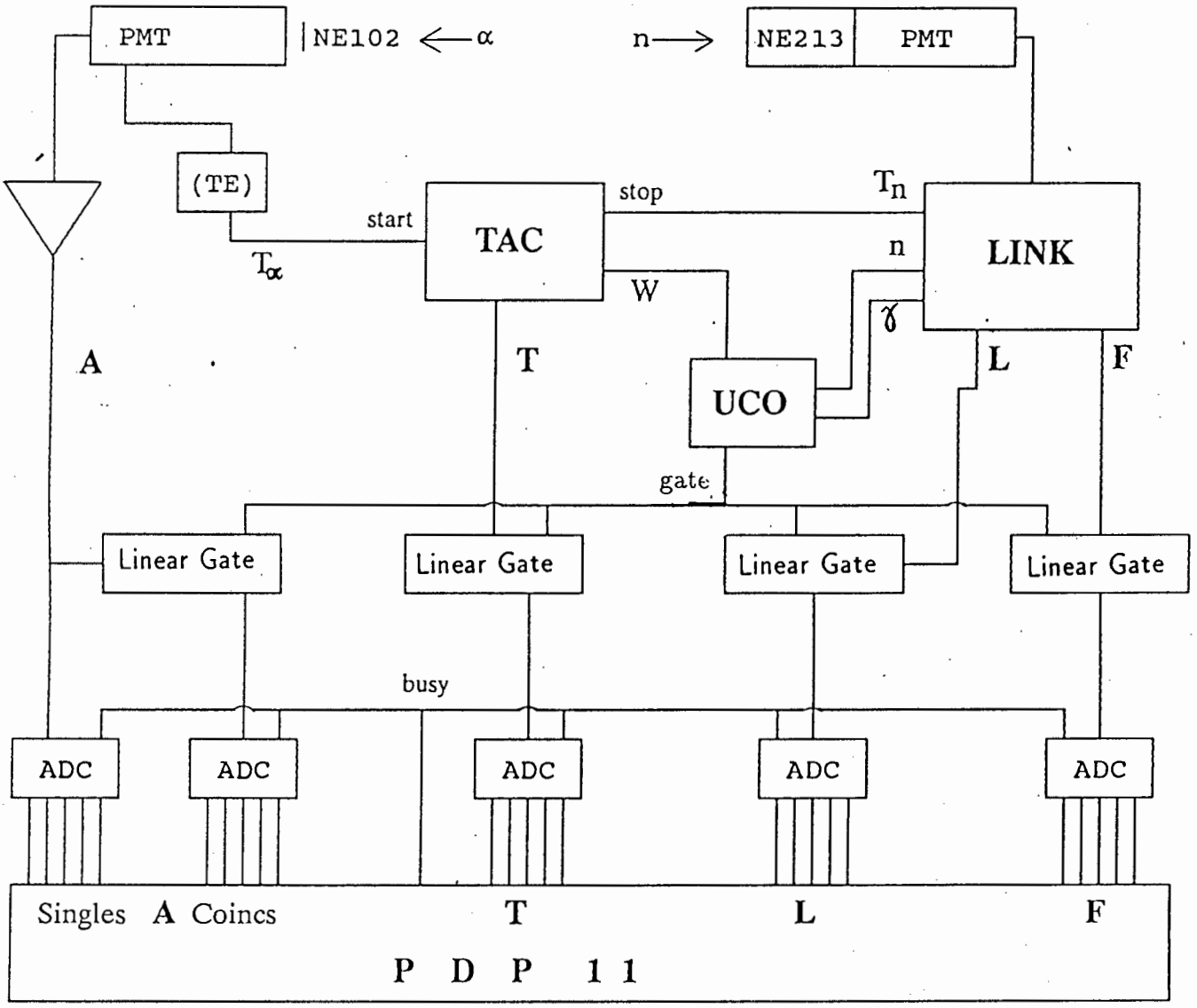

Figure 3.5: The electronics for the four-parameter coincidence experiment measuring coincidental α and neutrons from the T(d,n)α reaction. For the sake of clarity units such as preamplifiers, delays, LGS, GDGs and CFDs have been omitted. TE = timing electronics.

was therefore independent of dead time.
Off-line analysis was performed using OPDATA and PLOTDATA [80] packages on the UCT VAX.

3.3 Lineshape measurements

Pulse height spectra (lineshapes) were measured for two different detector geometries, firstly for cylindrical geometry using the standard 5 cm diameter by 5cm length Nuclear Enterprises BA1 cell used for neutron measurements, and secondly for one of the detectors (K2) actually used in the RAL experiment [20]. The K2 detector consists of a 13 by 13 by 7 cm rectangular cell of NE213 viewed by four photomultiplier tubes, two each at opposite 13 by 7 cm faces.
The measurements for the smaller detector provided data for an additional (and therefore more critical) check of the MC code MUGLU used to simulate the MCF experiments.

3.3.1 BA1 detector

The BA1 detector is a cylinder of NE213 viewed by a single phototube. As the phototube is prone to saturate when the photomultiplier voltage is set too high, it was tested at two voltages with an AmBe neutron-gamma source ($E\gamma$=4.436 MeV) to ensure linearity. The pulse height channel to equivalent electron energy (in MeVee[1]) calibration and calculation for the true zero of the pulse height scale was then done using the AmBe source and a ^{24}Na ($E\gamma$=2.75 MeV) and measuring the positions of the double-escape peaks (D) and compton edges (C). This calibration is shown in figure 3.6
Fig 3.7 shows the lineshape (points) for the BA1 detector for 14.1 MeV neutrons. The flat distribution due to H(n,n)H scattering is obvious. The hump at about 7 MeVee attributed to multiple scattering is also visible, as is the effect of nonlinear scintillator response, with the increase in counts at low pulse heights. The peak at about 1 MeVee which can be identified as arising from the C(n,α)Be reaction is clearly resolved. Part of the contribution by the C(n,n')3α breakup reaction can be seen in the large increase in counts per channel just above detector threshold.

[1]The MeVee scale indicates the energy of an electron impinging on the scintillator required to produce a pulse of light of a given size.

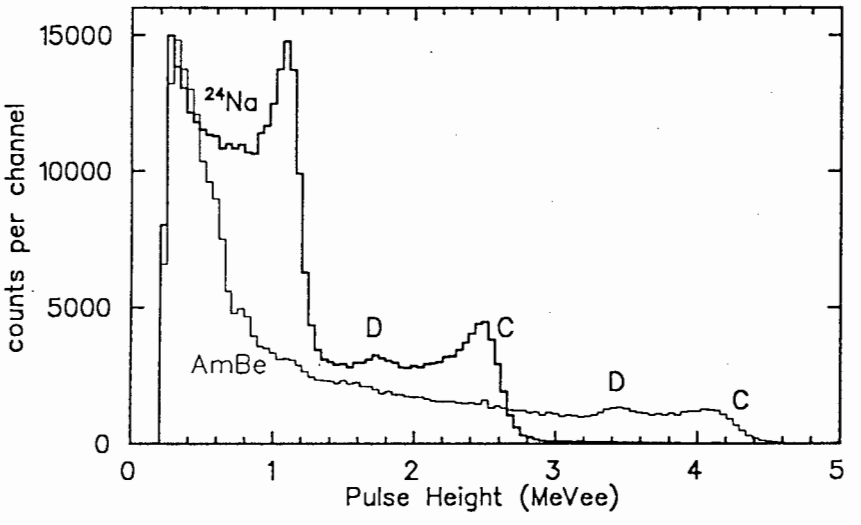

Figure 3.6: Gamma spectra calibrations of the BA1 detector. Feint curve: AmBe, bold curve: ^{24}Na. The double escape peaks are marked 'D' while the compton edges are marked 'C'

The calculated lineshape (smooth curve) was fitted to the data adjusting the vertical scaling and convolution with a gaussian of the MC lineshape as outlined at the end of chapter 2. The fit appears satisfactory for the n-p scattering portion of the lineshape.
The detector lineshape at lower pulse height was investigated in greater detail by running the photomultiplier at a higher voltage (hence gain). The pulse height to MeVee calibration was repeated using ^{60}Co and ^{24}Na γ sources. Fig 3.8 shows the measured lineshape (points) and the calculated lineshape (smooth curve). The MC lineshape was normalised to the measured spectrum at the 1 MeVee alpha peak, and convoluted with a gaussian varying with the square root of the pulse height. This has the same width for the same pulse height in MeVee as the gaussian used to convolute the calculated spectrum in figure 3.7.
The poor fit could be due to the inaccuracy of the alpha energy to pulse height relation or inaccurate input data used to model the alpha breakup energy spectrum, or a bug in the neutron detector code, which hitherto has evaded detection. It is difficult to interpret the lineshape, as the reactions involve pulses produced by detection of two or more charged particles, and

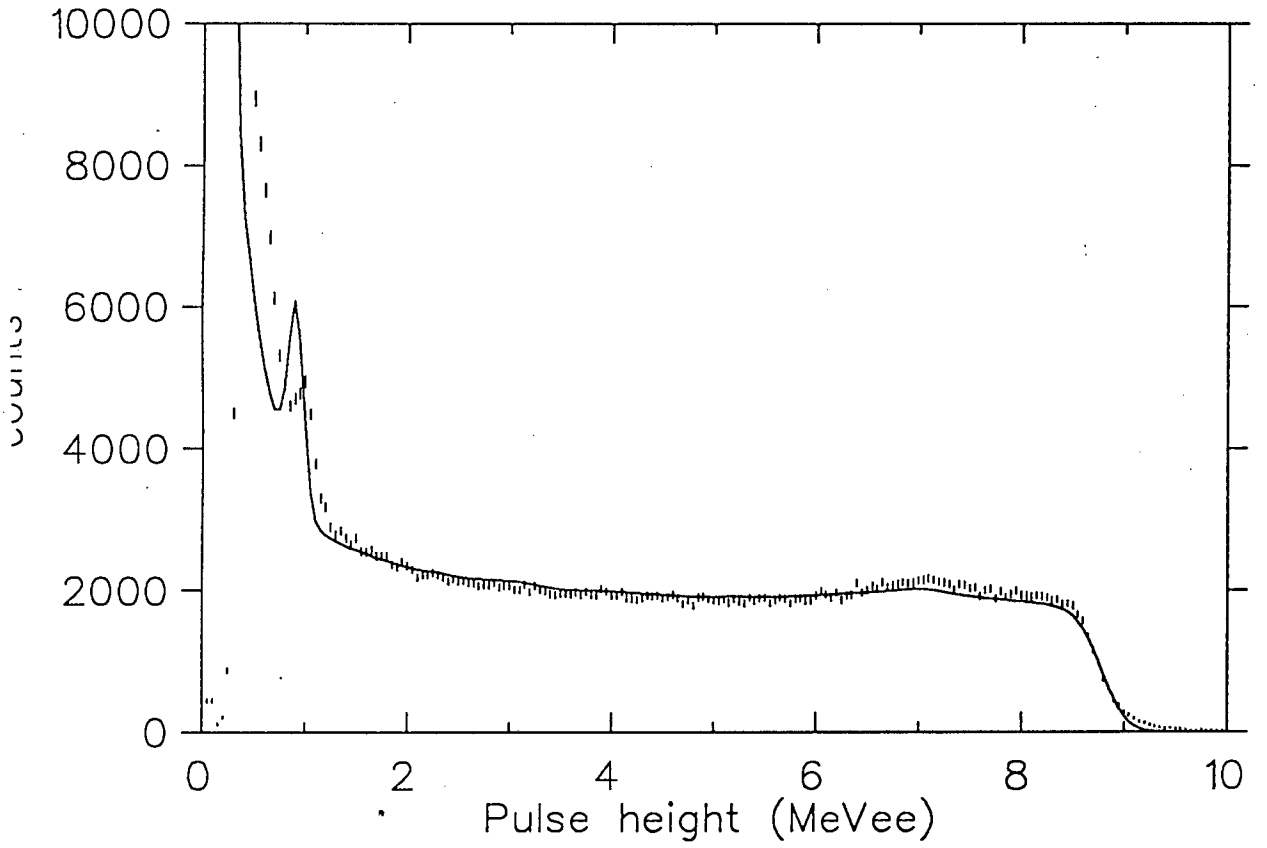

Figure 3.7: The line shape for the BA1 5 × 5 cm cylindrical detector for 14.1 MeV neutrons. Points: data from T(d,n)α reaction, smooth curve: lineshape from MUGLU fitted to the data.

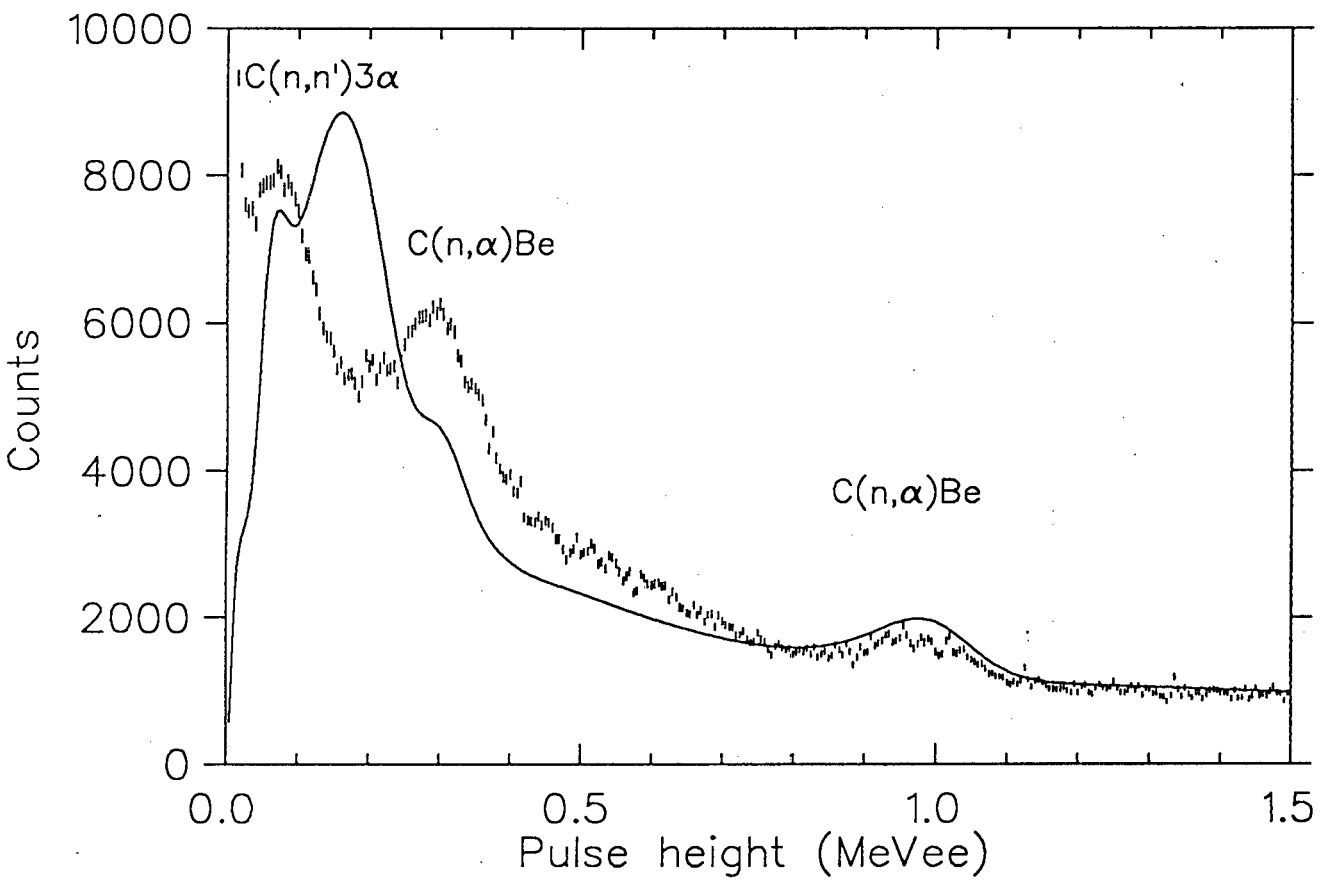

Figure 3.8: Lower energy region of the lineshape for the BA1 detector for 14.1 MeV neutrons measured at a higher photomultiplier voltage, showing the contribution to the proton recoil spectrum from the α producing reactions.

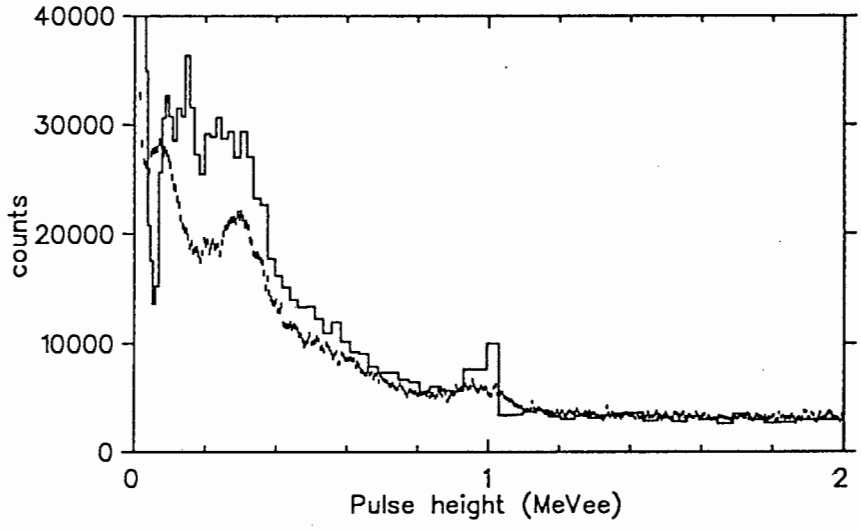

Figure 3.9: A comparison between the low pulse height regions of the lineshape from SCINFUL (histogram) and the measured lineshape (points).

the energy-to-pulse height relation for Be ions has not been measured. Figure 3.9 shows the output from SCINFUL [60]— a Monte Carlo based simulation of neutron detectors — compared with the measured spectrum. The experimental data are normalised to the same pulse height calibration and to the same number of counts per channel for the H(n,n)H part of the spectrum. As can be seen, the fit to the alpha part of the pulse height spectrum is not entirely successful. Both the MC codes, SCINFUL and MUGLU, seem to place the two peaks from the C(n,α)Be reaction in the correct place, though SCINFUL overshoots while MUGLU undershoots. Both codes place the peak lowest in pulse height in the same position shifted up a little from the peak in the measured spectrum. This suggests that the measured spectrum might be incorrectly calibrated.
An isometric plot of counts versus pulse shape and pulse height for the low pulse height region is shown in fig 3.10. Several features are noteworthy. The PSD and pulse height resolution diminish at low energies. However, it is clear that the alpha loci are moving off the proton locus to higher S, although the separation is only really noticeable for alpha particles with energy greater than 5.8 MeV (pulse height 0.5 MeVee) [81].

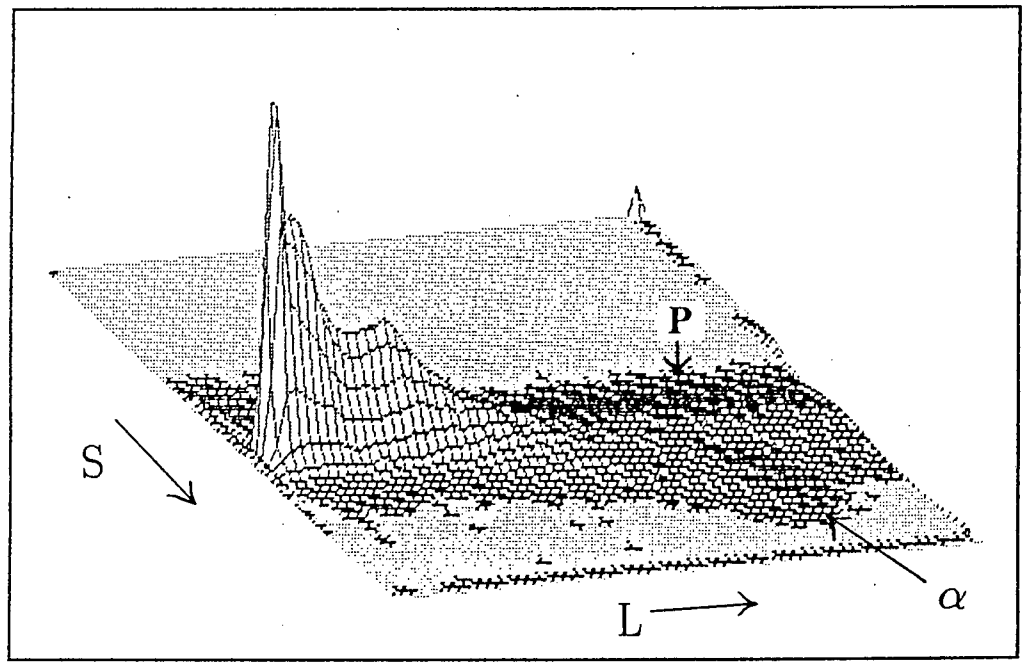

Figure 3.10: Isometric plot of the low pulse-height region of the BA1 detector. Note the alpha loci (marked 'α') moving off the proton locus (marked 'p').

Figure 3.11 shows the contributions from the two alpha producing reactions. The C(n,n')3α curve is enhanced by multiple scattering: the dashed curve arises from the inelastically scattered neutron subsequently scattering with a proton.
Comparison with measured [82,83,67] and calculated [84,82,85] line shapes for similar detectors is favourable.

3.3.2 The K detector

Calibrations similar to those for the BA1 detector were performed (fig. 3.12)
The measured lineshape for 14.1 MeV neutrons appears in figure 3.13. Again, the flat distribution from H(n,n)H scattering dominates. The hump at 7 MeVee from multiple scattering has become larger and broader, as about 30% of the scattered neutrons make subsequent scatters with protons in the detector. Note how the peak from the Be reaction has become a shoulder, and the 14.1 MeV proton edge has become broader. The larger volume has several effects on the lineshape: multiple scattering

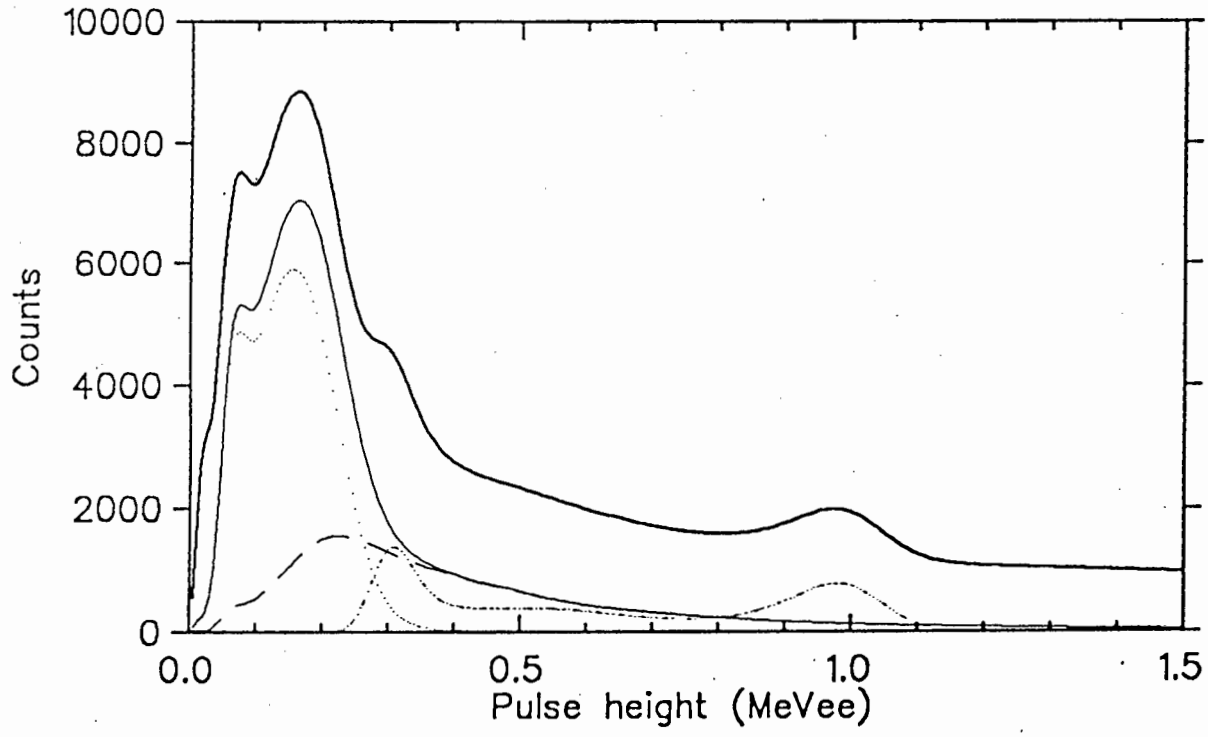

Figure 3.11: The contributions from the two alpha producing reactions to the line shape. Dot-dash curve: C(n,α)Be, Faint curve: C(n,n')3α with two components: dotted curve: Pure α, and dashed curve: C(n,n')3α followed by H(n',n')H. Bold curve: total.

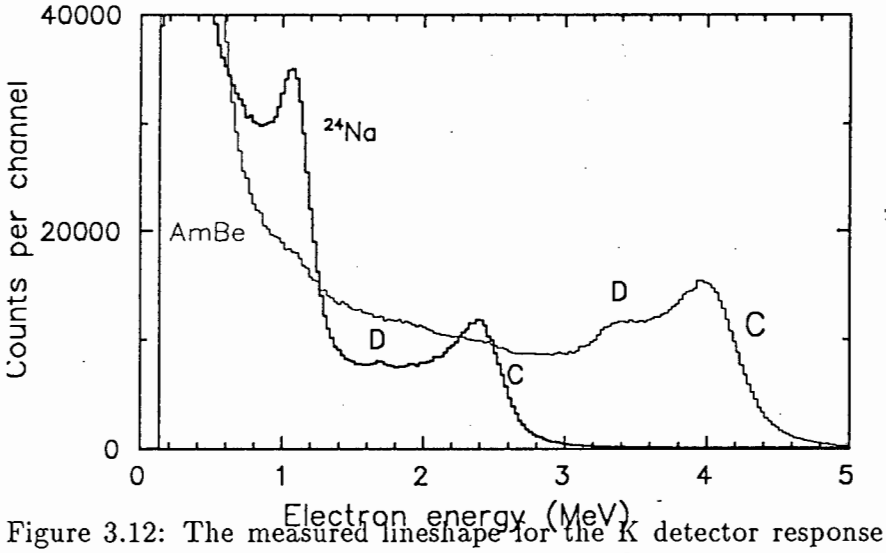

Figure 3.12: The measured lineshape for the K detector response to 4.44 MeV gammas (AmBe) and 2.7 MeV gammas ^{24}Na. Note the decrease in intensity of the double escape peaks (marked 'D') compared with fig 3.6

is greatly enhanced, as expected, and the second order moderating contributions play a larger role. Proton leakage is reduced, though as this is small, it is not very noticeable. The tail above 14 MeV which the MC calculation does not fit could be due to pileup effects that the link is not rejecting, or the non-uniformity of the light propagation in the detector, which was not corrected for in the MC simulations.

Figure 3.14 is a log-log plot of the calculated curve and the different contributions. The spectrum from np elastic scattering (1) shows a flattish distribution peaking at the double scattering hump. The alphas from C(n,α)Be are shown in curve (2) and those from C(n,n')3α in curve (3). The carbon elastic and inelastic contributions are shown in curves (4) and (5) respectively.

Figures 3.15 and 3.16 are two dimensional isometric plots of intensity as a function of pulse height L and pulse shape S for the BA1 and K2 detectors respectively. The bulge to higher S (shaded) due to np multiple scatters is clearly visible, and the separate locus for the alphas from carbon breakup into beryllium. As the size of the detector increases, more neutrons will scatter more than once, enhancing the bulge due to multiple scatters. This enhancement of the bulge for the K detector over the BA1 detector is seen

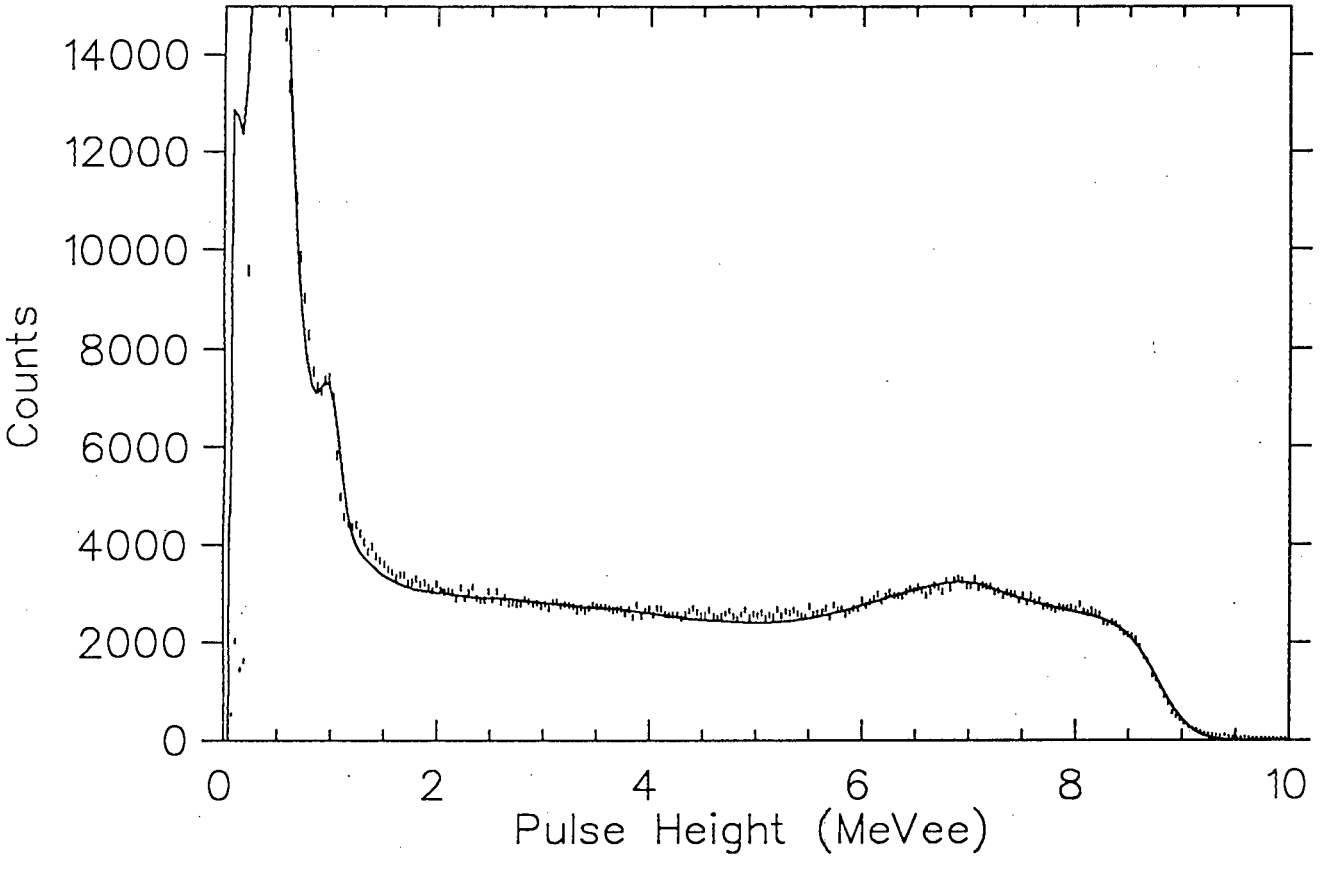

Figure 3.13: The measured and calculated lineshapes for the K detector response to 14.1 MeV neutrons. The smooth curve is the calculation from MUGLU fitted to the data (points).

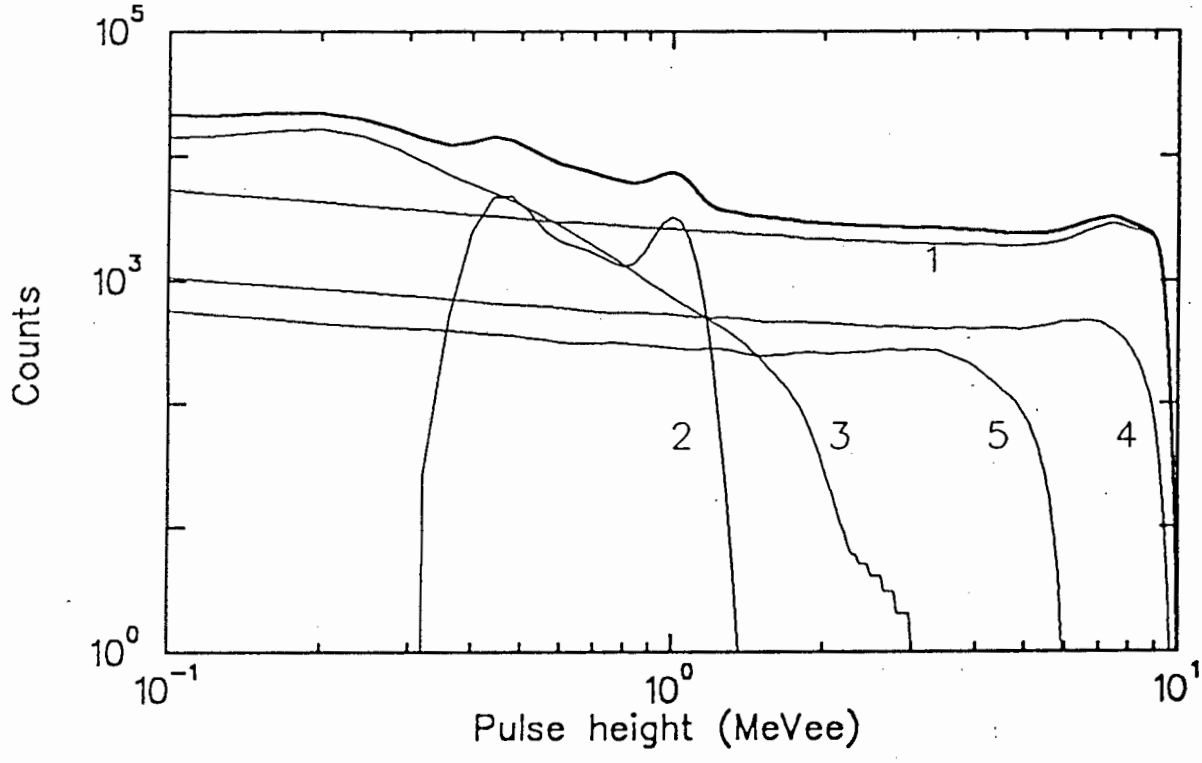

Figure 3.14: A log-log plot of the Monte Carlo lineshape (bold curve) for the K detector for 14.1 MeV neutrons. See section 3.3.2 for explanation of other curves.

clearly in figures 3.15 and 3.16.
The gamma calibration spectra show similar changes due to size effects as the neutron spectra. Note (fig 3.12) how the double escape peaks are reduced for the K detector relative to the BA1 detector as the photons from electron-positron annihilation after pair-production have greater chance of being detected.

3.3.3 Shielding effects

Both MUGLU and the T(d,n)α reaction enable simulations appropriate to detailed geometry of MCF experiments. For example the RAL experiment has two K detectors, one behind the other. The simulations can be used to estimate the effect they have on one another. In the actual RAL experiment, a pattern register indicates which of the neutron detectors have registered a neutron and coincidences between neutron detectors may be vetoed in analysis. These detailed conditions may be included in the simulations.
Figure 3.17 shows the lineshape from the K detector when it was shielded by another K detector as for detector 2 in the RAL experiment (fig 1.9). The calculated lineshape fits very well. Note how the lower pulse height regions are enhanced at the expense of the higher—the first detector moderates some of the neutrons before they impinge on the second detector. Figure 3.18 shows a comparison between lineshapes for shielded and unshielded (bold curve) detectors. The two curves were normalised at the multiple scattering hump (7.5 MeVee pulse height). Incorrect pulse height calibration has placed the np scattering edge at 9.3 MeVee instead of 8.7 MeVee.

3.3.4 Efficiencies

The efficiencies of the neutron detectors were measured and compared with the Monte Carlo calculations for several different values of detection threshold energy. The efficiencies were measured by taking the ratio of alpha-neutron coincidences to alpha singles on the assumption that all alphas detected would have a corresponding neutron passing through the neutron detector. The alpha singles were extracted from the background by fitting the coincidence spectra to the higher energy side of the singles alpha peak where the background was expected to be minimal. This is shown in figures 3.19 (BA1 detector) and 3.20 (K detector).

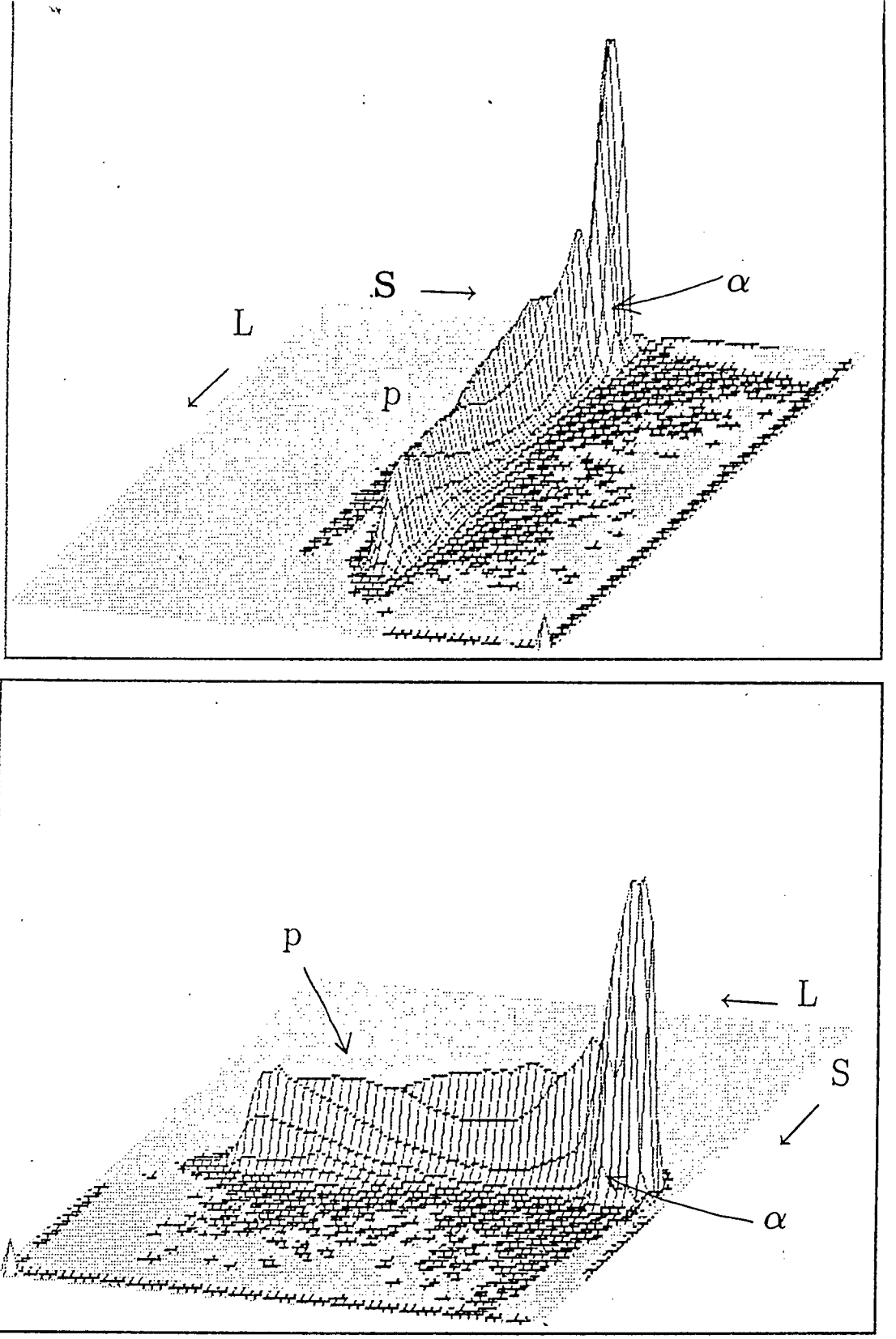

Figure 3.15: Isometric plots of L vs S for the BA1 detector response to 14 MeV neutrons. The alpha locus is marked 'α' and the multiple scattering bulge is highlighted. The proton locus is marked 'p'.

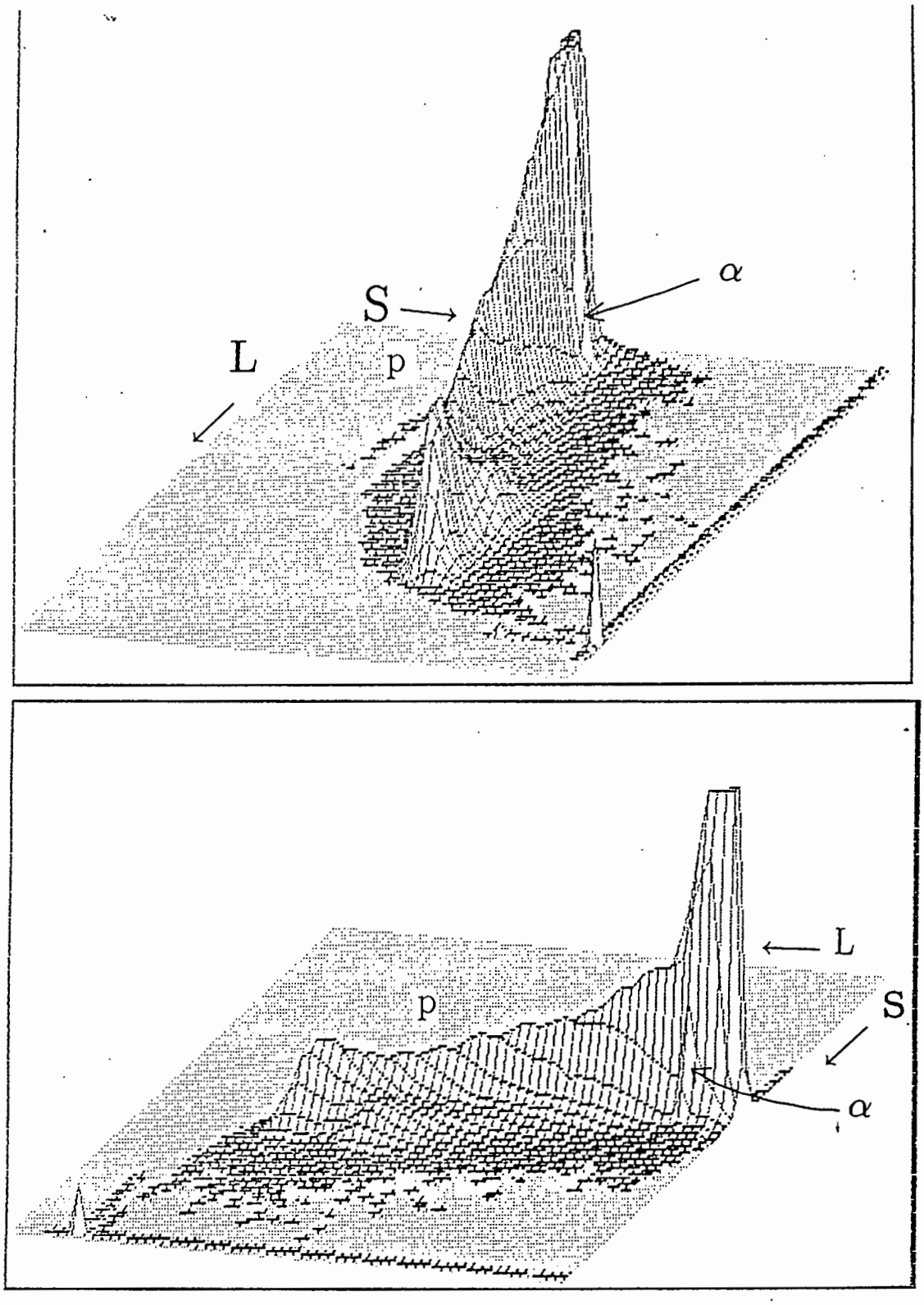

Figure 3.16: Isometric plots of L vs S for the K5 detector response to 14 MeV neutrons. Features marked as in previous diagram.

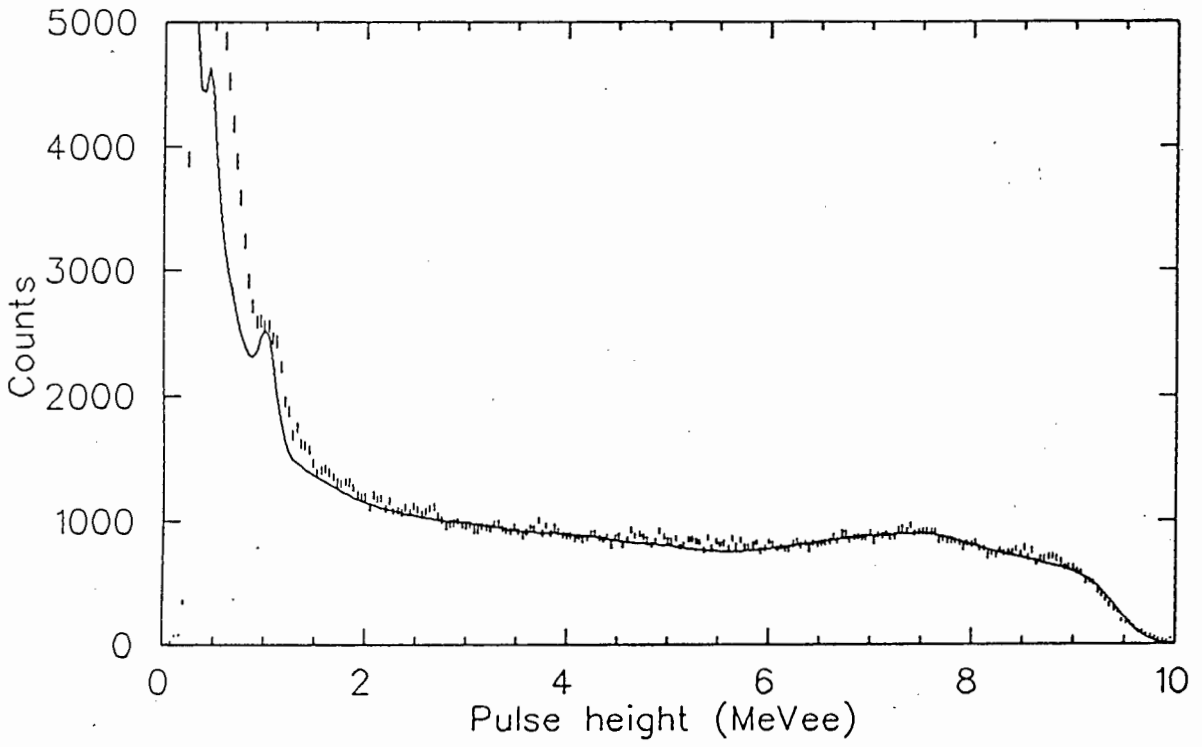

Figure 3.17: Lineshape for one K detector shielded by another K detector. The smooth curve is the fitted Monte Carlo lineshape. The pulse height calibration is incorrect and should be reduced by a factor of 1.07

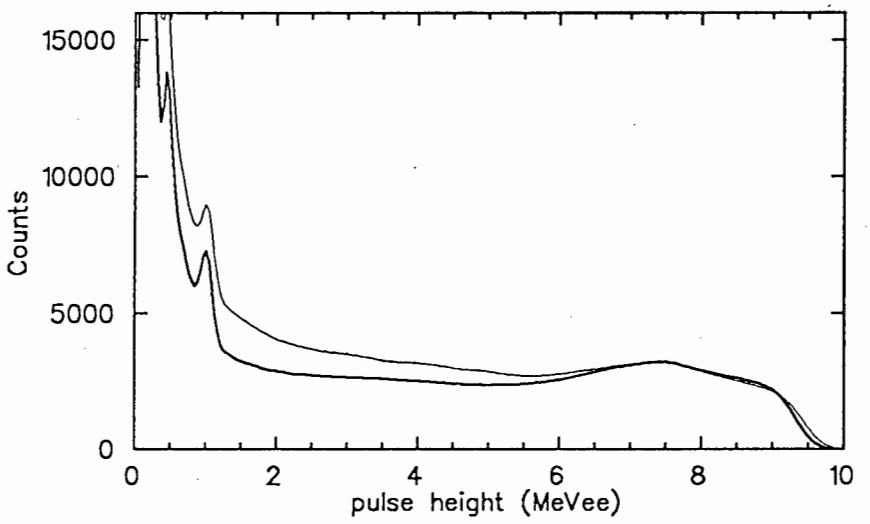

Figure 3.18: Comparison of Monte Carlo lineshapes for an unshielded (bold curve) and shielded detector

Once the number of alpha singles, and hence the number of neutrons impinging on the neutron detector, were known, the efficiency could be measured for various thresholds simply by integrating the neutron detector lineshape above a certain pulse height and dividing that number by the number of alpha singles.

Table 3.1 shows the measured and calculated efficiencies for the BA1 detector for various thresholds. The values taken from Verbinski et al. were measured for a 4.65 cm diameter by 4.6 cm BA213 cell with neutrons incident radially. The efficiencies were scaled to the ones measured in this work by correcting for the different path travelled through the detectors. For the BA1 detector used here, the path was 5 cm. For Verbinski, the average path was $4.65\pi/4$. This correction is good for a first approximation of detector efficiency. The agreement between MUGLU and the measured values is within the 10% estimated systematic error. The values from Verbinsky are also in agreement with MUGLU. Remeasurement of the efficiencies with the T(d,n)α associated particle system using a SBD in place of the plastic and calibrating the alpha detector using alpha sources are planned.

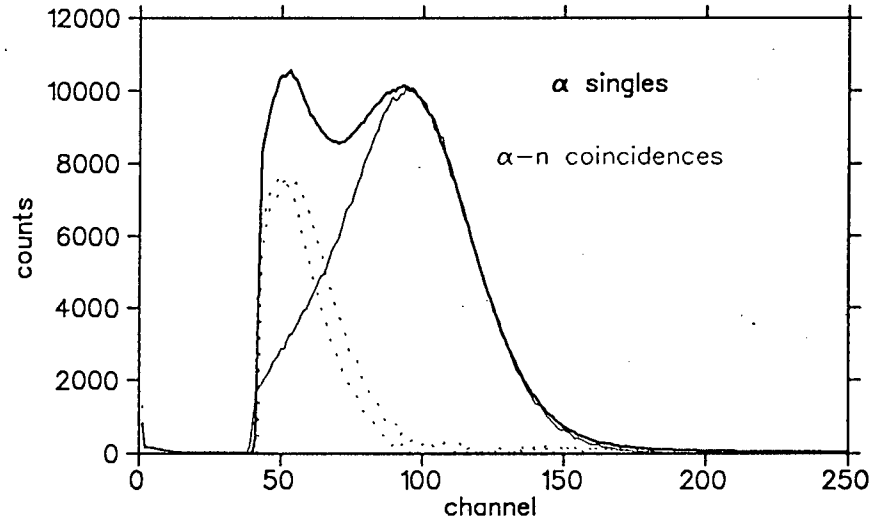

Figure 3.19: The alpha singles spectrum for the BA1 detector with the coincidence spectrum fitted. The dotted curve is the background after subtraction of the coincidences from the singles.

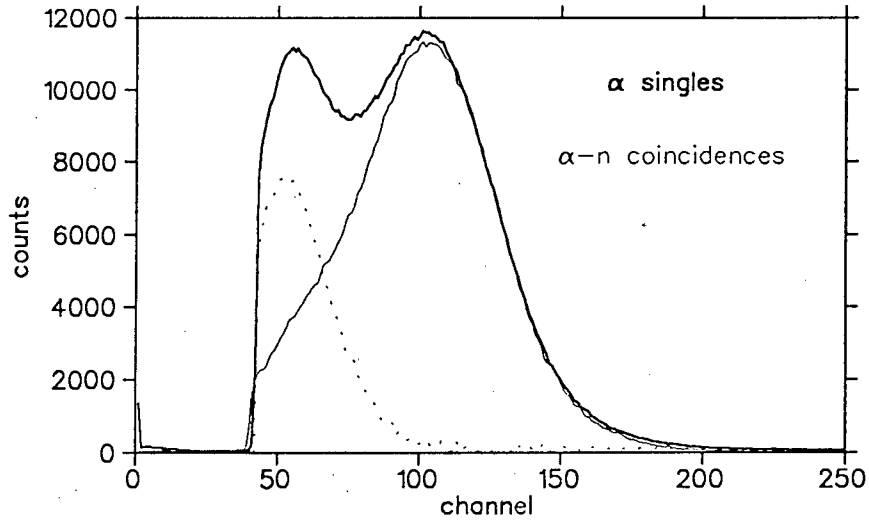

Figure 3.20: The alpha coincidence spectrum fitted to the alpha singles spectrum for the K detector. The dotted curve is the background.

Table 3.1: Table of efficiencies (in percent) for the BA1 detector measured (error of the order of 10%) and calculated at various thresholds for 14.1 MeV neutrons (this work). The values from Verbinski et al. have been scaled to the same detector dimensions. See text.

Threshold		This work		Verbinski et al. [86]	
MeVee	E_p (MeV)	Measured	Calculated	Uncorrected	Corrected
0.365	1.3	13.9	14.7	11.8	16.1
0.60	1.9	13.2	13.6	10.7	14.6
1.00	2.8	10.7	12.4	9.2	12.6
1.28	3.4	9.9	11.4	8.8	11.9

Note: Pantaleo et al. [84] obtain an efficiency of 11 % for a BA1 cell of NE213 for 14 MeV neutrons, with a detector threshold of 1.2 MeVee.

Table 3.2: Table of measured and calculated efficiencies for NE213 K detector response to 14 MeV neutrons incident on the 14 cm by 14 cm face. Measured values have an estimated systematic error of 10%

Threshold		K detector	
MeVee	E_p(MeV)	Measured	Calculated
0.365	1.3	20.3	22.6
0.60	1.9	17.5	20.4
1.00	2.8	15.6	18.1
1.28	3.4	14.2	17.0

Table 3.2 shows corresponding efficiencies for the K detector. The efficiencies measured in this work have little statistical error. The estimated systematic error of 10% or more arises from uncertainties in the fitting of alpha coincidence spectra to the measured alpha singles spectra. The agreement between measured and calculated efficiencies is not as good for the K detector as for the BA1 detector, the calculated values being 20% higher in some cases. Meaningful comparison cannot be made until more accurate measurements of the efficiencies have been done.
References containing information about efficiencies of organic scintillators to neutrons of energies in the tens of MeV range include [87,88,89,90]

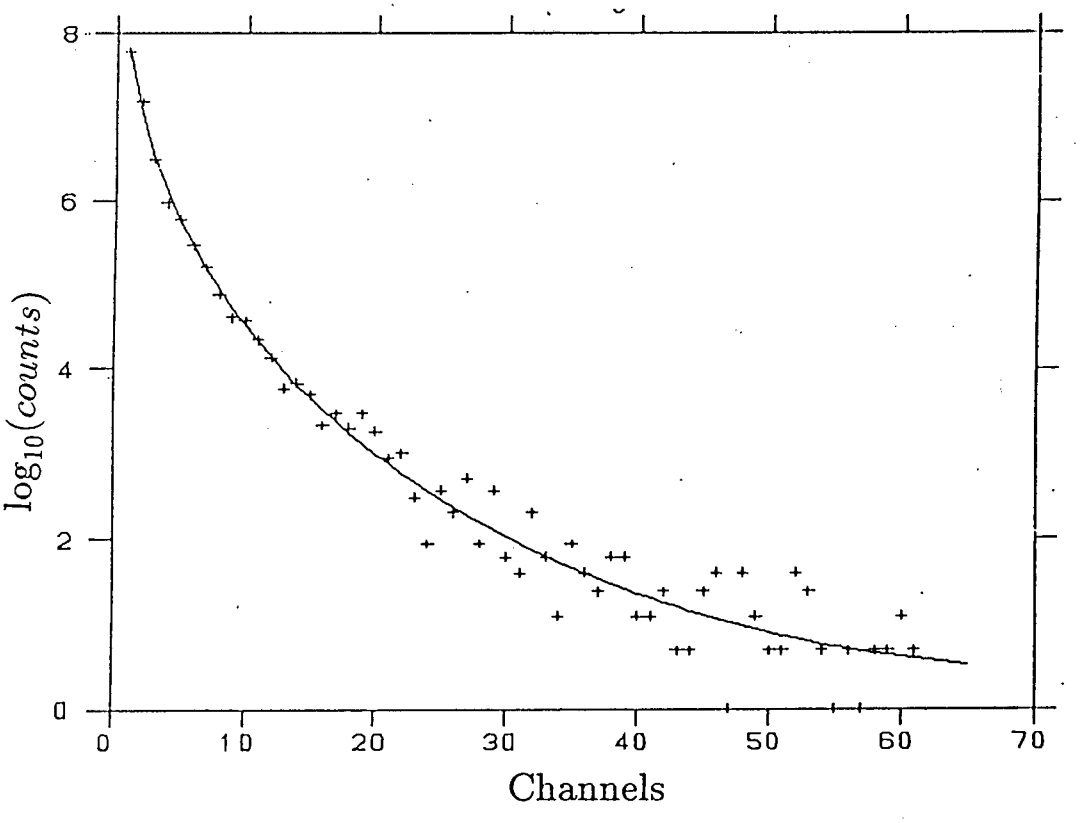

Figure 3.21: Neutron singles background measurement for muons incident on H_2 from the RAL June 1988 experiment.

3.4 RAL June 1988 neutron singles data

Fits of the Monte Carlo lineshapes and a background curve were made to neutron singles data from the RAL June 1988 sticking experiment [20] for the two collinear neutron detectors. The data were taken for the three different pressures: 1510, 710 and 490 torr. Lineshape fits for both detectors were made at 1510 torr, and fits to detector 1 were made for 710 and 490 torr.

The background was measured using hydrogen instead of deuterium and tritium in the target cell. A fit was made to the background. This curve was used in the neutron detector lineshape fits. The detector pulse height resolution was first set using the data at 1510 torr and kept constant for the other pressures, while the amplitude of the line shape and background was varied.

Figure 3.21 shows the background data measured for H_2 in the target cell. The solid line is a two exponential fit. Figures 3.22, and 3.23 show fits of the lineshape (solid line) and the background (crosses) to the data from the two detectors at 1510 torr. Note the slightly different shape of the data for detector 2, due to neutrons being moderated by detector 1.

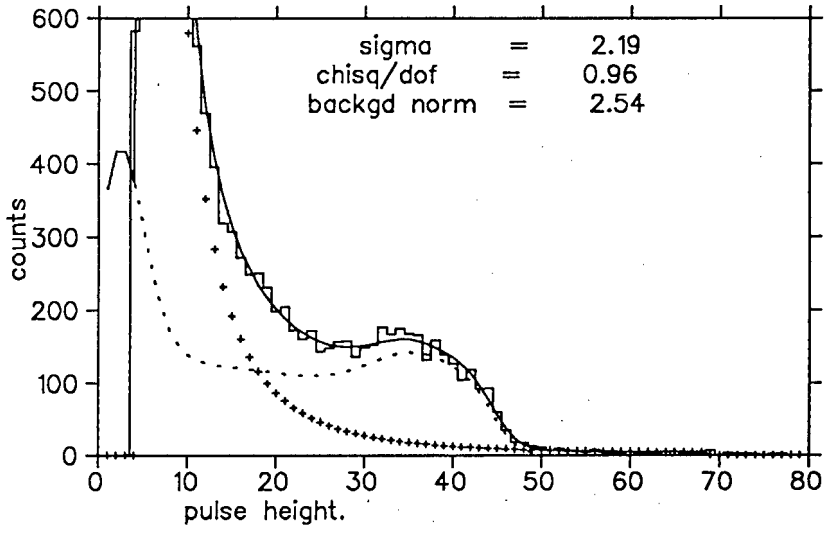

Figure 3.22: Fit of Monte Carlo lineshape (dotted line) and background (crosses) [sum: smooth curve] to RAL June 1988 neutron singles data for detector 1 (histogram) for gas pressure 1510 torr

Figures 3.24 and 3.25 are fits to lower pressures, with very much poorer statistics, in the last case the signal barely distinguishable above the background. These preliminary results seem to show that the neutron singles spectra are reducible in this way.

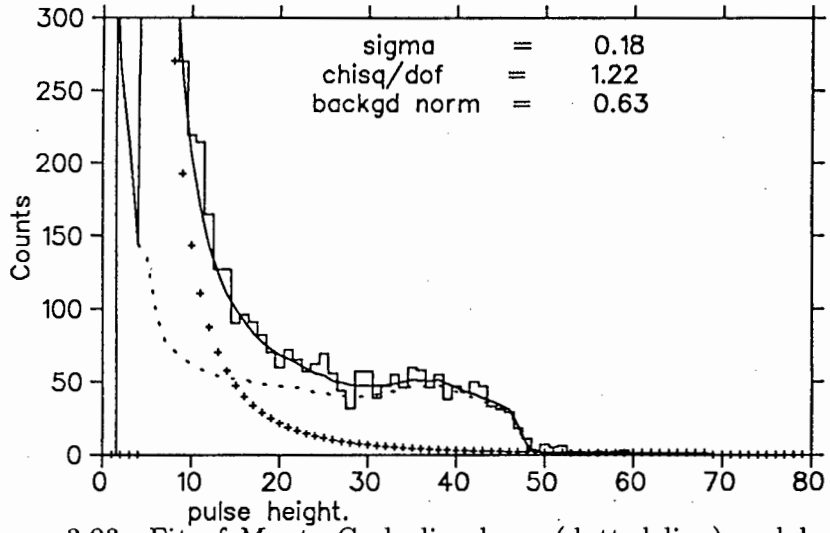

Figure 3.23: Fit of Monte Carlo lineshape (dotted line) and background (crosses) [sum: smooth curve] to neutron singles data for detector 2 (histogram) for gas pressure 1510 torr. Note the better pulse height resolution and different lineshape for the shielded detector.

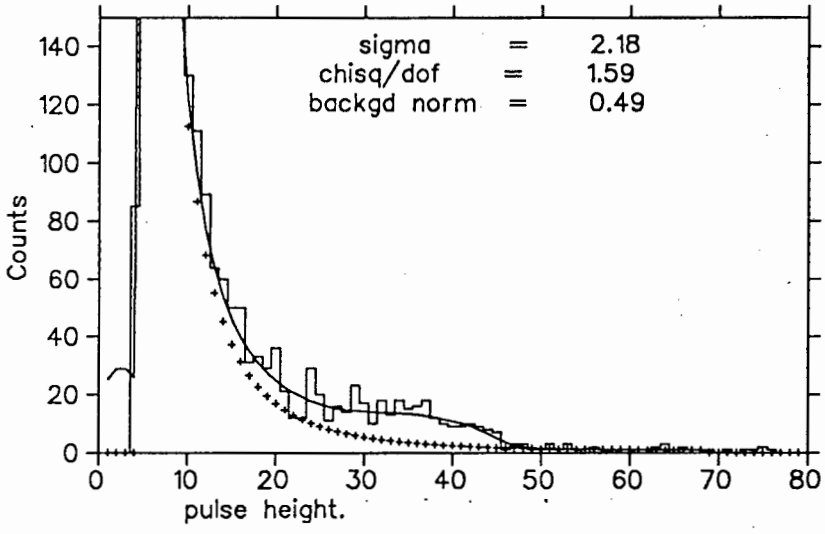

Figure 3.24: Fit of Monte Carlo lineshape and background to neutron detector 1 for gas pressure 710 torr

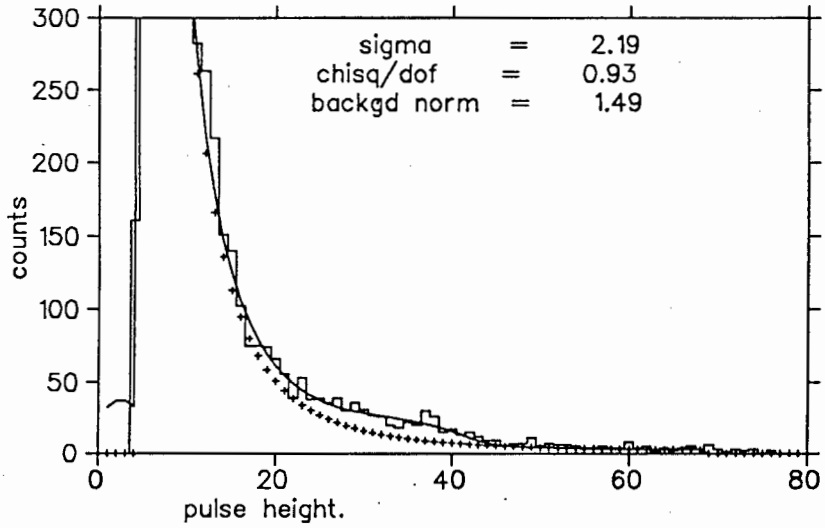

Figure 3.25: Fit of Monte Carlo lineshape and background to neutron detector 1 for gas pressure 490 torr

Chapter 4

Coincidence simulations from MUGLU

The main body of the results from MUGLU is presented here. This includes

1. E–T distributions for various experimental geometries, gas pressures and fusion distributions. These plots define the signature of sticking.
2. B factors (see section 1.3.2)
3. $\Phi(E_{thr})$ factors (fraction of $\alpha\mu$ striking the alpha detector above threshold E_{thr}) and
4. the fraction of fusions which lead to detectable α-n coincidences and neutron singles.

The B and Φ factors are necessary for determining ω_s^0 from the raw experimental data, while the number of coincidences per fusion, along with the simulated E–T distribution, is a useful measure of the performance of various proposed geometries and detection systems. The outputs from MUGLU are compared with results from the LAMPF and RAL experiments. Three experimental geometries, A, B and C as defined in chapter 2, are considered.

4.1 E–T plots

In direct measurements of ω_s^0 such as the LRG experiments, where the ratio of $\alpha\mu$ to α is measured, the energy of the alpha E and the time difference

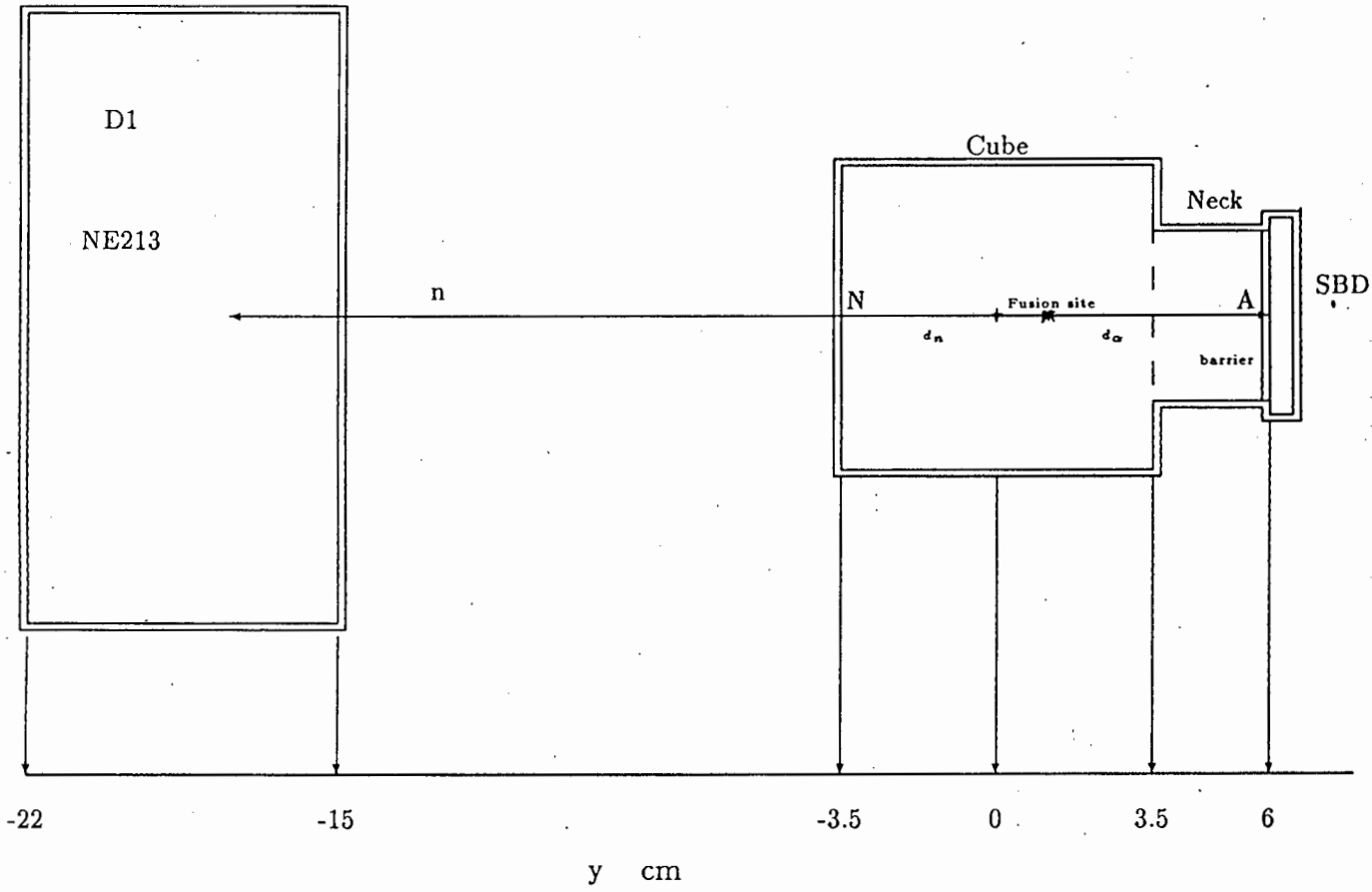

Figure 4.1: 1-D case: The E–T plots are built up in the section 4.1.1 using this geometry. Fusions are initially confined to line AN and the products constrained to travel along it. Position 0 along line AN signifies the centre of the muon beam, which is normal to the plane of the page.

between the alpha and neutron detection times T are plotted against each other in a scatter plot, using the correlation between E and T to facilitate both the separation of the α from the $\alpha\mu$ and the removal of background.

This correlation is a result of the path length d_α (see figure 4.1) of the alpha in the medium between fusion and detection: obviously, the longer the alpha has to travel, the more time it takes, and the more energy it loses to the surrounding medium.

T depends not only on the distance the alpha travels, but also (to a lesser extent) on the distance d_n the neutron travels between fusion and detection. This distance d_n depends on the position of fusion and on the position in the neutron detector at which the neutron produces its first energetic charged particle. E depends entirely on the amount of matter the alpha must travel through. This in turn depends on the pressure of the gas, the geometry of the apparatus — both of which should remain constant during the course of an experimental run — and the position of the fusion in the target chamber.

Thus plotting E versus T should ideally yield two separate loci, one for α and the other for $\alpha\mu$, as the α lose more energy over a certain distance than do the $\alpha\mu$.

4.1.1 Structure of the E–T plots

The structure of the E–T plots may be illustrated by considering a simple one-dimensional example in a target arrangement (figure 4.1) similar to that of geometry B, defined in section 2.2.

Equal numbers of fusions (with ω_s^0=50%) were considered occurring at each of 39 points along line AN (see figure 4.1). The points were 2.5 mm apart. The target box can be divided into two portions, the *cube* region and the *neck region*. The box was filled with D_2T_2 gas at 1500 Torr. The alphas forced arbitrarily to move along line AN were detected by a SBD which was covered with a 1.5 μm Havar barrier. The associated neutrons were detected at random depths over an exponential distribution dictated by the effective neutron cross section in the neutron detector.

Figure 4.2 is a plot of fusion position y along line AN in figure 4.1) versus T. The vertical bars are from the uncertainty in the position in the neutron detector at which the neutron interacts: each bar is about 0.7 ns long which represents the neutron travel time across the neutron detector. This uncertainty is purely a geometrical effect and can be reduced by making the neutron detectors thinner.

It is interesting to note that the time of flight is largely independent of

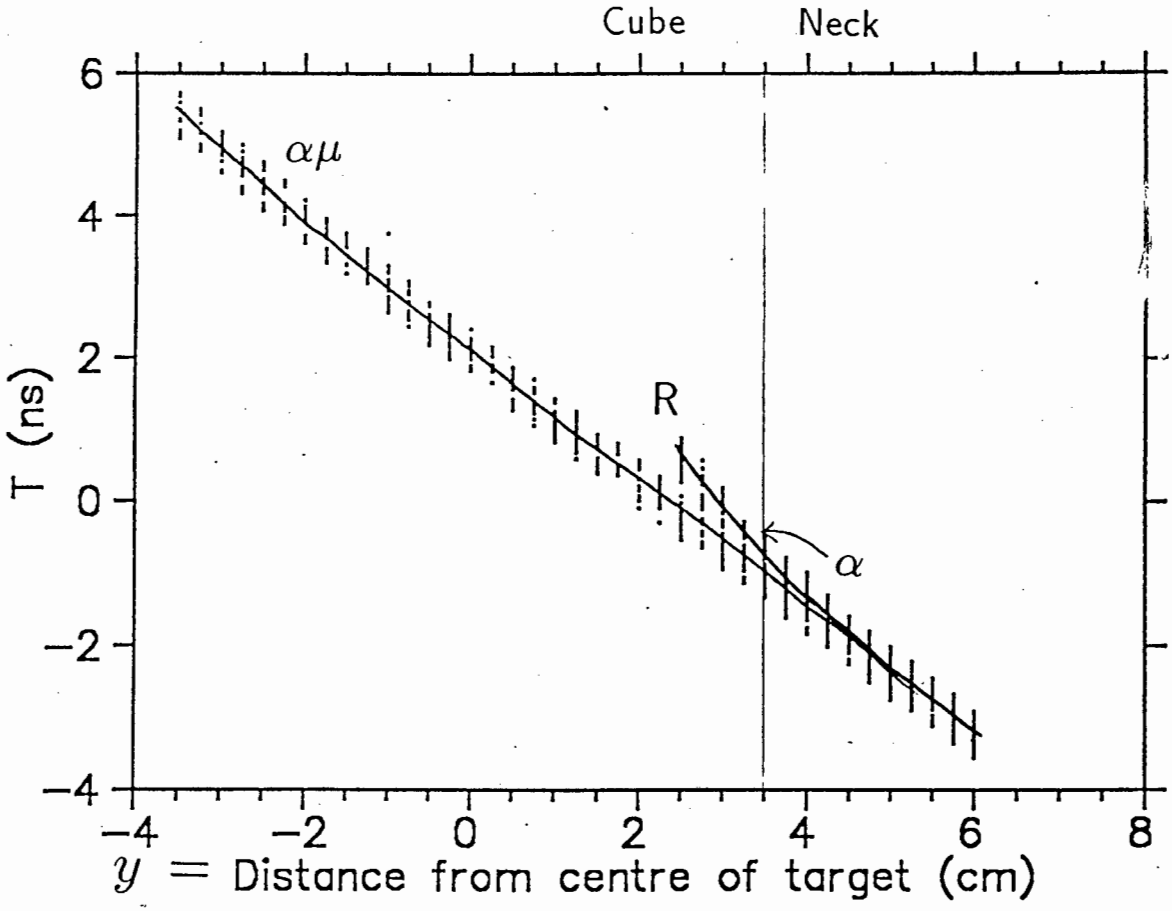

Figure 4.2: Position y of fusion in target box versus time difference T between alpha and neutron arrivals.

whether the particle is an α or an $\alpha\mu$. The time curve for the α seems to diverge from that of the $\alpha\mu$ only just before the α is ranged out (marked R on figure 4.2). Also shown on the figure is the demarcation between the cube and neck regions at $y = 3.5$ cm. $T < -0.5$ ns for fusions occurring in the neck.

Figure 4.3 shows the energy E of the detected alpha plotted versus fusion position y. The α not ranged out all land on line A in this plot. The $\alpha\mu$ which impinge unstripped on the detector fall onto line B; The continuum between lines B and C comprises $\alpha\mu$which are stripped in the 1.6μm layer of Havar on the front of the detector. If the muon is stripped at the front surface of the Havar film, the alpha travels through the foil as a doubly charged particle. It therefore loses more energy than if the muon was stripped, say, in the middle of the foil. The $\alpha\mu$ which are stripped in the gas fall between lines C and A.

Figure 4.4 shows the E–T plot resulting from a combination of Figures 4.3 and 4.2 for the same set of events, with time on the horizontal axis and energy on the vertical axis. The loci in figure 4.3 labelled A, B and C are indicated similarly in figure 4.4, and the time spread is again that associated with the position of neutron detection, as described earlier. There

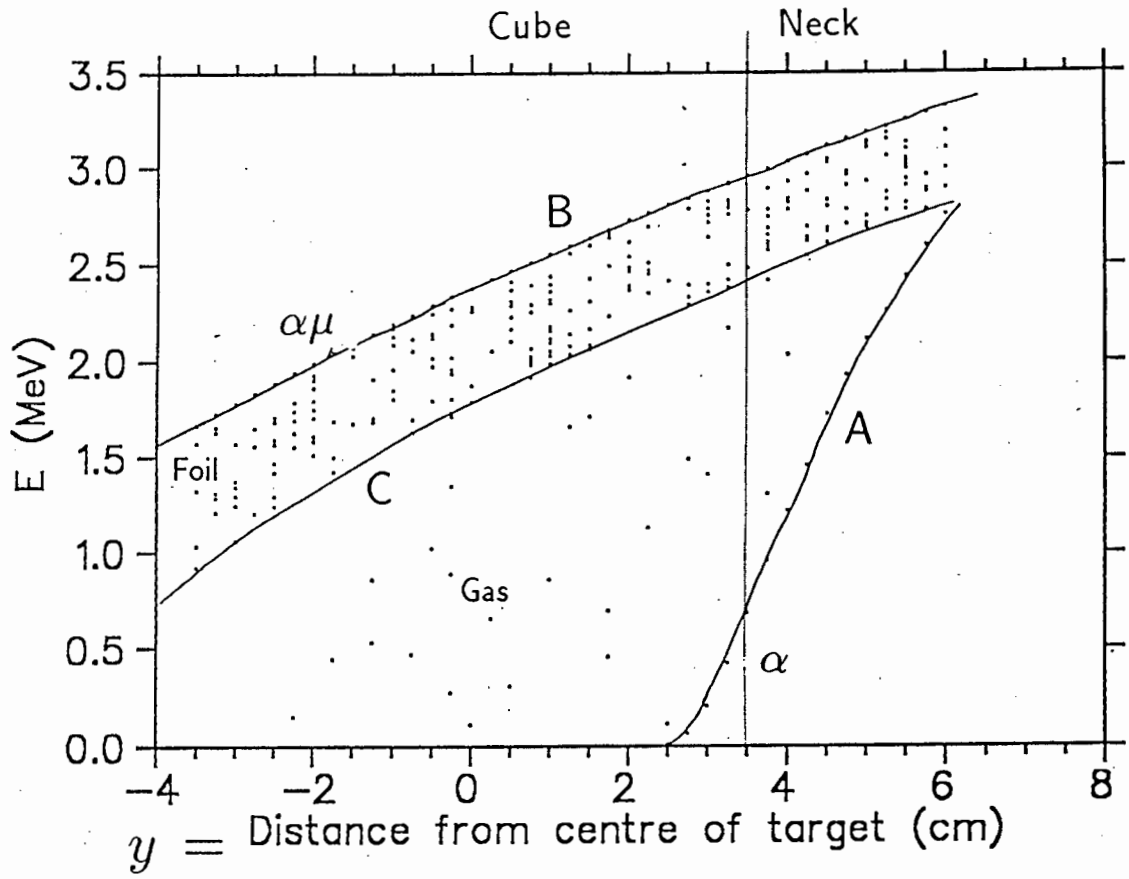

Figure 4.3: Position y of fusion in target box versus detected alpha energy E for fusions along line AN in figure 4.1

is no allowance for energy spread or additional time spread introduced by instrumental effects.

The loci for α and $\alpha\mu$ (lines A and B) are clearly separated in this plot. Note how line A approaches line C at about T= -3 ns, which corresponds to fusions taking place at the Havar surface protecting the alpha detector. For such fusions, an $\alpha\mu$ stripping on the Havar surface (line C) is indistinguishable from an α (line A). As the foil is very thin, the time taken for an $\alpha\mu$ to traverse it is negligible, so T is largely unaffected by stripping.

Figure 4.5 shows the E–T plot produced when restricting fusions to the same set of points along line AN (1-D) as before (figure 4.1) and allowing the angle of the fusion products to vary over 4π (3-D). This did not affect the results greatly, as the energy and time of flight and energy of the alpha are uniquely defined by the distance the alpha has to travel in the gas. The loci are smudged a little by the $\cos\theta$ effect in the metal layer, where energy alone is affected.

The next step in the generation of the E–T plots was to add the uncertainty due to the finite energy resolution of the alpha detector and the combined time resolution of the neutron and alpha detectors. Different resolution characteristics have been used for the three geometries presented

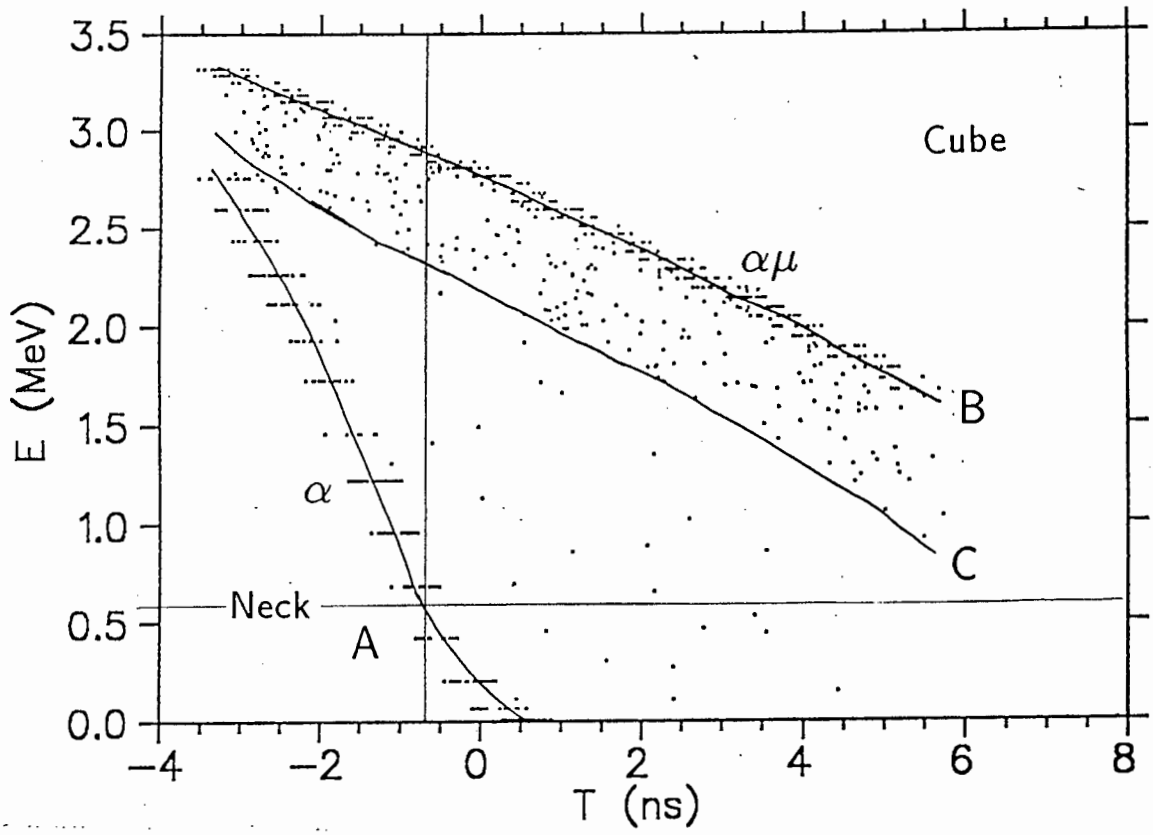

Figure 4.4: E–T plot for fusions taking place on line AN in figure 4.1 and alpha emission forced along line AN. See text.

here.

For a surface barrier detector of 4 cm dia, as used in geometry A the energy resolution of 2 % FWHM, or better, may be expected for 3 MeV α [91]. This has been assumed for the simulations in geometries A and B. For other energies, the resolution FWHM has been assumed to be proportional to the square root of the detected alpha energy. In the absence of beam-related backgrounds the time resolution for a 4 cm diameter, thickness $\leq$ 100 μm, expected to be 2.5 ns FWHM at best, due to the high capacitance of the detector. A composite detector of a similar size, planned for use in geometry B, should have a timing resolution of 1 ns FWHM or better. The time resolution for the NE213 neutron detector is approximately 1 ns.

Including the time resolution will cause the α and $\alpha\mu$ loci (figure 4.5) to spread into gaussians with FWHM corresponding to the time resolution. Line C in figure 4.5 represents a typical $\alpha\mu$ selection cut. For any time resolution less than 4 ns FWHM this cut will include 90-100% of $\alpha\mu$ which reach the barrier unstripped. Since there are approximately 100 times more α produced initially than $\alpha\mu$, the intensity of the α locus at the 1% level will be comparable to the intensity of the $\alpha\mu$ locus at its centre. Hence curves have been drawn around the α locus at the 1% level for FWHMs of 1, 2 and

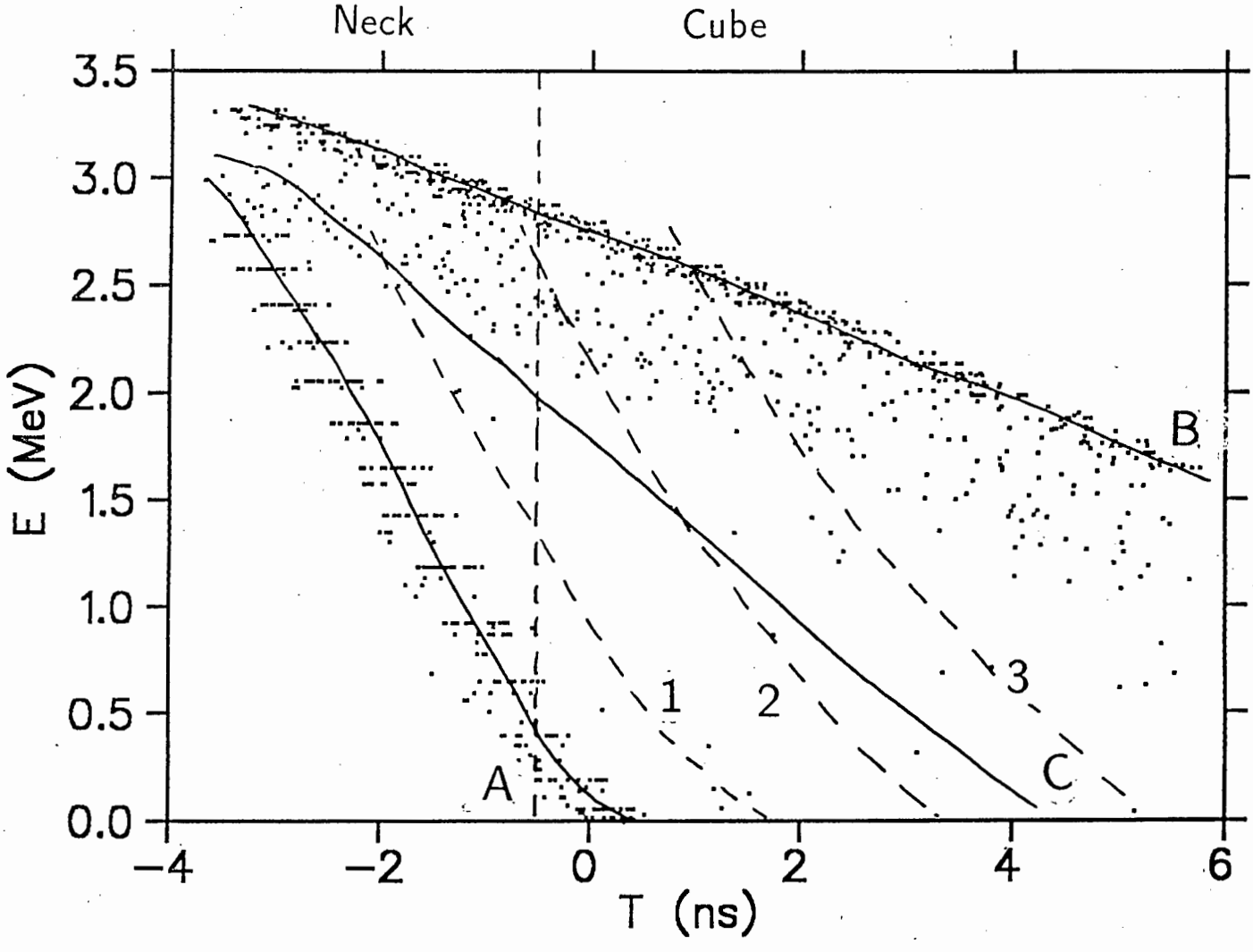

Figure 4.5: E–T plot with α emitted at all angles, fusions along line AN in figure 4.1. For explanation of curves 1, 2 and 3 see text.

Table 4.1: The three geometries for which E–T distributions were simulated.

Geometry	A	B	C
	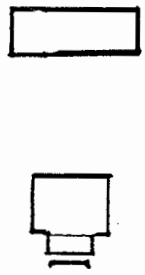	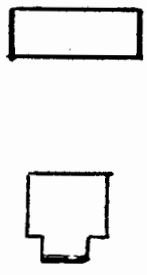	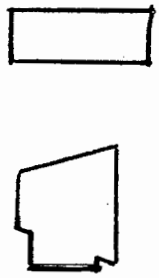
Detector	SBD	SBD	TFP
Windows	2×1.5μm mylar	none	none
Barrier	none	1.6 μm havar	1.6μm havar
Time resolution	3 ns FWHM	$\leq$ 1 ns FWHM	1.2 ns FWHM
Energy resolution	2 % @ 3 MeV	2 % @ 3 MeV	30 % @ 3 MeV

3 ns. With the position distribution of fusions estimated from the DEGRAD calculations, with muons scattering into the neck region, only about 10 % of alphas will fall above the 2 MeV line (see figure 4.15) which means that much less than one in every thousand α will break through and be mistaken for an $\alpha\mu$. The amount of alpha breakthrough can readily be obtained from the MUGLU results.

For the simulated E–T plot each event (E,T) had added to it (ΔE,ΔT), where ΔE and ΔT were selected from gaussian distributions of the appropriate FWHM.

The final generalisation is moving from the one dimensional case (fusions at points equally spaced along line AN) to the three dimensional case, with fusions taking place all over the cell with distribution $\rho(\vec{r})$ estimated from DEGRAD results, as described in section 2.3.

E–T plots were simulated for the three geometries defined in chapter 2. Table 4.1 summarises the detector characteristics assumed for the the geometries.

4.1.2 Geometry A

In geometry A there are two mylar windows at either end of the neck. Ideally, the windows are impervious to tritium and were designed to keep tritium out of the neck and away from the alpha detector.

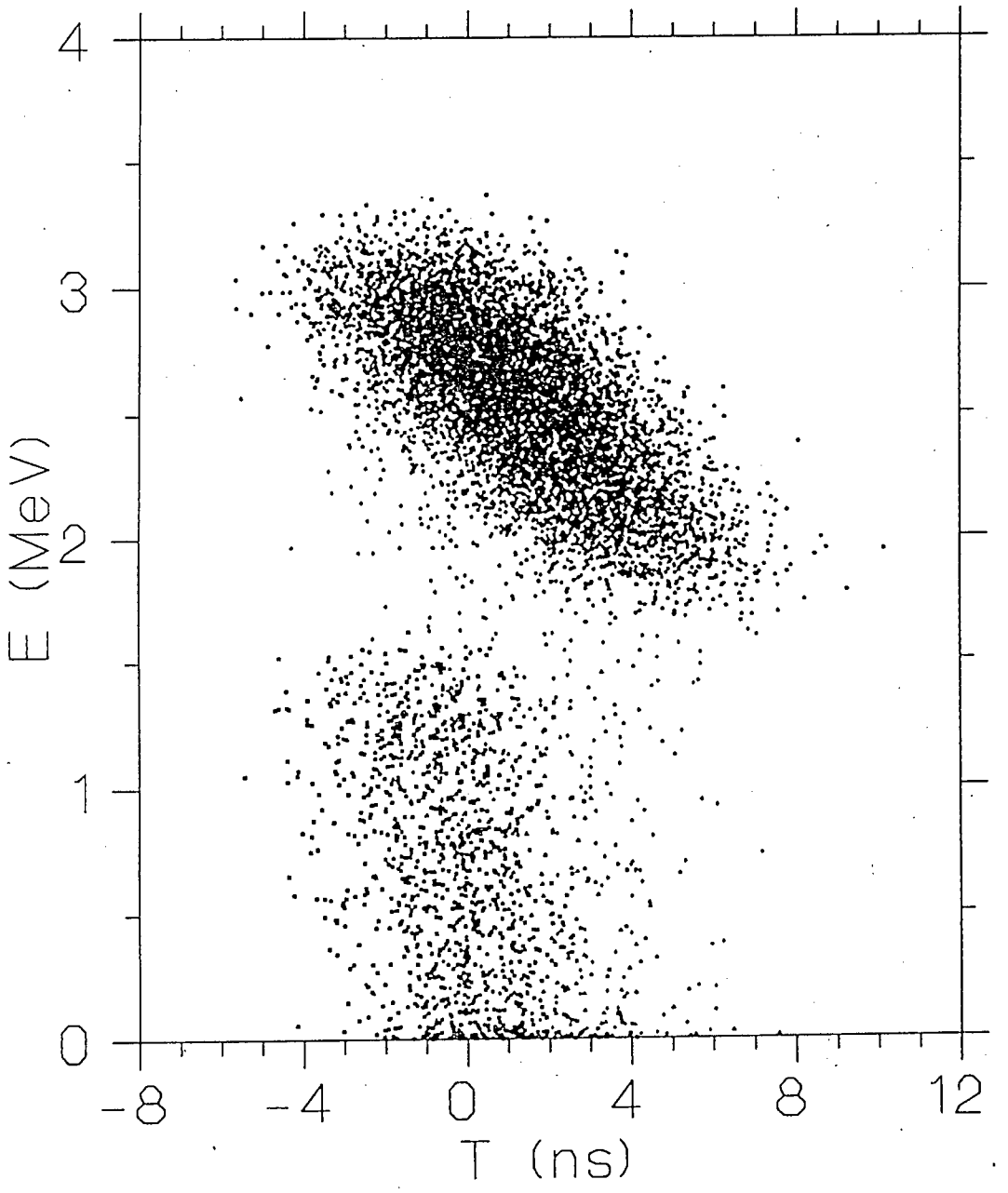

Figure 4.6: E_α–t-o-f plot for geometry A. ω_s^0=50%

Figure 4.6 shows the E–T plot generated for geometry A, with detector characteristics (table 4.1A) and other conditions similar to those used in the RAL experiment (figure 1.9). The gas pressure is 1510 Torr. Clear separation of the α and $\alpha\mu$ loci is noted, with most of the alphas ranged out. The events between the loci are $\alpha\mu$ stripped in the mylar windows or in the gas. 90% of the $\alpha\mu$ reach the detector with energy greater than 1.5 MeV, that is, $\Phi = 0.9$ for detector threshold of 1.5 MeV. 12% of the α strike the detector, but less than .01% of these have energy above 1.5 MeV.

Figure 4.7 has a more realistic ratio of α to $\alpha\mu$ with ω_s^0 set equal to 1%. In this figure, one can see that although most of the α are ranged out the number of α detected above an operating threshold such as 1 MeV will still exceed the number of $\alpha\mu$. The discrimination of $\alpha\mu$ from α is nevertheless still very good.

Figures 4.8 and 4.9 show similar plots for gas pressure of 750 and 490 Torr respectively. Measurements at RAL were taken at these two pressures to check the detection system. They were not used to determine ω_s^0.

Figure 4.10 shows the worst case, with tritium diffusion through the mylar windows leading to fusions taking place in the neck region. The two loci are not easily separable. The amount of diffusion is overly pessimistic.

The results from MUGLU have been compared with experimental data and Monte Carlo simulations from the LAMPF and RAL sticking experiments.

Comparison with LAMPF sticking experiments

Figure 4.11 shows a comparison between the coincidence alpha energy spectrum for 640 Torr from the LAMPF experiment [21] and results from MUGLU. The comparison is qualitative because the exact calibration of the energy scale was not given in the LAMPF data.

RAL Experimental data

Comparison with Monte Carlo results for the E–T from RAL distributions was not meaningful, as the time resolution was too poor to show any detail. The E–T distributions for the RAL experiments can be seen in appendix E.

Figures 4.12, 4.13 and 4.14 show comparisons between MUGLU results (curve) and RAL results (histogram) for the projected coincidence α energy spectra for 1500, 710 and 490 Torr gas pressure.

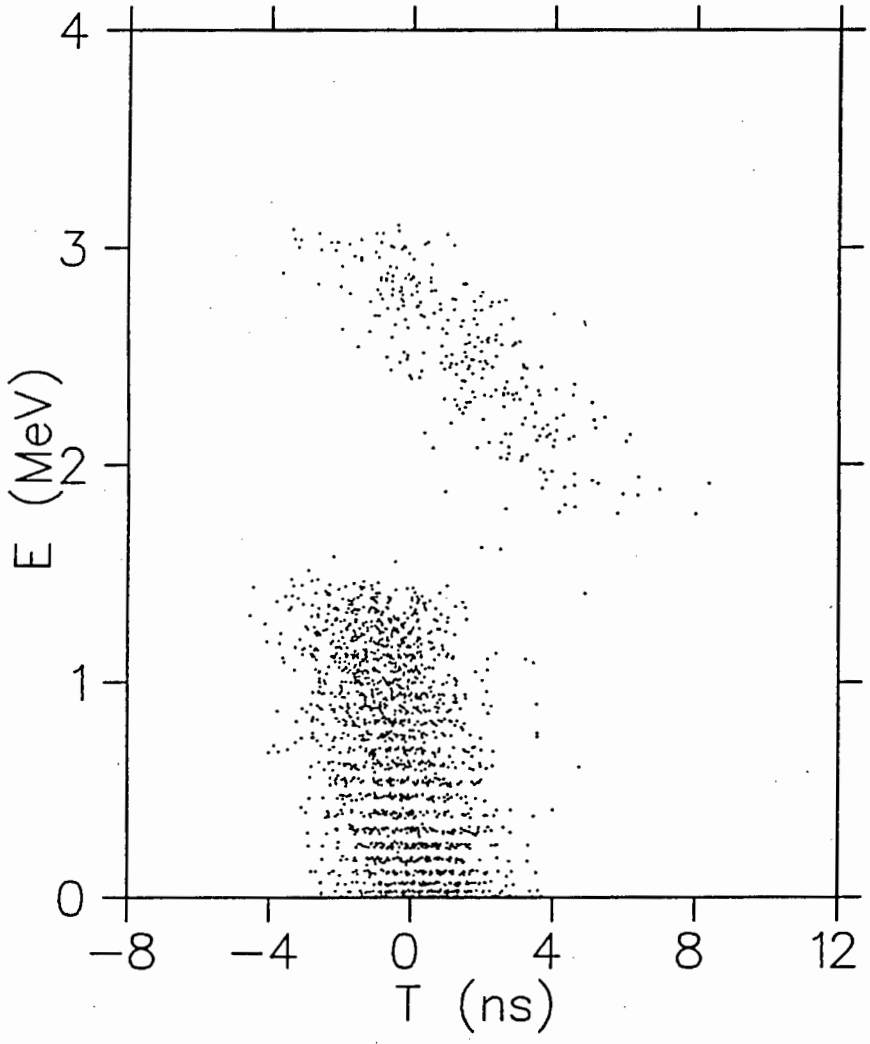

Figure 4.7: Geometry A: E–T plot with ω_s^0=1%, gas pressure: 1510 Torr. The striations parallel to the time axis arise from too coarse a step size in the numerical integration.

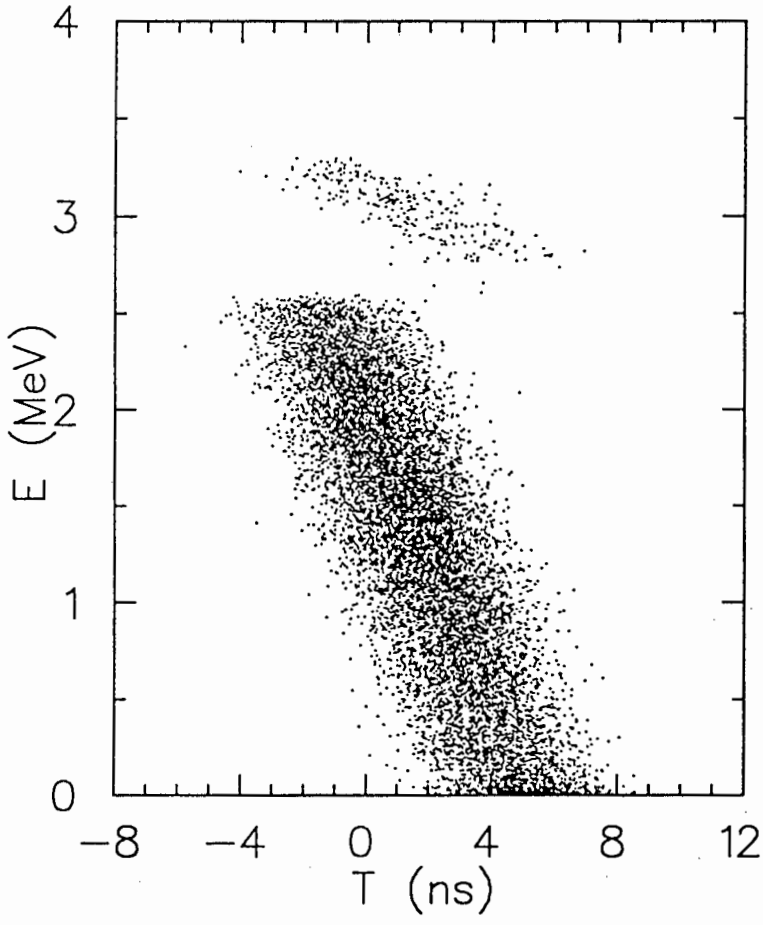

Figure 4.8: Geometry A, E–T plot, pressure 710 Torr, ω_s^0=1%

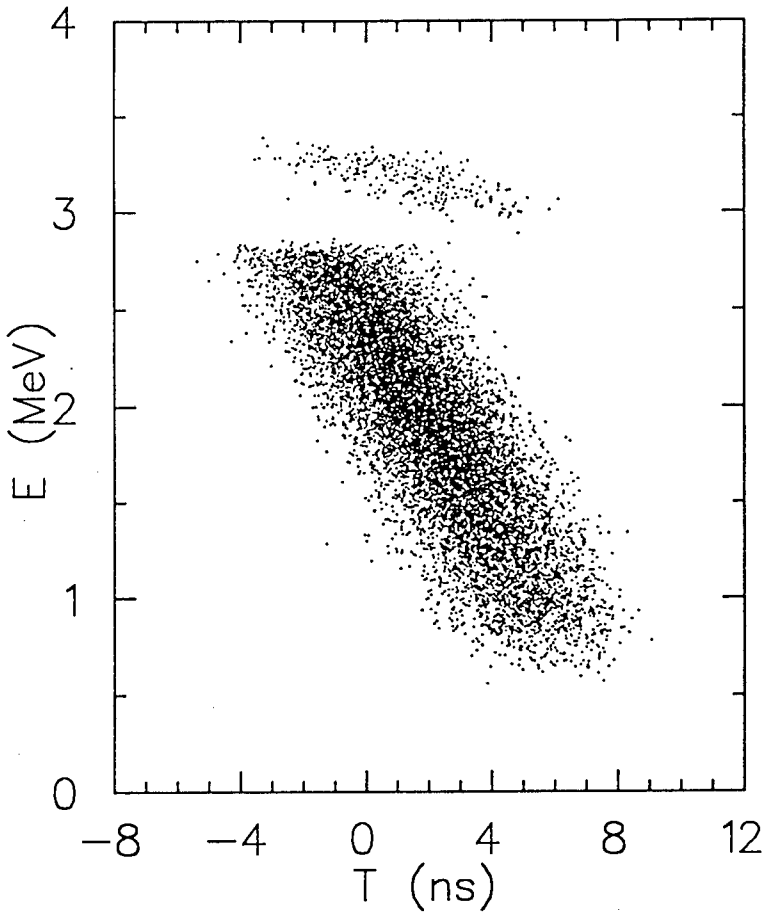

Figure 4.9: Geometry A, E–T plot, pressure 490 Torr, ω_s^0=1%

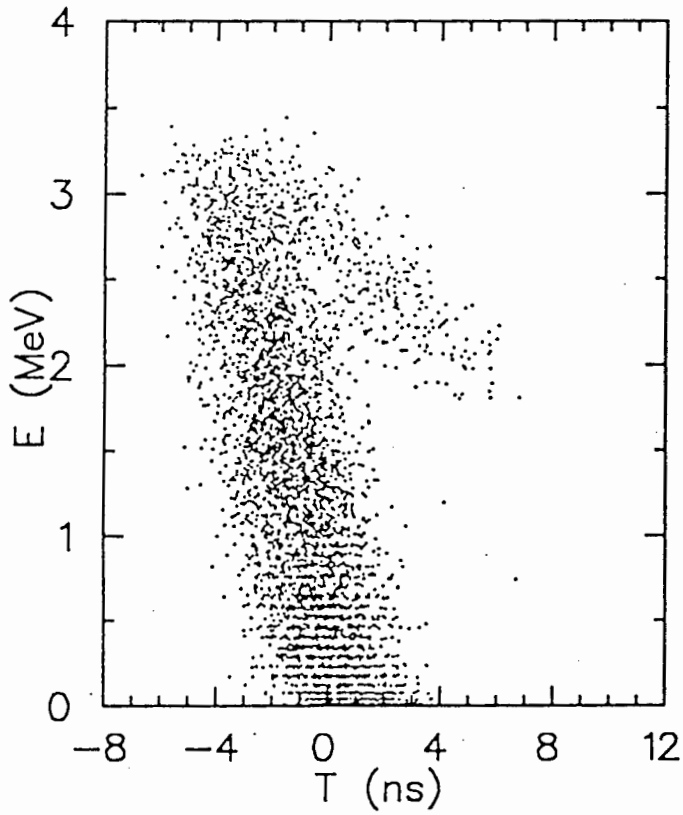

Figure 4.10: Geometry A, E–T plot, $p = 1510$ Torr, $\omega_s^0 = 1\%$, with tritium diffusion through the mylar windows. The fusion distribution thus includes fusions taking place in the neck region.

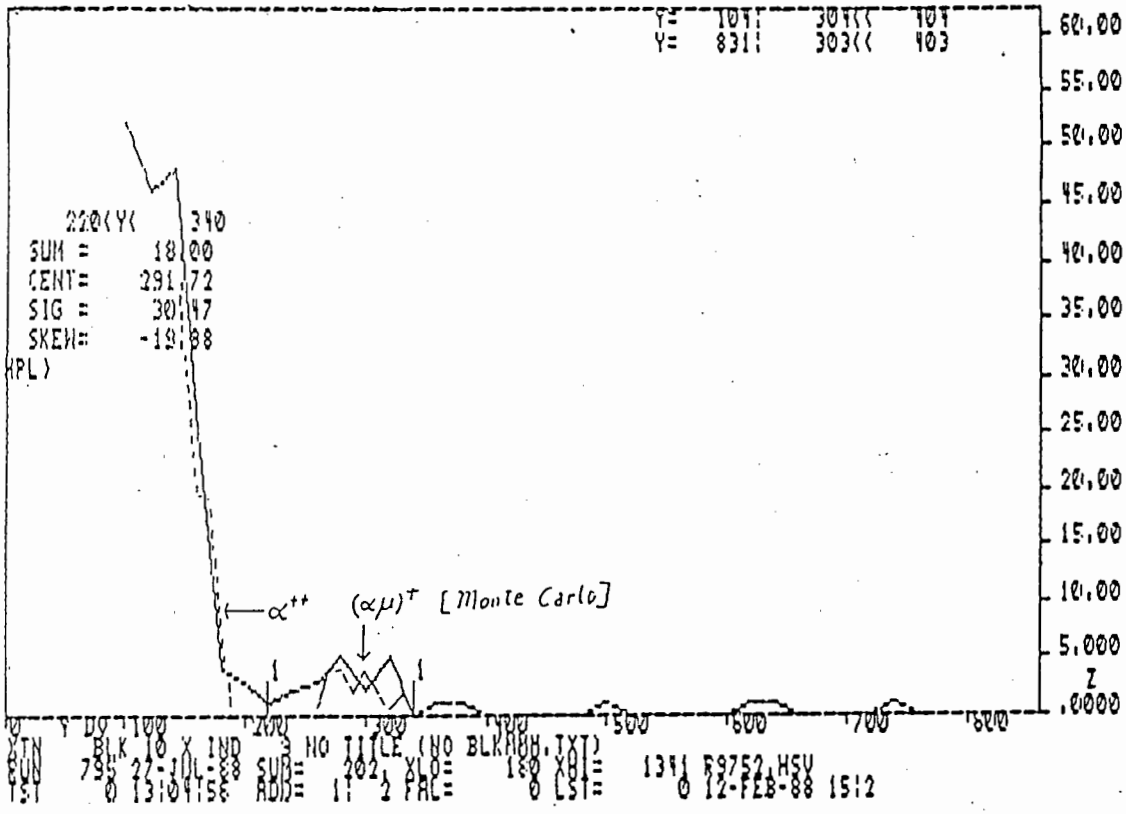

Coincidence alpha energy spectrum from LAMPF for gas pressure 640 Torr. The solid line is the measured spectrum while the dotted line is the spectrum calculated by LAMPF Monte Carlo. Figure reproduced from reference [21].

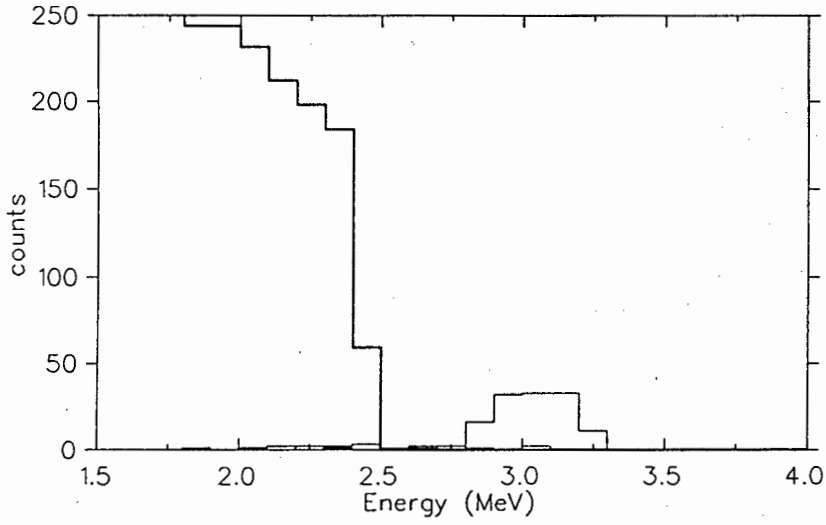

Figure 4.11: Alpha coincidence spectrum from MUGLU run for a geometry similar to the LAMPF geometry. Pressure 640 Torr, ω_s^0=1%.

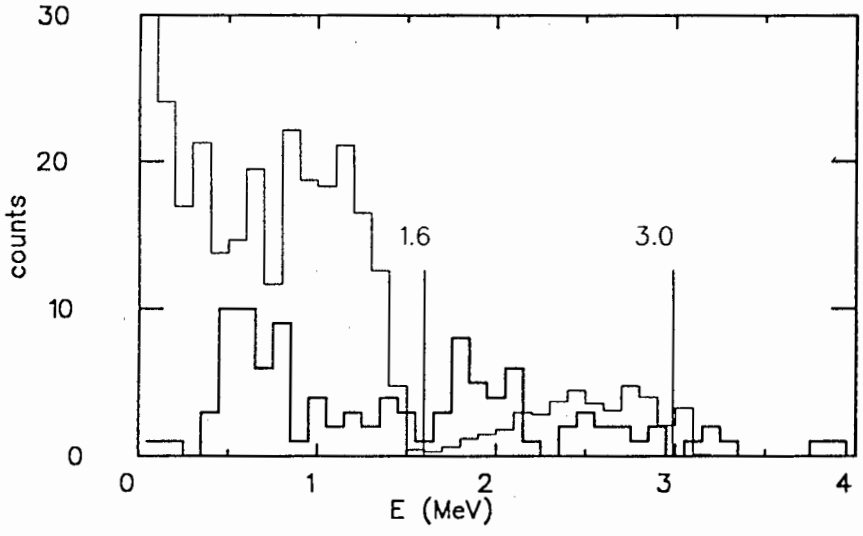

Figure 4.12: Alpha energy spectrum for geometry A, pressure=1500 Torr, ω_s^0=1%. Bold histogram: RAL June 1988 data, feint histogram: calculations by MUGLU

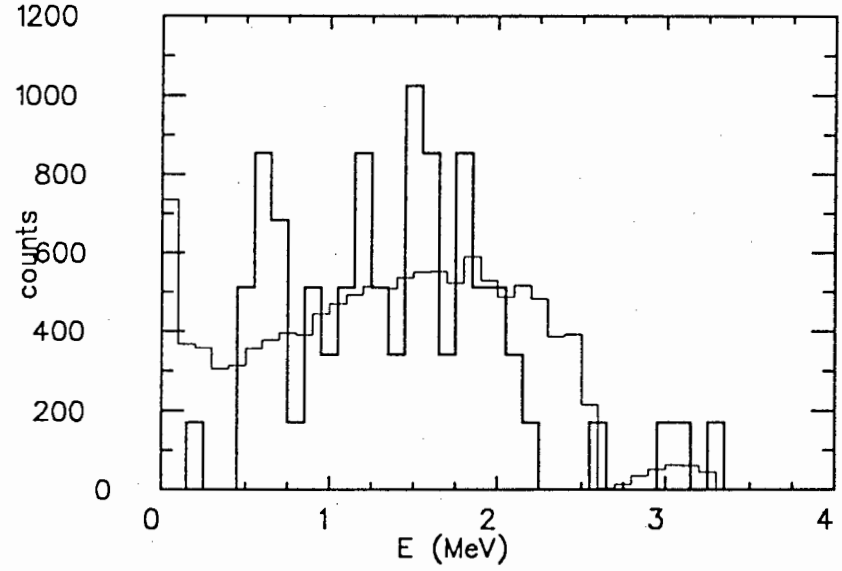

Figure 4.13: Alpha energy spectrum for geometry A, pressure=710 Torr, ω_s^0=1%. Bold histogram: RAL June 1988 data, feint histogram: calculations by MUGLU

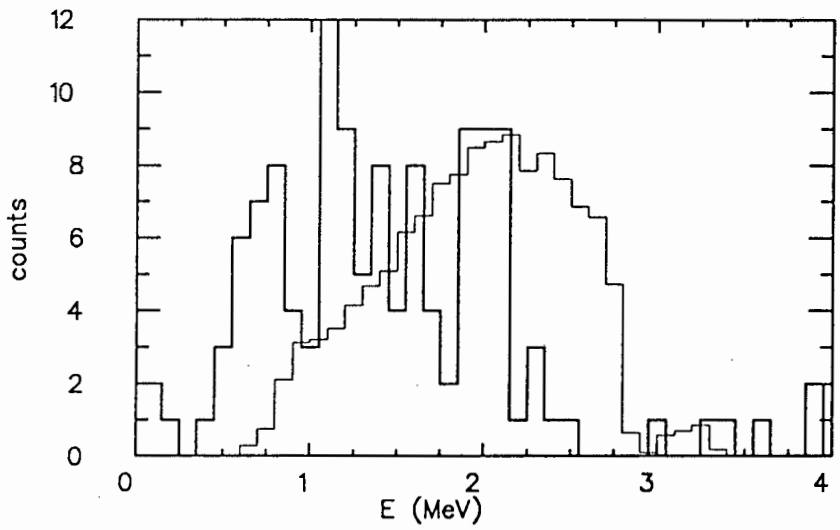

Figure 4.14: Alpha energy spectrum for geometry A, pressure=490 Torr, ω_s^0=.8%. Bold histogram: RAL June 1988 data, feint histogram: calculations by MUGLU

The paucity of the statistics for the experiment preclude quantitative comparison. However, it would appear from rough comparison at the three pressures that the fusion position distribution assumed in the simulations differs from the distribution obtained in the experiment, with far more fusions taking place at points furthest from the alpha detector in the latter case, shown by a higher occurrence of α and $\alpha\mu$ with lower energies for the experiment than for the simulations.

Geometry A would seem very promising for measuring E–T distributions if the mylar windows were really impervious to tritium diffusion. Under experimental conditions, it was found that tritium diffusion into the neck region was not negligible. The percentage of tritium in the target cell was seen to fall from 45% to 38% [92] over two days. This has two adverse effects:

1. The fusion distribution $\rho(\vec{r})$ is time dependent, as tritium diffuses into the neck, although in the apparatus used at RAL, the neck is out of the target proper and part of a larger volume of D_2 gas, thus diluting the tritium in neck. Figure 4.10 shows an E–T plot for geometry A with fusions in the neck region. The fusion distribution for this simulation assumes equal proportions of tritium in the neck as in the cell and thus is probably a bit pessimistic.

2. Once the tritium has diffused through the mylar windows, the SBD is unprotected against tritium beta decay. The 18 keV betas from this decay produce noise, which might degrade the time and energy resolution of the detector. This again is reduced to manageable levels by dilution of tritium in the large volume of deuterium surrounding the target box.

Probably the biggest problem with geometry A is that the system is very fragile and difficult to fill. The gas pressures in the cell and in the surrounding cavity have to be balanced very carefully in order not to place undue strain on the windows.

4.1.3 Geometry B

Geometry B is a far more robust setup than geometry A, with one chamber only, and no fragile windows, thus allowing the pressure of the gas to be varied easily. The drawback is that there may be a significant proportion of fusions in the neck. On the other hand the space distribution of fusions

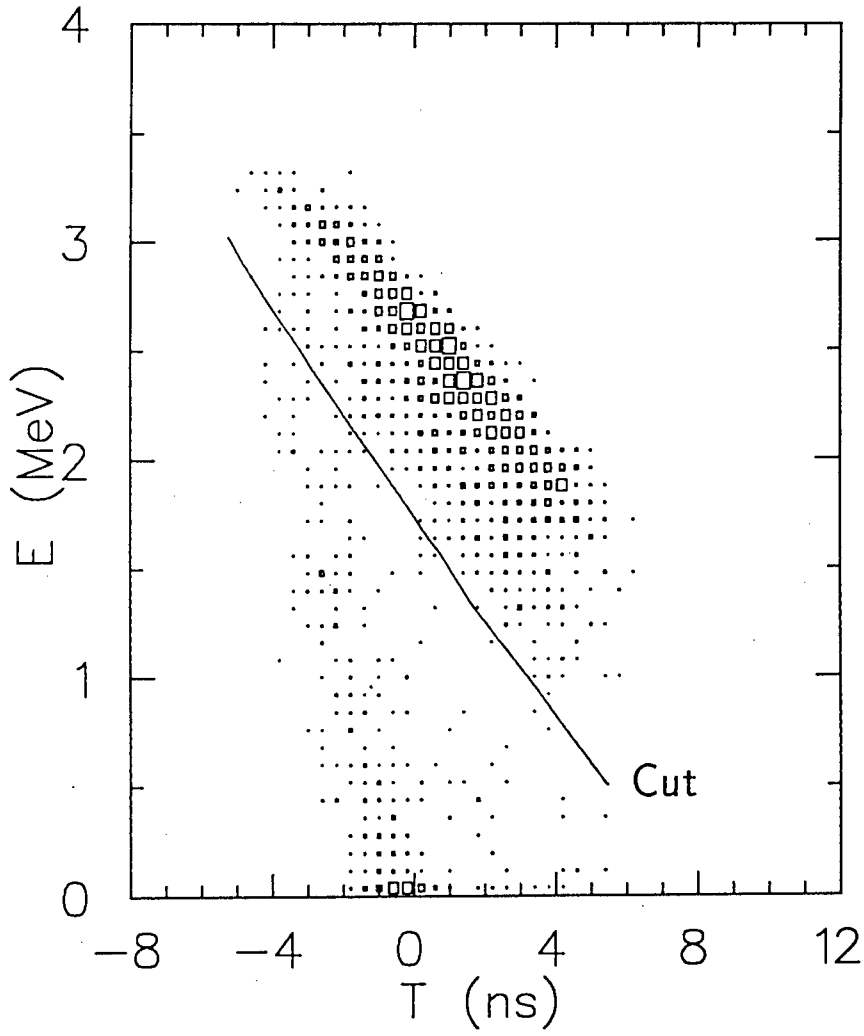

Figure 4.15: E–T plot for geometry B. Detector time resolution is 1 ns FWHM. Pressure = 1510 Torr, $\omega_s^0 = 50\%$

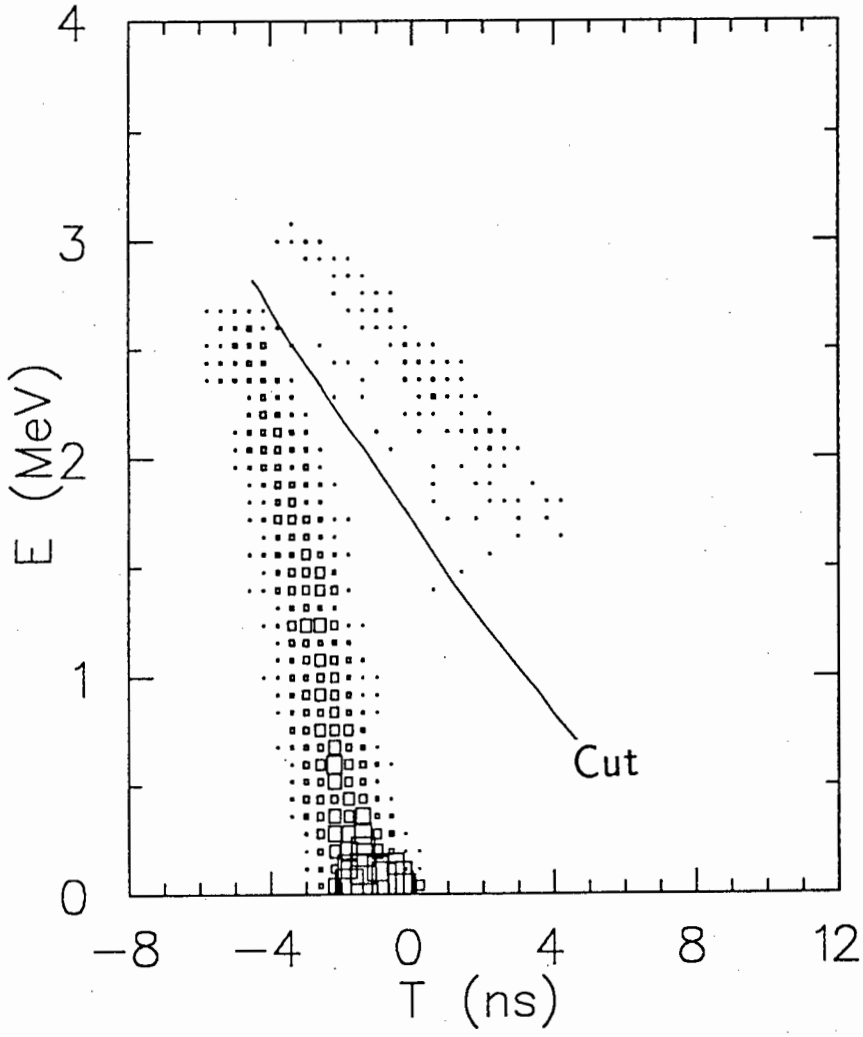

Figure 4.16: E–T plot for geometry B. Detector time resolution is 1 ns FWHM. Pressure = 1510 Torr, $\omega_s^0 = 1\%$

should be constant in time. Barriers of either Havar foil or a vacuum deposited layer of aluminium oxide appear to be efficient in protecting the detector from tritium [93].

Figure 4.15 is an E–T plot for geometry B with pressure 1510 Torr and $\omega_s^0 = 50\%$. The time and energy resolution of the system appears adequate for separation of α and $\alpha\mu$. Stripping in the barrier is considerable (20–40%), broadening the $\alpha\mu$ locus considerably.

Figure 4.16 is an E–T plot for $\omega_s^0 = 1\%$. The α and $\alpha\mu$ are well separated. The number of α in the plot is about 3% of the total number of α which would have made coincidences had they not been ranged out. This percentage varies with the number of muons scattering into the neck, as almost all α in this plot arise from fusions occurring in the neck. Figure 4.16 should be regarded with caution until an accurate estimate of the fusion distribution can be made.

However, the simulations suggest that a lower ω_s^0 could be measured in this way; and measurements could be made at a higher pressure, which has the twofold advantage of more fusions per muon, and reduced diffusion lengths of muonic atoms and mesomolecules.

4.1.4 Geometry C

The TFP used in geometry C has a non-linear response to α over the energy range detected in this experiment. As a result of this non-linearity, the scintillator response, calculated using the Birks formula (equation 2.23), to α is different to that for $\alpha\mu$. The plots are *pulse height* – time (L–T) plots, and the pulse height versus energy calibrations for α and $\alpha\mu$ are different.

Figure 4.17 shows an L–T plot simulated for the plastic scintillator. The pulse height resolution was taken to be 30% FWHM for a 3 MeV alpha, and was assumed to vary as $\sqrt{L}$; and a time resolution of 1.2 ns was assumed for this type of detector.

The α locus is marked A. The $\alpha\mu$ not stripped in the gas are spread out over a wide range of pulse height above line C. The distribution can be broken down as follows:

1. The slight clustering of $\alpha\mu$ marked 'F' from $\alpha\mu$ which stop in the plastic detector having deposited all their energy without being stripped is at the highest pulse height.

2. Beneath locus F these is a region E of almost even distribution of events from $\alpha\mu$ which are stripped in the scintillator before coming

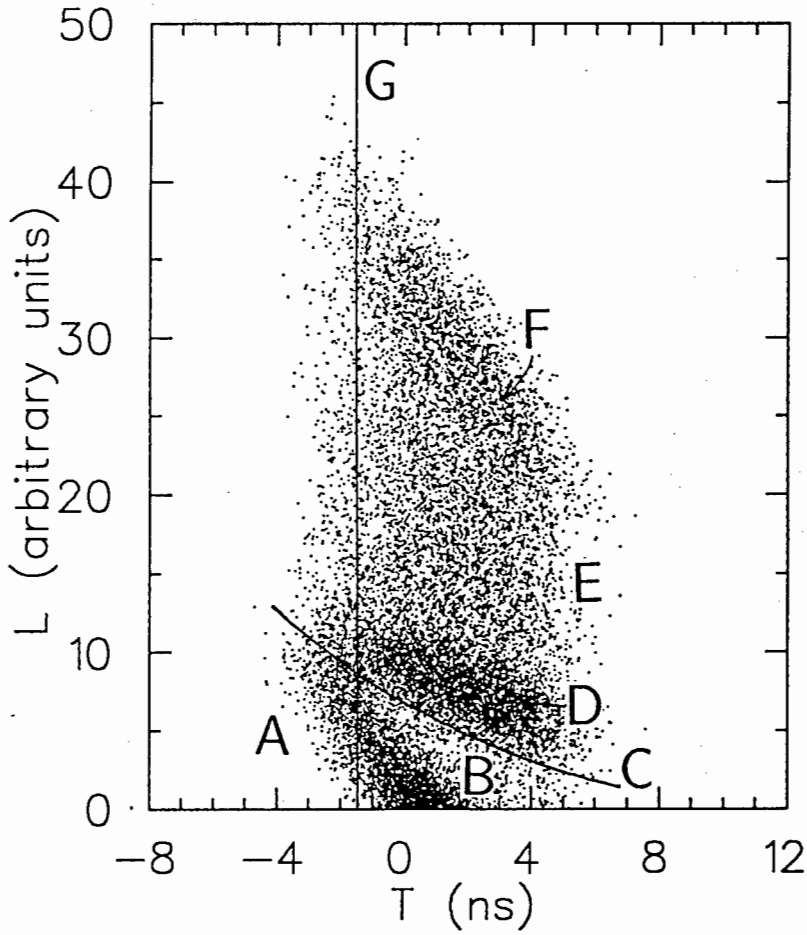

Figure 4.17: L–T plot for Geometry C, pressure 1500 Torr, ω_s^0=50% The data labelled in the plot are: A: α. B: $\alpha\mu$ stripped in the DT gas. D: $\alpha\mu$ stripped in the Havar foil covering the detector. E: $\alpha\mu$ stripped in the TFP before coming to rest F: $\alpha\mu$ stopping unstripped in the TFP.

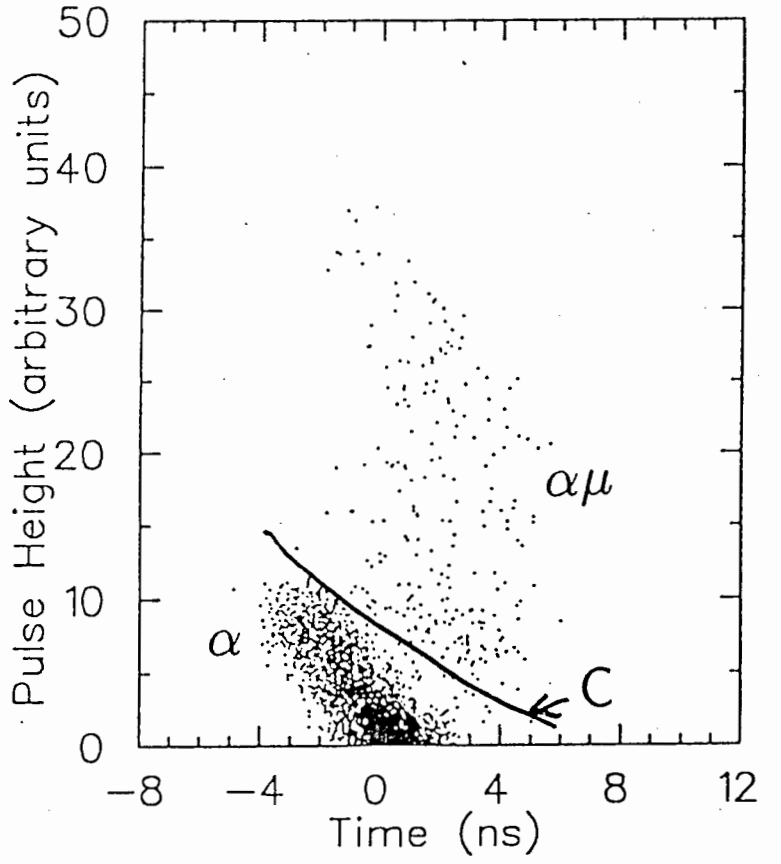

Figure 4.18: Geometry C, ω_s^0=1%

to rest. They thus deposit a portion of their energy as $\alpha\mu$ until they are stripped. The rest of their energy is lost as a doubly charged α, producing reduced pulse heights.

3. There is a further clustering of events just above line C from $\alpha\mu$ which are stripped in the protective layer in front of the detector, and are thus detected in the plastic as α.

The small fraction of events between line C and the α locus A is due to $\alpha\mu$ stripped in the gas.

Table 4.2: Distribution of α and $\alpha\mu$ in figure 4.17

Locus	Percentage of α and $\alpha\mu$ from fusion $p = 1510$ *Torr*
A – α^{++}	21
B – $\alpha\mu$ stripped in gas	8
D – $\alpha\mu$ stripped in barrier	36
E – $\alpha\mu$ stripped in NE102	41
F – $\alpha\mu$ unstripped	15

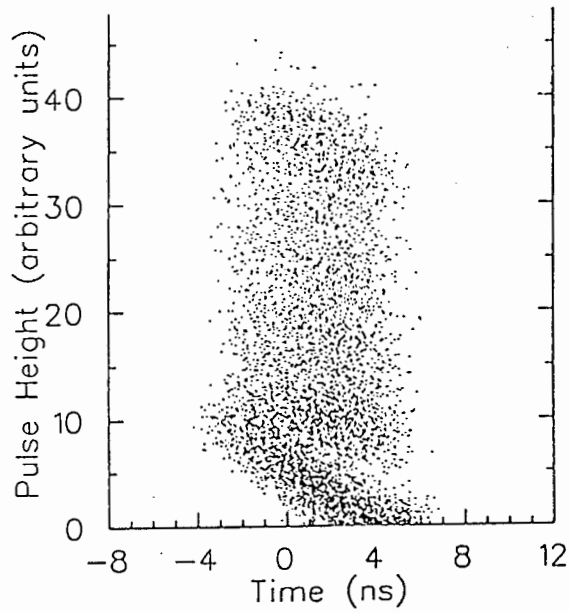

Figure 4.19: Geometry C, pressure 750 Torr, ω_s^0=50%

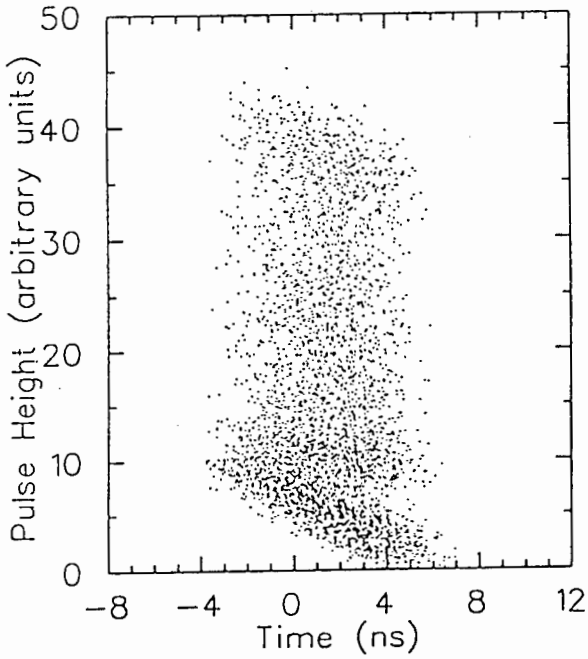

Figure 4.20: Geometry C, pressure 490 Torr, ω_s^0=50%

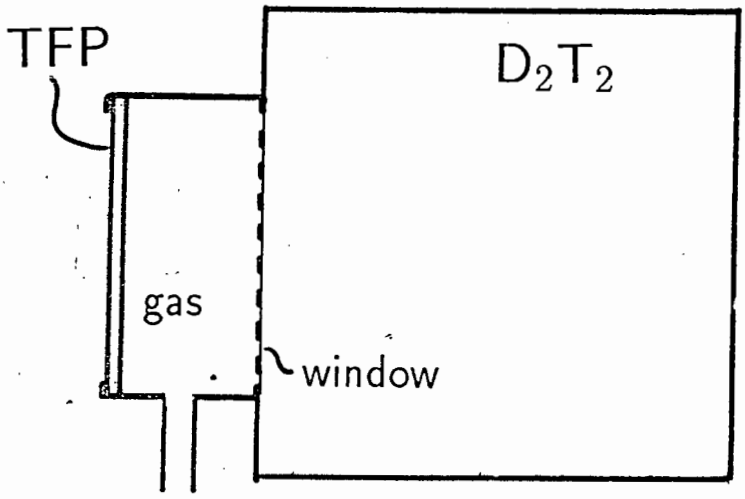

Figure 4.21: An apparatus to measure the μ stripping in gas. This consists of a DT target box coupled to a cell which can be filled with gas at various pressures. The α detector is a TFP

Note how the loci A and D merge at $T < -3$ ns (the neutron travel time from the alpha detector to the neutron detector) as did the equivalent loci for geometry B (figure 4.15). As for that geometry, this might necessitate making time cuts such as G (figure 4.17) to exclude fusions in the neck region.

Figure 4.18 shows the simulations made for the same pressure with $\omega_s^0 =$ 1%, a more realistic estimate. Table 4.2 shows the percentage of alphas in each group.

Two L–T plots for geometry C at lower pressures are shown in figures 4.19 and 4.20 for comparison with geometry A at similar pressures.

4.1.5 Stripping measurements

The structure of the $\alpha\mu$ signal on the above plots lends itself to measurement of $\alpha\mu$ stripping in various media, as the $\alpha\mu$ in locus D (figure 4.17) can easily be separated from $\alpha\mu$ in locus F. The change in ratio of counts between these two loci with barrier thickness can be used to calculate the stripping in the barrier.

Two methods of analysing L–T plots suggest themselves. The first is to convert the L and T coordinates into polar coordinates θ and ρ, choosing the origin at a point defined by the intersection of the two lines drawn through the centres of loci D and F (figure 4.22). Plotting projected intensity as a function of θ (figure 4.23) will allow an easy comparison of events in the two loci.

The stripping as a function of incident $\alpha\mu$ energy can be measured by taking time cuts for as short a time interval as possible for various T and projecting onto the pulse height axis. This is shown by lines marked T_c on figure 4.22. The resulting pulse height spectrum is shown in figure 4.24. The $\alpha\mu$ energy can be calculated from the position of the peak marked '$\alpha\mu$' to the extreme right of the spectrum. The number of $\alpha\mu$ stripping in the medium is given by the integral under peak D. Stripping in gas could be measured by replacing the neck with a cell filled with various pressures of gas (figure 4.21).

Hitherto, no measurements of the stripping of muons from $\alpha\mu$ have been performed. The above method may be a good way to test the calculations of stripping, including those by Cohen as used in this work.

Simulations have been done for two thicknesses of Havar barrier: 1.6 μm (figure 4.22) and 0.7 μm (figure 4.25); and for no barrier in front of the TFP (figure 4.26), to show the dependence of the intensity loci D and F on the thickness of foil.

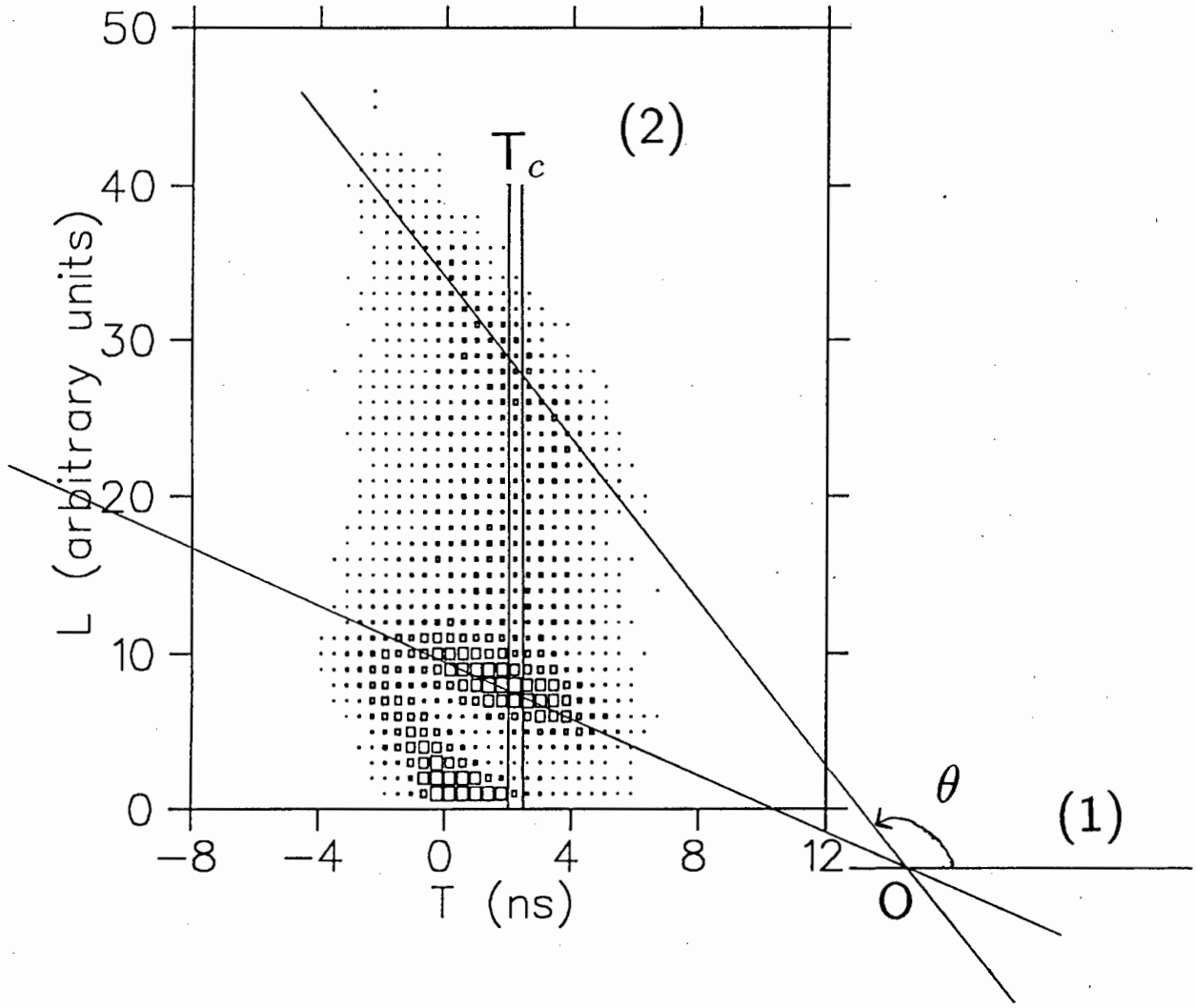

Figure 4.22: Analysis of the L–T plots: (1) converting the L and T coordinates to polar coordinates with the origin at point O, and projecting onto the θ axis; and (2) taking cuts Tc for certain T and projecting onto the L axis.

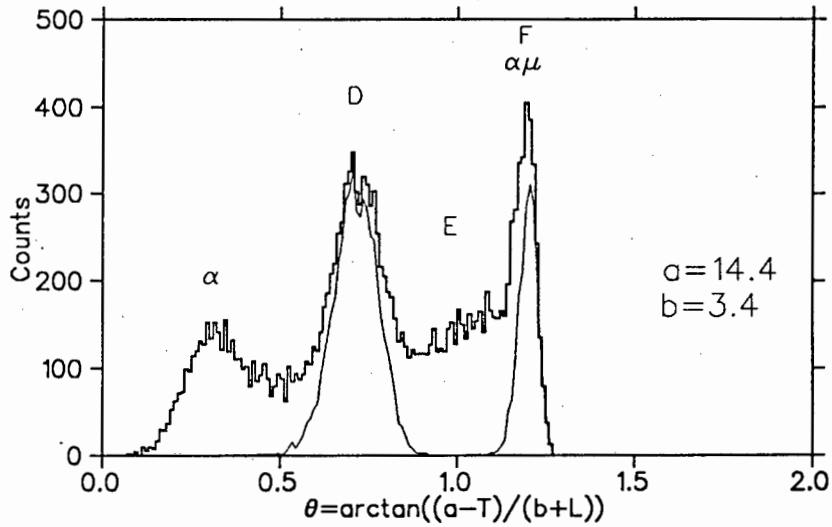

Figure 4.23: A plot of intensity versus θ obtained from (1) in figure 4.22 above.

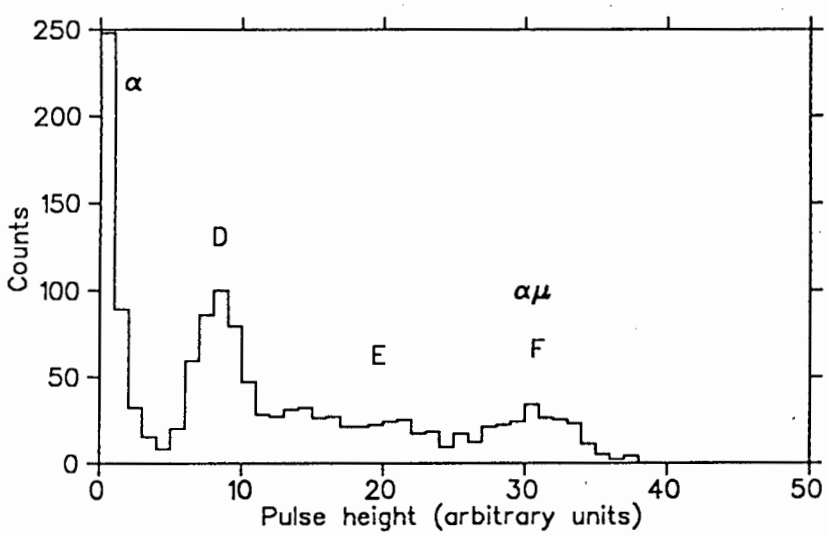

Figure 4.24: The projected pulse height spectrum for the cut Tc in figure 4.22. See text for explanation.

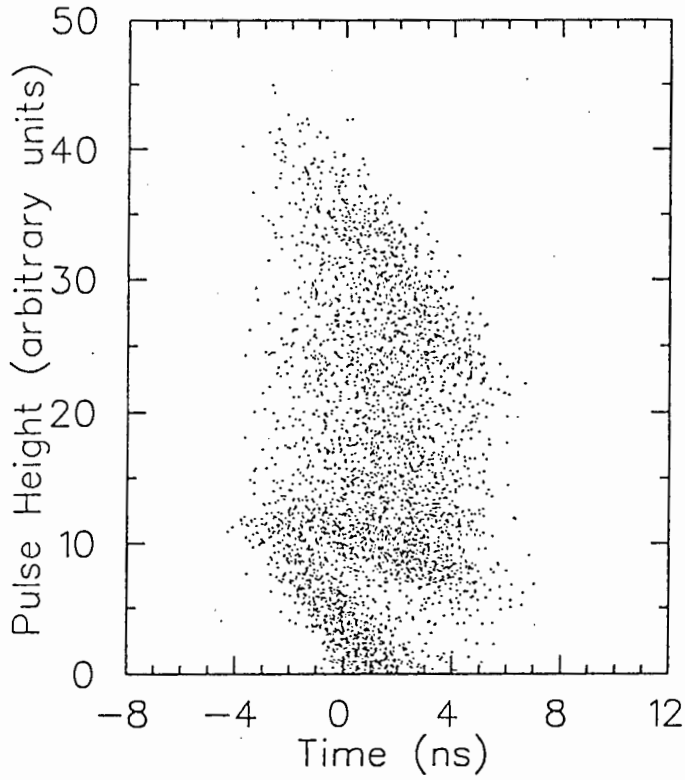

Figure 4.25: Stripping simulation for $0.7\mu m$ havar on NE102

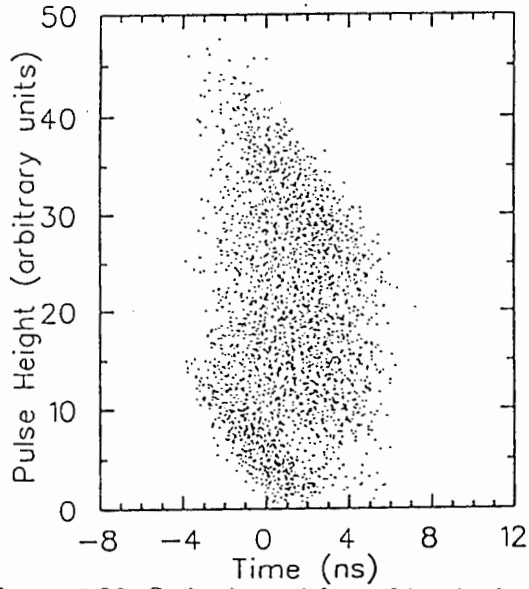

Figure 4.26: Stripping with nothing in front of NE102

4.2 B Factors

A main result of the coincidence simulations is the calculation of B factors for the two neutron detectors for geometry A.

For each fusion site $\vec{r}$ a factor $b(\vec{r})$ is defined as the probability that the extrapolated geometric path of a collinear $\alpha\mu$ associated with a detected fusion neutron intersects the alpha detector.

To a first approximation, $b(\vec{r})$ can be defined as:

$$b(\vec{r}) = \frac{\int\int \delta\left(\{\theta,\phi\} \in \Omega_\alpha(\vec{r})\right) \delta\left(\{\theta',\phi'\} \in \Omega_n(\vec{r})\right) d\theta d\phi}{\int\int \delta\left(\{\theta',\phi'\} \in \Omega_n(\vec{r})\right) d\theta d\phi} \quad (4.1)$$

where $\{\theta,\phi\}$ describe the angle in space of α emission from fusion, $\{\theta',\phi'\} = \{\pi-\theta,\pi+\phi\}$ the angle of neutron emission; $\Omega_\alpha(\vec{r})$ and $\Omega_n(\vec{r})$ are the solid angles subtended by the alpha and neutron detectors from fusion site $\vec{r}$; and the δ are Dirac δ, equal to 1 when the expression inside the brackets is true. This approximation assumes that the efficiency ϵ of the neutron detector is constant for the position and angle that the neutron strikes the detector. The neutron detector is thus position and angle insensitive (PAI) to the incoming neutron. This PAI approximation appears to have been used thus far in the calculation of B factors.

In reality, the efficiency of the neutron detector ϵ varies with position and angle of incident neutron. A more refined position and angle sensitive (PAS) calculation of $b(\vec{r})$ can be performed by including this effect:

$$b(\vec{r}) = \frac{\int\int \delta\left(\{\theta,\phi\} \in \Omega_\alpha(\vec{r})\right) \delta\left(\{\theta',\phi'\} \in \Omega_n(\vec{r})\epsilon(\vec{r},\theta',\phi')\right) d\theta d\phi}{\int\int \delta\left(\{\theta',\phi'\} \in \Omega_n(\vec{r})\epsilon(\vec{r},\theta',\phi')\right) d\theta d\phi} \quad (4.2)$$

The neutron detector efficiency does not cancel out in the above equation because the dirac δ are zero for different ranges of θ and ϕ.

For a fusion distribution $\rho(\vec{r})$ the factor B (equation 1.20, section 1.3.2) is:

$$B = \int_V \rho(\vec{r}) b(\vec{r}) d\vec{r} \quad (4.3)$$

where V is the volume of the target vessel

4.2.1 Point source factors $b(\vec{r})$

The variation of the *site* factor $b(\vec{r})$ as a function of position of fusion $\vec{r} = (x,y,z)$ in the target volume is presented in figures 4.28 and 4.29 as a series of

* $\theta,\phi \in \Omega_\alpha(\vec{r})$ means "the angle θ,ϕ in three dimensions is in the solid angle $\Omega_\alpha(\vec{r})$".

The symbols '$\in$' (element of) and 'ϵ' (efficiency) must not be confused with one another.

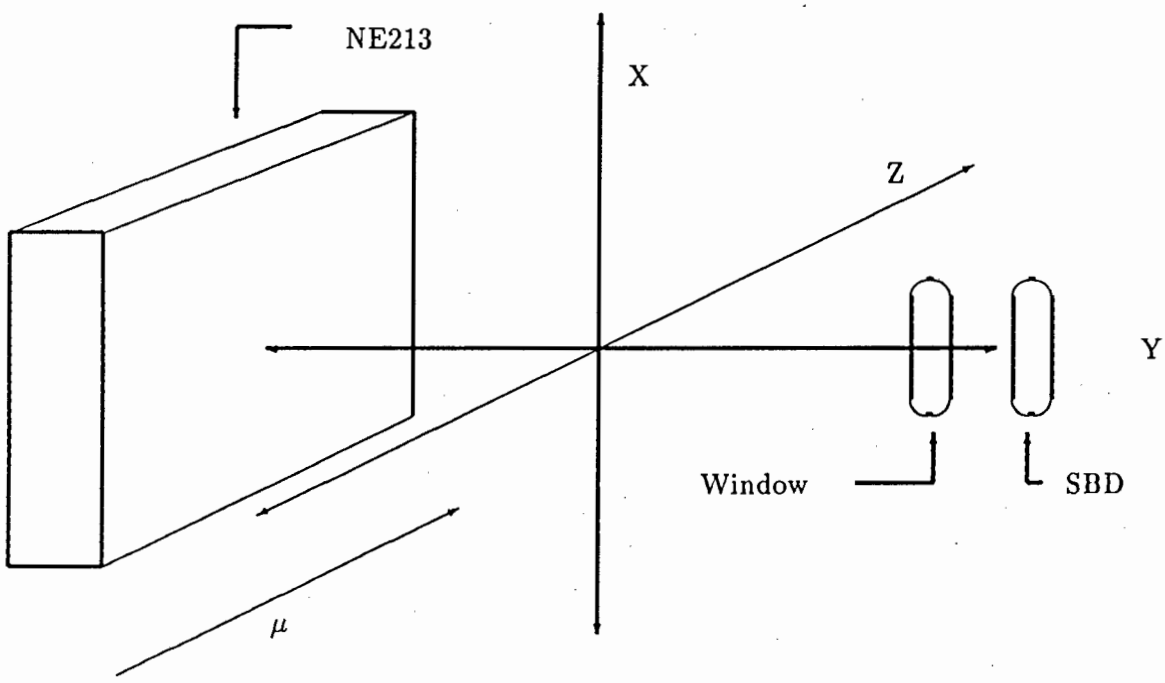

Figure 4.27: The coordinates used in the following $b(\vec{r})$ factor contour plots

contours in the XY ($z = const$) plane (see figure 4.27) for various positions along the beam (Z-axis).

The simulations calculate $b(\vec{r})$ simply by selecting a certain number of fusions at point $\vec{r}$ and allowing the collinear α–n angle to vary over 4π, thus calculating by Monte Carlo method the integrals in equations 4.1 and 4.2

Figures 4.28 and 4.29 show contour plots in the XY plane of the $b(\vec{r})$ factor for detector 1 at various positions z along the beam. Figure 4.30 is a comparison between $b(\vec{r})$ calculated using the PAI approximation (equation 4.1) and $b(\vec{r})$ calculated using PAS equation 4.2 for D1 at $z = 0$, i.e. at the central point in the target vessel. Note how the contours shrink quite noticeably for the PAI approximation. Figure 4.31 is a similar comparison for D2.

In the RAL experiment, events for which two or more detectors recorded neutrons, due to one neutron scattering in more than one detector, were rejected in analysis. The effect of this vetoing on the $b(\vec{r})$ is shown in figure 4.32. For D1 the contours expand slightly when the detectors are vetoed if both fire on one fusion. For D2 (not shown) the opposite occurs. The effect is very small compared with the PAI–PAS effect.

4.2.2 B factors for certain fusion distributions

The B factors calculated by integrating over different assumed fusion distributions $\rho(\vec{r})$ are presented in table 4.3. Each $\rho(\vec{r})$ is a gaussian in x and y increasing in width with increasing z. The gaussians are characterised by two parameters: the initial width w_i and the rate of increase in width p per centimetre along the Z axis, or muon beam.

Table 4.3 shows these parameters as the initial beam width w and width of beam on leaving the cell $w_f = w_i + pz$ at $z = 7$cm. The estimates from the DEGRAD results give a w_i and w_f of 1.5 and 4.3 cm respectively.

Several points are illustrated by this table and by the contour plots:

1. The B factors are very sensitive to $\rho(\vec{r})$. A change of about a centimetre in either initial width or final width brings about a 10% change in B factor.

   Similar changes are also seen in calculations by members of the RAL collaboration [91].

2. The ratio of B factors in reference [20] for the two detectors is 0.88, probably calculated in an approximation similar to the PAI approxima-

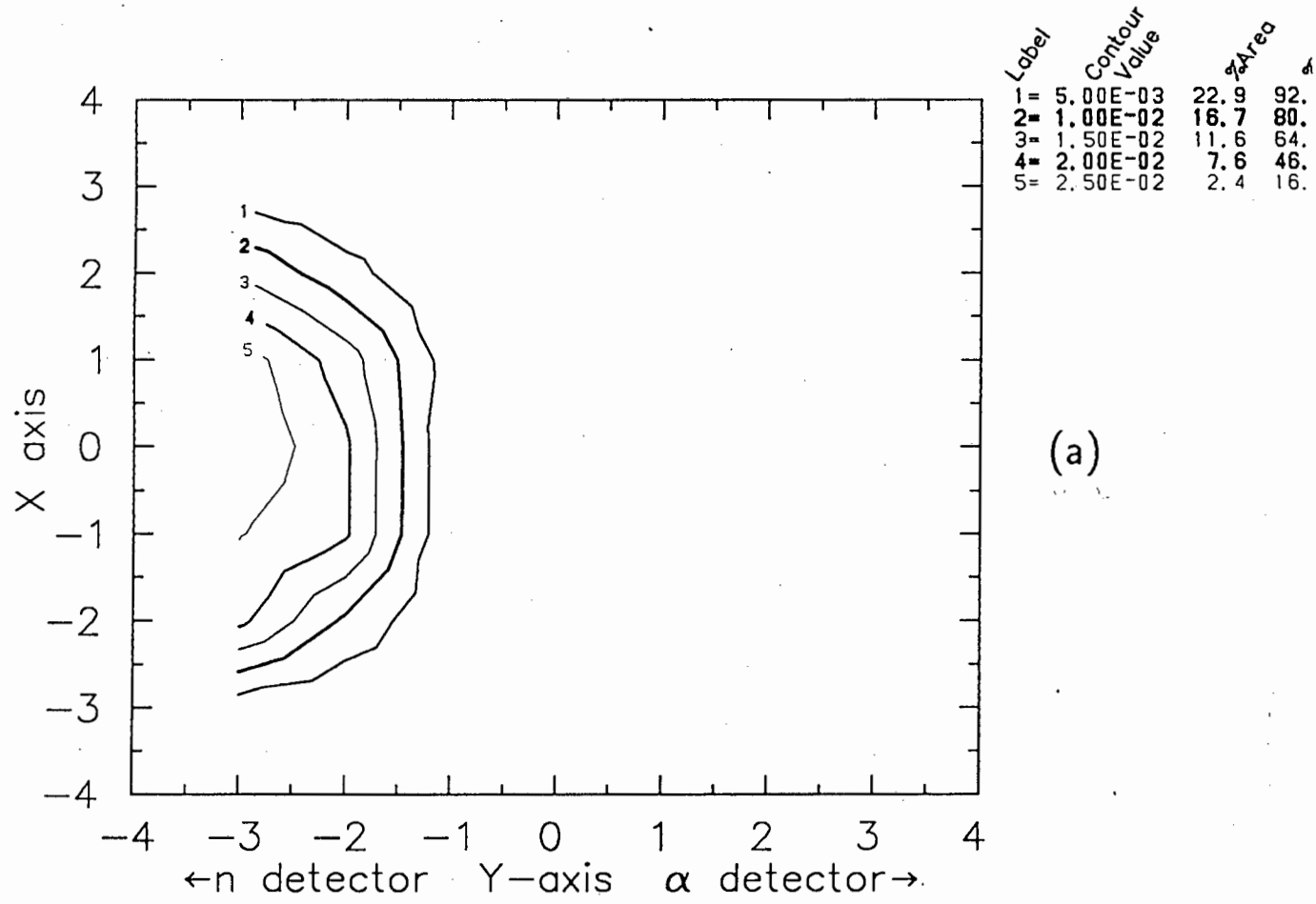

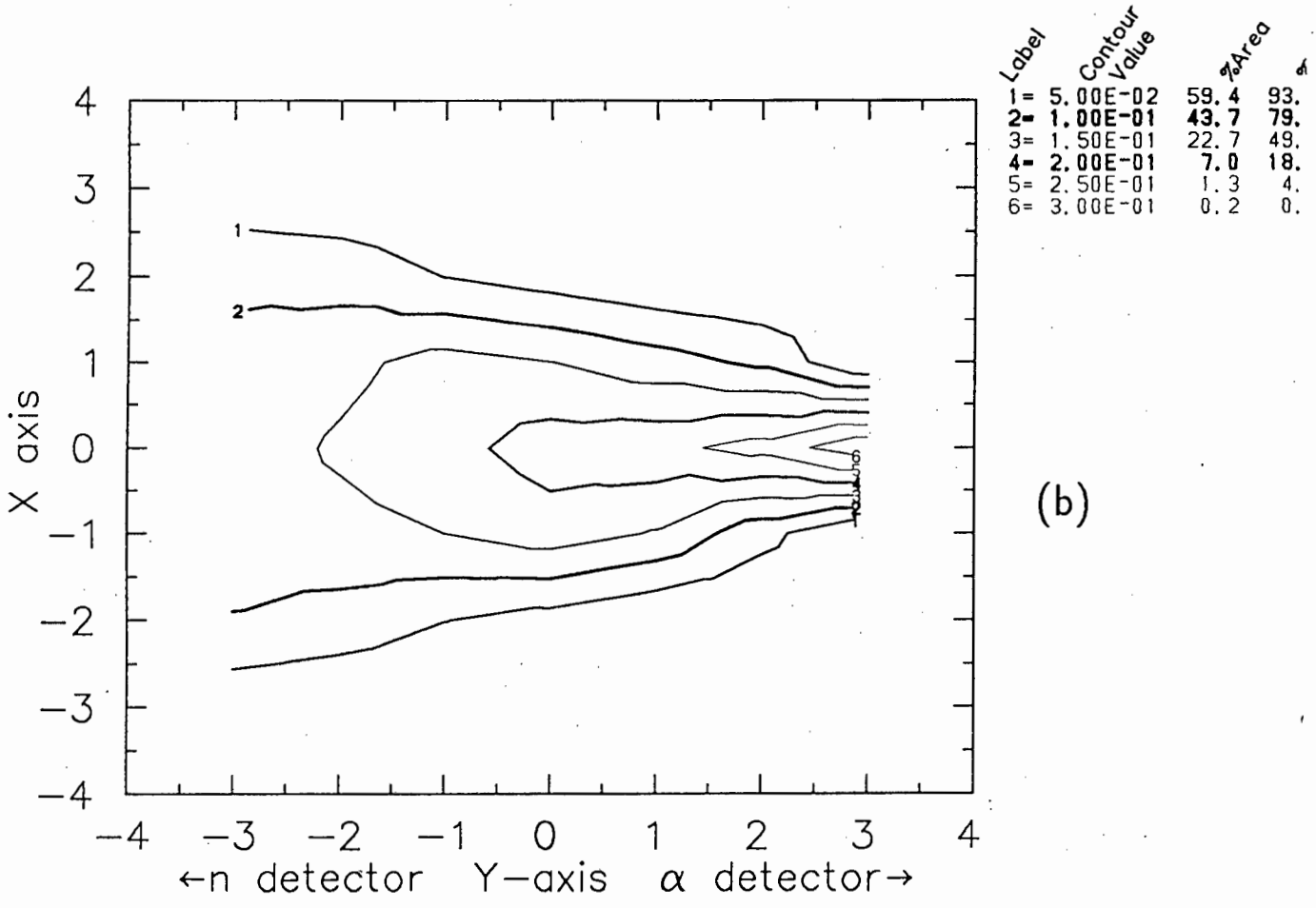

Figure 4.28: Contour plots of the b factors:(a) $b(x, y, -3)$; and (b) $b(x, y, -2)$ calculated using PAS equation 4.2 for neutron detector 1

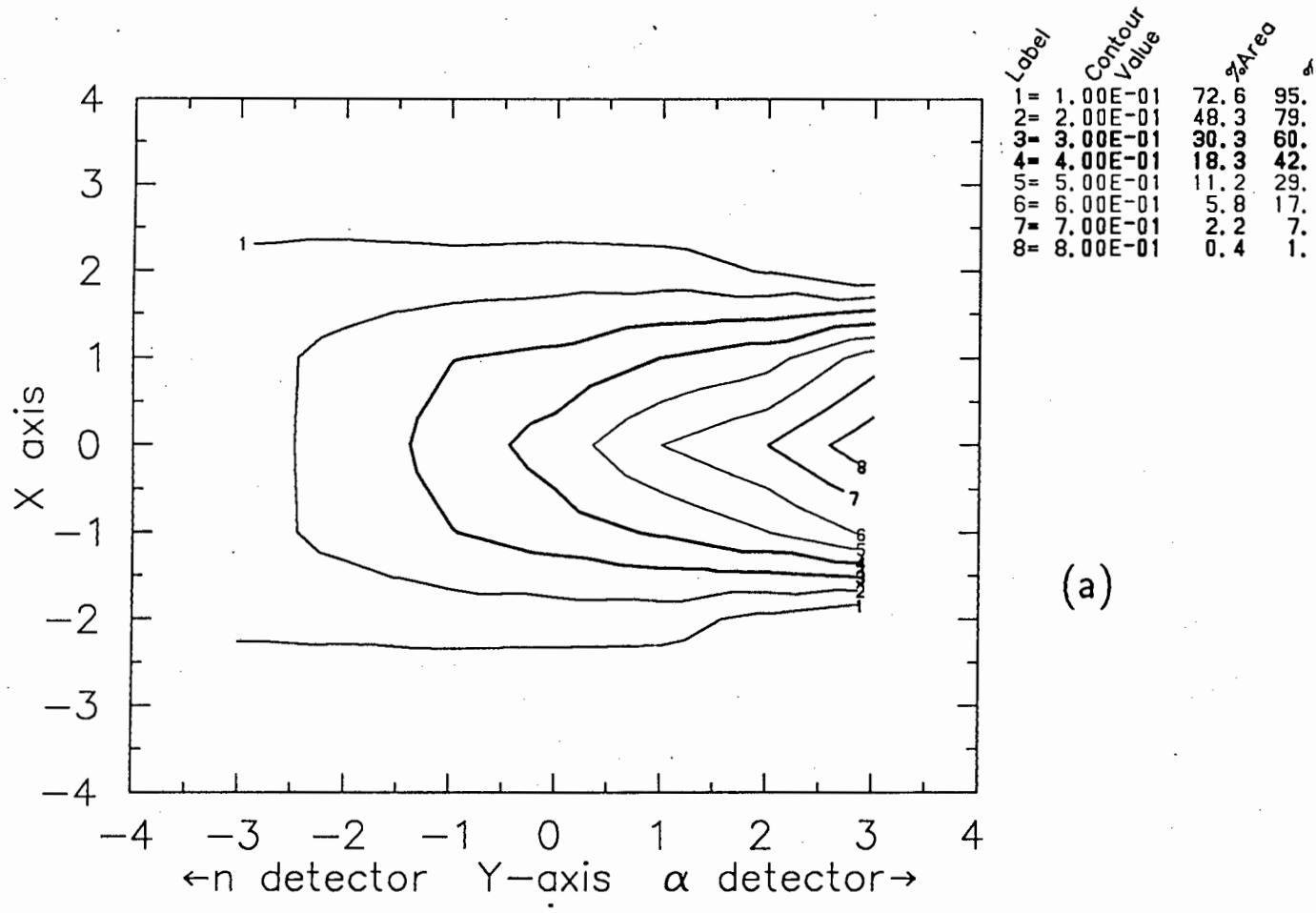

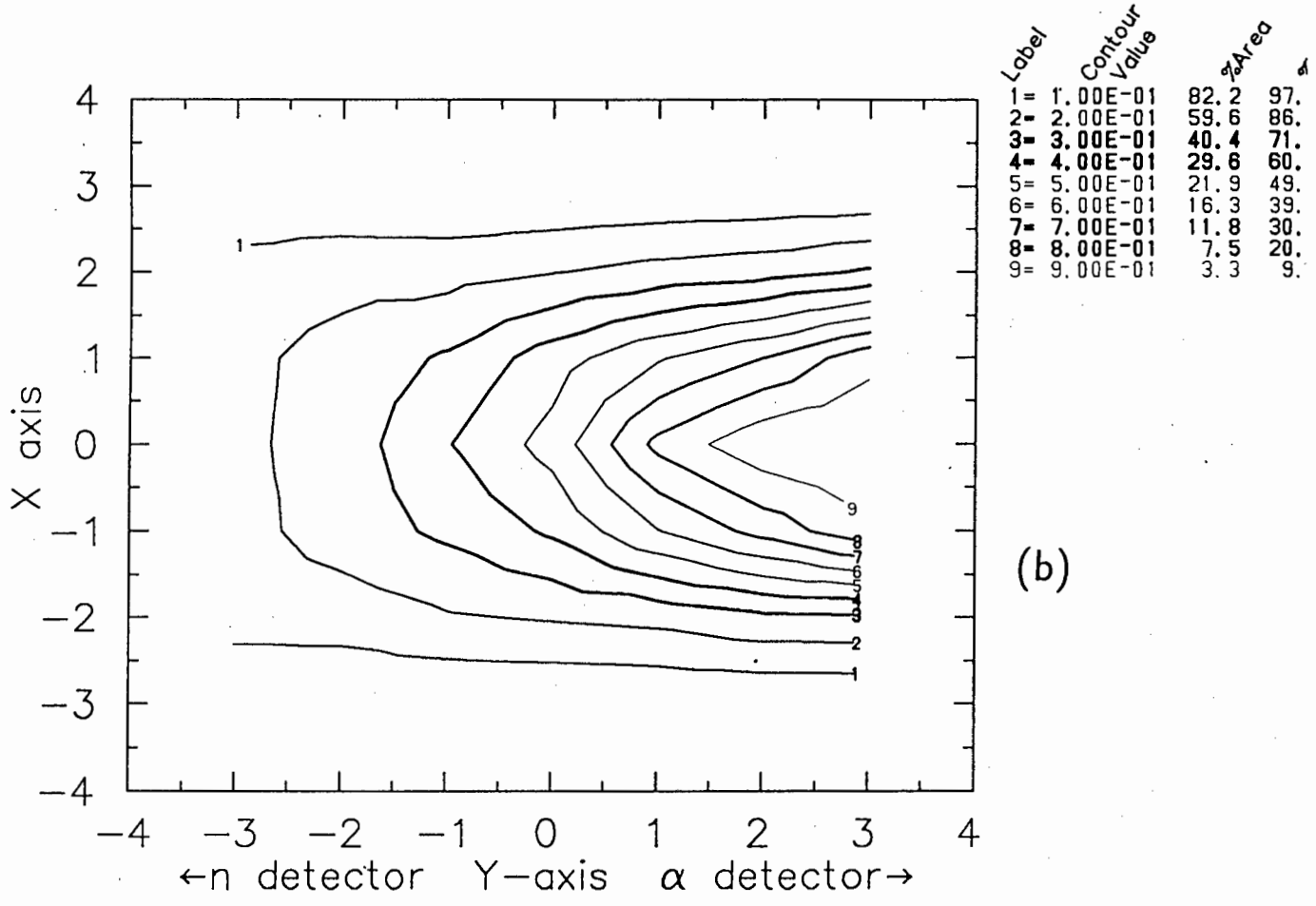

Figure 4.29: Contour plots of the b factor:(a) $b(x, y, -1)$ and (b) $b(x, y, 0)$ calculated using PAS equation 4.2 for neutron detector 1

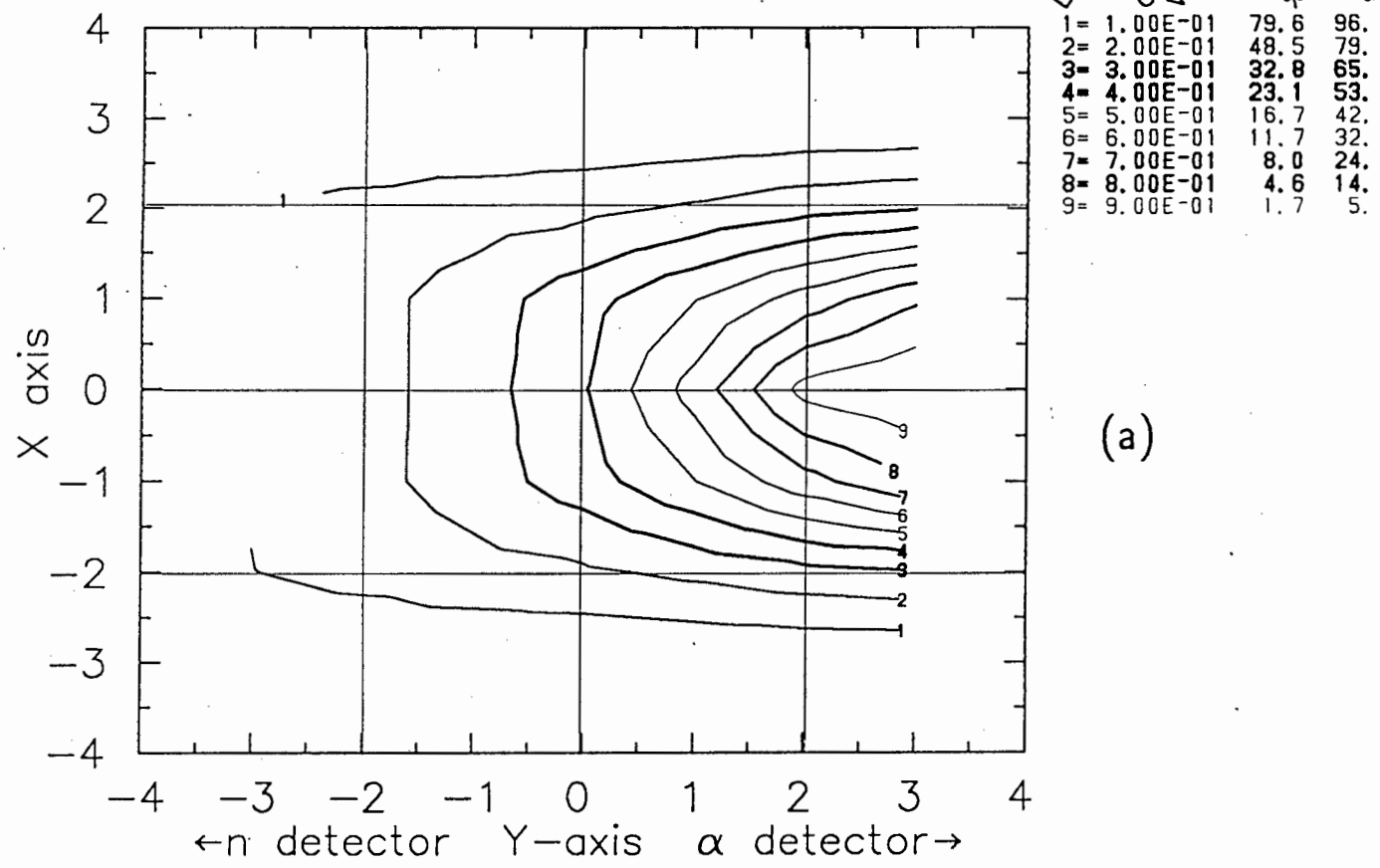

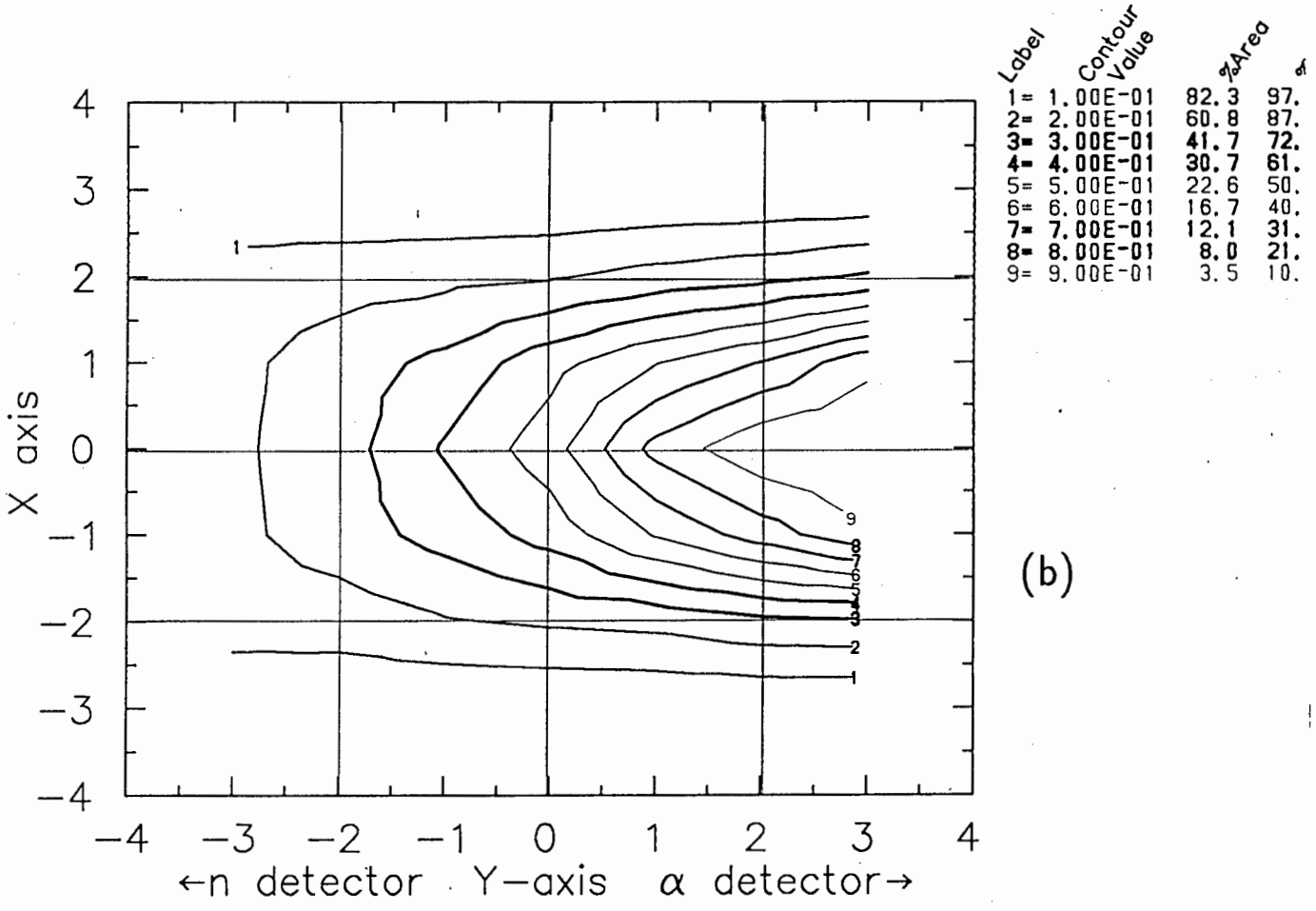

Figure 4.30: Contour plots of $b(x, y, 0)$ for neutron detector 1. Calculated (a) using the PAI approximation; and (b) using equation 4.2

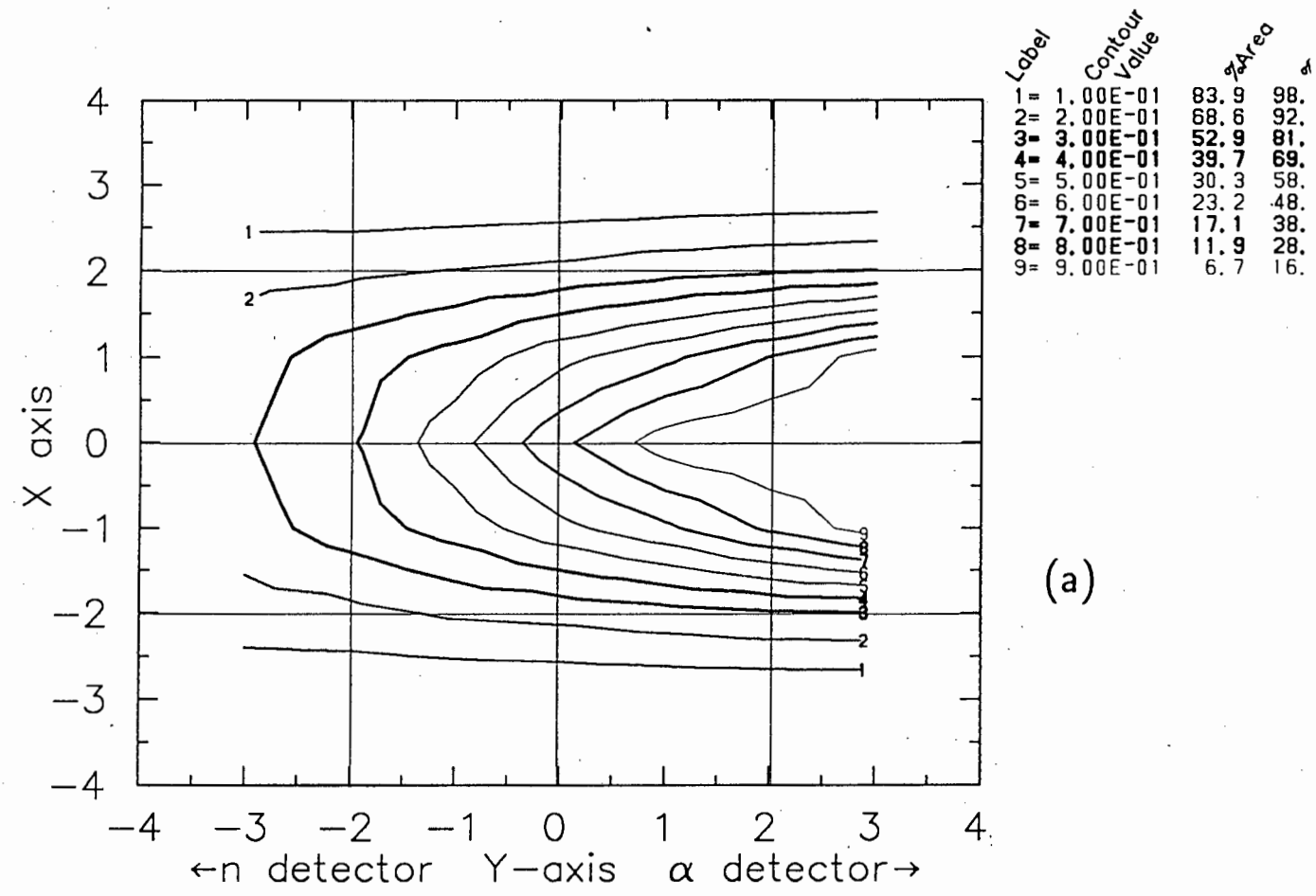

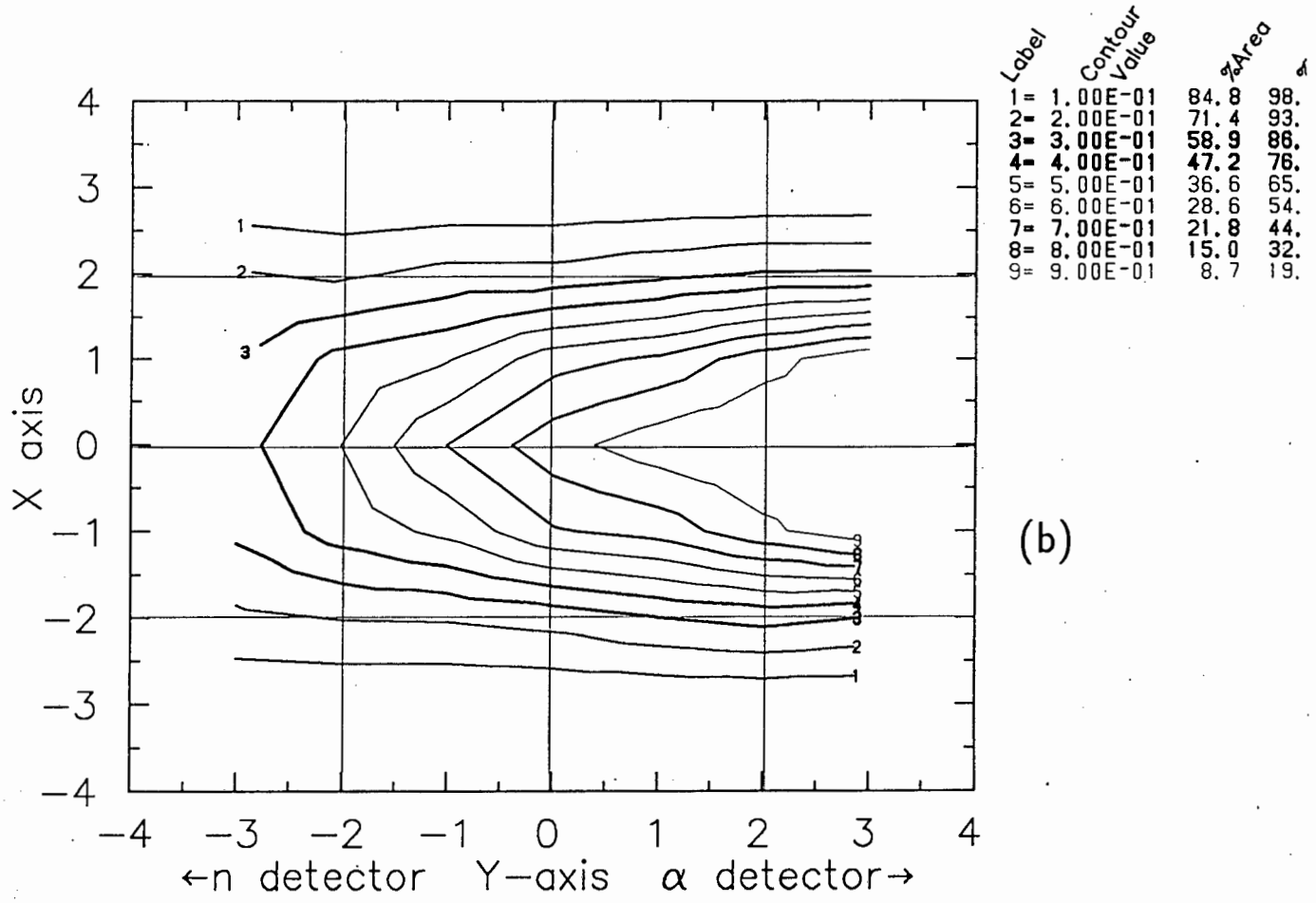

Figure 4.31: Contour plots of $b(x, y, 0)$ for neutron detector 2. (a) PAI approximation; and (b) PAS.

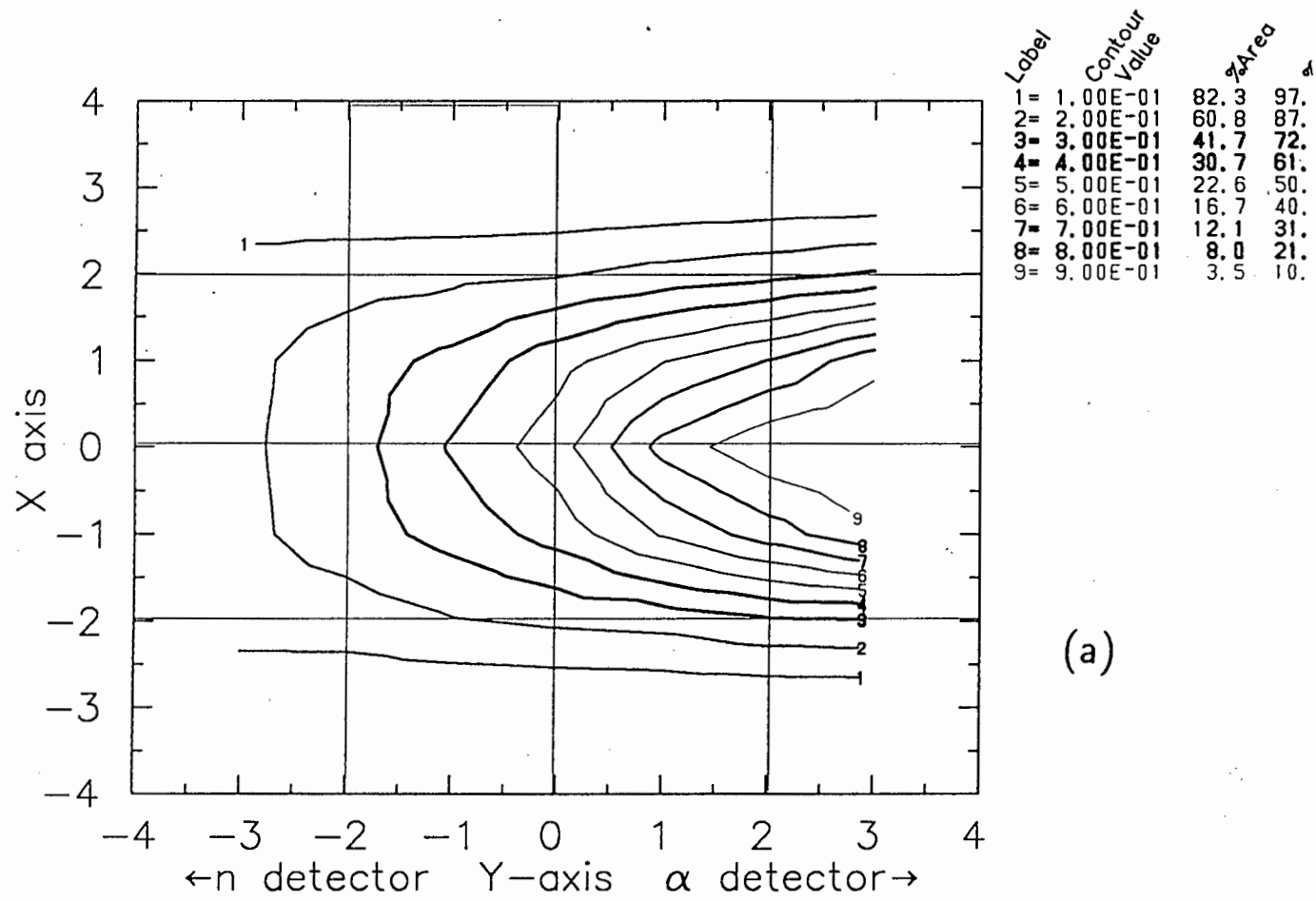

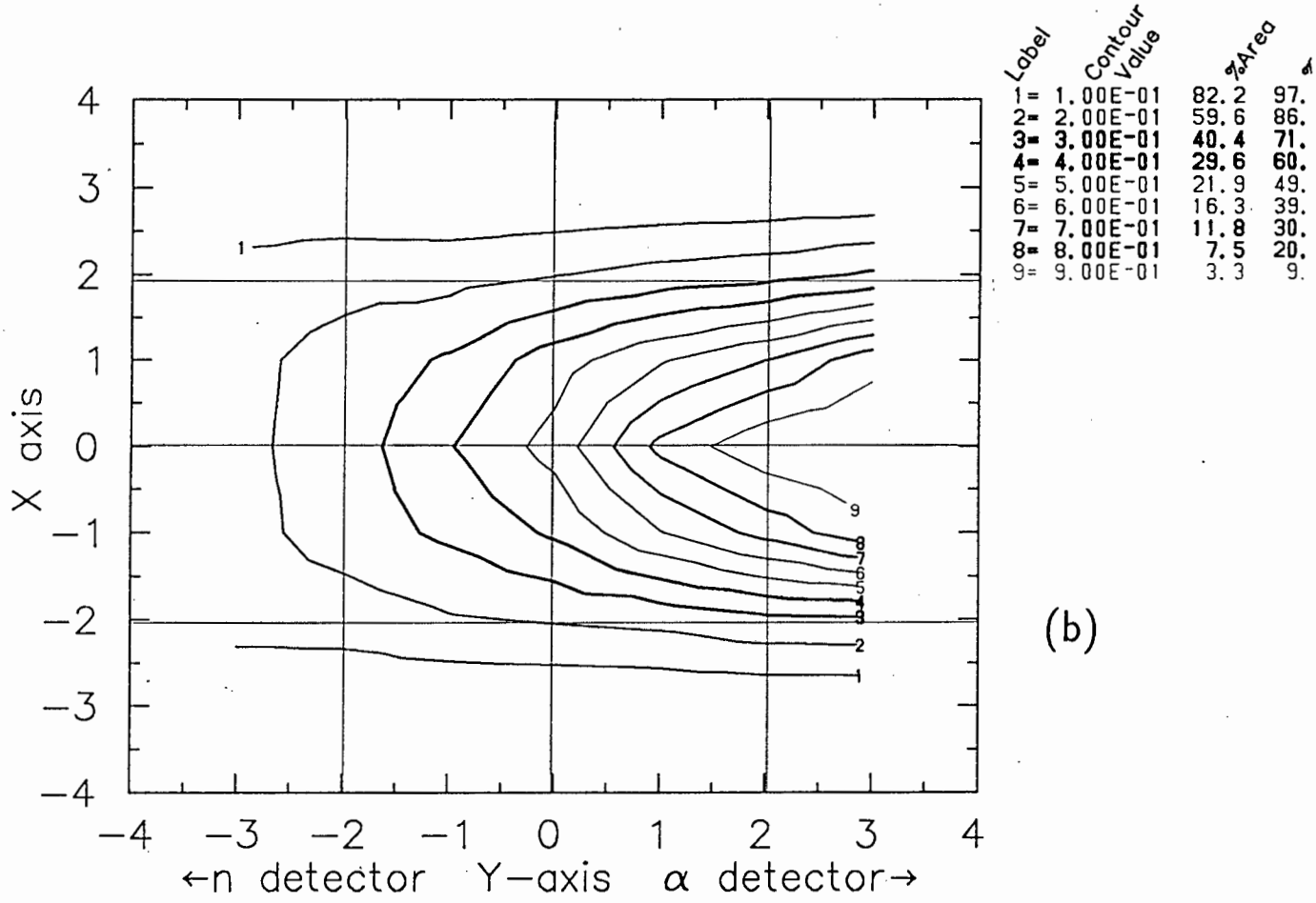

Figure 4.32: b factor contour plots for $z = 0$ for neutron detector 1. Comparison between detector 1 (a) unvetoed if both 1 and 2 fire and (b) vetoed if both fire.

Table 4.3: The dependence of B factors on fusion distribution and neutron detection. The equivalent B factors as reported in the preliminary measurements of the RAL experiment are 0.155 and 0.176 for D1 and D2 respectively [20].

Fusion distribution (σ)		PAI		PAS	
w_i (cm)	w_f (cm)	D1	D2	D1	D2
1	2.5	0.151	0.196	0.167	0.211
1	4	0.128	0.165	0.139	0.182
2	2	0.141	0.182	0.154	0.196
2	5	0.115	0.148	0.126	0.157
1.51	4.32	0.120	0.154	0.131	0.163

Note: the fusion distribution is characterised by a gaussian beam of initial FWHM w_i and final FWHM w_f

tion (equation 4.1). The ratios of the B factors calculated by MUGLU vary between 0.77 and 0.78 for various fusion distributions. Comparison of these ratios leads to the conclusion that the non-uniformity (PAS) in shielding[1] of D2 by D1 increases the B factor for D2 by about 10%.

3. It would seem that regarding the neutron detectors as uniformly efficient (PAI) in detecting neutrons will underestimate the B factors by about 8–11%, probably more in the case of detector 2.

To sum up, the B factors, in addition to being dependent on $\rho(\vec{r})$, are dependent on two further factors:

1. The geometry of the detection process in the finite volume of the neutron detector, and

2. The geometry of the shielding and scattering processes of neutrons before detection.

These last two items affect B by more than 10%.

The overall neutron detection efficiencies (zero threshold) remain fairly constant with spatial fusion distribution $\rho(\vec{r})$ and are 19.3 and 22.3 % for D1 and D2 respectively.

[1] the scattering of a neutron in D1 will not necessarily lead to its detection as the carbon elastic cross section is high and produces negligible light pulses.

4.3 Φ Factors

The $\phi(\vec{r}, E_{thr})$ factor is defined as the fraction of $\alpha\mu$ emitted from fusion site $\vec{r}$ in $\Omega_\alpha(\vec{r})$ striking the alpha detector* above threshold E_{thr}, and thus is a correction for the $\alpha\mu$ which would have reached the detector with sufficient energy had they not been stripped or ranged out in the gas.

Similar to B, $\Phi(E_{thr})$ can be expressed as an integral over the volume V of the target vessel:

$$\Phi(E_{thr}) = \int_V \phi(\vec{r}, E_{thr})\rho(\vec{r})d\vec{r} \tag{4.4}$$

In the RAL experiment, E_{thr} was set to 1.5 MeV alpha energy. This ensured that, given no tritium diffusion into the neck region, a negligible fraction of α were counted. It also ensured that all *unstripped* $\alpha\mu$ were above threshold. Most of the stripped $\alpha\mu$ fell below detector threshold. For the RAL June 1988 experiment, the percentage of $\alpha\mu$ stripped in the gas was calculated by Monte Carlo to be 5%, and 19% [92] were calculated to have stopped in the mylar windows. These calculations were revised slightly, giving a Φ factor of 0.84 [20].

The LAMPF values for stripping were 9.6 % for 6.4 cm gas at 640 torr and 4 % for 1.5 μm micron aluminised mylar window. [21]

The results for MUGLU agree with the above as far as α and unstripped $\alpha\mu$ are concerned. The percentage of $\alpha\mu$ stripped in the gas was calculated to be 9.6% while the stripping in the first mylar window[2] came to 3%. Between a third and a quarter of these stripped $\alpha\mu$ reached the detector above 1.5 MeV, giving a Φ factor of 0.9.

There is a large disparity between MUGLU and the RAL calculations, despite using the same same stripping calculations by Cohen [49]. There is good agreement between MUGLU and LAMPF. Reproduced in figure 4.33 is figure 5 from Cohen's paper. Highlighted in red is the surviving $\alpha\mu$ fraction curve vs distance for Be, which has similar stripping characteristics to mylar. The vertical line drawn in green on the figure is for foil thickness of 1.5 μm. Reading off the Be curve gives a surviving $\alpha\mu$ fraction of 0.97, or 3% stripping loss, which agrees with MUGLU calculations.

The curve for hydrogen is highlighted in blue. As it is for solid hydrogen, the distance (x) scale could not be used, but as $\alpha\mu$ lost on average 1.2 MeV in LRG type experiments, an estimate could be obtained from reading the

[2] the second mylar window was flush against the alpha detector and thus did not contribute to the Φ factor through stripping

* insert 'with energy'

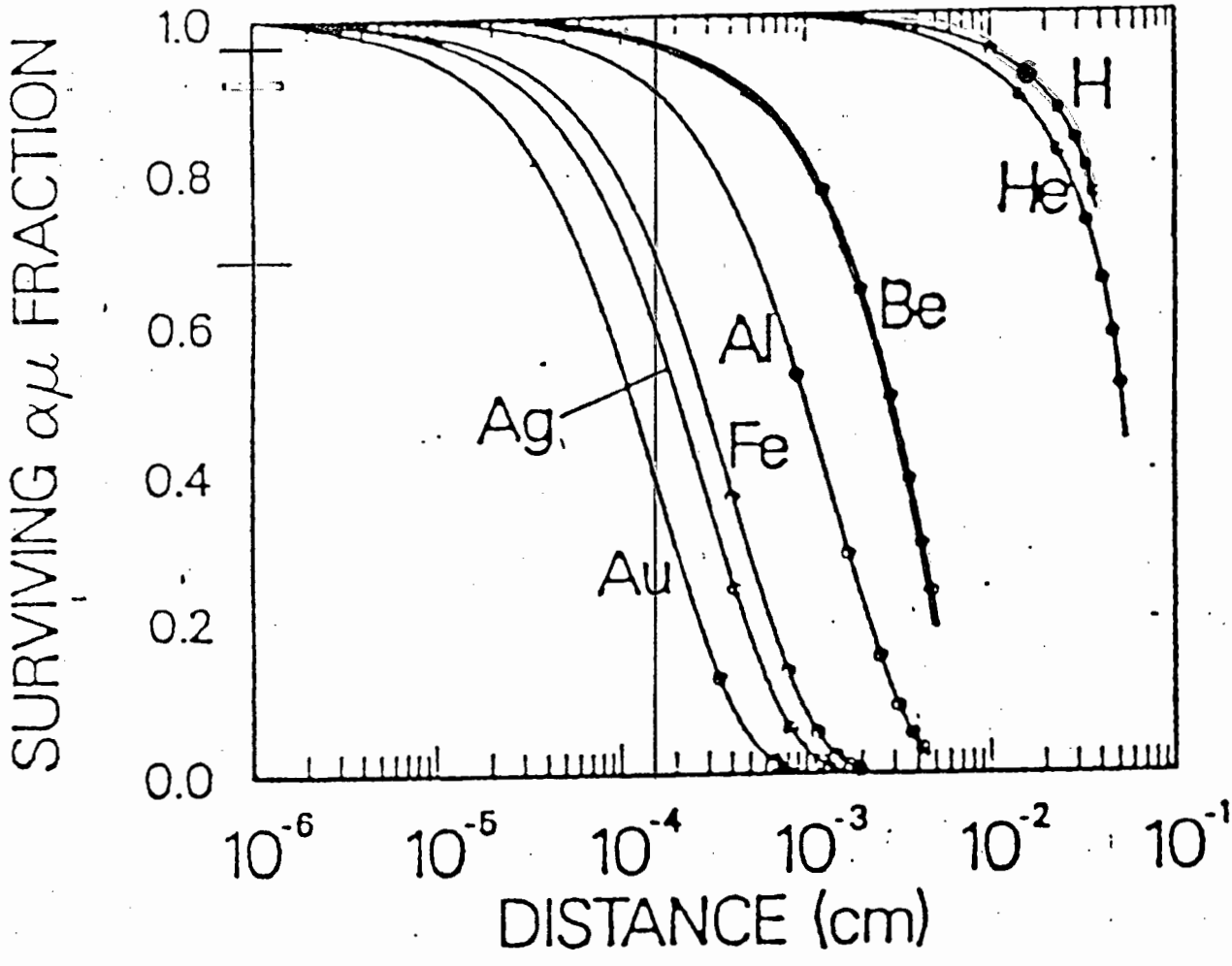

Reproduced from ref[49]

Figure 4.33: Surviving (unstripped) $\alpha\mu$ fraction as a function of depth in gold, silver, iron, aluminium, and beryllium foils, and in solid helium and hydrogen. The initial $\alpha\mu$ ion energy is 3.47 MeV; the circles on each curve show where the ion energy has been degraded to 3.0, 2.5, 2.0, 1.5, 1.0 and 0.5 MeV.

Table 4.4: The fraction of singles and coincidences per fusion for the three geometries calculated using the fusion distributions obtained from DEGRAD.

Events per fusion	Geometry A	Geometry B	Geometry C	LAMPF
Neutron singles $\times 10^{-2}$	1.57	1.54	4.78	1.31
$\alpha\mu$ singles $\times 10^{-4}$	3.4	4.1	5.0	3.6
n-$\alpha\mu$ coincs $\times 10^{-5}$	2.5	2.3	4.8	1.9

hydrogen curve at the 2.5 MeV spot (see caption to figure 4.33) marked in mauve. The surviving $\alpha\mu$ fraction is about 0.91. This again agrees with MUGLU. Finally the surviving $\alpha\mu$ fraction for Fe (0.63) agrees with MUGLU (0.65).

4.4 Detection rates

While MUGLU does not include the fraction of muons stopping in the gas, (DEGRAD can do this) or the fraction of fusions per stopped muon, they can calculate the fraction of coincidences and singles per fusion. Table 4.4 shows this ratio for the various geometries for two different fusion distributions. The efficiency of geometry A for detection of coincidences from fusion is not high (around 0.2 %), which is as expected, being the product of neutron detector efficiency ($\approx$ 20%) and solid angle subtended by the neutron and alpha detectors ($\approx$ 1% of 4π). The table is not meant as a comparison between the three geometries. The results give an estimate of the expected rates. Estimates from DEGRAD suggest that about 2% of the muons stop in the gas. Supposing that a stopped muon will give rise to a fusion about 15% of the time, we multiply the coincidence rate per fusion by 0.02, giving us about one detected α coincidence per two million incident muons, and about 300 neutron singles. An increase in rate could be achieved by using another pair of detectors, or moving the neutron detector closer, thus increasing the B factor.

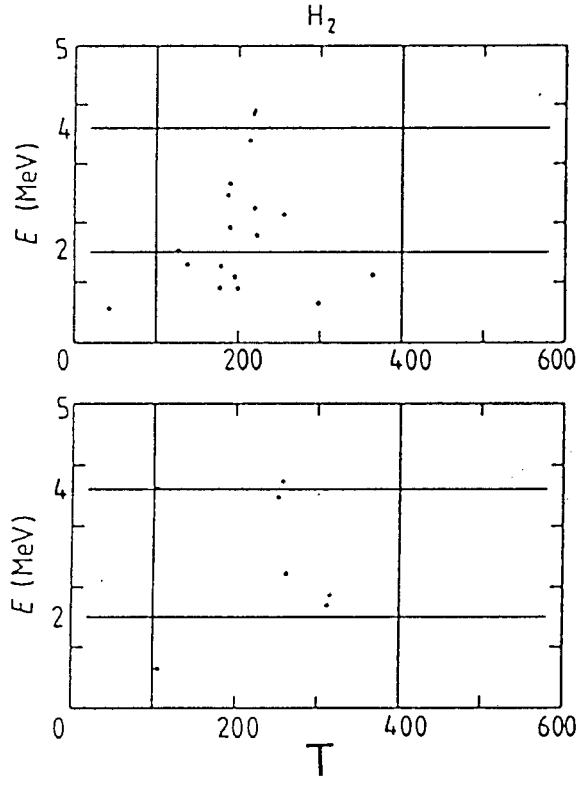

Figure 4.34: E–T signature for muons incident on pure H_2, measured at RAL in June 1988. Reproduced from reference [20]. The horizontal axis is time in nanoseconds. See appendix A, p 1534

4.5 Real Coincidence Background

Measurements of coincidences from muons impinging on a target of pure H_2 at RAL (figure 4.34) suggest a time correlated real coincidence background (RCB). This background has its most likely source in the production amid other particles of a charged-uncharged particle pair at the alpha detector. The charged particle is detected by the alpha detector while the uncharged particle (neutron) is detected by the neutron detector. The source of these particles could be a muon interacting weakly with the material fronting the alpha detector, or one of the aluminised mylar windows, or a neutron interacting first with the alpha detector and scattering into the neutron detector. Alternatively, a neutron could scatter in the neutron detector and then proceed to interact with the alpha detector. The latter scenario most unlikely. The neutron detectors are largely protected against charged particles.

RCB originating from the alpha detector would then produce events towards the left hand side of the E–T scatter plots (figure 4.35), in negative T, as the neutron is detected after the alpha. The energy deposited in the

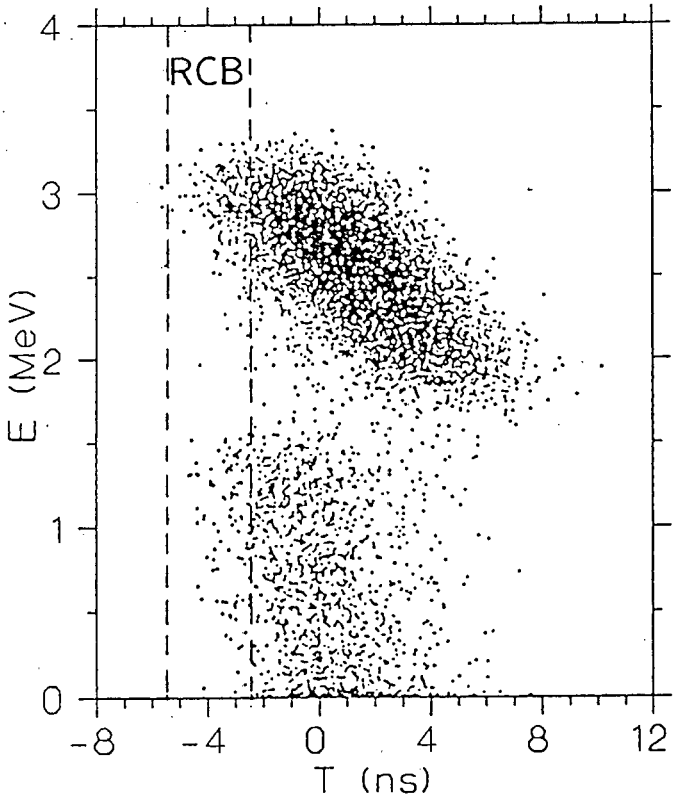

Figure 4.35: FWHM estimate of the extent of the RCB domain in an E–T plot for geometry A. The RCB originates at the alpha detector, and consists of 14 MeV neutrons. The time resolution is 2.7 ns FWHM, which is the distance in time between the vertical dashed lines.

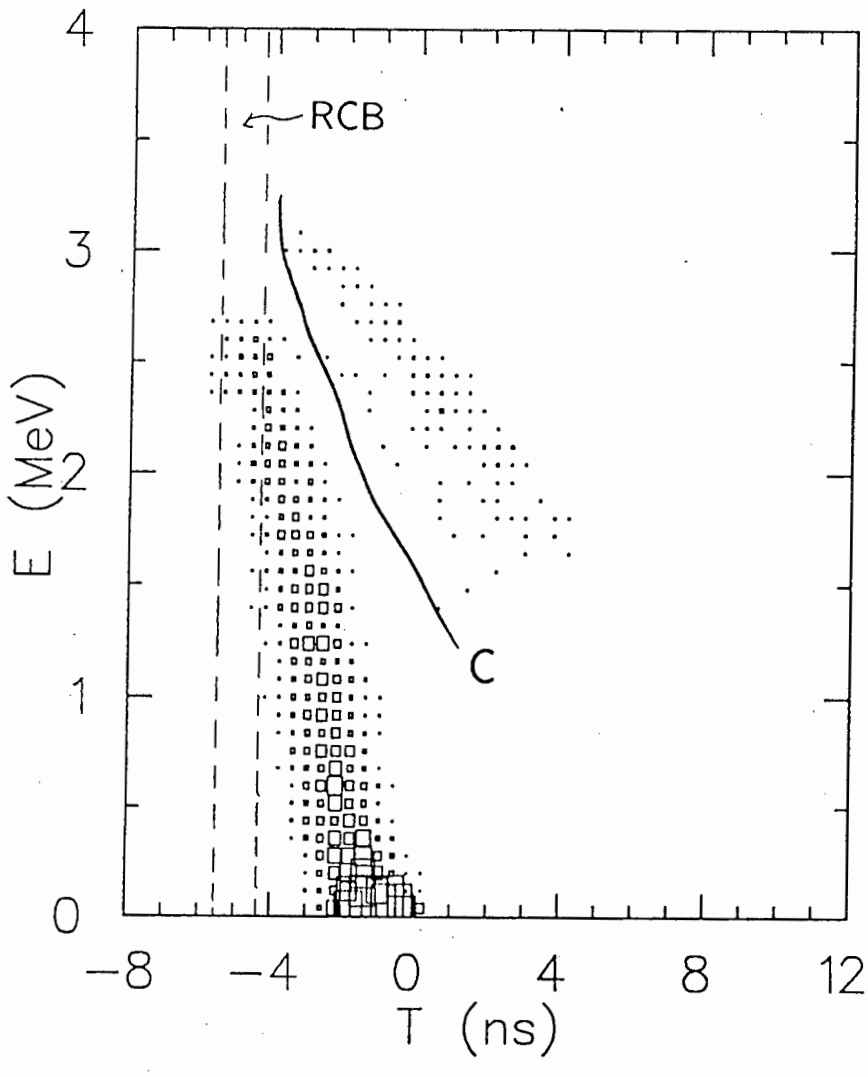

Figure 4.36: Estimate of the RCB domain for geometry B. The time resolution is 1 ns FWHM. A cut C should discriminate against RCB.

alpha detector will be largely independent of the neutron time travel. The RCB will thus form a vertical band, the width of which will depend partly on the energy spread of the neutrons, and partly on the time resolution of the system.

If the RCB signal is significant with regards the $\alpha\mu$ signal, then the time resolution of the system must be sufficient to cut it out. Figure 4.35 is an estimate of the extent of the RCB signal for geometry A, assuming the RCB neutrons have energies 10-15 MeV, and assuming that no RCB originates from the mylar window between the cube and the neck. A 30% improvement in time resolution should allow the RCB to be discriminated against.

Figure 4.36 shows the RCB estimate for geometry B. A time cut C will be necessary to exclude the RCB.

RCB can be reduced by, amongst other methods, making the alpha detector thin to reduce the probability of the higher energy charged particles interacting or covering all parts of the target box exposed to muons with high Z material.

Chapter 5

Conclusion

The simulations and T(d,n)α emulations set out to do the following:

1. To determine parameters essential for the analysis of the data for the LRG type of sticking experiment such as B and Φ.
2. To estimate and compare characteristics (such as signature) of existing and envisaged geometries.
3. To anticipate problems in the experiments e.g. RCB, and other applications, e.g. muon stripping measurements.

MUGLU has achieved these objectives in the following ways:

5.1 B and Φ factors

As far as the B and Φ factors are concerned, two important points come to light:

1. The fusion spatial distribution has a large effect on the experiment. This distribution will have to be precisely known. It could be determined either by computation (e.g DEGRAD), or by measurement during an experimental run using position sensitive neutron (light attenuation effects[1]) and alpha (segmentation) detectors and the neutron-alpha time difference. Either way, or perhaps both in conjuction, could

[1]The output from the paired photomultipliers at either end of the K detector can be compared. The nearer the interaction of a neutron to one end of the detector the greater the difference in pulses from the tubes at the two ends will be.

supply MUGLU with an accurate enough fusion distribution to calculate the B and Φ factors accurately.

2. The neutron detector efficiency varies significantly with position and angle of neutron incidence. This detection geometry effect together with non-uniform shielding reduces the B factors by an estimated 10% or more.

5.2 Features of the experiments

The simulations may be considered as having two aspects — neutron detection and coincidence measurements and signatures. The neutron detection simulation is consistent with the measured neutron detector response using the T(d,n)α reaction. The lineshapes and the absolute efficiencies for the simulations and measurements compare very well. The importance of the n-^{12}C reactions and the effect of geometry of detection, including shielding by other detectors, is shown.

For non-specialised use, neutron detector codes such as O5S and SCINFUL [60] are better in that they can be run for a wide range of incident neutron energies, and O5S [94] has proved to be in very good agreement with measured data for energies between zero and 20 MeV. Nevertheless, it is gratifying to note that an approach based on measured cross-sections and semi-empirical methods based on data measured independently can lead to a reasonably close correspondence with a measured lineshape, which is built up with several different interactions.

The alpha detector time resolution plays a large role in the E–T signature from the experiments. LAMPF/RAL experiments reported thus far have had relatively poor time resolution (FWHM $\geq$ 5 ns). Nevertheless it is known that a time resolution of less than a nanosecond is possible using e.g. segmented SBDs, or plastic scintillators. If we consider then a FWHM time resolution $\Delta T \leq$ 1ns for both n and α detectors, irrespective of the geometry, the main features differentiating the various geometries will be the energy resolution — poorer for plastic (geom C) — or the effects of fusions in the neck region, present in geometries B and C, but not (ideally) in A.

Geometry A (with $\Delta T \leq$ 1ns will look the best due to the absence of neck fusions — but in reality it seems unlikely that thin, self-supporting windows that are highly impermeable to tritium will be ever be available. The windows available for past RAL experiments present obvious problems

with unknown and changing fraction of fusions in the neck with diffusion of tritium into the neck, not to mention the fragility of the apparatus. Geometry B has the advantage of being more robust, and the barrier helps in the separation of $\alpha\mu$ from α. With the fusion spatial distribution used in this work, it appears that the neck fusions are not a problem, and can easily be removed using the same two dimensional cut in the E–T plane as used to select $\alpha\mu$.

The advantages of geometry C are both in the higher detection rates, and the simplicity, ruggedness and inexpensiveness of the plastic scintillator, which can be made into any shape or size. The time resolution of 1.2 ns required for extraction of the $\alpha\mu$ signal is readily obtainable. The separation of $\alpha\mu$ from α is possible, though the spread out nature of the $\alpha\mu$ signal could cause the signal to background ratio under the $\alpha\mu$ cluster to drop to unacceptable levels. Possibilities for $\alpha\mu$ stripping measurements arise.

The effects of RCB is speculative, and with RCB events originating near the alpha detector it would seem that, for geometry A at least they are easily shut out. Geometry B requires a time resolution of a nanosecond or better to reduce the effect of RCB on the signature sufficiently for its rejection.

Stripping measurements would appear feasible, given negligible RCB and good enough statistics, using geometry C.

This work presents a sample of the simulations possible with MUGLU. There is much scope for enhancing the accuracy and intricacy of the simulations. Given the necessary input to describe the conditions of the experiment (such as the structure of the muon beam) and characteristics of the equipment, it seems quite feasible to simulate sticking experiments reliably.

J. Phys. G: Nucl. Part. Phys. 16 (1990) 1529–1537.

Appendix A
Reproduction of J. Phys. G. 16 (1990) 1529-1537

A direct measurement of the alpha–muon sticking coefficient in muon-catalysed d–t fusion

J D Davies†, J B A England†, G J Pyle†, G T A Squier†, F D Brooks†, W A Cilliers†, A Bertin‡, M Bruschi‡, M Piccinini‡, A Vitale‡, A Zoccoli‡, S E Jones§, V R Bom||, C W E van Eijk||, H de Haan||, A N Anderson¶, M A Paciotti+, G H Eaton$ and B Alper*

† School of Physics and Space Research, University of Birmingham B15 2TT, UK
‡ Dipartimento di Fisica dell'Universitá, and Istituto Nazionale di Fisica Nucleare, Sezione di Bologna, Italy
§ Brigham Young University, Utah, USA
|| Delft University of Technology, The Netherlands
¶ Idaho Research, Boise, Idaho, USA
+ Los Alamos National Laboratory, Los Alamos, New Mexico, USA
$ Rutherford Appleton Laboratory, UK
* UKAEA, Culham, UK

Received 21 May 1990

Abstract. A direct method of determining the alpha–muon sticking coefficient ω_0 following muon-catalysed d–t fusion, by measuring the ratio of $(\alpha\mu)$–neutron coincidences to neutron singles, is described. Initial measurements have used a low-pressure D–T gas target and the pulsed muon beam at the ISIS facility of the Rutherford Appleton Laboratory and give a preliminary result of $\omega_0 = 0.0069 \pm 0.0040 \pm 0.0014$(sys).

1. Introduction

Negatively charged muons catalyse d–t fusion via the resonant formation of a muonic molecule in which the $dt\mu$ positive ion replaces a deuterium nucleus in the D_2 molecule. The fusion reaction $d + t \rightarrow \alpha(3.5\,\text{MeV}) + n(14.1\,\text{MeV})$ occurs rapidly by barrier penetration and the muon is generally released and so can catalyse further fusions during its 2.2 μs lifetime. However, there is a small probability ω_0 that the muon will be captured by the alpha particle produced in the fusion and, unless it is detached during the slowing down of the $(\alpha\mu)^+$ ion (i.e. reactivated), it will be removed from the catalysis cycle. The effective sticking coefficient ω is thus less than ω_0 and can be written

$$\omega = \omega_0(1 - R) \tag{1}$$

where R is the muon reactivation coefficient, which is obtained by integrating the muon stripping probability over the whole $\alpha\mu$ range. The sticking coefficient ω_0 is a basic observable in the theoretical description [1–4] of muon-catalysed fusion. Ultimately the number of fusions per muon is limited to ω^{-1}, thus accurate measures of ω_0 and R are important in assessing future possibilities of economical energy generation by this process.

0954-3899/90/101529 + 09 $03.50 © 1990 IOP Publishing Ltd

Theory gives $\omega_0 = 0.0089$–0.0093 [5, 6] and $R = 0.37$ [7] at liquid D–T densities, ρ_l, with only a small density dependence for ω via R, e.g. $R = 0.30$ at $0.1\rho_l$. Experimental measurements agree around $\omega = 0.0041$ for ρ_l [8–13], which is about six standard deviations less than theory, but vary between 0.005 ± 0.001 [9, 11] and 0.010 [8] at low densities; this allows the possibility of a large density dependence and even lower values of ω. These measurements are indirect and observe either the time evolution of the fusion neutrons or the K_α line from muonic helium using liquid targets [10, 13]. For the former ω is one of several parameters determined simultaneously from the analysis and represents a small loss term at long times; there is considerable controversy about the large corrections which increase in significance as the density is reduced. Obtaining ω from muonic x-ray measurements depends on untested cascade calculations. The present experiment [14], and an associated experiment [15] at the LAMPF facility of the Los Alamos National Laboratory (LANL), aim to determine ω_0 directly, in low-density conditions, from measurements of $\alpha\mu$–n coincidences. In the LANL experiment the coincidence rate is measured using D–T gas targets at two different pressures. At the higher pressure (1800 Torr) only $\alpha\mu$, being singly charged, can make coincidences, whereas α, being doubly charged, are ranged out in the D–T gas and the target windows, before they can reach the α detector. At the lower pressure (490 Torr) α as well as $\alpha\mu$ can make coincidences. The sticking coefficient may be calculated from the ratio of the coincidence rates provided the ratio of fusion rates at the two pressures is known.

The present work follows a different approach, exploiting the characteristics of the pulsed muon beam [14, 16, 17] of the ISIS facility at the Rutherford Appleton Laboratory (RAL) to obtain low backgrounds, thus allowing measurements of single neutron events from low-density D–T targets. A single set of measurements is made using a D–T target at a pressure of 1509 Torr and selecting only $\alpha\mu$–n events in the coincidence measurement. The ratio of these coincidences to the neutron singles, which originate from all fusions, is measured. This ratio is proportional to the sticking coefficient ω_0 and the constant of proportionality is simply the probability that a collinear $\alpha\mu$ associated with a detected fusion neutron reaches the α detector and is registered. For gas densities such that the $\alpha\mu$ have sufficient range to reach the detector, the probability factor is determined by geometrical considerations and in-flight stripping and may be estimated to better than 10% from Monte Carlo calculations. The sticking coefficient ω_0 is thus determined directly from the experimental measurement of the coincidence-to-singles ratio.

We report here on the characteristics and performance of this new direct method for determining the alpha–muon sticking coefficient and present a preliminary result obtained by this technique.

2. Experimental details

The experiment used a pulsed beam of negative muons having a small spot size, momentum 40 MeV/c and $\Delta p/p \simeq 5\%$, provided by the cloud muon facility [16, 17] associated with the ISIS proton synchrotron at RAL. Figure 1 shows the gas target together with the three NE213 liquid scintillators employed for neutron detection and the surface barrier detector (SBD) used to detect $\alpha\mu$. The silver target cell (a cube of side 70 mm) contained a D–T mixture at a pressure of 1509 Torr. The cell was housed in a substantial aluminium vessel containing D_2 gas at the same pressure

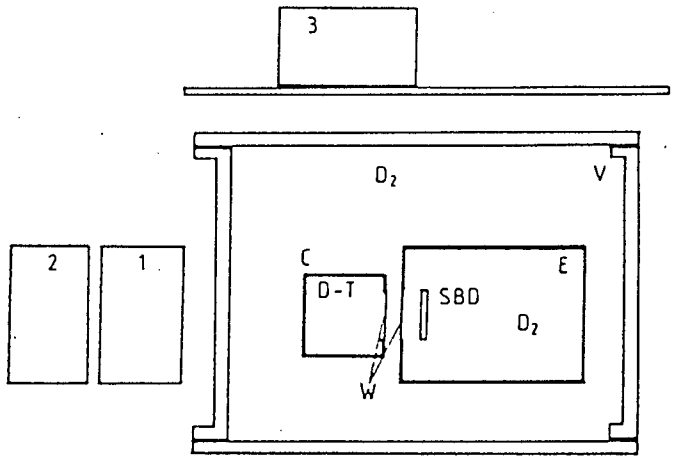

Figure 1. Experimental arrangement (schematic) viewed looking downstream along the muon beam, showing: silver target cell C containing D–T mixture; aluminised Mylar windows W; surface barrier detector SBD; and NE213 scintillation detectors 1–3. The enclosure E and the outer vessel V were filled with D_2 gas at the same pressure as the target.

as the cell and separated from the D–T mixture by an aluminised Mylar window (thickness 1.5 μm Mylar + 0.08 μm Al) to permit $\alpha\mu$ to exit to the SBD. The SBD, area 1000 mm^2 and only 50 μm thick (to reduce background), was enclosed in its own D_2 environment, at the same pressure and with an identical entrance window for the $\alpha\mu$. As in the LAMPF experiment [15], this dual window arrangement was designed to protect the SBD against the formidable tritium beta activity (750 Ci) present in the target cell. The arrangement ensured that tritium diffusing through the first window was diluted in the large outer D_2 volume adjoining the inter-window region, thereby reducing the rate of tritium diffusion through the second window, to the SBD. Diffusion through the first window reduced the tritium fraction in the target cell from its initial value of 45% to 38% over the period of the measurements (2 d).

The three NE213 detectors (figure 1), each 13 × 13 cm in area and 7 cm thick, used pulse shape to discriminate against gammas. Detectors 1 and 2 were placed so that either, in conjunction with the SBD, could register collinear $\alpha\mu$–n coincidences. Detector 3, by registering orthogonal coincidences, provided a measure of the coincidence background. The muon beam incident on the target was monitored by integrating a time-gated signal from a plastic scintillator 0.05 mm thick in transmission geometry, close to the entrance window of the target cell.

The incident muon beam entered the target cell normal to the plane of figure 1. At the target pressure used, about 1% of the muons stopped in the target gas, the rest stopping in the walls of the silver target cell. The muon lifetime in silver is reduced from 2200 ns to 90 ns by weak interaction processes. Thus, by delaying the start of data taking until 500 ns after the beam pulse, the effects of prompt background from muon interactions in the silver were greatly reduced. This delay also reduced the effects of high-energy background from the ISIS beam dump and the muon production target in the proton beam. The inside of the aluminium containment vessel was lined with lead to capture (rapidly) stray scattered muons and the entire detector system was shielded with lead and polythene (not shown in figure 1).

Signals from the scintillation detectors were processed in Link Systems pulse

shape discriminators (Models 5010 or 5020); these had been modified to allow the processing circuitry to be inhibited until a preset time (0.5 μs) after the second muon pulse in the ISIS beam time structure [17] and to provide an output signal F proportional to the fast scintillation component from NE213, as well as the standard signal L, which is proportional to the total light output. Signals from the SBD were processed using a conventional charge-sensitive preamplifier and slow amplifier system and the relative timing T_c between coincident NE213 and SBD signals was obtained via a TAC. The SBD timing signals were derived using crossover timing because preliminary attempts to use a fast voltage-sensitive preamplifier in the timing circuit revealed a poor signal-to-noise ratio of 3:1, due to the large capacitance (2200 pF) of the detector. A signal from any NE213 detector within the time window 0.5–7.5 μs after arrival of the second muon pulse and satisfying the condition $L > L'$, where L' is the pulse height corresponding to a 2 MeV proton, was defined as an event. The pulse heights L and F from the three NE213 detectors were recorded on tape or disc for all events, together with the event time T_μ relative to the second muon pulse, which was measured using a second TAC. The pulse height from the SBD and the output T_c from the associated TAC were also recorded, together with the L, F and T_μ outputs, for SBD–NE213 coincidences. The following constraints were applied in the off-line analysis of all events, including both coincidences and singles: (i) events in which more than one of the NE213 detectors responded were rejected; (ii) pulse shape discrimination based on comparison of the L and F outputs of the NE213 detectors was implemented so as to select neutron events and reject gamma events; and (iii) an event time cut of $T_\mu = 1$–7.5 μs was imposed, to discriminate against a background component showing a decay constant of 0.9 μs and attributed to muon capture in the aluminium beam pipe. Additional constraints, described below, were applied in the analysis of the coincidence events.

In addition to the runs made using the D–T target, a second, nominally identical SBD and target system filled with H_2 gas was used to determine backgrounds. Some additional runs were also made with the D–T target at lower pressures (710 and 490 Torr) to check the performance of the coincidence system under conditions in which α–n as well as $\alpha\mu$–n coincidences could be detected. After checking consistency between runs made under the same conditions, the raw data were summed to form single D–T (1509 Torr) and single H_2 runs for each of the three NE213 detectors. Figure 2 shows the pulse height spectra obtained from the three NE213 detectors for these summed runs. The background spectra measured using the H_2 target and shown by circles were measured for a smaller number of incident muons than the spectra measured using the D–T target (histograms) and have been multiplied by a factor of 1.96. This factor was determined by referring to the number of neutrons recorded at short event times, $T_\mu \leqslant 0.7$ μs, at which background dominates strongly, so that the number of neutrons in the normalised background run should approach closely to that in the D–T run. Recoil protons (0–14 MeV) from the d–t fusion neutrons can be identified clearly above background in the spectra from all three detectors in figure 2.

The off-line analysis of the neutron–SBD coincidence data included a further cut, applied to the L outputs of the NE213 detectors to select pulse heights in the range corresponding to recoil proton energies of 2.4–15 MeV. Figure 3 shows plots of $\alpha\mu$ energy against coincidence time delay for these data, presenting the H_2 background runs and the D–T runs in the left and right panels respectively. The coincidence data obtained using the D–T target (figure 3), if projected onto the T_c axis, show a

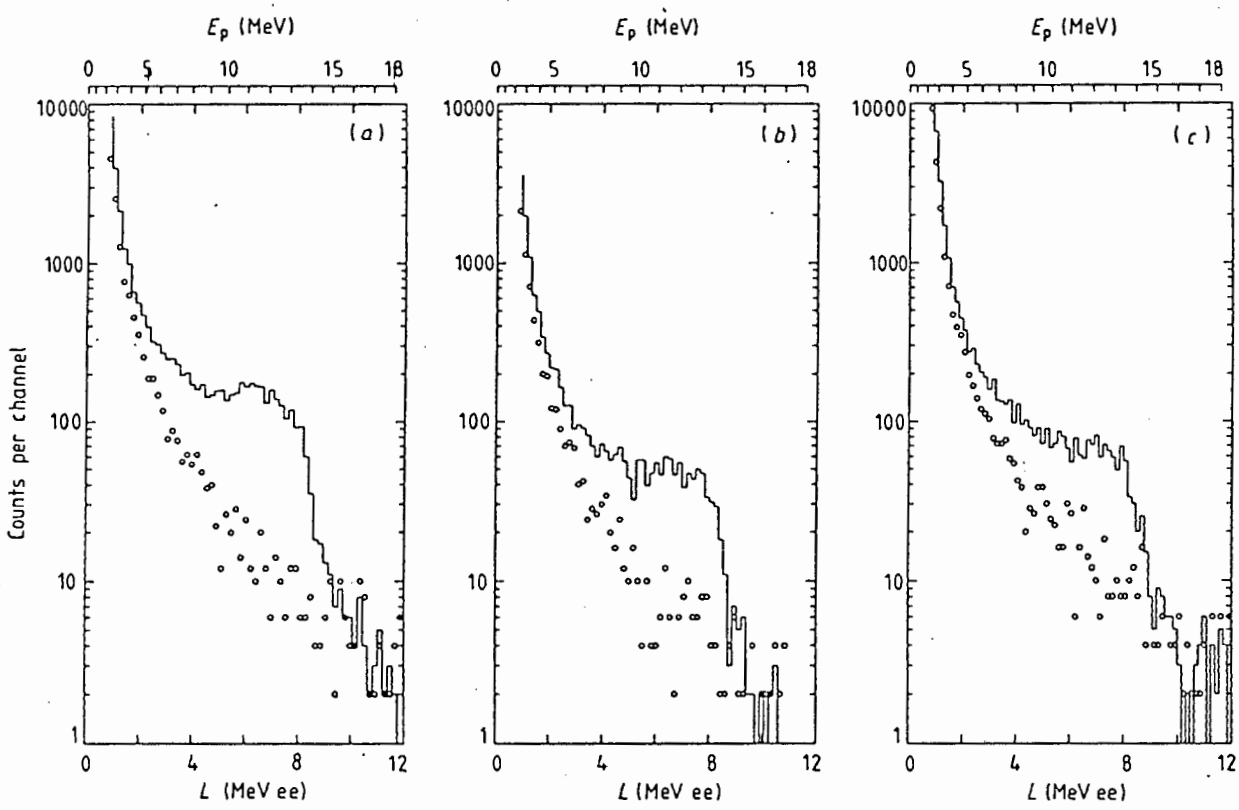

Figure 2. Pulse height spectra obtained from detectors 1–3 ((*a*)–(*c*) respectively) for muons incident on the D–T target (histograms) and the H_2 target (circles). The H_2 spectra have been normalised as described in the text. The pulse height scales, L, are calibrated in units of MeV ee (MeV electron equivalent), that is units which represent the electron energy required to give the pulse height indicated. The corresponding proton energies are shown above.

peak of FWHM about 28 ns at $T_c = 138$ ns, with a low intensity tail stretching out to about $T_c = 350$ ns. Better timing resolution (FWHM = 12 ns) was observed in tests made using a ^{252}Cf spontaneous fission source. The timing degradation under beam conditions was investigated and it appeared to be a result of slight baseline fluctuations in the output from the SBD to the crossover timing, coming from the very many small (and occasional large) SBD signals at beam arrival time ($T_\mu \leqslant 0$). A generous time window of $T_c = 50$–350 ns (figure 3) was used to select $\alpha\mu$–n coincidences from the D–T runs, in order to ensure that events in the wings of the coincidence peak were not lost. The corresponding time window for runs taken with the H_2 target was $T_c = 100$–400 ns, the shift of 50 ns being introduced to compensate for variations in the crossover timing characteristics of the different SBDs used with the H_2 and D–T targets respectively.

The energy window used on the SBDs to select $\alpha\mu$–n coincidences was set at 1.5–3.6 MeV (figure 3), the threshold of 1.5 MeV being chosen so as to exclude the small number of detected α–n coincidences produced by fusions in the region close to the exit window of the D–T target. Monte Carlo simulations show that the α from these fusions are not ranged out by the windows and the intermediate D_2 gas, and may reach the SBD with energies up to about 1 MeV, thus contributing to the events which are observed in this region of figure 3. The $\alpha\mu$ reaching the SBD have energies between 1 and 3 MeV, depending on their point of origin within the D–T target cell and whether the muon is stripped from the alpha in the gas or Mylar windows, en route to the detector. The fraction φ of the $\alpha\mu$ directed towards the SBD which reaches the SBD with energy exceeding 1.5 MeV was estimated from

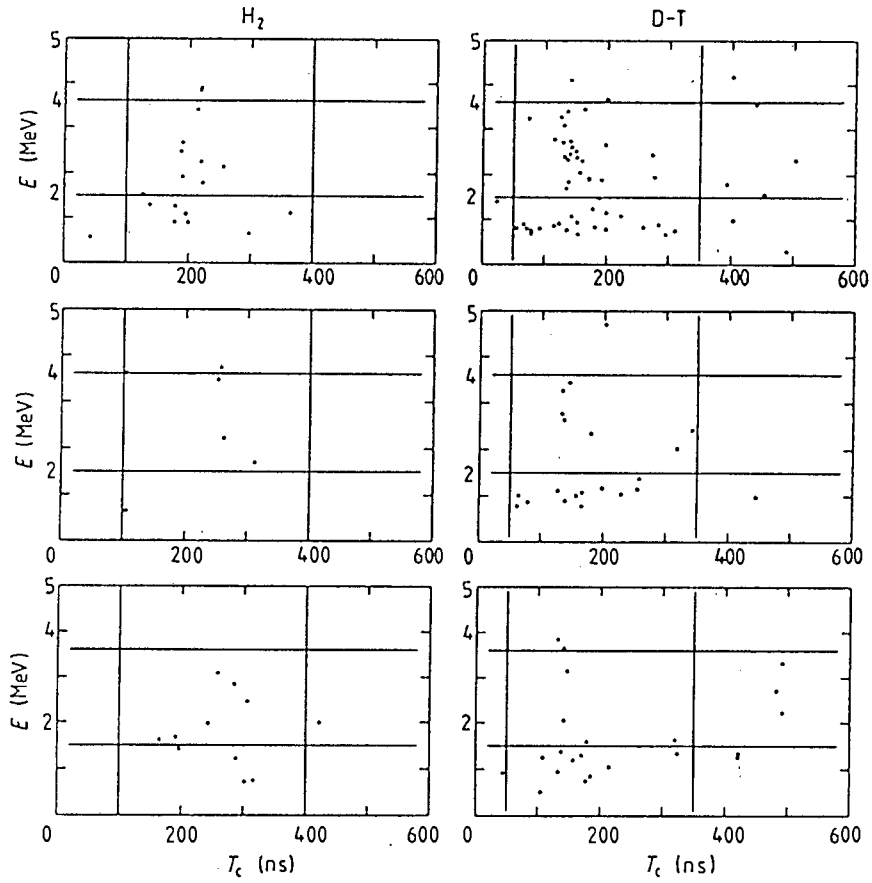

Figure 3. Coincidence events as function of $\alpha\mu$ energy E and coincidence time difference T_c. Panels top-to-bottom show data from detectors 1–3, left panels obtained using the H_2 target and right panels the D–T target. The lines within the panels show the cuts imposed on T_c and E in the analysis leading to the coincidence data in table 1. The number of incident muons for the H_2 data was estimated to be about half that for the D–T data.

Monte Carlo simulations based on the stripping calculations of Cohen [18] and was found to be $\varphi = 0.84$ for the conditions of this experiment.

The data obtained from detector 1 using the H_2 target show a concentration of events (figure 3) at times $T_c = 200 \pm 30$ ns, indicating that a significant fraction of these events are real coincidences rather than accidental coincidences. The data from detectors 2 and 3, H_2 target, show lower coincidence rates and no evidence of concentration at $T_c \approx 200$ ns. These features, together with the fact that detector 1 was closer to, and less shielded from, the muon beam (figure 1) than detectors 2 and 3, suggest that the real coincidence component from detector 1 is beam-associated. The real coincidences may be due, indirectly, to muons which find their way into light elements (H, C or Al) in, or close to, the beam and thus survive, as muonic atoms or muo-molecules, to event times $T_\mu > 1\ \mu$s, before being captured by nuclei. Energetic charged particles and neutrons emitted in coincidence from the ensuing nuclear interactions could be responsible for the real coincidence component, which would thus also be present as a real coincidence background (RCB) in the data taken using the D–T target.

The levels of RCB present in the D–T coincidence data from detectors 1 and 2 were estimated in two ways: (i) from the measurements made using the H_2 target; and (ii) from the coincidences recorded by detector 3 for the D–T target. The

Table 1. Numbers of coincidences and neutron singles.

		Coincidences			
Detector	Singles, N_n	Raw	RCB	Accidental	N_c
1	8417 ± 157	24	11	4	9 ± 6
2	4291 ± 121	7	4	0	3 ± 3

orthogonal geometry of detector 3 with respect to the SBD implies that all such coincidences should be attributed to background and the time distribution of the D–T data from this detector (figure 3) shows further evidence of the RCB component. Method (i), after normalising the H_2 data by a factor of two, as used for the singles spectra (figure 2), indicated RCB levels of 16 and 6 events for detectors 1 and 2 respectively. Method (ii), assuming an isotropic distribution of the RCB and normalising by the ratios (1.23 and 0.62) of the singles neutron rates of detectors 1 and 2 to that of detector 3, indicated levels of 5 and 2 events for the two detectors. Since fusion competes with the suggested RCB mechanism, for muons surviving beyond 1 μs, we expect a lower RCB rate per muon in the D–T target than in the H_2 target, and hence that method (i) will overestimate the RCB. Method (ii), in contrast, may be expected to underestimate the RCB, since this background, by its nature, is likely to contain fewer orthogonal coincidences than collinear coincidences. The averages of the values obtained from methods (i) and (ii) have therefore been used, giving RCB levels of 11 and 4 events for detectors 1 and 2 respectively, as shown in table 1.

The numbers of accidental coincidences shown in table 1 were estimated from the numbers of events within the E window but outside the T_c windows in figure 3. The increased accidental coincidence rate seen with the D–T target as compared with the H_2 target (figure 3) can be attributed to the significantly higher (fusion) neutron rate associated with the D–T target (figure 2). The numbers of single events shown in the table were estimated by integrating the spectra of figure 2 (corrected for background) between the same pulse height limits (corresponding to $E_p = 2.4$–15 MeV) as applied in the coincidence analysis.

3. Results and discussion

The number N_n of singles neutrons registered by an NE213 detector, for N_0 d–t fusions in the target, may be written

$$N_n = \varepsilon N_0 \tag{2}$$

where ε is the relevant detection efficiency of the neutron detector.

Assuming that all α–n coincidences are excluded by the SBD energy window (figure 3), the number N_c of real fusion coincidences registered between this neutron detector and the SBD is given by

$$N_c = \varepsilon \omega_0 \varphi B N_0 \tag{3}$$

where the factor B represents the probability that the extrapolated geometric path of a collinear $\alpha\mu$ associated with a detected fusion neutron intersects the SBD and φ represents the fraction of these particles which reach the detector with energy

greater than the threshold (1.5 MeV). The product φB may be estimated to better than 10% from Monte Carlo calculations. The sticking coefficient ω_0 is thus, from equations (2) and (3), given by

$$\omega_0 = N_c/\varphi B N_n \tag{4}$$

and is thus obtained directly from the measurements N_c and N_n.

Monte Carlo calculations give B values of 0.155 and 0.176 for the coincidences from detectors 1 and 2 respectively. With the value $\varphi = 0.84$ and the data of table 1, we obtain $\omega_0 = 0.0082 \pm 0.0055$ from detector 1 and $\omega_0 = 0.0047 \pm 0.0047$ from detector 2. A slight improvement in accuracy is obtained by combining the data for both detectors and using a B factor estimated for the combined detector system. This gives the result

$$\omega_0 = 0.0069 \pm 0.0040 \pm 0.0014(\text{sys})$$

for the initial sticking coefficient, the systematic uncertainty reflecting an allowance for a 10% uncertainty in the Monte Carlo estimations of φB and for some systematic error in the data reduction procedures.

The preliminary value reported from the direct measurement of ω_0 at LANL is [15] $\omega_0 = 0.0080 \pm 0.0015 \pm 0.0012(\text{sys})$. This was obtained from the ratio of coincidence rates measured using a target geometry similar to that of the present experiment, at D–T pressures of 1800 and 490 Torr. It was not possible to measure neutron singles rates in the LANL experiment, hence the sticking coefficient was determined by assuming that the fusion rate per incident muon scales as the square of the D–T target gas pressure p. Scaling as p^2 is based on the expectation that: (i) the number of muon captures forming $d\mu$ or $t\mu$; and (ii) the formation rate of $dt\mu$ are each proportional to the target density, and hence to the pressure. However, the decrease with pressure may not be linear for the former because of the increasing fraction of muons that, having stopped in the gas, are transferred to the target walls, or for the latter, because of the increasing importance of epithermal $dt\mu$ production [19], that is direct $dt\mu$ formation during the increasingly longer thermalisation time of the muonic atom. The data obtained at 710 and 490 Torr demonstrate that the dependence of the fusion rate on pressure could be determined by extending the present experiment. This would be equivalent to measuring the $dt\mu$ formation rate at high temperatures [20].

The present preliminary result is consistent with the LANL value [15] and is independent of theoretical assumptions concerning the mechanism of muon-catalysed fusion. The LANL value, in contrast, depends on the assumed p^2 dependence of the fusion rate in D–T targets, which still needs to be tested experimentally. The indirect experiments that determine ω, and hence ω_0, from the time evolution of fusion neutron emission [8, 9, 11, 12] are inherently vulnerable to systematic errors, for example through their dependence on knowledge of neutron detection efficiencies. The density dependence assigned to q_{1s}, the fraction of muons that reach the $d\mu$ ground state, is also important in evaluating these measurements [21] and the difference between $\omega = 0.005$ [9, 11] and $\omega = 0.010$ [8] reported for low densities could arise from this source. The need for a more accurate measurement of ω_0 obviously remains. The present method, used in conjunction with the RAL pulsed muon source, should be capable of meeting this need.

These investigations have been supported in part by the Science and Engineering

Research Council, the Foundation for Fundamental Research on Matter (FOM), the Netherlands Organisation for Scientific Research (NWO) and the Foundation for Research Development (FRD). We gratefully acknowledge helpful discussions with J S Cohen concerning the evaluation of muon-stripping effects. Two of us (FDB and WAC) record our thanks for hospitality extended by the University of Birmingham.

References

[1] Breunlich W H, Kammel P, Cohen J S and Leon M 1989 *Ann. Rev. Nucl. Part. Sci.* **39** 311
[2] Leon M 1989 *AIP Conf. Proc.* **181** 94
[3] Ponomarev L I and Fiorentini G 1987 *Muon Catalyzed Fusion* **1** 3
[4] Ponomarev L I 1988 *Muon Catalyzed Fusion* **3** 629
[5] Hayward S F, Monkhorst H M and Szalewicz K 1988 *Phys. Rev.* A **37** 3393
[6] Kamimura M 1989 *AIP Conf. Proc.* **181** 330
[7] Cohen J S 1987 *Phys. Rev. Lett.* **58** 1407
[8] Jones S E *et al* 1983 *Phys. Rev. Lett.* **51** 1757; 1986 *Phys. Rev. Lett.* **56** 588
[9] Breunlich W H *et al* 1987 *Phys. Rev. Lett.* **58** 329
[10] Bossy H *et al* 1987 *Phys. Rev. Lett.* **59** 2864
[11] Petitjean C 1989 *Fusion Engng Design* **11** 255
[12] Nagamine K *et al* 1988 *Muon Catalyzed Fusion* **2** 73
[13] Nagamine K 1990 *μCF89, Oxford, RAL Report Number 90-022*
[14] Alper B *et al* 1990 *μCF89, Oxford, RAL Report Number 90-022*
[15] Paciotti M A *et al* 1989 *AIP Conf. Proc.* **181** 38
[16] Eaton G H *et al* 1988 *Nucl. Instrum. Methods* A **269** 483
[17] Brooks F D, Davies J D, Pyle G J, Squier G T A and Eaton G H 1988 *Muon Catalyzed Fusion* **2** 85
[18] Cohen J S 1988 *Phys. Rev.* A **37** 2343
[19] Cohen J S and Leon M 1985 *Phys. Rev. Lett.* **55** 52
[20] Kammel P 1985 *Lett. Nuovo Cimento* **43** 349
[21] Jones S E 1989 *AIP Conf. Proc.* **181** 2
Anderson A N 1989 *AIP Conf. Proc.* **181** 57

Appendix B

Reproduction of paper in μCF6:(1991) (in press)

SIMULATION AND EMULATION OF DIRECT MEASUREMENTS OF ω_0 IN dt μCF

C.G.L. HENDERSON, F.D. BROOKS and W.A. CILLIERS
Department of Physics, University of Cape Town, Rondebosch 7700, South Africa

G.J. PYLE and G.T.A. SQUIER
School of Physics and Space Research, University of Birmingham, Birmingham B15 2TT, UK

Monte Carlo simulations have been used to model and study characteristics of alpha–neutron coincidence detection systems used in direct experimental measurements of the initial sticking coefficient ω_0 in dt μCF. Some characteristics of these systems have also been measured experimentally, using the ^{3}H(d, n)^{4}He reaction to emulate dt μCF.

1. Introduction

Several of the direct methods proposed or used to measure sticking coefficients in muon catalyzed fusion [1] depend on differences in stopping powers to distinguish singly- and doubly-charged fusion products. In the experiment of the RAL collaboration [2], for example, range differentiation occurs in tha gas (D–T and D_2) and the thin mylar windows (fig. 1(a)) traversed by the α or $\alpha\mu$ en route to the surface barrier detector (SBD). At a target pressure of 1500 Torr, most of the $\alpha\mu$ which are emitted towards the SBD reach this detector with energy exceeding 1.5 MeV, whereas α are either ranged out in the gas and target windows or arrive at the SBD with $E < 1.5$ MeV. A threshold of 1.5 MeV therefore selects only $\alpha\mu$ for measurement of coincidences with fusion neutrons detected by the NE213 scintillators (fig. 1(a)). The number of coincidences N_c and neutron singles N_n are recorded simultaneously. All fusions contribute to the neutron singles; thus, after subtracting backgrounds, the initial sticking coefficient ω_0 is obtained directly from the ratio of coincidences to singles,

$$\omega_0 = N_c/\phi B N_n, \tag{1}$$

where B is the probability that the extrapolated geometric path of a collinear $\alpha\mu$ associated with a detected fusion neutron intersects the SBD, and ϕ is the fraction of coincident $\alpha\mu$ on such paths which reach the SBD with energy exceeding the threshold of 1.5 MeV. The factors B and ϕ are estimated from Monte Carlo simulations (MCS) based on stopping power data, neutron cross sections [3] and muon stripping data [4].

© J.C. Baltzer AG, Scientific Publishing Company

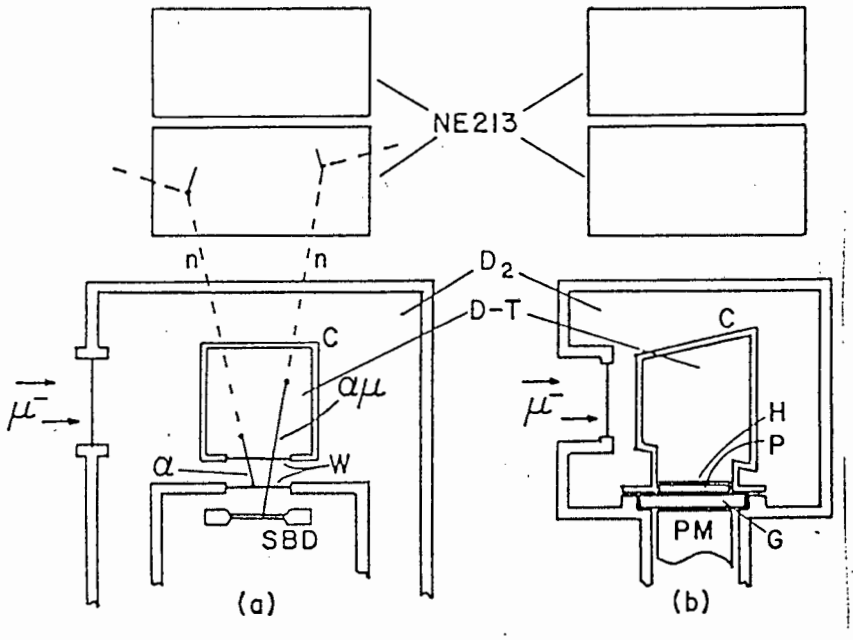

Fig. 1. Schematic diagrams of: (a) the RAL detection system; and (b) a proposed alternative system in which a 0.1 mm thick plastic scintillator P, protected by a 1.6 μm havar barrier H, detects the αμ. W are thin, aluminium-coated mylar windows, G is a glass window and the D–T target cells C are made of silver.

The low background levels attainable [2] using the RAL pulsed muon beam should allow the ratio N_c/N_n to be measured to a few percent. A comparable precision is therefore demanded in the calculation of B and ϕ, in order to determine ω_0 accurately. We report here on simulations of the RAL experiment and of an alternative geometry (fig. 1(b)). In order to check the MCS, we have also used the ^{3}H(d, n)^{4}He reaction to emulate dt μCF experimentally, and compared α–n coincidence measurements made in this way with those predicted by the simulations.

2. Monte Carlo simulations (MCS)

Simulations of the μCF experiments (fig. 1) were initiated by estimating the spatial distribution of fusions in the D–T targets using the code DEGRAD. An arbitrary sticking fraction of 0.5 was assumed in order to determine the characteristics of the two types of fusion with similar statistical accuracy, and the histories of individual collinear fusion pairs, n and α or n and αμ, were simulated. The α and αμ were tracked with energy decreasing in steps of 1–10 keV, using the data calculated by Cohen [4] to estimate the probability of muon stripping at each point along the αμ path. Neutron interactions with both the carbon and the hydrogen components of the scintillators were considered and neutron histories, including multiple scatterings,

were followed until the neutron either escaped from the system or dropped to an energy less than 0.1 MeV. The output from the MCS included detector efficiencies and singles and two-parameter spectra in addition to the B and ϕ factors.

3. Emulation of dt μCF

Alpha–neutron coincidences imitating those from dt μCF were obtained by using a DC deuteron beam to induce the reaction $^{3}H(d, n)^{4}He$ in a tritium gas target (fig. 2(a)) at a pressure of 400 Torr. An aperture A (diam. 2 mm) on the side of the cell, sealed by a 1.6 μm havar window, allowed α emitted at 90° to the deuteron beam to escape to the detector D, which was either an SBD or a thin NE102 plastic scintillator. The incident energy was adjusted so that deuterons entering the T_2 gas were degraded to 108 keV (the energy of the well-known resonance for this reaction) at the intersection of the beam with the α exit direction. Coincident 14.1 MeV neutrons emitted at the associated angle of 84° were detected in the NE213 scintillator, using a LINK 5010 pulse shape discriminator to reject gamma background events. The correct deuteron energy was easily found by tuning the beam energy for maximum coincidence rate using a smaller neutron detector (50 mm diam.) placed at the associated neutron angle.

Measured and simulated response functions (pulse height spectra) for an NE213 detector ($130 \times 130 \times 70$ mm) that was used in the RAL experiment are shown in fig. 2(b). The histogram shows the spectrum measured using the emulation system (fig. 2(a)). Curve M shows the simulated spectrum from the MCS and curves A–E show the components of M. Spectra M and A–E have been convoluted with a Gaussian distribution to simulate the pulse height resolution of the system. The width of this Gaussian was adjusted for best fit at the 14.1 MeV recoil proton edge and constrained to vary as $\sqrt{L}$ for other pulse heights L.

Several features of the response function M are clarified by reference to the components A–E. The main component A, due to n–p elastic scattering, shows a rise at high pulse heights which is due to neutrons undergoing multiple n–p scattering in the detector. The steep rise at low pulse heights is attributed to neutron reactions on the carbon component of the scintillator, particularly $^{12}C(n, \alpha)^{9}Be$ (component B) and $^{12}C(n, n')3\alpha$ (component C). Components D and E are associated with the n–p scattering (proton recoils) of neutrons which have first been degraded by scattering on carbons, elastic scattering in the case of D and inelastic scattering to the ^{12}C 4.43 MeV level in the case of E. It is evident that neutron interactions with carbon have a significant effect on the response function at 14.1 MeV and should be considered when using low thresholds for neutron detection in dt μCF.

The arrangement of fig. 2(a) may also be used to determine the absolute efficiency of the NE213 detetctor for detecting 14.1 MeV neutrons, provided every α detected is associated with a neutron entering the NE213. Preliminary measurements by this method give efficiencies consistent with those estimated from the MCS.

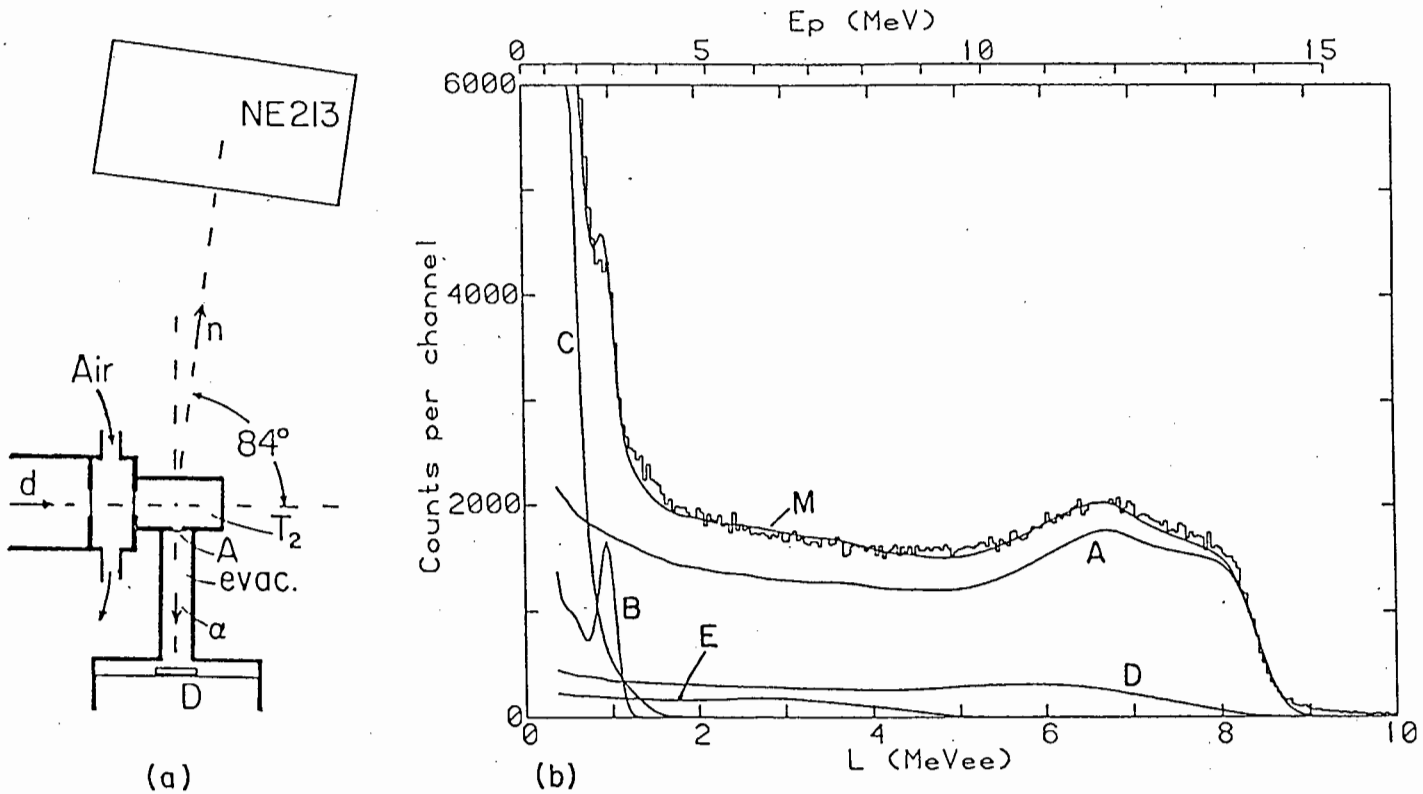

Fig. 2. (a) Schematic diagram of the system for emulating μCF experiments via the ^{3}H(d, n)^{4}He reaction. (b) Response function of NE213 detector (130 × 130 × 70 mm) for 14.1 MeV neutrons, showing experimental measurement (histogram), Monte Carlo simulation M and components A–E of M. The NE213 pulse height L is calibrated in MeV electron equivalent. The calibration against proton energy is shown above.

Absolute neutron detection efficiencies, although essential for some other μCF experiments, are not required for the sticking experiments considered here.

4. Coincidence distributions and backgrounds

The agreement between the simulated and emulated response functions (fig. 2(b)) lends confidence to the MCS and encourages its use in calculations of B and ϕ and in studies of other features of μCF experiments. Figure 3 shows, for example, simulations of the numbers of coincidences as a function of the time difference $T = T_\alpha - T_n$ between neutron and alpha detection and either: (a) the energy E measured by the SBD, or (b) the pulse height L measured by the plastic scintillator. In the simulations for the RAL system, we assume a time resolution of 3.0 ns (FWHM) and an energy resolution of 0.15 MeV (FWHM) at 3.5 MeV (varying as $\sqrt{E}$ at other energies) for the SBD. The alternative system (fig. 1(b)), which detects alphas in a thin plastic scintillator protected from the beta activity of the tritium by a thin (1.6 μm) havar barrier [5], achieves better timing, but at the expense of considerably degraded energy resolution. In the simulations for this system, we use the data obtained from the emulation experiments (section 3); a time resolution of 1.0 ns (FWHM) and pulse height resolution of 50% (FWHM) for 1.5 MeV alphas, varying as $\sqrt{L}$ for other energies.

The discrete loci of $\alpha\mu$–n coincidences in the E–T or L–T planes in fig. 3 provide the means for identifying and measureing sticking in these experiments. The events below these loci include the small fraction of α which reach the SBD or the plastic scintillator and some of the small fraction $(1 - \phi)$ of $\alpha\mu$ which are stripped of their μ before reaching the SBD (fig. 3(a)) or the havar barrier (fig. 3(b)). The MCS did not simulate any background coincidences, whereas actual experiments would generate background due to both accidental coincidences (from non-associated particles) and real coincidences (from associated, non-fusion particles). Experience at RAL [2] showed fewer accidental coincidences (which spread evenly in the T coordinate) than real coincidence background (RCB) events. Muon–nucleus interactions in the material surrounding the D–T gas (cell walls and alpha detector) are a possible source of the RCB. The target cells (fig. 1) are made from high-Z material (silver) so as to remove muons not captured in the D–T gas (the vast majority) very rapidly and the RAL data analysis excludes events earlier than 1 μs after the beam pulse to allow time for this muon scavenging to be completed. Muon–nucleus interactions in the surroundings may nevertheless persist beyond 1 μs, at a low level, if, for example: (a) a small fraction of dμ or tμ atoms formed in the D–T target gas diffuse slowly to the cell walls, or (b) multiple scattering leads to a few muons capturing in light elements ($Z < 15$) in or near to the alpha detector. In either case, since 40 MeV or more energy may be released in a muon–nucleus interaction, the products responsible for the RCB signals are likely to include some high-energy particles and the spread in T for RCB events should therefore be less than for fusion events. If

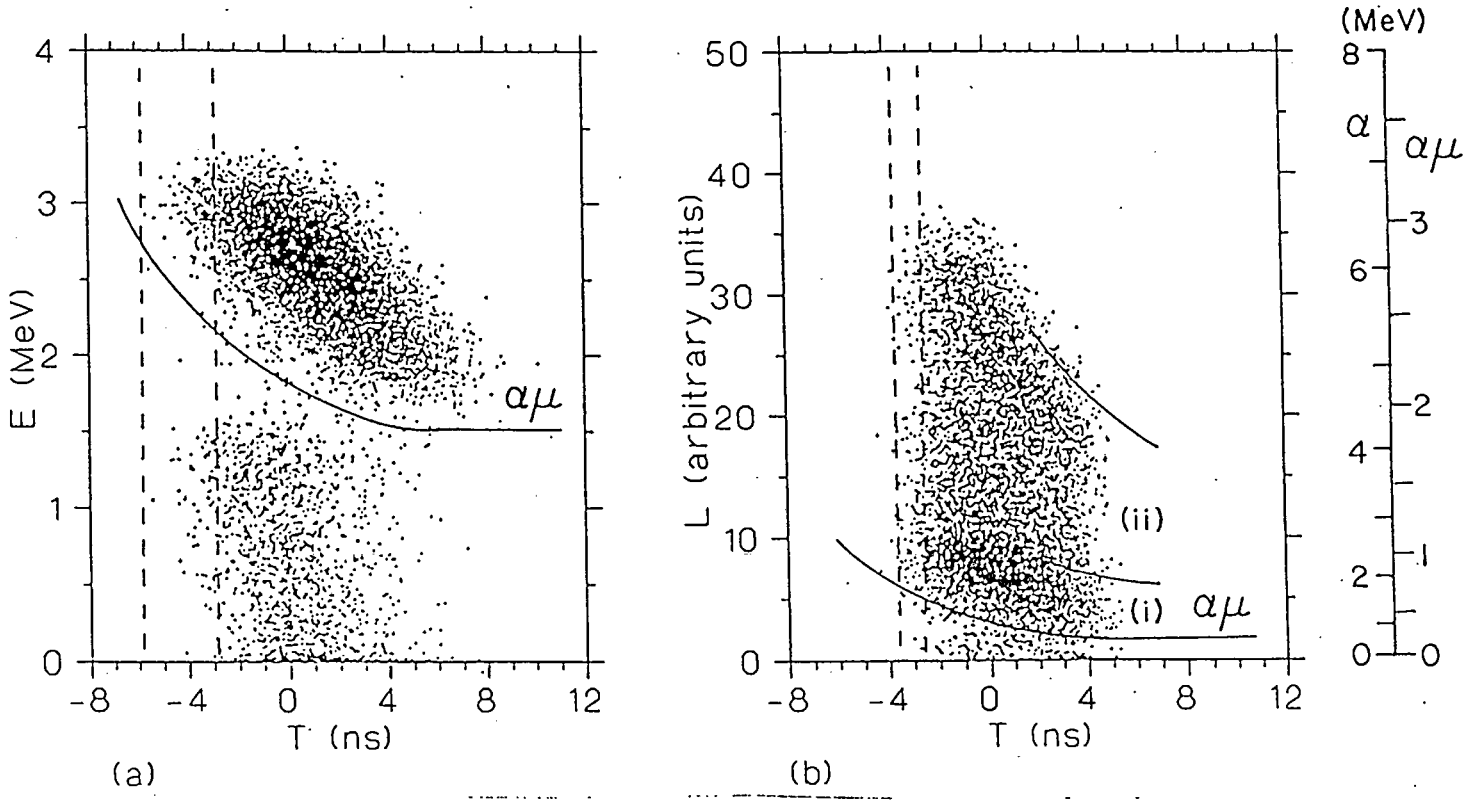

Fig. 3. Monte Carlo simulations of coincidences as a function of the alpha–neutron time difference T and detected α or $\alpha\mu$ energy E (or pulse height L) for: (a) the RAL system (fig. 1(a)) at a target pressure of 1500 Torr, and (b) the alternative system (fig. 1(b)) at a target pressure of 1800 Torr. The solid lines indicate cuts to select $\alpha\mu$ and the dashed lines show FWHM for the time distributions of RCB originating in or near to the alpha detectors. In (b) $\alpha\mu$ which are: (i) stripped in the havar, and (ii) remain unstripped for part or all of their path in the plastic are indicated. The calibrations of the plastic scintillator pulse height scale against energy, for α and $\alpha\mu$, respectively, are shown on the right-hand side.

all RCB were due to mechanism (b) alone, for example, then time distributions of these events should form groups of FWHM corresponding to the system time resolution and located as shown by the dashed lines in fig. 3. Time resolution may therefore be important for discriminating against RCB.

The simulation (fig. 3(b)) for the alternative system (fig. 1(b)) shows the $\alpha\mu$ locus broadening into two regions corresponding to $\alpha\mu$ which: (i) are stripped in the havar, or (ii) remain unstripped for part or all of their passage to rest in the plastic. The well-known saturation quenching effects in organic scintillators are responsible for this broadening. Quenching is smaller (and thus pulse height is larger) for (ii) than for (i) because the charge of the particle over part of its path in the plastic is half that of a bare alpha.

The results of the simulations (fig. 3) show that both of the systems considered (fig. 1) should discriminate effectively against α–n coincidences. The RAL system (fig. 1(a)) gives better separation than the alternative system (fig. 1(b)) using the plastic scintillator, but may be inferior to the plastic in discriminating against RCB due to poorer time resolution. If the RCB is indeed due to high-energy particles mimicking the $\alpha\mu$ in the fusion signature, then discrimination against this background could be enhanced by inserting a second scintillator of longer scintillation decay time between the plastic and the glass window in fig. 1(b), to form a phoswich. Fusion signals would then be characterised by a fast component alone (plastic only), whereas RCB signals would contain both slow and fast components. Pulse shape discrimination could then be used to discriminate against RCB. Tests made using the emulator system (fig. 2(a)) have verified that a detector of this type will operate successfully.

Acknowledgements

We thank the Science Research Council (UK) and the Foundation for Research Development (SA) for financial support, the RAL collaboration for stimulating discussions, A.P. Back, S.S. Jagpal and D. Momsen for technical support, and M.S. Allie, A. Buffler, M.J. Oliver and H.W. Schmitt for their assistance during the experiments.

References

[1] W.H. Breunlich, P. Kammel, J.S. Cohen and M. Leon, Ann. Rev. Nucl. Part. Sci. 39(1989)311.
[2] J.D. Davies et al., J. Phys. G, in press.
[3] *CINDA 76/77* (IAEA, Vienna, 1977).
[4] J.S. Cohen, Phys. Rev. A37(1988)2343.
[5] W.A. Cilliers and F.D. Brooks, this volume.

Appendix C

Extension of MUGLU to 63 MeV neutrons

The neutron detector code was modified to produce lineshapes for NE213 for 63 MeV neutrons. The cross-sections for neutrons on carbon are not well known at this energy, and the carbon contribution other than the $^{12}C(n,p)^{12}B$ was disregarded.

In an experiment to measure the np capture cross section [43], a BA2 cell of NE213 is used as an active target. The neutrons impinging on the NE213 undergo the capture reaction $H(n,\gamma)d$. The deuteron is detected by the pulse it makes in the NE213, while the gammas are detected by a ring of NaI detectors around the target. In order to obtain the absolute cross section of the capture reaction, amongst other things, the number of incident neutrons must be known. This is done by measuring the number of H(n,n)H elastic scatters. Since the H(n,n)H cross section is well known, and the number of protons in the cell can easily be obtained, the number of H(n,n)H events can be used as a benchmark for the cross sections of various reactions in the detector.

With PSD, the various charged particles produced by neutrons interacting in the detector can be separated, namely electrons, protons, deuterons etc. Further, the protons which escape from the scintillator can be separated from those which come to rest within the scintillator volume. Figure C.1 is a density plot of L and S for 63 MeV neutrons incident on the BA1 detector. The escaping protons are lost amongst the electron signal.

Figure C.2 shows the proton locus in figure C.1 projected onto the L axis [95]. The contribution from the C(n,p)B reaction is hatched. Due to

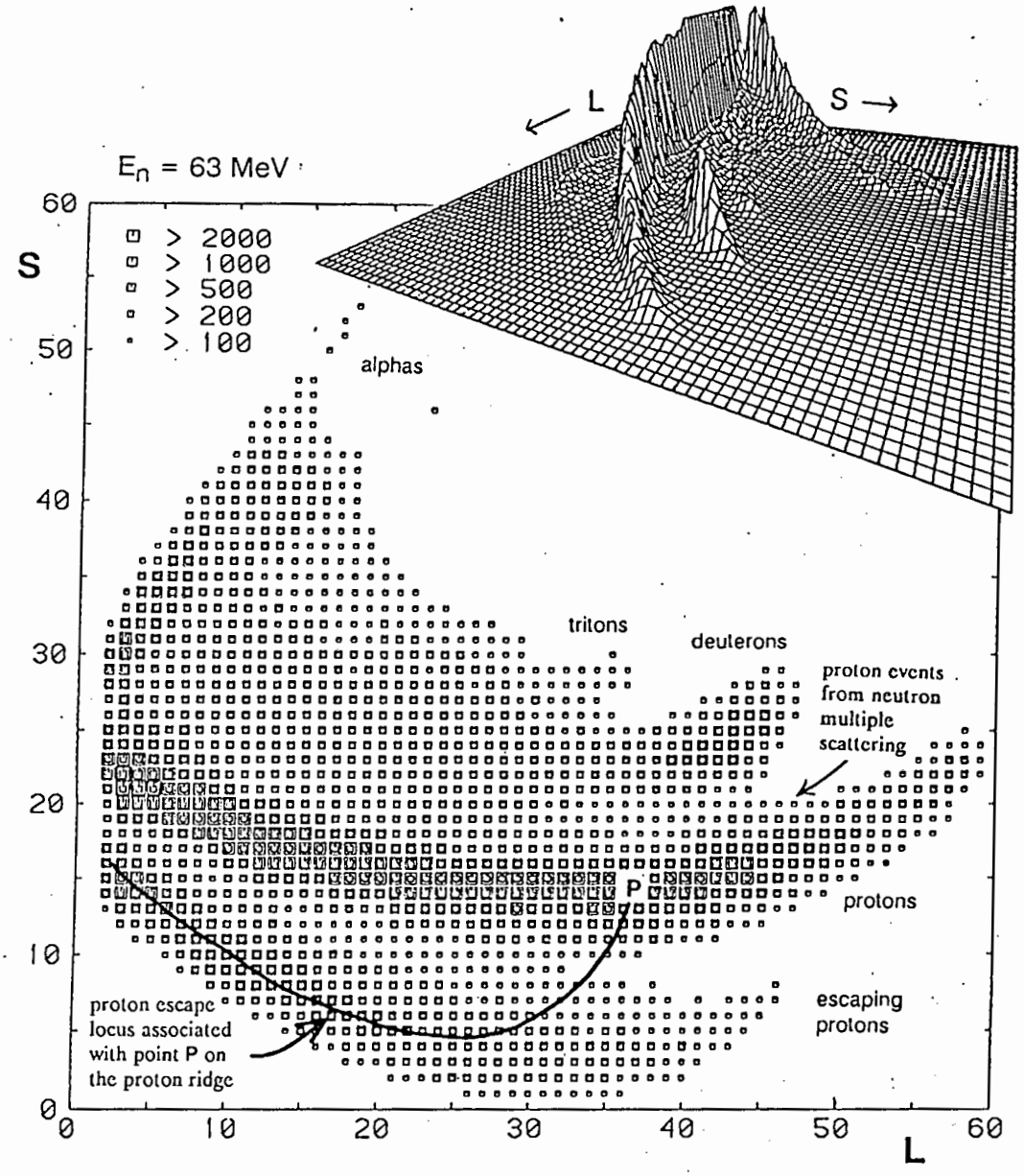

Figure C.1: LS density plot of the response of a BA1 cell to 63 MeV neutrons impinging radially. Reproduced here by kind permission of A. Buffler.

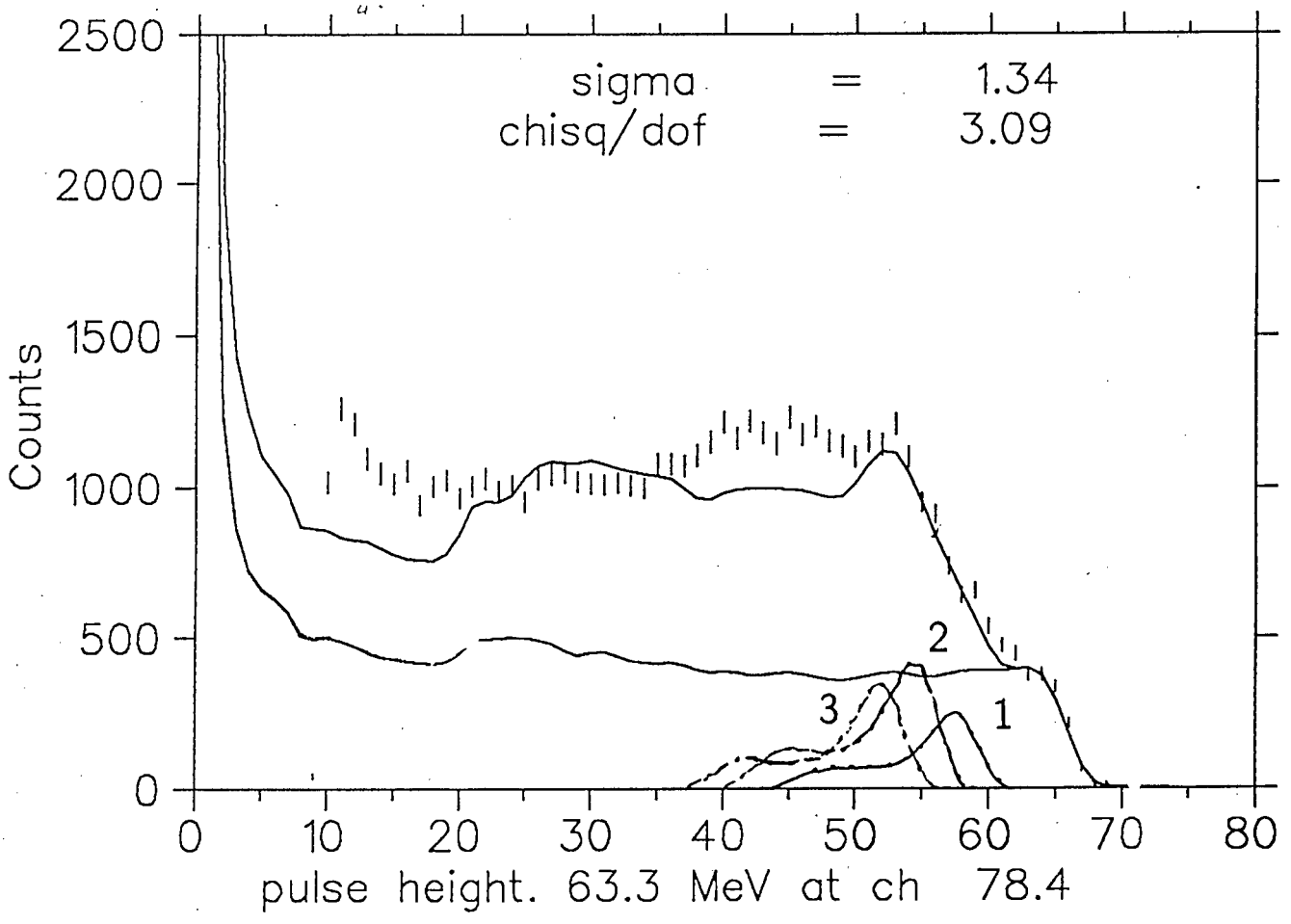

Figure 3.2: Points — a projection onto the L axis of the proton locus (labelled P in fig. C.1). The smooth curve is a fit of the calculated non-escaping proton locus and the contribution of the C(n,p)B reactions from MUGLU Included are three peaks (1) from the ground state of $^{1}2B$, (2) from the 4.3 MeV state, and (3) the giant dipole resonance (7.4 MeV), and a continuum.

the 12 MeV Q value of the above reaction, the maximum energy a proton can have from an n-Carbon reaction is 51 MeV, while the maximum proton energy from np elastic scattering is of course 63 MeV. By fitting a calculated curve (non-escaping protons) from MUGLU to the last 12 MeV of the proton spectrum, the H(n,n)H elastic scattering contribution can be separated and corrected for escaping protons. Figure C.3 shows one such fit (dashed curve). The solid curve is the corrected proton spectrum as calculated by MUGLU.

The modifications made to MUGLU include the addition of the C(n,p)B reactions, tagging of the escaping protons, and allowance for the considerable space charge saturation which occurs in the PM tube for pulses at these energies. New expressions for the specific energy loss of protons in NE213 and hence for the Birks relation had to be used to cope with the higher energies involved. The proton spectrum from the C(n,p)B reaction was estimated from McNaughton et al. [96], Ford et al. [97], and Subramanian et al. [98]. A detailed description of the use of MUGLU for the estimation of proton recoil spectra is given in ref. [95]. Future H(n,γ)d experiments are underway at NAC, Faure, South Africa, using larger (K) detectors and detectors to catch the escaping protons, which will require further modification of MUGLU.

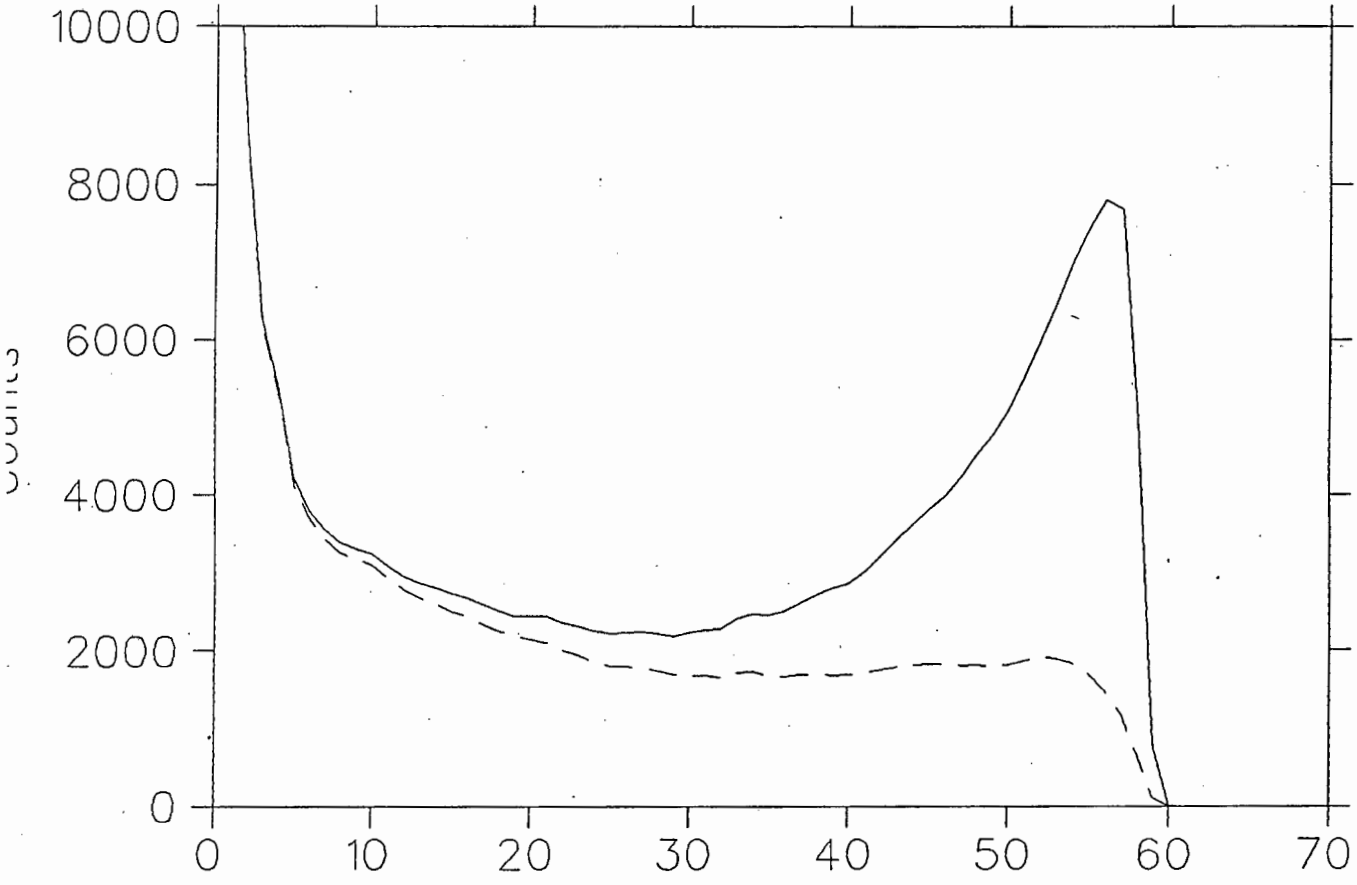

Figure 3.3: The fitted H(n,n)H pulse height spectrum from MUGLU. Lower curve: Non-escaping recoil protons. Higher curve: all proton recoils.

Appendix D

Monte Carlo technique

The basic building block of the Monte Carlo technique [99,100,101] is the choosing of a number at random according to a given distribution. This number is then processed, i.e. either used in an equation, or has questions asked about it, e.g. is this number within a certain range?

Applying the Monte Carlo method involves breaking up a complex problem into simple steps, each of which follows from the previous step with a certain probability, or which is a process described by a probability law. For example, in the detection of a neutron, there is a certain probability that it will scatter, say, on a proton. A random number is selected. Depending on this number, a decision is made whether the incoming neutron did, in fact, scatter on a proton. If it did, then the next step is calculated, which selects the angle of scatter at random according to the measured or theoretical H(n,n)H elastic scattering angular distribution. The angles of the neutron and proton are used to make further assumptions about the process. If the neutron is found not to have scattered with a proton, then another decision is called for: did the neutron interact with a carbon nucleus? — and so on. Obviously, the above scenario has to be enacted many times in order to expose the underlying probability functions. It is also quite clear that the result cannot be arrived at analytically. In general, if a system governed by probability laws depends on another such system, the Monte Carlo approach will be necessary.

D.1 Random choices over a distribution

All Monte Carlo computer codes are based on pseudorandom number generators (PRGs). These functions produce a series of random-like numbers between 0 and 1 which has a uniform distribution. In many cases, this uniform distribution is sufficient, for example, if an event has a 60% chance of happening, one decides whether it has happened or not simply by calling the PRG and then asking the question (see figure D.1: 'is the number returned by the PRG less than 0.6?'.

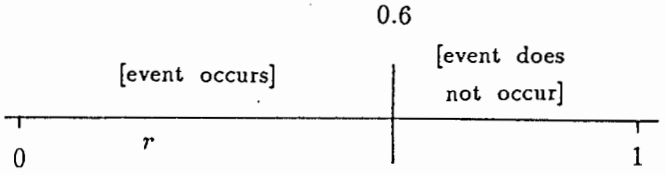

Figure D.1: Using the PRG to determine whether an event with 60% probability has occurred

There are two techniques for converting a uniform distribution of random numbers into a non-uniform distribution.

D.1.1 Von Neumann rejection method

The rejection method involves at least two calls to the PRG, or throws of the dice, if you will. Suppose we are trying to select a random number x according to a distribution $f(x)$, over an interval (a, b) (see figure D.2. Firstly, the local maximum $\mathcal{F}$ of the function $f(x)$ over the interval (a, b) is found. Then a trial value of x_t is selected from the *uniform* distribution bounded by a and b such that

$$x_t = a + r_1(b - a) \tag{D.1}$$

where r_1 is a number returned by the PRG. The probability function $f(x_t)$ is evaluated at x_t. A second number r_2 is requested from the PRG.
If

$$r_2 \leq f(x_t)/\mathcal{F}, \tag{D.2}$$

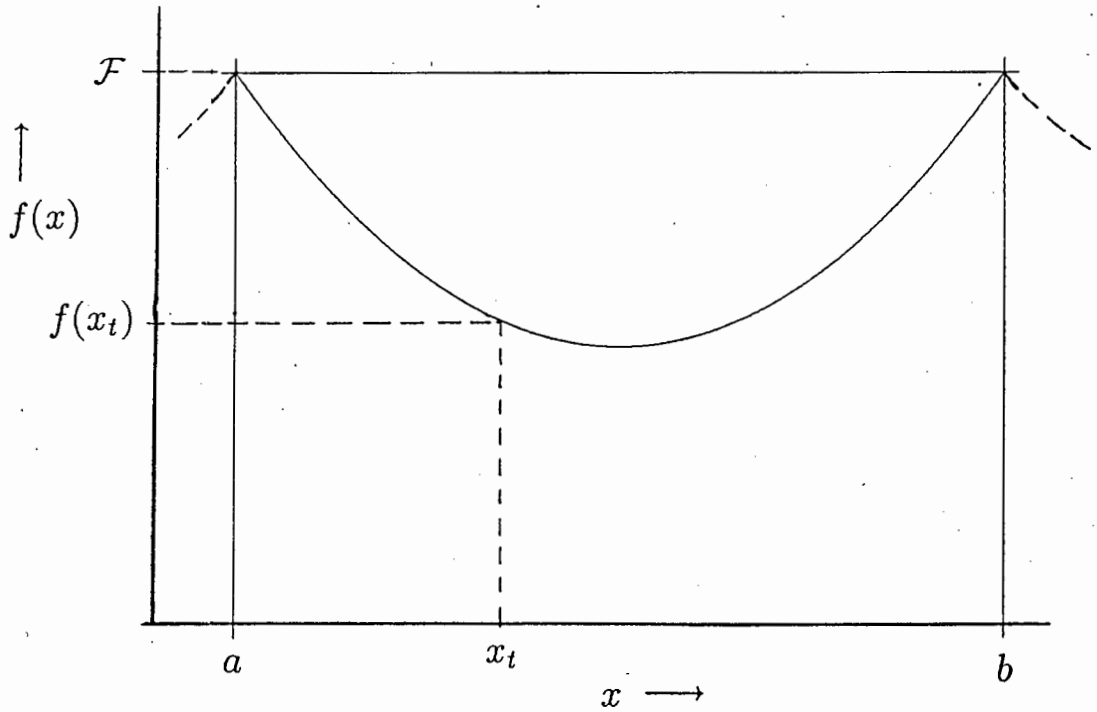

Figure D.2: The use of the rejection technique to select a series of random numbers x from a probability distribution $f(x)$. In this case, x is an angle $\cos\theta$ and $f(x)$ is the angular distribution of recoil protons from np elastic scattering.

then X_T is accepted and control passes to the next step in the Monte Carlo.

If

$$r_2 > f(x_t)/\mathcal{F}, \tag{D.3}$$

then the number x_t is *rejected* and another x_t must be chosen and the process repeated. Clearly, the greater the value of $f(x_t)$, the less the likelihood of x_t being rejected using this method. A histogram of x_t, built up over many repetitions of the rejection process, will eventually approximate $f(x)$.

D.1.2 Cumulative distribution method

The cumulative distribution method for selecting a random variable x from a distribution $f(x)$ involves in general solving the following equation for x:

$$F(x) = \int_{-\infty}^{x} f(x')dx' = r \tag{D.4}$$

where $F(x)$ is the *cumulative distribution function* corresponding to $f(x)$ (see figure D.3) and r is a random number selected from a uniform distribution such that $0 < r < F(+\infty)$. As we normally choose x from an interval (a, b), it is sufficient to choose r such that

$$0 \leq r \leq F(b) - F(a) \tag{D.5}$$

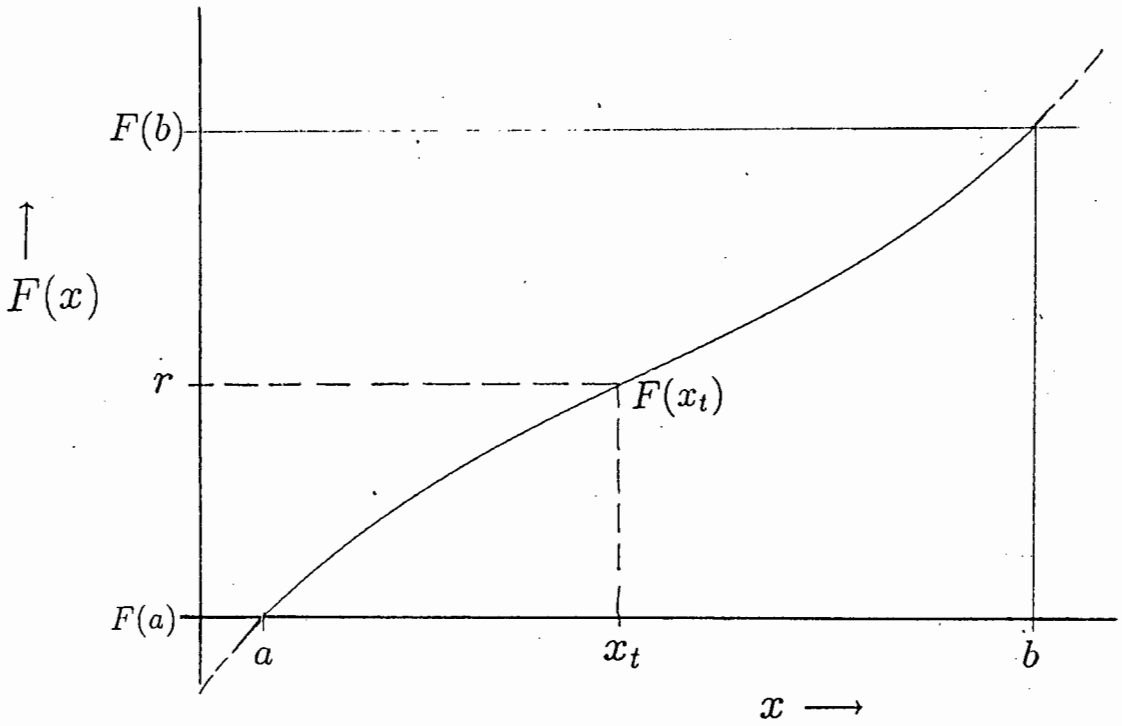

Figure D.3: Selection of a random number x from a probability distribution $f(x)$ using the cumulative distribution method. The x and $f(x)$ are the same as in the figure above. In this case, $F(x)$, the cumulative distribution function of $f(x)$ is plotted against x. See text.

or

$$0 \leq r \leq \int_a^b f(x')dx' \tag{D.6}$$

The equation to solve for x_t is then

$$F(x_t) = \int_a^{x_t} f(x')dx' \tag{D.7}$$

This method lends itself to numerical integration. Once the limits of r have been established, it is a simple matter to integrate $f(x)$ for example using trapezium rule until $F(x) > r$.

If equation D.7 can be solved analytically, then the cumulative distribution method is the way to go. If it cannot, then it is more efficient to use the rejection method, unless the average of f is much smaller than $\mathcal{F}$ (f may be a steeply increasing/decreasing concave function). If this is the case, the rejection method might require more operations to select a number than the numerical integration uses. It is possible to replace $f(x)$ with a table of data, in which case, the value of the distribution is read from the table using x as a pointer.

An example of the employment of the cumulative distribution method is seen when selecting the angle that the neutron is scattered after smiting a proton in the NE213 liquid scintillator. The distribution function i.e. the

angular differential cross section (see equation 2.24), is given as

$$\frac{d\sigma}{d\Omega} = \frac{\sigma}{4\pi}\left[\frac{1 + b\cos^2\theta}{1 + b/3}\right] \tag{D.8}$$

where $b = (E_n/90)^2$ and θ is the centre of mass angle of the recoil proton. Since we are selecting a solid angle, we are selecting a random $\cos\theta$. The cumulative distribution function is then:

$$F(\cos\theta) = \int_{-1}^{\cos\theta} \frac{d\sigma}{d\Omega} d\Omega \tag{D.9}$$

$$= \frac{\sigma}{4\pi(1 + b/3)} \int_0^{2\pi} \int_{-1}^{\cos\theta} \left(1 + b\cos^2\theta'\right) d(\cos\theta') d\phi \tag{D.10}$$

$$= \frac{\sigma}{2(1 + b/3)} \left[\cos\theta' + \frac{b}{3}\cos^3\theta'\right]_{-1}^{\cos\theta} \tag{D.11}$$

$$= \frac{\sigma(1 + b/3 + \cos\theta + b/3\cos^3\theta)}{2(1 + b/3)} \tag{D.12}$$

Clearly, in this case, $a = -1$ and $b = 1$, $F(a) = 0$ and $F(b) = \sigma$. Hence we must pick the random number r such that

$$0 \leq r \leq \sigma \tag{D.13}$$

and solve

$$F(\cos\theta) = r \tag{D.14}$$

for r. This is easily done, after a bit of donkey-work, applying the rule for the solution of the cubic equation. The proton recoil angle is thus obtained:

$$\cos\theta = \sqrt[3]{a + \sqrt{27/b^3 + a^2}} + \sqrt[3]{a - \sqrt{27/b^3 + a^2}} \tag{D.15}$$

where

$$a = \frac{3(\sigma/2 - r)(1 + b/3)}{\sigma b} \tag{D.16}$$

Even though this cumulative distribution function is soluble, it takes far less computing time to use the rejection method, especially for lower energies and thus nearly flat distributions!

D.1.3 Cumulative rejection method

The third selection method employed is used when the random variable x is itself the subject of a numerical integration. The probability function $f(x_s)$ is then evaluated at each step x_s of the numerical integration. An example is the muon stripping calculation performed while the $\alpha\mu$ is slowing in a medium (see section 2.5.2). Instead of calculating the total stripping cross section numerically for each $\alpha\mu$, using the rejection method to calculate the position of stripping, and then calculating the energy loss of the $\alpha\mu$ prior to stripping; the probability p_s of the muon being stripped from the $\alpha\mu$ for each step was calculated and a random number r between 0 and 1 requested from the PRG.
If

$$r < p_s, \tag{D.17}$$

then the muon was taken as having been stripped from the $\alpha\mu$ and the numerical integration continues, now for an α slowing in the medium.
If

$$r > p_s, \tag{D.18}$$

then the very idea of the $\alpha\mu$ being stripped while traversing that bite of medium was rejected, and the $\alpha\mu$ allowed to continue unmolested until the next step of the numerical integration.

D.2 Multiple Choice

The last selection method employed in MUGLU is the multiple choice method, where the process involves selecting one of several options each with different probability of occurring. This best illustrated in an example.

When a neutron interacts in the neutron detector, it can participate in a variety of interactions (see section 2.6.1, figure 2.15, and table 2.1), each of which has a certain cross section. The total cross section σ_T of the liquid NE213 is calculated, followed by the effective cross-section. The probability of a neutron penetrating a distance x into a medium without clobbering a nucleus is given by:

$$p = 1 - \exp(-\tau\sigma_T x) \tag{D.19}$$

where τ is the number of atoms per square centimetre in the medium. A large volume of NE213 is considered — as opposed to the limited volume in the detector — such that $p \longrightarrow 0.99$[1]. A value for x is selected using the

[1] for the K5 detector, p is about 0.25.

cumulative distribution method (equation D.19 slips easily into the right form — see ref.[99], page 185). If the chosen x causes the interaction to take place outside the detector, i.e. x is larger than the neutron's extrapolated path through the detector, then the neutron has passed though the detector and is not seen. If x places the interaction within the detector, we have to decide what type of interaction took place.

The neutron can do one of five things:

1. it can undergo elastic scattering with a proton — cross section σ_{np},
2. it can scatter elastically with a carbon nucleus — cross section $\sigma_{nC(el)}$,
3. it can scatter inelastically with a carbon nucleus — cross section $\sigma_{nC(in)}$,
4. it can smash the carbon nucleus into three alpha particles ($C(n,n')3\alpha$) — cross section $\sigma_{nC3\alpha}$,
5. or it can break the carbon nucleus into an alpha and a beryllium nucleus ($C(n,\alpha)^9Be$) — cross section $\sigma_{nC\alpha Be}$.

The PRG is called on to deliver a random number r_1 uniformly distributed between 0 and 1. This is multiplied by σ_T to arrive at r, a random number between 0 and σ_T.

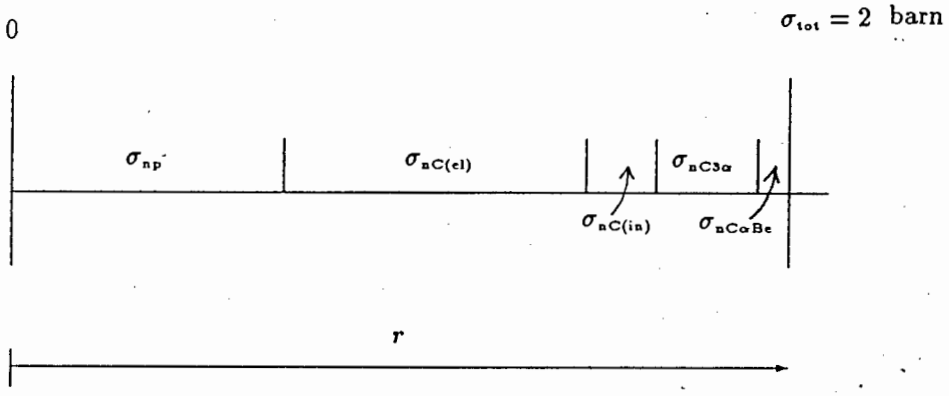

Figure D.4: Selecting the type of interaction the neutron undergoes in the neutron detector. See text.

Now the various cross sections are 'stacked' on top of each other, as figure D.4 suggests. If r falls between 0 and σ_{np}, the neutron is considered

to have undergone elastic scattering with a proton and the appropriate train of events set in motion. If r falls between σ_{np} and $\sigma_{np} + \sigma_{nC(el)}$, then the portion of the code dealing with elastic scattering with carbon is activated, and so on. In this way, the program decides first whether or not there will be an interaction, using the total cross section, and then homes in on what type of reaction it was.

The reader will have noticed that this approach to neutron detection is not the same as that set out in the opening paragraphs of this appendix. Both methods are valid, but the multiple choice method is much more efficient, killing, as it were, five birds with two stones.

Bibliography

[1] F. C. Frank. *Nature*, **160** (4068):525–527, 1947.

[2] C. M. G. Lattes, G. Occhialini, and C.F. Powell. *Nature*, **160** (4066):453–456, 1947.

[3] D. L. Livesey. *Atomic and Nuclear Physics.* Ginn Blaisdell; Waltham, Mass., 1966.

[4] L. Alvarez et al. *Adv Exp Phys*, α:72–79, 1972.

[5] L. Alvarez et al. *Phys. Rev.*, **105**(3):1127–1128, 1957.

[6] A. Ashmore et al. *Proc. Phys. Soc (London)*, **71**:161, 1958.

[7] V. P. Dzhelepov et al. *Sov. Phys. JETP*, **23**:820, 1966.

[8] E. A. Vesman. *Sov. Phys. JETP Lett*, **5**:113, 1967.

[9] S. S. Gershtein and L. P. Ponomarev. *Phys. Lett. B*, **72B** (1):80–82, 1977.

[10] V. M. Bystritsky et al. *Phys. Lett. B*, **94B**:476, 1980.

[11] C. Petitjean. *Fus Engng Design*, **11**:255, 1989.

[12] H. Bossy et al. *Phys. Rev. Lett.*, **59** (25):2864–2867, 1987.

[13] K. Nagamine. *μCF89*, RAL REP no. 90-022:, 1989.

[14] S. E. Jones et al. *Phys Rev Lett*, **51** (19):1757–1760, 1983.

[15] S.E. Jones, A.N. Anderson et al. *Phys Rev Lett*, **56** (6):588–591, 1986.

[16] W. H. Breunlich et al. *Phys. Rev. Lett.*, **58** (4):329–332, 1987.

[17] K. Nagamine. *Muon Cat. Fusion*, **2**:73, 1988.

[18] S. E. Jones. *Nature*, **321** :329–332, 1986.

[19] S. I. Vinitsky. *Sov. Phys. JETP*, **52**:353, 1980.

[20] J. D. Davies et al. *J. Phys. G*, **16** :1529–1537, 1990.

[21] M. A. Paciotti et al. In *MCF Workshop, NY:AIP conf proc 1988*, page 181, 1989.

[22] C. Petitjean, K.Lou et al. In *μCF89,RAL REP no.90-022*, pages 32–34, 1989.

[23] C. Petitjean, K. Lou et al. *PSI preprint*, pr-90(-38), 1990.

[24] P. Baumann et al. In *μCF89*, page 38, RAL-90-022, 1989.

[25] K. Lou, C. Petitjean et al. *PSI preprint*, pr-90(-40):, 1990.

[26] S. S. Gershtein, Yu. V. Petrov, L. Ponomarev, L. Somov, and M. Faifman. *Sov. Phys. JETP*, **51** (6):1053–1058, 1980.

[27] L. Bracci and G. Fiorentini. *Phys Rep*, **86** (2):169–216, 1982.

[28] H. Rafelski. PhD thesis, 1987.

[29] J. D. Jackson. *Phys. Rev.*, **106** :2, 1957.

[30] Ya. B. Zel'dovich and S. S. Gershtein. *Sov. Phys. Usp.*, **3** (4):593–623, 1961.

[31] S. I. Vinitsky. *Sov. Phys. JETP*, **47**:444, 1979.

[32] B. Müller, H. Rafelski, and J. Rafelski. In *μCF89,RAL REP no.90-022*, pages 81–84, 1989.

[33] B. Müller and J. Rafelski. *Phys. Lett. B*, **164B** :223, 1985.

[34] L. Bracci and G. Fiorentini. *Nuclear Physics A*, **364**:383, 1981.

[35] J. D. Jackson. Proc. muon-catalysed fusion workshop. 1984.

[36] D. Ceperley and B. Adler. *Phys. Rev. A*, **A31** :1999, 1985.

[37] S. S. Gershtein et al. *Sov Phys JETP*, **53**:872, 1981.

[38] J. S. Cohen. *Muon Cat. Fusion*, **1**:179, 1987.

[39] C. Petitjean, K. Lou et al. *PSI preprint*, pr-90(-39), 1990.

[40] S. E. Jones and A. N. Anderson. In *μCF89*, page 13, RAL-90-022, 1989.

[41] G.F.Knoll. *Radiation Detection and Measurement.* Volume 1, J. Wiley and Sons, N.Y., 1987.

[42] F. D. Brooks, J. Davies, G. Pyle, G. Squier, and G. Eaton. *Muon Cat. Fusion*, **2**:85–92, 1988.

[43] M. S. Allie et al. *NAC/AK/*, 90(-01):item 7.1.1, 1990.

[44] C. G. L. Henderson, F. D. Brooks, W. A. Cilliers, G. J. Pyle, and G. T. A. Squier. *Muon Cat. Fusion*, **6** , 1991. In press.

[45] G. T. A. Squier. *Private communication* .

[46] P. Jipsen. Eloss, a program to calculate the energy loss of energetic particles in matter. 1984. Available on the UCTVAX, UCT.

[47] J. B. Marion and F. C. Young. *Nuclear Reaction Analysis.* North Holland, Amsterdam, 1968.

[48] H. H. Anderson and J. F. Ziegler. *Stopping Power and Ranges of Ions in Matter.* Volume 3,4,5, Pergamon NY, 1977.

[49] J. S. Cohen. *Phys. Rev. A*, **37** (7):2343–2348, 1988.

[50] J. B. Birks. *Proc. Phys. Soc.*, **A64**:874, 1951.

[51] F. D. Brooks. *Nucl. Instr. & Meth.*, **162**:477ff, 1979.

[52] T. Batsch and M. Moszynski. *Nucl. Instr. & Meth.*, **123**:341–352, 1975.

[53] A. del Guerra. *Nucl. Instr. & Meth.*, **135** :337–352, 1976.

[54] J. L. Gammel. *Fast Neutron Physics.* Volume 2, Interscience NY, 1963.

[55] J. B. Marion and J. L. Fowler, editors. *Fast Neutron Physics*, page 2209. Interscience, 1963.

[56] R. C. Haight, S. M. Grimes, R. G. Johnson, and H. H. Barschall. *Nucl. Sci. Eng.*, **87** :41–47, 1984.

[57] A. P. Stevens. Master's thesis, UCT, 1974.

[58] B. Antolković and Z. Doleneć. *Nuclear Physics A*, **237A**:235–252, 1975.

[59] B. Antolković, I. Šlaus, D. Plenković, P. Macq, and J. Meulders. *Nuclear Physics A*, **394** :87–108, 1983.

[60] J.K. Dickens. *ORNL*, 6462:, 1988.

[61] J.K. Dickens. *Computers in Physics*, **Nov/Dec**:, 1989.

[62] G. Haouat, J. Lachkar, J. Sigaud, Y. Patin, and F. Cocu. *Nucl. Sci. & Eng.*, **65** :331–346, 1978.

[63] E. Mezzetti, B. Minetti, and A. Pasquarelli. *Lett. Nuovo Cim.*, **22** (3):91–101.

[64] F. D. Smit and F. D. Brooks. *Nuclear Physics A*, **465**:429–444, 1987.

[65] R. Madey, F. Waterman, A. Baldwin, J. Knudson, J. Carlson, and J. Rapaport. *Nucl. Instr. & Meth.*, **151**:445–450, 1978.

[66] D.L. Smith, R.G. Polk, and T.G. Miller. *Nucl. Instr. & Meth.*, **64** :157–166, 1968.

[67] V. V. Verbinsky, W. R. Burrus, T. E. Love, W. Zobel, N. Hill, and R. E. Textor. *Nucl. Instr. & Meth.*, **65** :8–25, 1968.

[68] Y. Uwamino, K. Shin, M. Fujii, and T. Nakamura. *Nucl. Instr. & Meth.*, **204**:179–189, 1982.

[69] G. W. Clark. *IRE Trans. Nucl. Sci.*, **NS-7**:164, 1960.

[70] R. de Leo, G. D'Erasmo, A. Pantaleo, and G. Russo. *Nucl. Instr. & Meth.*, **119**:559–567, 1974.

[71] R. Gardner and K. Verghese. *Nucl. Instr. & Meth.*, **93** :163–167, 1971.

[72] R. Kuijper, C. Tiesinga, and C. Jonker. *Nucl. Instr. & Meth.*, **42**:56–60, 1966.

[73] A. Schaarschmidt and H. Keller. *Nucl. Instr. & Meth.*, **72** :82, 1969.

[74] F. James and M. Roos. MINUIT. *Computer Pysics Communications*, **10**:343–367, 1975.

[75] J. Fowler, J. Cookson, M. Hussain, R. Schwartz, M. Swinhoe, C. Wise, and C. Uttley. *Nucl. Instr. & Meth.*, **175** :449–463, 1980.

[76] H. H. Barschall, L. Rosen, and R. F. Taschek. *Rev Mod Phys*, **24**(1):1–14, 1952.

[77] D. G. Schuster. *Nucl. Instr. & Meth.*, **76**:35–42, 1969.

[78] C. M. Bartle, F. D. Brooks, D. T. L. Jones, W. M^{c}Murray, and R. Verbruggen. *Nucl. Instr. & Meth.*, **180**:165–171, 1981.

[79] H. Liskien and A. Paulsen. *Nuclear Data Tables*, **11**(7):569–619, 1973.

[80] J. L. Chuma. PLOTDATA *command reference manual.* Technical Report TRI-CD-87-03b, TRIUMF, 1990.

[81] L. A. Perkins and M. C. Scott. *Nucl. Instr. & Meth.*, **166** :451–464, 1979.

[82] M. Anghinolfi, G. Ricco, P. Corvisiero, and F. Masulli. *Nucl. Instr. & Meth.*, **165** :217–224, 1979.

[83] J. Lockwood, C. Chen, L. Friling, D. Schwartz, R. St. Onge, A. Galonsky, and R. Doering. *Nucl. Instr. & Meth.*, **138**:353–362, 1976.

[84] A. Pantaleo, L.Fiore, G. Guarino, V. Paticchio, G. D'Erasmo, E. Fiore, and N. Colonna. *Nucl. Instr. & Meth.*, **291**:570–576, 1990.

[85] J. Watson and R. Graves. *Nucl. Instr. & Meth.*, **117** :541–549, 1974.

[86] W. R. Burrus and V. V. Verbinsky. *Nucl. Instr. & Meth.*, **67** :181–196, 1969.

[87] Plasek, Miljanic, Valkovic, Liebert, and Phillips. *Nucl. Instr. & Meth.*, **111** :251–252, 1973.

[88] S. Thornton and J. Smith. *Nucl. Instr. & Meth.*, **96** :551–555, 1971.

[89] S. Howe, P. Lisowski, G. Russell, N. King, and H. Donnert. *Nucl. Instr. & Meth.*, **227** :565–570, 1984.

[90] R. C. Byrd and W. C. Sailor. *Nucl. Instr. & Meth.*, **274**:494–500, 1989.

[91] F. D. Brooks. *Private communication.*

[92] B. Alper et al. In *μCF89*, pages 35–38, RAL-90-022, 1989.

[93] W. A. Cilliers and F. D. Brooks. *Muon Cat. Fusion*, **6** , 1991. In press.

[94] R. E. Textor and V. V. Verbinski. *ORNL*, **-4160**:, 1968.

[95] A. Buffler. Master's thesis, UCT, 1990.

[96] M. M^{c}Naughton, N. King, F. Brady, and J. Ullmann. *Nucl. Instr. & Meth.*, **129**:241–245, 1975.

[97] T. Ford, G. Needham, F. Brady, J. Romero, and C. Castaneda. *Nucl. Instr. & Meth.*, **228** :81–88, 1984.

[98] T. S. Subramanian et al. *Phys. Rev. C*, 28(2):521–528, 1983.

[99] R. Ehrlich. *Physics and Computers: Problems, Simulations, and Data Analysis.* Houghton Mifflin Co., Boston, 1973.

[100] Cashwell and Everett. *The Monte Carlo Method for Random Walk Problems.* 519.282.

[101] W. K. Wilcke. *Nucl. Instr. & Meth.*, **225** :132–137, 1984.